

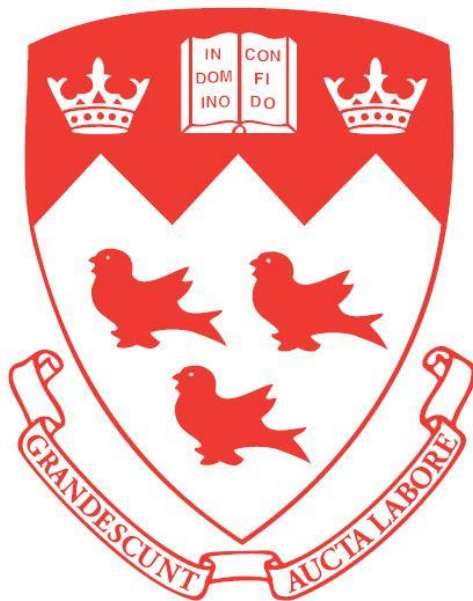
Critical Evaluation and Thermodynamic Modeling of High Alloy Fe-Mn-Al-Si-C-P System

Zhimin You

Department of Mining and Materials Engineering

McGill University, Montreal, Quebec, Canada

August 2020



A thesis submitted to McGill University in partial fulfilment of the requirements of the degree of

Doctorate of Philosophy

©Zhimin You, 2020

Dedication

To my parents, my brother, and my sister in China

Tables of Content

Abstract.....	6
Résumé.....	8
Acknowledgements	10
Preface and Contributions of Authors.....	12
List of Figures.....	14
List of Tables	20
List of Abbreviations and Symbols	22
Chapter 1: Introduction	26
1.1 Background	26
1.2 Objective	27
1.3 CALPHAD Method.....	28
1.4 Organization of the Thesis	30
References	31
Chapter 2: Thermodynamic Modeling	34
2.1 Critical Evaluation and Optimization.....	34
2.2 FactSage Software.....	37
2.3 Thermodynamic Models	39
2.3.1 Pure Elements and Stoichiometric Compounds	39
2.3.2 Liquid Solution.....	42
2.3.3 Solid Solutions.....	49
Reference.....	52
Chapter 3: Critical Evaluation and Thermodynamic Optimization of the Fe-P System.....	54
Abstract	54
3.1. Introduction	55

3.2 Thermodynamic Models	57
3.2.1 Pure Elements and Stoichiometric Compounds	57
3.2.2 Liquid Solution.....	59
3.2.3 Solid Solutions.....	61
3.3 Critical Evaluation and Thermodynamic Optimization	62
3.3.1 Phase Diagram.....	62
3.3.2 Thermodynamic Properties of Iron Phosphides	67
3.3.3 Thermodynamic Properties of Liquid Solution	76
3.3.3.1 Dissolution of Phosphorus in Liquid Fe from Gas Phase	77
3.3.3.2 Activity of Fe and P in Liquid Solution.....	80
3.3.3.3 Enthalpy and Gibbs Energy of Mixing	86
3.4 Application of Optimized Database to Dephosphorization Calculation for Liquid Fe.....	87
3.5 Summary	90
Acknowledgments.....	91
References	91
Chapter 4: Thermodynamic Optimization of the Mn-P and Fe-Mn-P Systems.....	99
Abstract	99
4.1. Introduction	100
4.2. Thermodynamic Models	102
4.2.1 Pure Elements and Stoichiometric Compounds	102
4.2.2 Solid Solutions.....	103
4.2.3 Liquid Solution.....	104
4.3 Critical Evaluation and Thermodynamic Optimization	108
4.3.1 The Fe-P and Fe-Mn System.....	111
4.3.2 The Mn-P System.....	113
4.3.2.1 Phase Diagram	113
4.3.2.2 Liquid Solution	114
4.3.2.3 Stoichiometric Manganese Phosphides.....	118

4.3.3 The Fe-Mn-P System.....	127
4.3.3.1 Phase Diagram	128
4.3.3.2 Thermodynamic Property of Liquid Solution.....	136
4.3.3.3 Predicted Phase Diagrams of the Fe-Mn-P System	141
4.3.3.4 Improvements of Present Optimization Compared to Previous Assessments	144
4.4 Summary	145
Acknowledgments.....	145
References	146
Chapter 5: Critical Evaluation and Thermodynamic Optimization of the Al-P and Fe-Al-P Systems.....	155
Abstract	155
5.1 Introduction	156
5.2. Thermodynamic Models	158
5.2.1 Pure Elements and Stoichiometric Compounds	158
5.2.2 Solid Solutions.....	159
5.2.2.1 FCC _{Al} Solid Solutions.....	160
5.2.2.2 Disordered/Ordered BCC Solid Solutions	161
5.2.2.3 Other Solid Solutions (Al ₈ Fe ₅ , Al ₁₃ Fe ₄ , Me ₃ P, Me ₂ P).....	162
5.2.3 Liquid Solution.....	163
5.3 Critical Evaluation and Thermodynamic Optimization	166
5.3.1 The Fe-P and Fe-Al Systems	170
5.3.2 The Al-P System.....	171
5.3.3 The Fe-Al-P System	177
5.3.3.1 Phase Diagram	177
5.3.3.2 Liquid Surface Projection	183
5.3.3.3 Activity of P in Liquid Fe-Al-P Solution.....	184
5.4 Summary	185
Acknowledgments.....	186

References	186
Chapter 6: Critical Thermodynamic Modeling of the Fe-Si-P and Fe-C-P Systems	193
Abstract	193
6.1 Introduction	194
6.2. Thermodynamic Models	195
6.2.1 Pure Elements and Stoichiometric Compounds	195
6.2.2 Solid Solutions.....	197
6.2.2.1 Disordered FCC_A1, BCC_A2, Diamond_A4 Solid Solutions	197
6.2.2.2 Ordered BCC_B2 Solid Solution.....	198
6.2.2.3 Other Solid Solutions (Me ₃ P, Me ₂ P, MeP).....	199
6.2.3 Liquid Solution.....	200
6.3. Critical Evaluation and Thermodynamic Optimization	203
6.3.1 The Fe-Si-P System.....	210
6.3.1.1 Binary Systems (Fe-P, Si-P and Fe-Si Systems)	210
6.3.1.2 Ternary Fe-Si-P system.....	213
6.3.2 The Fe-C-P System.....	221
6.3.2.1 Binary Systems (Fe-C and C-P Systems)	221
6.3.2.2 Ternary Fe-C-P System.....	223
6.4. Summary	234
Acknowledgments.....	235
References	235
Chapter 7: Comprehensive Scholarly Discussion	243
References	246
Chapter 8: Summary and Suggestions for Future Work.....	247
8.1 Summary	247
8.2 Suggestions for Future Work	250
References	251

Chapter 9: Contribution to Original Knowledge.....	253
Appendix A: Application of the Present Thermodynamic Database to the Dephosphorization of Ferromanganese (FeMn) Alloys	255
Abstract	255
A. 1 Introduction	256
A. 2 Thermodynamic Models.....	258
A. 2. 1 Pure Elements and Stoichiometric Compounds	258
A. 2. 2 Solid Solutions.....	259
A. 2. 3 Liquid Solution	260
A.3 Prediction of Present Database.....	261
A.4 Phosphorous Refining of Ferromanganese Alloys.....	263
A.4.1 Dephosphorization Approaches.....	263
A.4.2 Determination of the Flux Composition	267
A.4.3 Effect of Temperature on Dephosphorization	272
A.4.4 Effect of Flux Quantity on Dephosphorization	274
A.4.5 Effect of Initial Si Content on Dephosphorization	275
Summary	277
Acknowledgements	277
References	278

Abstract

High alloy steels are attracting increasing interest among researchers because of their advanced mechanical properties, corrosion resistance, electromagnetic properties, etc. Besides, addition of light alloying elements like Al and Si into the high alloy steels can also reduce the steel weight, which has very promising application in eco-friendly automobile industry. On the other hand, introduction of the Mn in steels increases the solubility of phosphorus because of its high affinity with phosphorus. The six component Fe-Mn-Al-Si-C-P alloy system is very important for production of the advanced high strength steels and ferro alloys. In the present study, the available thermodynamic database of the Fe-Mn-Al-Si-C system was slightly revised and extended by including phosphorus to develop an accurate and self-consistent thermodynamic database of the Fe-Mn-Al-Si-C-P system using the CALculation of PHase Diagrams (CALPHAD) method.

In the present thermodynamic modeling, the liquid phase was described using the Modified Quasichemical Model (MQM) with consideration of short-range ordering in the molten alloys. Besides, appropriate geometric interpolation techniques based on the nature of involved binary systems were also introduced for each ternary solution to reduce the model parameters and improve the predictability of ternary and higher-order systems simultaneously. The solid solutions were modeled using the Compound Energy Formalism (CEF) considering the crystallographic structure of each solid solution. The thermodynamic properties of P in the liquid and solid alloys, thermodynamic stability of all intermediate phosphides, various types of phase diagrams (liquidus, solidus, isopleth diagrams, isothermal sections, liquid projections, etc.) of the Fe-Mn-Al-Si-C-P system were critically evaluated and optimized to reproduce all reliable experimental data.

The behavior of P in the sub-systems of the Fe-Mn-Al-Si-C-P alloy was accurately described based on the present thermodynamic database with very small number of model parameters. The present database is compatible with other thermodynamic databases in FactSage, and can be applied to the calculation of the dephosphorization reaction of molten high alloy steels. The distribution of P between molten steel and slag at various temperatures was calculated accurately. In addition, the thermodynamic database constructed in the present study can also be used to predict unexplored phase diagrams and thermodynamic properties of the Fe-Mn-Al-Si-C-P system.

Résumé

Les aciers fortement alliés suscitent un intérêt croissant parmi les chercheurs en raison de leurs propriétés mécaniques avancées, de leur résistance à la corrosion, de leurs propriétés électromagnétiques, etc. De plus, l'ajout d'éléments d'alliage légers comme Al et Si dans les aciers fortement alliés peut également réduire le poids de l'acier, ce qui est une application prometteuse dans l'industrie automobile écologique. En revanche, l'introduction du Mn dans les aciers augmente la solubilité du phosphore en raison de sa forte affinité avec le phosphore. Le système d'alliage à six composants Fe-Mn-Al-Si-C-P est très important pour la production des aciers à haute résistance et des ferro-alliages avancés. Dans la présente étude, la base de données thermodynamique disponible du système Fe-Mn-Al-Si-C a été légèrement révisée et étendue en incluant le phosphore pour développer une base de données thermodynamique précise et cohérente pour le système Fe-Mn-Al-Si-CP en utilisant la méthode de CALculation des diagrammes de PHase (CALPHAD).

Dans la modélisation thermodynamique actuelle, la phase liquide a été décrite en utilisant le modèle quasi-chimique modifié (MQM) en tenant compte de l'ordre à courte portée dans les alliages fondus. De plus, des techniques d'interpolation géométrique appropriées basées sur la nature des systèmes binaires impliqués ont également été introduites pour chaque solution ternaire afin de réduire les paramètres du modèle et améliorer simultanément la prévisibilité des systèmes ternaire et d'ordre supérieur. Les solutions solides ont été modélisées à l'aide du formalisme énergétique des composés (CEF) en tenant compte de la structure cristallographique de chaque solution solide. Les propriétés thermodynamiques du P dans les alliages liquides et solides, la stabilité thermodynamique de tous les phosphures intermédiaires, les différents types de

diagrammes de phases (liquidus, solidus, diagrammes isoplèthes, coupes isothermes, projections des liquides, etc.) du système Fe-Mn-Al-Si-C-P ont été évalué de manière critique et optimisé pour reproduire toutes les données expérimentales fiables.

Le comportement de P dans les sous-systèmes de l'alliage Fe-Mn-Al-Si-C-P a été décrit avec précision avec la base de données thermodynamique actuelle avec un très petit nombre de paramètres du modèle. La présente base de données est compatible avec d'autres bases de données thermodynamiques de FactSage et peut être appliquée au calcul de la réaction de déphosphoration des aciers fondus fortement alliés. La distribution du P entre l'acier fondu et le laitier à diverses températures a été calculée avec précision. De plus, la base de données thermodynamiques construite dans la présente étude peut également être utilisée pour prédire des diagrammes de phases inexplorés et les propriétés thermodynamiques du système Fe-Mn-Al-Si-C-P.

Acknowledgements

The accomplishment of this dissertation would not be possible without the help from many people who contributed their favors throughout my study in McGill University.

First of all, I am very indebted to my supervisor Prof. In-Ho Jung for acceptance of my application to this Ph.D program, instructive supervision, enthusiastic encouragement and financial support during my study in McGill University and Seoul National University. Prof. In-Ho Jung has inspired me a lot especially by his discerning idea on research and innovative capability on converting theoretical knowledge to industrial applications. His diligence and enthusiasm on research, kind assistance and encouragement in my life have also set a good example for me. In addition, I would like to express my sincere appreciation to my co-supervisor Prof. Mainul Hasan who gave me good ideas for completing my project and current thesis writing.

Then, I would like to thank my parents for giving me the life, bringing me up, educating me and encouraging me on my study all the time. And also, I would like to express my gratitude towards my elder sister, elder brother and brother-in-law who have been supporting me unselfishly. Additional thanks to my little nephew Yifan Feng, who always brings me lots of cheers and joyfulness.

I am also very grateful to Dr. Min-Kyu Paek who worked as a postdoctoral fellow in my group. He helped me a lot with my study and also gave me courage during my hard time in life.

I also appreciate the aids from my other group members including Dr. Pierre Hudon, Dr. Marie-Aline Van Ende, Dr. Zhijun Zhu, Dr. Senlin Cui, Mr. Weitong Du, Ms. Yumin Zhang, Ms. Xintong Du, Dr. Junghwan Kim, Dr. Dong-Geun Kim, Dr. Bikram Konar, Dr. Sourav Kumar Panda, Dr. Elmira Moosavi, Mr. Jaesung Lee et al. in various ways.

The kind help from my good friends Dr. Baoqi Guo and Dr. Shuang Gao is very appreciated. I also would like to thank many other friends who prayed for me in Canada and China.

The administrative help from Ms. Barbara Hanley, Ms. June Persaud and Ms. Leslie Bernier during my Ph.D is also very appreciated.

I acknowledge McGill University for offering me the McGill Engineering Doctorate Award (MEDA), and financial support from Tata Steel Europe, Voestalpine Stahl, RioTinto Iron and Titanium, Hyundai Steel, Doosan Heavy Industry and Construction, Natural Sciences and Engineering Research Council of Canada (NSERC), POSCO, JFE Steel, Nucor Steel, RHI, RIST, Nippon Steel and Sumitomo Metals Corp., Schott A.G.

Lastly, I would thank the God almighty for giving me courage and strength to overcome the difficulties and complete this dissertation.

Preface and Contributions of Authors

All the work presented in the thesis was performed in the High Temperature Thermochemistry Laboratory in the Department of Mining and Materials Engineering, McGill University. Four chapters are included in this Ph.D thesis and have been and will be submitted for publication:

Chapter 3: Critical Evaluation and Thermodynamic Optimization of the Fe-P System by Zhimin You and In-Ho Jung, published in Metallurgical and Materials Transactions B.

Chapter 4: Thermodynamic Optimization of the Mn-P and Fe-Mn-P Systems by Zhimin You and In-Ho Jung, on revision for being published in CALPHAD.

Chapter 5: Critical Evaluation and Thermodynamic Optimization of the Al-P and Fe-Al-P Systems by Zhimin You and In-Ho Jung, published in Journal of Phase Equilibria and Diffusion.

Chapter 6: Critical Evaluation and Thermodynamic Modeling of the Fe-Si-P and Fe-C-P Systems by Zhimin You and In-Ho Jung, to be submitted to Metallurgical and Materials Transactions B.

Appendix A: Application of the Present Thermodynamic Database to the Dephosphorization of Ferromanganese (FeMn) Alloys by Zhimin You and In-Ho Jung, to be submitted: September, 2020.

For all the work presented, the author of current thesis is the main investigator, who is in charge of the research plan, literature review and data analysis, thermodynamic modeling and database development, and manuscript preparation. All thermodynamic modeling, manuscript writing and

corrections during the present study were finished under the supervision and guidance of Professor In-Ho Jung. Besides, Dr. Pierre Hudon assisted the translation of the abstract from English to French.

List of Figures

Chapter 1

Figure 1.1 Flow chart of the present thermodynamic optimization using the CALPHAD method.....	28
--	----

Chapter 2

Figure 2.1 Geometric models: (a) Kohler model, (b) Kohler / Toop model, (c) Muggianu Model, and (d) Muggianu / Toop Model.....	47
Figure 2.2 Schematic graph of the two sublattices $(A, B)_m(C, D)_n$ solid solution model.....	50

Chapter 3

Figure 3.1 Present optimized phase diagram of the Fe-P system (a) compared with experimental data, and (b) compared with previous assessments.....	65
Figure 3.2 Phase diagram of the Fe-P system in the Fe-rich region.....	67
Figure 3.3 Heat capacities C_p stoichiometric compounds (a) Fe_3P , (b) Fe_2P , and (c) FeP	69
Figure 3.4 Thermodynamic properties of iron phosphides in the Fe-P system (a) $\Delta H_{298.15 K}^\circ$, (b) $\Delta H_{900 K}^\circ$, and (c) $S_{298.15 K}^\circ$	72
Figure 3.5 Gibbs energies of formations of Fe_3P and Fe_2P from γ -Fe and $P_2(g)$	74
Figure 3.6 Equilibrium partial pressures of phosphorus vapor of reactions (a) $4FeP(s) = 4Fe_2P(s) + P_2(g)$, (b) $2FeP_2(s) = 2FeP(s) + P_2(g)$, and (c) $4FeP_2(s) = 4FeP(s) + P_4(g)$, depending on the temperature.....	75
Figure 3.7 Standard Gibbs energy change for the reaction of P_2 dissolution in liquid Fe.....	78
Figure 3.8 Activity of Fe in the liquid Fe-P solution at 1550 °C, along with experimental data...	81

Figure 3.9 Activity of P(l) in the liquid Fe-P solution with reference to pure P(l) as a standard state at (a) 1650 °C, (b) 1600 °C, (c) 1536 °C, (d) 1500 °C, (e) 1400 °C, and (f) 1300 °C.....83

Figure 3.10 Enthalpy and Gibbs energy of mixing of the Fe-P liquid solution at 1550 °C optimized in the present study in comparison with experimental data.....87

Figure 3.11 (a) Distribution coefficient of P, and (b) dissolved [P] content in molten Fe after dephosphorization of the liquid Fe-P solution with molten slag at 1550 °C to 1700 °C89

Chapter 4

Figure 4.1 Optimized phase diagrams of the (a) Fe-P (b) Fe-Mn, and (c) Mn-P systems.....113

Figure 4.2 Enthalpy of mixing of the liquid solutions in the (a) Fe-P and (b) Mn-P systems.....115

Figure 4.3 Calculated activities (a) a_P^R , and (b) a_{Mn}^R of the liquid Mn-P solution in the references of pure liquid P and Mn, compared to experimental data.....117

Figure 4.4 Heat capacities of (a) MnP, (b) Mn₂P, and (c) Mn₃P in the Mn-P system.....119

Figure 4.5 Standard enthalpy of formation $\Delta H_{298.15K}^\circ$ and entropy $S_{298.15K}^\circ$ of stoichiometric manganese phosphides at 298.15 K.....121

Figure 4.6 Gibbs energy of formations of (a) Mn₃P, (b) Mn₂P, (c) Mn₃P₂, and (d) MnP from CUB-Mn and P₂(g).....124

Figure 4.7 Calculated equilibrium vapor pressures of P₂ and P₄ gas of the reactions (a) $4MnP(s) = 2Mn_2P(s) + P_2(g)$ and (b) $2MnP_3(s) = 2MnP(s) + P_4(g)$, compared to experimental data.....126

Figure 4.8 Calculated phase diagram of the Fe₂P-Mn₂P system, compared to experimental data.....129

Figure 4.9 Calculated isopleths of the Fe-Mn-P system at mass ratios of (a) Fe: Mn = 1: 9, (b) Fe: Mn = 5: 5, (c) Fe: Mn = 9: 1, and (d) Fe: Mn = 19: 1, compared to experimental data.....	129
Figure 4.10 Calculated phase diagrams of the Fe-Mn-P system at (a) wt. %P = 1, (b) wt. %P = 6, and (c) wt. %P = 12, compared to experimental data.....	131
Figure 4.11 Calculated isothermal section in the Fe-rich region of the Fe-Mn-P system at 1000 °C, compared to experimental data.....	133
Figure 4.12 Isothermal phase diagram of the Fe-Mn-P system at 800 °C.....	134
Figure 4.13 Liquidus projection of the Fe-Mn-P system between 1000 °C and 1500 °C, compared to experimental data.....	135
Figure 4.14 Calculated activities (a) a_{P}^{R} , (b) a_{Fe}^{R} , and (c) a_{Mn}^{R} in various liquid Fe-Mn-P solutions, compared to experimental data	137
Figure 4.15 Calculated activities of (a) P(l) at $x_{\text{Mn}} = 0.016 - 0.20$ and 1550 °C, and (b) Mn(l) at $x_{\text{Mn}} = 0.036 - 0.041$ and 1500 °C of the liquid Fe-Mn-P, compared to experimental data.....	138
Figure 4.16 Effect of Mn on the activity coefficient of P in the liquid Fe-Mn-P solution at 1400 °C and 1550 °C, compared to experimental data.....	140
Figure 4.17 Predicted Henrian activity coefficient of P in the Fe-Mn melts at 1400 °C to 1700 °C.....	141
Figure 4.18 Predicted phase diagrams of the (a) Fe ₃ P-Mn ₃ P system and (b) FeP-MnP system...	142
Figure 4.19 Predicted iso-activity contours of (a) Fe(l), (b) Mn(l), and (c) P(l) of the liquid Fe-Mn-P solution at 1550 °C.....	143

Chapter 5

Figure 5.1 Optimized phase diagrams of the (a) Fe-P system and (b) Fe-Al system.....	170
Figure 5.2 The Al-P phase diagram in the (a) full composition and (b) Al-rich region.....	173

Figure 5.3 Heat capacity of AlP against the temperature.....	174
Figure 5.4 Vaporization pressures of Al(g) and P ₂ (g) above solid AlP phase.....	177
Figure 5.5 Calculated isopleths of the Fe-Al-P system at (a) wt. %P = 6, (b) wt. %P = 9, (c) wt. %Al = 10, and (d) wt. %Al = 25, compared to the experimental data.....	178
Figure 5.6 Isothermal phase diagram of the Fe-Al-P system on the Fe-rich corner at 1000 °C, compared to experimental data.....	180
Figure 5.7 Isothermal diagrams of the Fe-Al-P system at (a) 450 °C, (b) 650 °C, and (c) 800 °C..	181
Figure 5.8 Liquid projection of the Fe-Al-P system together with experimental data.....	183
Figure 5.9 Effect of Al on the activity coefficient of P in the liquid Fe-Al-P solution at 1400 °C and 1600 °C, compared to experimental data	185

Chapter 6

Figure 6.1 Calculated phase diagrams of the (a) Fe-P, (b) Si-P, and (c) Fe-Si systems.....	211
Figure 6.2 Pseudobinary (a) FeSi – FeP (b) FeSi – FeSi ₄ P ₄ and (c) FeSi ₂ – FeSi ₄ P ₄ diagrams in the ternary Fe-Si-P system compared to experimental data.....	214
Figure 6.3 Calculated isopleths of the Fe-Si-P system at (a) wt. %Si = 7 and (b) wt. %P = 13, compared to experimental data.....	216
Figure 6.4 Calculated isothermal section of the Fe-Si-P system on the Fe-rich corner at 1000 °C, compared to experimental data.....	217
Figure 6.5 Calculated liquidus surface projection of the Fe-Si-P system between 1000 °C and 1500 °C, compared to experimental data	218
Figure 6.6 Effect of Si on the activity coefficient of P (γ_P^{Si}) in the liquid Fe-Si-P alloys from 1400 to 1600 °C, compared to experimental data.....	220

Figure 6.7 Calculated solubility of $P_2(g)$ in the Si-Fe melts at 1450 °C under the partial pressure of $P_{P_2(g)} = 0.184$ Pa, compared to experimental data.....	221
Figure 6.8 Calculated phase diagrams of the (a) Fe-C and (b) C-P systems.....	222
Figure 6.9 Calculated vertical phase diagrams of (a) $Fe_{91}P_9 - Fe_{95.5}C_{4.5}$, (b) $Fe_{92}P_8 - Fe_{97}C_3$, (c) $Fe_{98}P_2 - Fe_{98}C_2$, (d) $Fe_{98.4}P_{1.6} - Fe_{98.4}C_{1.6}$, and (e) Fe - $Fe_{97}P_{1.5}C_{1.5}$ in weight percent, compared to experimental data.....	223
Figure 6.10 Variation of the temperature along with P content of the Fe-C-P system at wt. %C = 2.4, compared to experimental data.....	226
Figure 6.11 Variation of the temperature with P content along the metastable liquidus reaction Liquid = FCC_A1 + Fe_3C , together with experimental data.....	227
Figure 6.12 Calculated isothermal sections of the Fe-C-P system on the Fe-rich corner at (a) 900 °C, (b) 950 °C, (c) 1000 °C, and (d) 1100 °C, compared to experimental data.....	228
Figure 6.13 Calculated solubility of C in molten Fe with increasing P content between 1300 °C and 1600 °C, compared to experimental data.....	232
Figure 6.14 Calculated Liquidus surface projection of the Fe-C-P system on the Fe-rich corner, compared to experimental data.....	234

Appendix A

Figure A.1 Solubility of C affected by the P content in the (a) high Mn hot metal and (b) FeMn alloys of the Fe-Mn-C-P system at 1400 °C, compared to experimental data.....	262
Figure A.2 Predicted P partition coefficient between molten slag and (a) high Mn hot metal and (b) high-C FeMn alloys based on present database, compared to experimental data.....	263
Figure A.3 Variation of the P content in metal (100 g) with the contents of BaO and MnO of the flux (15 g) at 1300 °C.....	269

Figure A.4 Variations of the quantity of all stable phases with the BaO content at 1300 °C at (a) wt.%MnO = 10, (b) wt.%MnO = 15, (c) wt.%MnO = 20, and (d) wt.%MnO = 25 of the flux...270

Figure A.5 Variations of the amount of all stable phases and the dissolved [P] content of FeMn alloys with the BaO content at 1300 °C when m(MnO) = 22.67 wt.% of the flux.....271

Figure A.6 Effect of the temperature on the (a) dephosphorization efficiency, (b) activity of each slag component, and (c) formation of gas species.....272

Figure A.7 Variation of each alloy component with the added amount of flux in the composition of 41wt.%BaO-22.67wt.%MnO-36.33wt.%BaCl₂ at 1361 °C.....274

Figure A.8 Effect of initial Si content of the flux on (a) dephosphorization efficiency and (b) formation of stable phases.....275

List of Tables

Chapter 3

Table 3.1	Summary of crystal structure information of all solid phases in the Fe-P system.....	63
Table 3.2	Optimized model parameters for the Fe-P system (J/mol, J/mol-K).....	63
Table 3.3	Invariant reactions of the Fe-P system in the present study.....	66

Chapter 4

Table 4.1	Summary of crystal structure information of all solid phases in the Fe-Mn-P system..	108
Table 4.2	Optimized model parameters for the Fe-Mn-P system (J/mol, J/mol-K).....	109
Table 4.3	Invariant reactions of the Mn-P system optimized in the present study.....	114
Table 4.4	Invariant reactions of the Fe-Mn-P system with experimental data.....	136

Chapter 5

Table 5.1	Summary of crystal structure information of all solid phases in the Fe-Al-P system..	166
Table 5.2	Optimized model parameters for the Fe-Al-P system (J/mol, J/mol-K).....	167
Table 5.3	Standard enthalpy of formation ($\Delta H_{298.15K}^{\circ}$) of AlP in the Al-P system.....	175
Table 5.4	Standard entropy ($S_{298.15K}^{\circ}$) of AlP in the Al-P system.....	176
Table 5.5	Invariant reactions of the Fe-Al-P system with experimental data.....	184

Chapter 6

Table 6.1	Summary of crystal structure information of all solid phases in the Fe-Si-P system..	204
Table 6.2	Summary of crystal structure information of all solid phases in the Fe-C-P system..	205
Table 6.3	Optimized model parameters for the Fe-Si-P system (J/mol, J/mol-K).....	205
Table 6.4	Optimized model parameters for the Fe-C-P system (J/mol, J/mol-K).....	208
Table 6.5	Invariant reactions of the Fe-Si-P system with experimental data.....	219
Table 6.6	Invariant reactions of the Fe-C-P system with experimental data.....	234

Appendix A

Table A.1 Chemical composition (wt.%) of starting high-C FeMn alloy (100 grams).....267

Table A.2 Optimal composition (wt.%) of the BaO-MnO-BaF₂ flux.....271

List of Abbreviations and Symbols

a_P^H	Activity of phosphorus in the Henrian standard state
a_P^R	Activity of phosphorus in the Raoultian standard state
$a_P^{wt.\%}$	Activity of phosphorus in the 1 wt.% standard state
ACM	Acid Calorimetry Method
AE	Aging Examination
BWRMM	Bragg-Williams Random Mixing Model
CALPHAD	CALculation of PHase Diagrams
CA	Chemical Analysis
CCM	Calorimetry Combustion Measurement
CEF	Compound Energy Formalism
C_p	Molar heat capacity, J/mol/K
CM	Calorimetry Method
CMT	Casting Microsonde Test
DCM	Drop Calorimetry Method
DM	Diffusion Method
DTA	Differential Thermal Analysis
DSC	Differential Scanning Calorimeter
EE	Electrolytical Etching
EMF	Electromotive Force
EPMA	Electron Probe Microanalysis
ESM	Electrolytic Separation Method
G	Molar Gibbs energy, J/mol

G^{mg}	Magnetic contribution to the Gibbs energy, J/mol
G_T°	Molar Gibbs energy of the pure component at temperature T , J/mol
G^{ex}	Excess Gibbs energy, J/mol
$G_S^{disorder}$	Gibbs energy contribution of the disordered part, J/mol
$g(\tau)$	Polynomial fraction
HEM	Hot Extraction Method
H_T°	Molar enthalpy of pure component at temperature T , J/mol
HT	Holding Test
$[i]$	The component i in molten steel
(i)	The component i in slag
IAC	Infrared Analysis with Combustion
KEM	Knudsen effusion method
L_i	Interaction parameter of the i order
L_P	The distribution of phosphorus between slag and metal ($L_P = \text{wt. \%}(P)/\text{wt. \%}[P]$)
MA	Microscopic Analysis
ME	Microscopic Examination
MBM	Molybdenum Blue Method
MLE	Mass Loss Effusion
MQM	Modified Quasichemical Model
M_i	Molar atomic weight of element i
MT	Magnetic Test
MSA	Mass Spectroscopic Analysis
MSM	Magnetic Susceptibility Measurement

n_i	The number of moles of component i , mole
n_{AA}, n_{BB}, n_{AB}	The numbers of moles of (A-A), (B-B) and (A-B) pairs, mole
P	The fraction of the magnetic enthalpy absorbed above the critical temperature
PCM	Phosphorus Colorimetric Method
P_2^+, P^+	Intensities of ions P_2^+ and P^+ , respectively
q_{AB}^{ij}	Interaction parameter between A and B species (i, j: power of the mole fraction of A and B species, J/mol
R	Gas constant, J/mol/K
QM	Quenching Method
QTM	Quantitative Television Microscope
SEM-EDS	Scanning Electron Microscopy/Energy Dispersive X-ray Spectroscopy
$S_{298.15K}^\circ$	Standard entropy at 298.15 K, J/mol/K
S_T°	Molar entropy at temperature T , J/mol
SM	Scale Measurement
T	Temperature in the unit Kelvin (K)
TA	Thermal Analysis
TCFM	Temperature Controlled Filtration Method
TM	Transportation Method
T_C	Curie temperature, K
T_N	Neel temperature, K
x_i	Mole fraction of component i
X_{AA}, X_{AB}, X_{BB}	Pair fraction of (A-A), (A-B), (B-B) pairs
XMA	X-ray Microprobe Analyzer

XRD	X-ray Diffraction
XRF	X-ray Fluorescence
y_i	Site fraction of component i in the designated sublattice
Y_A, Y_B	Coordination equivalent fractions of components A and B
Z_A, Z_B	Coordination number of atoms A and B, respectively
Z_{AA}	Coordination number when all nearest neighbors of A atoms are A atoms (Z_{BA}, Z_{BB} defined in the analogous manner)
τ	The ratio of instant temperature to critical temperature (Curie or Neel temperature)
β	Average magnetic moment per mole of atoms, B
γ_P^0	Henrian activity coefficient of phosphorus
Δg_{AB}	Gibbs energy change of forming 2 moles of (A-B) pairs in the atom pair exchange-reaction
ΔG_{BCC}^{order}	Gibbs energy contribution of long-range ordering, J/mol
$\Delta S^{conf.}$	Configurational entropy of mixing, J/mol/K
$\Delta H_{298.15K}^\circ$	Standard enthalpy of formation at 298.15 K, J/mol
ΔH_{max}^{mix}	The most negative value for the enthalpy of mixing, kJ/mol

Chapter 1: Introduction

1.1 Background

High alloy steels have aroused increasingly wide interest because of their advanced mechanical properties, weight-lightening characteristics, and electromagnetic properties etc. Meanwhile, there are some challenging difficulties in the upstream and downstream processes during producing high alloy steels. For example, the phosphorus in steels originated from the raw materials (iron ores, flux, coke etc.) can causes serious steel defects such as weld brittleness and cracks, despite very low amount. However, it is hard to control P below the allowed concentration especially at the presence of the alloying element such as Mn and Cr, etc. that has high affinity to P.

The currently available thermodynamic database for molten steels was developed mainly using the Bragg-Williams Random Mixing Model (BWRMM) based on the experimental data in the Fe-rich region. However, the chemical reactions such as deoxidation, nitrogen degassing and dephosphorization reactions during the refining process of high Mn steel and high Si steel are not calculated very accurately using the currently available database stored in FactSage and Thermocalc [1]. Moreover, the phase equilibria (some liquidus and solidus, phase transformation between solid phases, etc.) of high alloy steels are not described accurately either. Although several low-order P-containing high alloy steel systems have recently been thermodynamically optimized by researchers, the discrepancies left in some binary and ternary systems were still not resolved and the multicomponent systems are poorly predicted in the existing modeling studies. This is probably due to inappropriate selection of the model or model parameters used in the database. In the previous assessments based on the BWRMM, the random mixing of entropy was assumed and an intrinsic Muggianu interpolation technique was used to predict the Gibbs energy of the ternary

solution from binary excess parameters, which is the limitation of this model especially when the solution is highly deviated from the ideal mixing assumption. Using the BWRMM, the excessive interaction parameters especially big temperature-dependent terms are always required to reproduce the experimental data of the binary and ternary systems. This may cause a miscibility gap and hypothetical solid phases appearing at very high temperature region. Besides, excessive model parameters can also cause inconsistency when extending from low-order systems to multicomponent systems. Therefore, it is essential to develop a more accurate and self-consistent thermodynamic database for the high alloy steel applications encompassing from refining to the final steel product.

1.2 Objective

The objective of the present study is to develop a new thermodynamic database for the entire Fe-Mn-Al-Si-C-P six-component system containing all solid and liquid phases by including P in the existing Fe-Mn-Al-Si-C database. This system is a key alloy for advanced high strength steels. In the present study, all P-containing sub-systems of the Fe-Mn-Al-Si-C-P alloys were critically optimized using the CALculation of PHase Diagrams (CALPHAD) method. Besides, some of the sub-systems of the Fe-Mn-Al-Si-C alloys were also slightly revised based on previous modeling results [2-8]. The developed thermodynamic database for the Fe-Mn-Al-Si-C-P system will be part of the big database of the Fe-Mn-Al-Si-Cr-Ni-Ti-Nb-C-O-N-P-S system in future FSstel database in FactSage software [1].

1.3 CALPHAD Method

In the present study, thermodynamic modeling of all the P containing sub-systems of the Fe-Mn-Al-Si-C-P alloys was performed using the CALculation of PHase Diagrams (CALPHAD) method (<http://www.calphad.com>), which was originally introduced by Kaufman and Bernstein [9] in 1970s, and then developed by Saunders and Miodownik [10], Fabrichnaya et al. [11], Lukas et al. [12], Kattner [13], and Liu and Wang [14] etc.

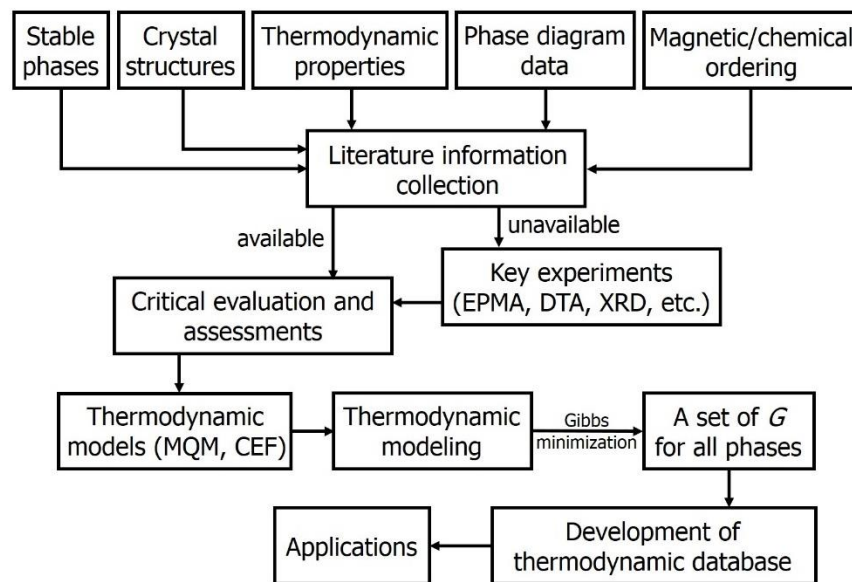


Figure 1.1 Flow chart of the present thermodynamic optimization using the CALPHAD method

The CALPHAD approach is based on the fact of phase diagram as a manifestation of the equilibrium thermodynamic properties of the system. The phase diagram is a very powerful tool for predicting the state of a system under different conditions (temperature, chemistry, pressure, etc). Therefore, this approach is usually employed to model thermodynamic properties for each phase and simulate the behavior of multicomponent phases, aiming at promoting computational thermodynamics by developing a self-consistent thermodynamic database based on the critical

assessment of available data. Overall, the CALPHAD method is one of the most effective ways to predict complex thermochemistry process in the multicomponent system. It helps understand various industrial and technological processes and becomes more and more popular in new materials and processes designing.

The flow chart of present thermodynamic optimization using the CALPHAD method is demonstrated in **Fig. 1.1**. Firstly, the literature data of stable phases such as crystal structures (site occupations, symmetry, etc.), thermodynamic properties (Gibbs energies, enthalpies, entropies, heat capacities, activities, etc.), and phase diagram (liquidus, solidus, isopleths, isothermal sections, liquid projections, solubilities, other phase boundaries, etc.), magnetic ordering and chemical ordering were collected. Then the accuracy and reliability of collected experimental data must be strictly evaluated in terms of sample preparation, experimental procedures and techniques, systematic errors, data analysis approaches, etc. In the case of experimental data are not available in the literature, key phase diagram experiments may be needed to clarify the phase relations of target systems. In the present study, experiments are not necessary for the optimization. Thirdly, appropriate thermodynamic models were selected based on the structures of studied phases. In this work, the Modified-Quasichemical Model (MQM) [15,16] and Compound Energy Formalism (CEF) [17] were used to describe the liquid phases and solid solutions, respectively. The MQM proposed by the FactSage group has an outstanding advantage in describing liquid solutions specially with strong short-range ordering. The CEF is widely used to model the solid solutions. Afterwards, thermodynamic modeling was performed by determining Gibbs energy expressions of all stable phases on the basis of Gibbs energy minimization with assist of FactSage software [1]. The adjustable model parameters of Gibbs energy expressions were determined by reproducing

the reliable experimental data. Before completing the database development, the accuracy and consistency in describing the optimized system and extended higher-order system have to be carefully checked. Finally, the construction of thermodynamic database was completed and can be used to back-calculate unexplored phase diagrams and thermodynamic properties of the studied system for various applications.

1.4 Organization of the Thesis

The current PhD thesis consists of eight chapters and it is organized as follows:

Chapter 1 introduces the project background and objective of the present study. Besides, the CALPHAD method used for the present thermodynamic modeling of high alloy steel systems is introduced, and organization of current thesis is given.

Chapter 2 presents the overview of thermodynamic models used for thermodynamic optimization of all phases (pure elements, stoichiometric compounds, liquid solutions and solid solutions) involved in the present study.

Chapter 3 presents the thermodynamic modeling results of the binary Fe-P system. As the most fundamental steel system containing P, the Fe-P system is very important for dephosphorization of high alloy liquid steels. Much emphasis is put on the determination of thermodynamic properties of P in the molten Fe. The dephosphorization reactions at the steel/slag interface of different temperatures and compositions were also calculated with combination of the FToxid database in FactSage to validate the accuracy of the present database.

Chapter 4 presents the critical evaluation and thermodynamic modeling of the Mn-P and Fe-Mn-P systems. Thermodynamic properties of all stable Mn phosphides and ferromanganese

phosphides were critically optimized based on available experimental data. The thermodynamic behavior of P in molten Mn was compared with that in molten Fe.

Chapter 5 presents the critical thermodynamic optimization results of the binary Al-P and ternary Fe-Al-P systems. The optimized Gibbs energy of stoichiometric AlP compound, thermodynamic behavior of P in liquid Al and Fe-Al alloys, and phase equilibria of various isopleths and isothermal sections of the Fe-Al-P system were calculated in comparison with available experimental data.

Chapter 6 presents the critical evaluation and thermodynamic optimization results of the Fe-Si-P and Fe-C-P systems. Thermodynamic properties of P in Fe-rich and Si-rich liquid solution regions, various vertical phase diagrams, isothermal sections and liquid projections of the ternary Fe-Si-P and Fe-C-P systems are in good agreement with available experimental data.

Chapter 7 summarizes the results included in the present PhD thesis and also gives some suggestions for the future work based on the present study.

Chapter 8 highlights the contributions of present PhD work to the original knowledge.

Appendix A presents the application of the thermodynamic database developed in this study to the dephosphorization calculations of high Mn alloys using proper fluxes. The optimal chemistry of the flux for maximizing the dephosphorization efficiency was obtained. Besides, effects of conditions on the dephosphorization reactions were also investigated.

References

1. C. W. Bale, P. Chartrand, S. A. Degterov, G. Eriksson, K. Hack, R. B. Mahfoud, and S. Petersen, FactSage Thermochemical Software and Databases, *CALPHAD*, 2002, 26(2), p 189-228.
2. W. Huang, An Assessment of the Fe-Mn System, *CALPHAD*, 1989, 13(3), p 243-252.

3. S. L. Cui and I. H. Jung, Critical Reassessment of the Fe-Si System, *CALPHAD*, 2017, 56, p 108-125.
4. M. K. Paek, J. J. Pak, and Y. B. Kang, Phase Equilibria and Thermodynamics of Mn-C, Mn-Si, Si-C Binary Systems and Mn-Si-C Ternary System by Critical Evaluation, Combined with Experiment and Thermodynamic Modeling, *CALPHAD*, 2014, 46, p 96-102.
5. M. S. Kim and Y. B. Kang, Thermodynamic Modeling of the Fe-Mn-C and the Fe-Mn-Al Systems using the Modified Quasichemical Model for Liquid Phase, *J. Phase Equilib. Diffu.*, 2015, 36(5), p 453-470.
6. A. T. Phan, M. K. Paek, and Y. B. Kang, Phase Equilibria and Thermodynamics of the Fe-Al-C System: Critical Evaluation, Experiment and Thermodynamic Optimization, *Acta Mater.*, 2014, 79, p 1-15.
7. K. Shubhank and Y. B. Kang, Critical Evaluation and Thermodynamic Optimization of Fe-Cu, Cu-C, Fe-C Binary Systems and Fe-Cu-C Ternary System, *CALPHAD*, 2014, 45, p 127-137.
8. P. Chartrand, Unpublished research. *Ecole Polytechnique*, Montreal, Canada. 2004.
9. L. Kaufman and H. Bernstein, Computer Calculation of Phase Diagrams with Special Reference to Refractory Materials, *Academic Press*, New York, 1970.
10. N. Saunders and P. Miodownik, *CALPHAD, Pergamon Materials Series*, vol. 1 Ed. R. W. Cahn 1998.
11. O. Fabrichnaya, S. K. Saxena, P. Richet, and E. F. Westrum, Thermodynamic Data, Models, and Phase Diagrams in Multicomponent Oxide Systems: An Assessment for Materials and Planetary Scientists Based on Calorimetric, Volumetric and Phase Equilibrium Data. *Springer Science & Business Media*, Berlin, Heidelberg, 2004.

12. H. L. Lukas, S. G. Fries, and B. Sundman, Computational Thermodynamics: the CALPHAD Method, *Cambridge: Cambridge University Press*, vol. 131, 2007.
13. U. R. Kattner, The CALPHAD Method and Its Role in Material and Process Development, *Tecnologia em Metalurgia, Materiais e Mineracao*, 2016, 13(1), p 3.
14. Z. K. Liu and Y. Wang, Computational Thermodynamics of Materials, *Cambridge, Cambridge University Press*, 2016.
15. D. Pelton, S. A. Degterov, G. Eriksson, C. Robelin, and Y. Dessureault, The Modified Quasichemical Model I-Binary Solutions, *Metall. Mater. Trans. B*, 2000, 31(4), p 651-659.
16. D. Pelton and P. Chartrand, The Modified Quasi-chemical Model: Part II. Multicomponent Solutions, *Metall. Mater. Trans. A*, 2001, 32(6), p 1355-1360.
17. M. Hillert, The Compound Energy Formalism, *J. Alloys Compounds*, 2001, 320(2), p 161-176.

Chapter 2: Thermodynamic Modeling

2.1 Critical Evaluation and Optimization

In the present study, thermodynamic modeling of all the sub-systems of the Fe-Mn-Al-Si-C-P alloys are performed using the CALculation of PHase Diagrams (CALPHAD) method based on the critical evaluation of all available phase equilibria and thermodynamic data, aiming at obtaining one set of consistent Gibbs energies expressions of all phases as functions of temperature and composition. During the data evaluation, the discrepancies among available experimental data need to be resolved and only reliable data can be selected for further thermodynamic optimization. The optimization of a system follows the order from low-order systems to high-order systems to ensure self-consistency of the database. The model parameters of low-order systems are automatically adopted in the calculations of high-order systems. In this way, once a large self-consistent thermodynamic database is developed, it can be utilized to calculate any unexplored phase diagrams and thermodynamic properties of the systems of interest. Besides, the developed database can be applied to various industrial productions and assist in understanding the thermochemistry process of different conditions.

During the process of thermodynamic evaluation and optimization using CALPHAD approach, the following procedures are followed:

i. the system of interest is well-defined. As mentioned above, the optimization undergoes in the order of low-order systems to high-order systems, so the unaries (Fe, Mn, Al, Si, C, P in various solid states, liquid state, gaseous species), binary systems (Fe-P, Mn-P, Al-P, Si-P, C-P, Fe-Mn,

Fe-Al, Fe-Si, etc.), ternary systems (Fe-Mn-P, Fe-Al-P, Fe-Si-P, Fe-C-P, etc.), quaternaries and even multicomponent systems are defined;

ii. in the process of data evaluation, all available data from the literature for the system of interest are collected: (1) thermodynamic data including heat capacity, entropy, enthalpy, Gibbs energy, vapor pressure, chemical potential and activity data, etc.; (2) phase equilibria data like liquidus, solidus, solubility, melting point and various phase boundaries of multiphases; (3) crystallographic structure information like prototype, space group, Pearson symbol, lattice parameters, etc; (4) magnetic ordering and chemical ordering of stable phases in the studied system;

iii. ahead of the thermodynamic optimization, the reliability of all collected literature data should be critically evaluated. Once all available experimental data are in good consistency, then thermodynamic optimization is directly performed by reproducing the data as much as possible. In the cases that experimental data from different sources are not consistent with each other, experimental error limits and incoherencies within the data are checked by evaluating the sample preparations, experimental procedures and techniques, characteristics ways, etc. Other possible experimental errors, for example, total pressure of all gaseous phosphorus species (gaseous P, P₂, P₄), which was often taken as the partial pressure of P₂ gas, must be carefully used in the evaluation. Eventually, reliable experimental data are reproduced with minimum model parameters. Occasionally, it is hard to judge the accuracy of experimental data from very limited information, so other experimental results by the same authors can also be referred to judge the reliability of their experiments. In addition, systematic evaluation between preliminary thermodynamic optimization and multiple systems is always helpful for obtaining consistent assessment;

iv. in the case that the available literature data are not sufficient for determining the Gibbs energies all involved phases of a system, key experiments may be needed to explore the phase diagrams and thermodynamic properties of the target system;

v. with available experimental data ready for the thermodynamic optimization, proper models are selected based on the nature or crystal structure of the phases to calculate the Gibbs energies. The number and scale of model parameters highly depends on the model selected for the modeling. A good thermodynamic model can minimize the model parameters and improve the predictability of thermodynamic database for the high-order and multicomponent systems simultaneously;

vi. thermodynamic modeling is performed following the order from low-order systems to high-order systems. The model parameters of low-order parameters are automatically taken advantage of in the high-order systems to keep the consistency of the thermodynamic database. In addition, reduction of model parameters and enhancement of the predictability of the database in high-order systems can also be achieved by introducing appropriate geometric interpolation techniques in the ternary liquid solutions. Basically, it is highly preferred to minimize of the model parameters used in the database without sacrificing the accuracy in reproducing experimental data;

vii. once the preliminary optimizations of all the unary, binary and ternary systems are finished, then tests on the multicomponent systems are necessary to check the accuracy and consistency of the database. Besides, the model parameters of low-order systems can also be reoptimized to compensate the discrepancies left in different phases and systems to ascertain overall consistency of the developed thermodynamic database.

2.2 FactSage Software

FactSage [1] is a commercial software introduced in 2001 as the fusion of the FACT-Win/F*A*C*T (Thermfact, Canada) and ChemSage/SOLGASMIX (GTT-Technology, Germany) thermochemical packages [2]. This software runs on a PC operating under Microsoft Windows and consists of a series of information, database, calculation and manipulation modules. In FactSage software, complex calculations in the fields of materials science, pyrometallurgy, hydrometallurgy, electrometallurgy, corrosion, glass technology, combustion, ceramics, geology, etc. can be performed using the databases stored behind the software. The accuracy of thermodynamic calculations in FactSage depends on the accuracy of the databases. At the moment, there are 18 databases available in the most updated FactSage 7.3. They are ELEM, FTdemo, FactPS, SGPS, FToxid, FTsalt, FTmisc, FTOxCN, FTfrtz, FThall, FThehg, FTpulp, FTlite, FTnucl, FSscop, FSlead, FSstel, FSupsi, SGsold, SGTE2011, SGTE2014, SGTE2017, BINS, SGUN, SGnobl, SpMCCBN, and TDnucl databases. The details of the database are available elsewhere [2]. The most important database relevant to the present study are the following four databases:

- The **FactPS** database contains more than 4800 pure stoichiometric solids, liquids, and gases phases. In particular, the Gibbs energy data of gas phase such as O₂, N₂, CO, CO₂, P₂, etc. are all taken from this database.
- The **FSstel** is specialized database for steel, which is an updated version of the SGTE solution database [3] and is similar to the TCFE database in ThermoCalc software [4]. It is mainly used for phase diagram calculations. The **FSstel** database contains 31 elements (Al, B, Bi, C, Ca, Ce, Co, Cr, Cu, Fe, Hf, La, Mg, Mn, Mo, N, O, Nb, Ni, P, Pb, S, Sb, Si, Sn, Ta, Ti, V, W, Zn, Zr) in over 205 completely assessed binary alloy systems, approximately 100 ternary and 20 quaternary systems, in which there are stable 133 solution phases and 447 stoichiometric

compounds. In the **FSstel** database of FactSage 7.3, the liquid solutions are described using Modified Quasichemical Model (MQM) [5,6]. This database is intended for calculating the steelmaking processes including (1) reduction of O and S content by de-O and de-S of the melt, (2) constitution of a wide range of steels, including austenitic, ferritic and duplex stainless steels, carbide and nitride formation, (3) conditions for heat treatment operations to produce a desired constitution, (4) conditions for scrap re-melting to maintain as low concentrations as possible of undesired “tramp elements”, and (5) melt-crucible interactions, etc.

- The **FTmisc** database is mainly developed for the applications on impurity refining of liquid metals, and non-ferrous smelting process. In particular, the liquid Fe solution (**FTmisc-FeLq**) database was developed using the United Interaction Parameter Formalism (UIPF) [7] with the well-known interaction parameters recommended by JSPS [8]. This database covers over 30 dilute elements in the Fe melt (Fe-Ag-Al- B-C-Ca-Ce-Co-Cr-Cu-H-La-Mg-Mn-Mo-N-Nb-Ni-O-Pb-Pd-S-Si-Sn-Ta-Ti-U-V-W-Zr). That is, the accuracy can only be ensured in the Fe-rich liquids with dilute alloy components.
- The **FToxid** database contains data of pure oxides and oxides solutions of 23 elements for the molten slag, numerous solid solutions and all available stoichiometric compounds in the Al_2O_3 -CaO-SiO₂-MgO-FeO-Fe₂O₃-MnO-TiO₂-Ti₂O₃-CrO-Cr₂O₃-ZrO₂-NiO-CoO-Na₂O-K₂O-B₂O₃-Cu₂O-As₂O₃-GeO₂-PbO-SnO-ZnO-P₂O₅-S-F system. The database containing both liquid slag and solid phases. This is very important database for general pyrometallurgical process involving ores, slag, refractories, non-metallic inclusion, etc.

Compared to FSstel and FTmisc thermodynamic databases in currently most updated FactSage 7.3 version, the current PhD work with optimized parameters gives more accurate and self-consistent descriptions of the Fe-Mn-Al-Si-C-P system over the full composition range.

2.3 Thermodynamic Models

2.3.1 Pure Elements and Stoichiometric Compounds

The Gibbs energies of pure elements and stoichiometric compounds are calculated using the following equation:

$$G_T^\circ = H_T^\circ - T \cdot S_T^\circ \quad (2.1)$$

where G_T° , H_T° and S_T° are the Gibbs energy, enthalpy and entropy at temperature T in Kelvin, respectively. The Gibbs energies of pure elements are directly taken from the Scientific Group Thermodata Europe (SGTE) database [9]. In the present study, various pure solid phases in crystallographic structures such as FCC_A1, BCC_A2, HCP_A3, CBCC_A12, CUB_A13, Diamond_A4, etc. liquid and gaseous Fe, Mn, Al, Si, C and P elements are taken into account. The Gibbs energies of involved stoichiometric compounds were calculated from the enthalpy and entropy as functions of the heat capacity C_P at given temperature as follows:

$$H_T^\circ = \Delta H_{298.15K}^\circ + \int_{T=298.15K}^T C_P dT \quad (2.2)$$

$$S_T^\circ = S_{298.15K}^\circ + \int_{T=298.15K}^T (C_P / T) dT \quad (2.3)$$

where $\Delta H_{298.15K}^\circ$ is the standard enthalpy of formation at 298.15 K, $S_{298.15K}^\circ$ is the standard entropy at 298.15 K, and C_P is the heat capacity. That is, the Gibbs energies (G_T°) of stoichiometric compounds can be calculated from $\Delta H_{298.15K}^\circ$, $S_{298.15K}^\circ$ and C_P .

Basically, the C_p expression of each compound can be determined by fitting the experimental C_p data. In the case of no available experimental C_p data for a stoichiometric compound, then its C_p expression can be predicted using Neumann-Kopp (NK) rule [10] or from heat capacity expression of neighboring compounds of the same system. For example, the C_p of Fe_3P , Fe_2P and FeP are determined based on their experimental C_p data, but the C_p expression of FeP_2 with no available experimental data is estimated from those of Fe_3P , Fe_2P and FeP . The $\Delta H_{298.15\text{K}}^\circ$ is usually determined from calorimetry measurements and $S_{298.15\text{K}}^\circ$ is integrated from low temperature C_p data below 298.15 K. And also, $\Delta H_{298.15\text{K}}^\circ$ and $S_{298.15\text{K}}^\circ$ are sometimes back-calculated from high temperature data, which can be Gibbs energy, enthalpy, entropy, heat capacity, activity, partial pressure of gas species, etc. at high temperatures. If there are no available experimental information for $\Delta H_{298.15\text{K}}^\circ$ and $S_{298.15\text{K}}^\circ$, then they can also be adjusted within reasonable ranges to reproduce other experimental data.

In the present study, the Gibbs energies of following stoichiometric intermediate compounds were considered:

- i.* the Fe-P system: Fe_3P , Fe_2P , FeP , FeP_2 ;
- ii.* the Mn-P system: Mn_3P , Mn_2P , Mn_3P_2 , MnP , MnP_3 ;
- iii.* the Al-P system: AlP ;
- iv.* the Si-P system: SiP , SiP_2 ;
- v.* the Fe-Al system: Fe_2Al_5 , FeAl_2 ;
- vi.* the Fe-Si system: Fe_2Si , Fe_5Si_3 , FeSi , FeSi_2 ; Fe_3Si_7 ;
- vii.* the Fe-C system: Fe_3C ;

viii: the Mn-Al system: $Mn_{23}Al_{99}$, Mn_4Al_{11} , $MnAl_{12}$, $MnAl_4$, $MnAl_6$;

ix: the Mn-Si system: Mn_6Si , Mn_9Si_2 , Mn_3Si , Mn_5Si_3 , $MnSi$, $Mn_{11}Si_{19}$;

x: the Mn-C system: $Mn_{23}C_6$, Mn_3C , Mn_5C_2 , Mn_7C_3 ;

xi: the Al-C system: Al_4C_3 ;

xii: the Si-C system: SiC ;

xiii: the Fe-Si-P system: $FeSi_4P_4$;

xiv: the Mn-Si-C system: Mn_5SiC , Mn_8Si_2C ;

xv: the Al-Si-C system: Al_8SiC_7 , Al_4SiC_4 .

When a pure element or stoichiometric compound exhibits magnetic behavior, an additional magnetic contribution term G^{mg} , which was originally proposed by Inden [11] and then modified by Hillert and Jarl [12], has to be taken into account in describing the Gibbs energy:

$$G^{mg} = RT \ln(\beta + 1) g(\tau) \quad (2.4)$$

where, τ is given by T/T^* and T^* is the critical temperature of magnetic transition associated with Curie temperature T_C for ferromagnetic materials or Neel temperature T_N for antiferromagnetic materials. β is the average magnetic moment per mole of atoms expressed in Bohr magnetons.

$g(\tau)$ is a polynomial fraction derived by Hillert and Jarl [12]:

$$g(\tau) = 1 - \left[\frac{79\tau^{-1}}{140P} + \frac{474}{497} \left(\frac{1}{P} - 1 \right) \left(\frac{\tau^3}{6} + \frac{\tau^9}{135} + \frac{\tau^{15}}{600} \right) \right] / D \quad \dots \tau \leq 1 \quad (2.5)$$

$$g(\tau) = - \left(\frac{\tau^{-5}}{10} + \frac{\tau^{-15}}{315} + \frac{\tau^{-25}}{1500} \right) / D \quad \dots \tau > 1 \quad (2.6)$$

where $D = \frac{518}{1125} + \frac{11692}{15975} \left(\frac{1}{P} - 1 \right)$, and the value of P can be considered as the fraction of the magnetic enthalpy absorbed above the critical temperature depending on the structure. P is 0.40 for the simple BCC_A2 phase while P is 0.28 for other common phases.

2.3.2 Liquid Solution

In a liquid solution with no interaction between the components, all components are randomly distributed in the solution. In this case, the Gibbs energy of the liquid solution is calculated using:

$$G = \sum_{i=1}^n xG_i^{\circ} + RT \sum_{i=1}^n x_i \ln(x_i) \quad (2.7)$$

where G_i° is the Gibbs energy of pure liquid component i , x_i is the mole fraction of component i , T is the temperature in Kelvin (K), and $R \sum_{i=1}^n x_i \ln(x_i)$ is the contribution of configurational entropy to the Gibbs energy resulted from random mixing in one dimensional Ising approximation.

When the components of the liquid solution have the same probability to occupy any lattice sites, then the Gibbs energy of the solution is expressed by the regular solution model (random mixing model) as follows:

$$G = \sum_{i=1}^n xG_i^{\circ} + RT \sum_{i=1}^n x_i \ln(x_i) + G^{ex} \quad (2.8)$$

where G^{ex} is the excess Gibbs energy describing the interaction among the components of the liquid solution. In the A-B liquid solution, for example, G^{ex} is often expressed as a polynomial in the mole fraction as follows:

$$G^{ex} = \sum_{i,j} q_{AB}^{ij} x_A^i x_B^j \quad (2.9)$$

where q_{AB}^{ij} is the interaction parameter and can be temperature-dependent. There are also a few more mathematical polynomial expressions for describing the excess Gibbs energy G^{ex} . One of the most popular expressions is “Redlich-Kister” polynomial expressed as below:

$$G^{ex} = x_A x_B \sum_{i=0}^n L_i (x_A - x_B)^i \quad (2.10)$$

here L_i is the interaction parameters which can also be temperature dependent. The type of the model as expressed in **Eq. (2.10)** depends on the value of n used in the optimization as follows:

i. $n = 0$, it is the regular solution model as described below:

$$G^{ex} = x_A x_B L_0 \quad (2.11)$$

ii. $n = 1$, it is the sub-regular solution model as described below:

$$G^{ex} = x_A x_B (L_0 + L_1 (x_A - x_B)) \quad (2.12)$$

iii. $n = 2$, it is the sub-sub-regular solution model as described below:

$$G^{ex} = x_A x_B (L_0 + L_1 (x_A - x_B) + L_2 (x_A - x_B)^2) \quad (2.13)$$

In many cases, however, the model for the liquid solutions with assumption of random mixing of components is lacking in accuracy, especially in the liquid solutions exhibiting significant deviation from ideal mixing. Different components of the liquid solution have tendency to be together in terms of energetic reason, that is, the atoms of the solution exhibit short-range ordering. Besides, the enthalpy of mixing shows a “V” shape in terms of composition. For example, the enthalpy of mixing of the Fe-P solution has a minimum value at around $x_P = 0.33$ (Fe: P = 2: 1). In this situation, some new models such as the associate solution model and quasi-chemical model were developed to describe the liquid solution considering short-range ordering (SRO).

In the current PhD thesis, the liquid solution was described using the Modified Quasichemical Model (MQM) [5,6] considering the short-range ordering of the nearest-neighbor atoms was used to describe liquid Fe-P solution. Compared to the conventional regular solution model (Bragg-Williams Random Mixing Model), the MQM gives more realistic thermodynamic description of the entropy of the liquid phase. In the MQM, the Gibbs energy of pair formation can be expanded as a polynomial in the pair fraction instead of the component fraction, and the coordination numbers are allowed to vary with composition for describing the short-range ordering of the liquid solution. These modifications provide greater flexibility in reproducing experimental data of the binary system and combining the binary parameters to higher-order solutions.

In the case of A-B liquid solution, the molecules of atoms A and B are assumed to be distributed over the quasilattice sites. The atom pair exchange-reaction of the A-B liquid solution can be expressed as follows:



where $(i-j)$ represents the nearest-neighbor pair between components i and j , and Δg_{AB} is the Gibbs energy change of forming 2 moles of $(A-B)$ pairs. The Gibbs energy of the liquid solution can be calculated by the following equation:

$$G_L^{sol.} = (n_A G_A^o + n_B G_B^o) - T \Delta S^{conf.} + n_{AB} (\Delta g_{AB} / 2) \quad (2.15)$$

where n_A and n_B are the numbers of moles of A and B atoms, and G_A^o and G_B^o are the molar Gibbs energies of pure components A and B. $\Delta S^{conf.}$ is the configurational entropy of mixing given by random distribution of the $(A-A)$, $(B-B)$ and $(A-B)$ pairs.

$$\Delta S^{conf.} = -R(n_A \ln X_A + n_B \ln X_B) - R \left[n_{AA} \ln \left(\frac{X_{AA}}{Y_A^2} \right) + n_{BB} \ln \left(\frac{X_{BB}}{Y_B^2} \right) + n_{AB} \ln \left(\frac{X_{AB}}{2Y_A Y_B} \right) \right] \quad (2.16)$$

here n_{AA} , n_{BB} and n_{AB} are the numbers of moles of (A-A), (B-B) and (A-B) pairs, and X_{AA} , X_{AB} and X_{BB} are the pair fraction of the corresponding atom pairs. Y_A and Y_B are the coordination equivalent fractions of components A and B. The pair fractions X_{AA} , X_{AB} , X_{BB} and coordination equivalent fractions Y_A , Y_B can be calculated as follows:

$$X_{AA} = n_{AA} / (n_{AA} + n_{AB} + n_{BB}) \quad (2.17)$$

$$X_{AB} = n_{AB} / (n_{AA} + n_{AB} + n_{BB}) \quad (2.18)$$

$$X_{BB} = n_{BB} / (n_{AA} + n_{AB} + n_{BB}) \quad (2.19)$$

$$Y_A = X_{AA} + \frac{1}{2} X_{AB} \quad (2.20)$$

$$Y_B = X_{BB} + \frac{1}{2} X_{AB} \quad (2.21)$$

Δg_{AB} is the model parameter for reproducing the Gibbs energy of the binary A-B solution, which can be expanded as a polynomial in terms of the atomic pair fractions X_{AA} and X_{BB} as follows:

$$\Delta g_{AB} = \Delta g_{AB}^o + \sum_{i \geq 1} g_{AB}^{i0} X_{AA}^i + \sum_{j \geq 1} g_{AB}^{0j} X_{BB}^j \quad (2.22)$$

where Δg_{AB}^o , g_{AB}^{i0} and g_{AB}^{0j} are the adjustable model parameters that can be functions of the temperature. In the MQM, the coordination numbers of atoms A and B, Z_A and Z_B , are allowed to vary with composition to reproduce the short-range ordering of the liquid phase and expand to higher-order systems using proper geometric interpolation technique.

$$\frac{1}{Z_A} = \frac{1}{Z_{AA}^A} \left(\frac{2n_{AA}}{2n_{AA} + n_{AB}} \right) + \frac{1}{Z_{AB}^A} \left(\frac{n_{AB}}{2n_{AA} + n_{AB}} \right) \quad (2.23)$$

$$\frac{1}{Z_B} = \frac{1}{Z_{BB}^B} \left(\frac{2n_{BB}}{2n_{BB} + n_{AB}} \right) + \frac{1}{Z_{BA}^B} \left(\frac{n_{AB}}{2n_{BB} + n_{AB}} \right) \quad (2.24)$$

here Z_{AA}^A is the value Z_A when all nearest neighbors of a A atom are A atoms, and Z_{AB}^A is the value of Z_A when all nearest neighbors of the A atom are B atoms. Z_{BB}^B and Z_{BA}^B are defined in an analogous manner.

The MQM can be easily extended from binary systems to ternary and multicomponent systems. For simplicity, the ternary 1-2-3 liquid solution is taken as an example. The pair exchange reaction between M and N atoms of the 1-2-3 solution distributed over the quasi-lattice sites is as follows:

$$(M - M) + (N - N) = 2(M - N); \Delta g_{MN} \quad (2.25)$$

here M, N = 1, 2, 3, (M-M), (M-N) and (N-N) represent the first-nearest-neighbor pairs between components M and N, and Δg_{MN} is the Gibbs energy change of forming 2 moles of (M-N) pairs.

The Gibbs energy of the liquid solution is calculated using:

$$G_L^{sol.} = \sum_{M=1}^3 n_M G_M^o - T \Delta S^{conf.} + \sum_{N>M} \sum_{M=1}^3 n_{MN} (\Delta g_{MN} / 2) \quad (2.26)$$

where n_M is the number of the moles of atom M (M = 1, 2, 3) in the liquid solution, G_M^o is the molar Gibbs energy of pure liquid M, n_{MN} is the number of the moles of M-N pairs, Δg_{MN} is the Gibbs energy change of forming 2 moles of (M-N) pairs, and $\Delta S^{conf.}$ is an approximate configurational entropy of mixing given by the following expression:

$$\Delta S^{conf.} = -R \sum_{M=1}^3 n_M \ln x_M - R \left[\sum_{M=1}^3 n_{MM} \ln \left(\frac{x_{MM}}{Y_M^2} \right) + \sum_{N>M} \sum_{M=1}^3 n_{MN} \ln \left(\frac{x_{MN}}{2Y_M Y_N} \right) \right] \quad (2.27)$$

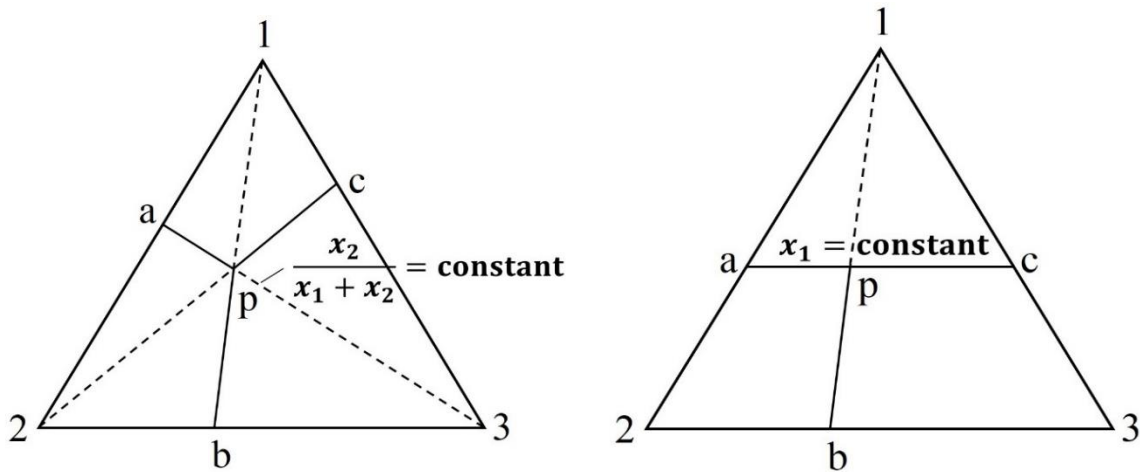
where x_M is the mole fraction of component M, n_{MM} is the number of moles and x_{MN} is the mole fraction of each type of atom pairs (1-1, 2-2, 3-3, 1-2, 1-3, 2-3), and Y_M and Y_N is the coordination equivalent fraction of components M, N (M, N = 1, 2, 3), they are defined as follows:

$$x_M = n_M / \sum_{i=1}^3 n_i \quad (2.28)$$

$$x_{MN} = n_{MN} / (\sum_{i=1}^3 n_{ii} + \sum_{\substack{i=1 \\ j>i}}^3 n_{ij}) \quad (2.29)$$

$$Y_M = x_{MM} + \frac{1}{2} \sum_{M \neq N} x_{MN} \quad (2.30)$$

In the MQM used for the ternary and higher-order systems, various geometric interpolation techniques [6] based on the nature of each binary system within a ternary system are used to predict the Gibbs energy of the liquid solution. If necessary, ternary correction terms can also be further introduced to give more precise description of the Gibbs energy of the ternary liquid solution. Four types of geometric interpolation models including symmetric Kohler model and Muggianu model, and asymmetric Kohler/Toop model and Muggianu/Toop model are commonly used by the FactSage community, as demonstrated in **Fig. 2.1**. For example, the Toop interpolation technique with P as the asymmetric component is adopted for the Fe-Mn-P liquid solution in the present database, because the Fe-P and Mn-P liquid solutions deviate significantly from ideal mixing while the Fe-Mn liquid solution is almost in ideal mixing.



(a) Kohler model

(b) Kohler / Toop model

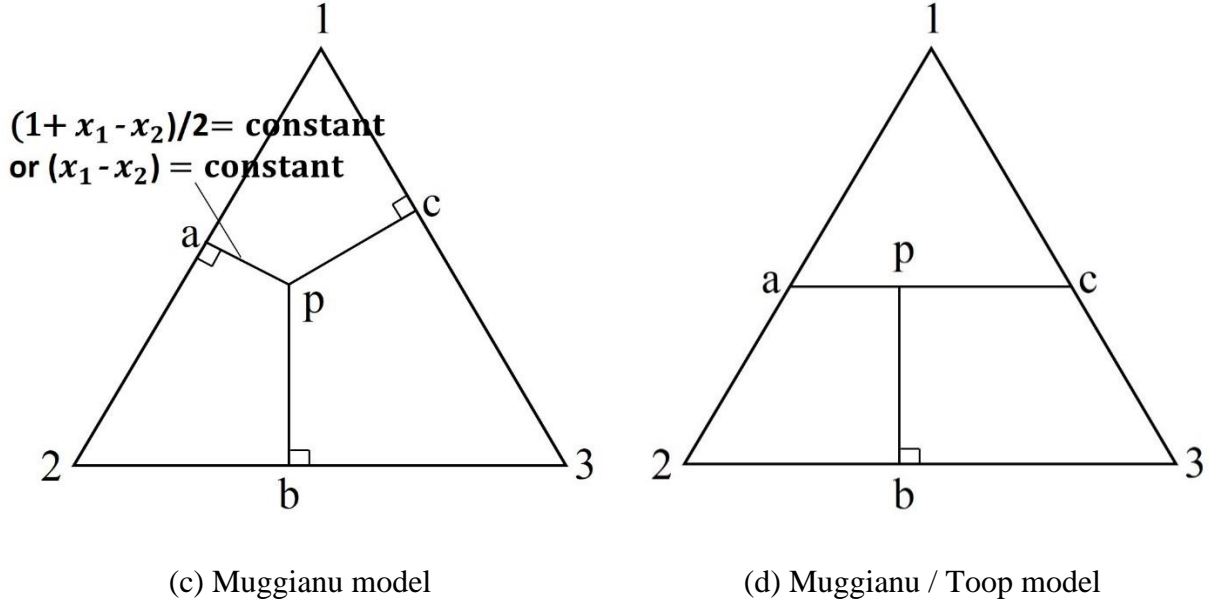


Figure 2.1 Geometric models: (a) Kohler model, (b) Kohler / Toop model, (c) Muggianu model, and (d) Muggianu / Toop model

In the present optimization for all P-containing systems, only Kohler and Kohler / Toop interpolation techniques are used. In the case of an asymmetric ternary 1-2-3 solution with component “1” as asymmetric component. the Δg_{12} and Δg_{13} between asymmetric components (1 and 2, 1 and 3) are calculated by:

$$\Delta g_{12} = \Delta g_{12}^{\circ} + \sum_{(i+j) \geq 1} g_{12}^{ij} x_{11}^i (x_{22} + x_{23} + x_{33})^j + \sum_{i \geq 0, j \geq 0, k \geq 1} g_{12(3)}^{ijk} x_{11}^i (x_{22} + x_{23} + x_{33})^j \left(\frac{Y_3}{Y_2 + Y_3} \right)^k \quad (2.31)$$

$$\Delta g_{13} = \Delta g_{13}^{\circ} + \sum_{(i+j) \geq 1} g_{13}^{ij} x_{11}^i (x_{22} + x_{23} + x_{33})^j + \sum_{i \geq 0, j \geq 0, k \geq 1} g_{13(2)}^{ijk} x_{11}^i (x_{22} + x_{23} + x_{11})^j \left(\frac{Y_2}{Y_2 + Y_3} \right)^k \quad (2.32)$$

and Δg_{23} between symmetric components (2 and 3) is calculated by:

$$\begin{aligned} \Delta g_{23} = & \Delta g_{23}^{\circ} + \sum_{(i+j) \geq 1} g_{23}^{ij} \left(\frac{x_{22}}{x_{22} + x_{23} + x_{33}} \right)^i \left(\frac{x_{33}}{x_{22} + x_{23} + x_{33}} \right)^j \\ & + \sum_{i \geq 0, j \geq 0, k \geq 1} g_{23(1)}^{ijk} \left(\frac{x_{22}}{x_{22} + x_{23} + x_{33}} \right)^i \left(\frac{x_{33}}{x_{22} + x_{23} + x_{33}} \right)^j Y_1^k \end{aligned} \quad (2.33)$$

where g_{12}^{ij} , g_{13}^{ij} , g_{23}^{ij} are the binary liquid parameters; $g_{12(3)}^{ijk}$, $g_{13(2)}^{ijk}$ and $g_{23(1)}^{ijk}$ are the ternary liquid parameters.

2.3.3 Solid Solutions

The Gibbs energies of the solid solutions were modeled using the Compound Energy Formalism (CEF) [13] considering crystallographic structures. In the sub-systems of the Fe-Mn-Al-Si-P system, the disordered FCC_A1, BCC_A2, HCP_A3, CBCC_A12, CUB_A13, etc. solid solutions are described with one sub-lattice approach for the substitutional site. Take A-B-C system as an example, the molar Gibbs energies of its substitutional solutions are calculated as follows:

$$\begin{aligned} G_s^{sol} = & \sum_{i=A,B,C} x_i G_i^{\circ} + RT \sum_{i=A,B,C} x_i \ln x_i \\ & + \sum_{m=0,1,2,\dots} x_A x_B^m L_{A,B} + \sum_{k=0,1,2,\dots} x_B x_C^k L_{B,C} + \sum_{p=0,1,2,\dots} x_A x_C^p L_{A,C} \\ & + \sum_{q=0,1,2,\dots} x_A x_B x_C^q L_{A,B,C} + G^{mg} \end{aligned} \quad (2.34)$$

where x_i is the mole fraction of component i ($i = A, B, C$) in the substitutional site. G_i° is the molar Gibbs energy of pure solid i . R and T are the gas constant (8.314 J/mol-K) and the temperature in Kelvin (K); ${}^m L_{i,j}$ is the adjustable binary interaction parameters between components i and j ($i, j = A, B, C$); ${}^q L_{A,B,C}$ is the adjustable ternary parameters of component A, B, C; G^{mg} is the magnetic contribution to the Gibbs energy, which was also described by Hillert and Jarl [12] using **Eqs. (2.4-2.6)**. The magnetic transition temperature and Bohr magneton can be described by a linear combination of pure element properties with the excess terms in the forms of R-K polynomial.

In the case of solid solutions with more than one sublattice like two sublattices (A, B)_m(C,D)_n. The schematic graph of this two sublattices solid solution model is demonstrated in **Fig. 2.2**.

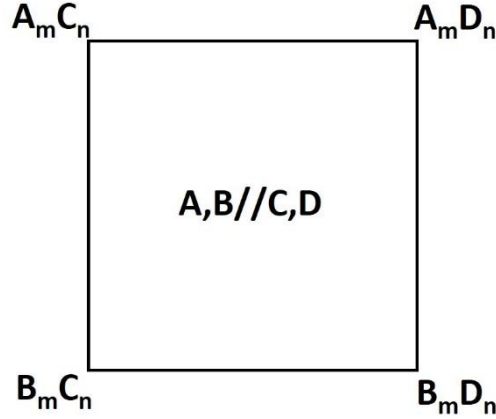


Figure 2.2 Schematic graph of the two sublattices (A, B)_m(C, D)_n solid solution model

As shown in the figure, $A_m C_n$, $A_m D_n$, $B_m C_n$, and $B_m D_n$ are the end-members of the solid solution. The Gibbs energy per formula unit of this phase can be described using Compound Energy Formalism (CEF) [13] as follows:

$$\begin{aligned}
 G_S^{sol.} = & y_A y_C G_{A:C} + y_A y_D G_{A:D} + y_B y_C G_{B:C} + y_B y_D G_{B:D} \\
 & + mRT (y_A \ln y_A + y_B \ln y_B) + nRT (y_C \ln y_C + y_D \ln y_D) \\
 & + \sum_{i=0,1,2,\dots} \left(\sum_{m=C,D} y_A y_B y_m^i L_{A,B:m} + \sum_{n=A,B} y_n y_C y_D^i L_{n:C,D} \right) + \sum_{i=0,1,2,\dots} y_A y_B y_C y_D^i L_{A,B:C,D} + G^{mg}
 \end{aligned} \tag{2.35}$$

where $G_{A:C}$, $G_{A:D}$, $G_{B:C}$, $G_{B:D}$ are Gibbs energies of the end-members of $A_m C_n$, $A_m D_n$, $B_m C_n$, and $B_m D_n$, respectively; y_A , y_B and y_C , y_D are the site fractions of components A, B on the first sublattice ($y_A + y_B = 1$) and components C, D on the second sublattice ($y_C + y_D = 1$), respectively; ${}^i L_{A,B:m}$ and ${}^i L_{n:C,D}$ interaction parameters between components A and B on the first sublattice, and between components C and D on the second sublattice. ${}^i L_{A,B:C,D}$ is the reciprocal

interaction parameter with the first sublattice occupied by components A, B and the second sublattice occupied by components C, D.

In some solid solutions, there exists order-disorder transition in terms of temperature and composition. This type of transition belongs to second order transition. To describe this type of phase transition, the Gibbs energies of both the disordered part and ordered part need to be considered simultaneously. At the moment, only the transition in face centered cubic (FCC) and body centered cubic (BCC) structures can be accurately described. For the FCC phase, there are disordered FCC_A1 structure and ordered FCC_L10 and FCC_L12 structures. For the BCC phase, disordered BCC_A2 and ordered BCC_B2 and BCC_D03 crystal structures are included.

In the description of the Gibbs energy of a phase with order-disorder transition, the disordered and ordered parts need to be considered simultaneously. Take the transition between disordered BCC_A2 and ordered BCC_B2 of the M-K system as an example. The BCC phase was modeled considering disordered part described with the model (M, K)(Va)₃ and the ordered part described with the model (M, K)_{0.5}(M, K)_{0.5}(Va)₃. The Gibbs energy of the BCC solid solution is calculated using the following expression:

$$G_{BCC}^{sol.} = G_S^{disorder} + \Delta G_{BCC}^{order} \quad (2.36)$$

where $G_S^{disorder}$ is the Gibbs energy contribution of the disordered part, which can be calculated using **Eqs. (2.34)** and **(2.35)**, ΔG_{BCC}^{order} is the Gibbs energy contribution of long-range ordering. When the site fractions of component i ($i = M, K$) in the first sublattice equals to that in the second sublattice ($y'_i = y''_i$), then the ordering contribution ΔG_{BCC}^{order} equals to zero and the Gibbs energy

of BCC phase is the same as the Gibbs energy of disordered BCC_A2 ($G_S^{disorder}$). When $y_i' \neq y_i''$, then the ordering contribution ΔG_{BCC}^{order} becomes negative and is calculated using **Eq. (2.37)**.

$$\begin{aligned}
G_{BCC}^{order}(y_i', y_j'') &= y_M' y_M'' G_{M:M} + y_K' y_K'' G_{K:K} \\
&+ y_M' y_K'' G_{M:K} + y_K' y_M'' G_{K:M} \\
&+ 0.5RT \left(y_M' \ln y_M' + y_K' \ln y_K' \right) \\
&+ 0.5RT \left(y_M'' \ln y_M'' + y_K'' \ln y_K'' \right) \\
&+ \sum_{\substack{i=M,K \\ p=0,1,2\dots}} y_M' y_K'' y_i'' L_{M,K:i}^p + \sum_{\substack{j=M,K \\ p=0,1,2\dots}} y_j' y_M'' y_K'' L_{j:M,K}^p + \sum_{\substack{j=M,K \\ p=0,1,2\dots}} y_M' y_K' y_M'' y_K'' L_{M,K:M:K}^p + G^{mg}
\end{aligned} \tag{2.37}$$

here i, j represent M, K. y_M', y_K' and y_M'', y_K'' are site fractions of components M, K in the first and second lattice of the formula $(M, K)_{0.5}(M, K)_{0.5}(Va)_3$. In the composition of site fractions of component i in the first sublattice equals to that in the second sublattice ($y_i' = y_i''$), then the ordering contribution ΔG_{BCC}^{order} is zero and the Gibbs energy of BCC is the same as the Gibbs energy of disordered BCC_A2 ($G_S^{disorder}$) calculated in **Eq. (2.34)**. In the case of $y_i' \neq y_i''$, then the ordering contribution ΔG_{BCC}^{order} becomes negative and the Gibbs energy of BCC phase with consideration of disorder/order transit is calculated using **Eq. (2.36)**.

Reference

1. W. Bale, P. Chartrand, S. A. Degterov, G. Eriksson, K. Hack, R. B. Mahfoud, and S. Petersen, FactSage Thermochemical Software and Databases, *CALPHAD*, 2002, 26(2), p 189-228.
2. <http://www.factsage.com/>.
3. www.sgte.org, SGTE database.
4. <https://www.thermocalc.com/>.
5. D. Pelton, S. A. Degterov, G. Eriksson, C. Robelin, and Y. Dessureault, The Modified Quasichemical Model I-Binary Solutions, *Metall. Mater. Trans. B*, 2000, 31(4), p 651-659.

6. D. Pelton and P. Chartrand, The Modified Quasi-chemical Model: Part II. Multicomponent Solutions, *Metall. Mater. Trans. A*, 2001, 32(6), p 1355-1360.
7. C.W. Bale, A.D. Pelton, The Unified Interaction Parameter Formalism: Thermodynamic Consistency and Applications, *Metall. Trans. A*, 1990, 21, p 1997-2002.
8. JSPS, Steelmaking Data Sourcebook, *19th Committee on Steelmaking*, Gordon & Breach Science, New York, USA, 1988.
9. T. Dinsdale, SGTE Data for Pure Elements, *CALPHAD*, 1991, 15(4), p 317-425.
10. J. Leitner, P. Vončka, D. Sedmidubsky, and P. Svoboda, Application of Neumann-Kopp Rule for the Estimation of Heat Capacity of Mixed Oxides, *Thermoch. Acta*, 2010, 497(1-2), p 7-13.
11. G. Inden, Project Meeting CALPHAD V, Max-Planck-Inst, *Eisenforschung*, Dusseldorf, Germany, 1976, p 111.
12. M. Hillert and M. Jarl, A Model for Alloying in Ferromagnetic Metals, *CALPHAD*, 1978, 2(3), p 227-238.
13. M. Hillert, The Compound Energy Formalism, *J. Alloys Compound*, 2001, 320(2), p 161-176.

Chapter 3: Critical Evaluation and Thermodynamic Optimization of the Fe-P System

Zhimin You¹, In-Ho Jung²

1. Department of Mining and Materials Engineering, McGill University, 3610 University Street, Montreal, QC, H3A 0C5, Canada

2. Department of Materials Science and Engineering, and Research Institute of Advanced Materials (RIAM), Seoul National University, 1 Gwanak-ro, Gwanak-gu, Seoul, 08826, South Korea

(published online in Metallurgical and Materials Transactions B, August 18, 2020, DOI:

<https://doi.org/10.1007/s11663-020-01939-0>)

Abstract

Thermodynamic optimization of the Fe-P system was performed using the CALculation of PHase Diagrams (CALPHAD) method based on critical evaluation of all available phase equilibria and thermodynamic data. The Gibbs energies of liquid phase and solid solutions were described using the Modified Quasichemical Model and Compound Energy Formalism, respectively. The Fe-P phase diagram, thermodynamic properties of P in liquid Fe and stability of intermediate iron phosphides (Fe_3P , Fe_2P , FeP and FeP_2) in the entire composition range were reoptimized for resolving the discrepancies left in the previously optimized database. Several problems in previous assessments were resolved and a more accurate and consistent description of the Fe-P system was achieved compared to experimental data. The distribution of P between molten Fe-P alloys and slag at different temperatures was also calculated to present the applicability of the present work to steel dephosphorization calculation.

Keywords: Thermodynamic optimization, Fe-P system, CALPHAD, Iron phosphides, Dephosphorization

3.1. Introduction

Phosphorus in steels mainly originates from the raw materials such as iron ores, flux, coke etc. Phosphorus can improve the hardness, toughness, corrosion resistance and machinability in free-cutting steels, but in most cases, it is an undesirable impurity in steels and ferroalloys despite the relatively minor amount. For example, a very small amount of P in steel (about 0.04 wt.%) can result in weld brittleness and apparently increase the tendency of crack. Therefore, it is essential to control P tightly in steels. By controlling the proper chemistry of slag, phosphorus can be removed from the metal and transferred into the slag in the forms of P_2O_5 and phosphates.[1] For a liquid containing relatively high P content, stoichiometric iron phosphides can precipitate as the temperature decreases and the type of precipitated phosphide depends on the temperature and overall P content. Iron phosphides are often used as alloying agents to produce high P steels in the steelmaking process. In addition, iron phosphides can be produced as semiconductors because of their excellent performance in high power and high frequency applications.

To comprehend the thermodynamic behavior of P in Fe, numerous experimental studies and computational modeling have been performed. Experimental studies on the phase equilibrium and thermodynamic properties of the Fe-P system were reviewed by Okamoto [2], who proposed a partial diagram of the Fe-P system in the Fe-rich region. Recently, Schlesinger [3] summarized thermodynamic properties of different forms of phosphorus and iron phosphides based on reported information. The Fe-P system was thermodynamically assessed by Spencer and Kubaschewski [4], Gustafson [5], Shim et al. [6], Ohtani et al. [7] and Cao et al. [8,9]. Spencer and Kubaschewski [4] evaluated the thermodynamic properties and phase boundaries of each phase. Gustafson [5] performed a thermodynamic description of the Fe-P system in the composition up to 50 at.%P

within SGTE communication. However, a two-liquid miscibility gap is calculated in the P-rich region. Likewise, Shim et al. [6] assessed the partial Fe-P system up to 50 at.%P using the CALculation of PHase Diagrams (CALPHAD) method, and better reproduction of the BCC_A2 phase boundary was achieved compared to previous calculations by Gustafson [5]. However, the liquidus line and stability of P in liquid Fe apparently deviate from experimental data. In more recent modeling work by Ohtani et al. [7], the Fe-P system was thermodynamically optimized in the full composition range and five stoichiometric phosphides including Fe₃P, Fe₂P, FeP, FeP₂ and FeP₄ were considered. However, the thermal stability of the P-rich phosphide compounds such as FeP₂ and FeP₄ were estimated to be much higher than those of Fe₃P, Fe₂P and FeP. Recently, Cao et al. [9] reassessed the Fe-P system by adopting thermodynamic properties of iron phosphides recommended by Zaitsev et al. [10], who carried out experiments by means of differential scanning calorimetry (DSC) and the Knudsen effusion method (KEM) with mass-spectrometric analysis. The melting temperatures of FeP₂ and FeP₄ were lower than the results by Ohtani et al. [7] while the stability of FeP was overestimated for unknown reason. Experimental data of thermodynamic properties of P in liquid Fe were neglected in the optimization by Cao et al. [9].

The thermodynamic database based on the CALculation of PHase Diagrams (CALPHAD) method is a powerful tool for new materials design and process optimization. The database of target system is developed by means of thermodynamic modeling (optimization), aiming at obtaining one set of the consistent Gibbs energies of all phases as functions of temperature and composition. In the optimization, all available phase equilibria and thermodynamic data such as activity, entropy, enthalpy, and Gibbs energy, etc are critically evaluated simultaneously. The discrepancies between available data are resolved in the critical evaluation process, and the Gibbs energy functions for

all related phases in target system are derived. Predictions on unexplored thermodynamic properties and phase equilibria are possible by interpolations and extrapolations in a thermodynamically correct manner.

The aim of the present study is to develop an accurate thermodynamic database for the Fe-P system. The Modified Quasichemical Model (MQM) [11,12] and Compound Energy Formalism (CEF) [13] were used to describe the liquid and solid solutions, respectively. All available phase diagram and thermodynamic data in the literature were critically evaluated for determining consistent Gibbs energy functions of liquid, FCC_A1, BCC_A2, Fe₃P, Fe₂P, FeP and FeP₂ phases. To validate the accuracy of the present thermodynamic description, the distribution of P between molten Fe-P alloy and molten CaO-FeO-Fe₂O₃ slag was also calculated. This is part of comprehensive study for developing a wide high alloy steel database containing Fe-Mn-Al-Si-Cr-Ni-Ti-Nb-C-O-N-P-S. All the thermodynamic calculations were performed using FactSage software [14].

3.2 Thermodynamic Models

3.2.1 Pure Elements and Stoichiometric Compounds

The Gibbs energies of all pure elements Fe and P were taken from the Scientific Group Thermodata Europe (SGTE) database [15], and intermediate phosphides Fe₃P, Fe₂P, FeP and FeP₂ of the Fe-P system were treated as stoichiometric compounds in the present study. The Gibbs energies of pure elements and stoichiometric compounds were calculated as follows:

$$G_T^\circ = H_T^\circ - T \cdot S_T^\circ \quad (3.1)$$

$$H_T^\circ = \Delta H_{298.15K}^\circ + \int_{T=298.15K}^T C_p dT \quad (3.2)$$

$$S_T^\circ = S_{298.15K}^\circ + \int_{T=298.15K}^T (C_p / T) dT \quad (3.3)$$

where G_T° , H_T° and S_T° are the Gibbs energy, enthalpy and entropy at temperature T , $\Delta H_{298.15K}^\circ$ is standard enthalpy of formation at 298.15 K, $S_{298.15K}^\circ$ is the standard entropy at 298.15 K, and C_p is the heat capacity. In this study, the heat capacities of Fe₃P, Fe₂P and FeP were determined as the function of temperature by fitting experimental C_p data. In the case of FeP₂ with no available C_p data, its C_p expression was estimated based on those of Fe₃P, Fe₂P and FeP.

When a pure element or stoichiometric compound exhibits magnetic behavior, an additional magnetic contribution term G^{mg} needs to be accounted for describing its Gibbs energy. The magnetic contribution to the Gibbs energy of FCC_A1, BCC_A2 and Fe₃P phases were described using an empirical expression proposed by Inden [16] and modified by Hillert and Jarl [17] as follows:

$$G^{mg} = RT \ln(\beta + 1) g(\tau) \quad (3.4)$$

where, τ is given by T/T^* and T^* is the critical temperature of magnetic transition associated with Curie temperature T_C for ferromagnetic materials or Neel temperature T_N for antiferromagnetic materials. β is the average magnetic moment per mole of atoms expressed in Bohr magnetons.

$g(\tau)$ is a polynomial fraction derived by Hillert and Jarl [17]:

$$g(\tau) = 1 - \left[\frac{79\tau^{-1}}{140P} + \frac{474}{497} \left(\frac{1}{P} - 1 \right) \left(\frac{\tau^3}{6} + \frac{\tau^9}{135} + \frac{\tau^{15}}{600} \right) \right] / D \quad \dots \tau \leq 1 \quad (3.5)$$

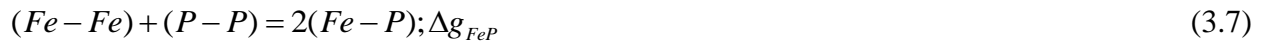
$$g(\tau) = - \left(\frac{\tau^{-5}}{10} + \frac{\tau^{-15}}{315} + \frac{\tau^{-25}}{1500} \right) / D \quad \dots \tau > 1 \quad (3.6)$$

where $D = \frac{518}{1125} + \frac{11692}{15975} \left(\frac{1}{P} - 1 \right)$, and the value of P can be considered as the fraction of the magnetic enthalpy absorbed above the critical temperature depending on the structure. P is 0.40 for the simple BCC_A2 phase while P is 0.28 for other common phases.

3.2.2 Liquid Solution

In the present study, the Modified Quasichemical Model (MQM) [11,12] considering the short-range ordering of the nearest-neighbor atoms was used to describe liquid Fe-P solution. Compared to the conventional Bragg-Williams Random Mixing Model (BWRMM), the MQM gives a more realistic thermodynamic description of the entropy of the liquid phase. In the MQM, the Gibbs energy of pair formation can be expanded as a polynomial in the pair fraction instead of the component fraction, and the coordination numbers are allowed to vary with composition for describing the short-range ordering of the liquid solution. These modifications provide greater flexibility in reproducing experimental data of the binary system and combining the binary parameters to higher-order solutions.

In the binary Fe-P liquid, the Fe and P atoms are assumed to distribute over the quasilattice sites. The atom pair exchange-reaction of the Fe-P liquid solution can be described as follows:



where $(i-j)$ represents the nearest-neighbor pair between components i and j , and Δg_{FeP} is the Gibbs energy change of forming 2 moles of $(Fe-P)$ pairs. The Gibbs energy of the liquid solution can be calculated by the following equation:

$$G_L^{sol.} = (n_{Fe} G_{Fe}^o + n_P G_P^o) - T \Delta S^{conf.} + n_{FeP} (\Delta g_{FeP} / 2) \quad (3.8)$$

where n_{Fe} and n_P are the numbers of moles of Fe and P atoms, and G_{Fe}° and G_P° are the molar Gibbs energies of pure liquid Fe and P. $\Delta S^{conf.}$ is the configurational entropy of mixing given by random distribution of the (Fe-Fe), (P-P) and (Fe-P) pairs.

$$\Delta S^{conf.} = -R(n_{Fe} \ln X_{Fe} + n_P \ln X_P) - R \left[n_{FeFe} \ln \left(\frac{X_{FeFe}}{Y_{Fe}^2} \right) + n_{PP} \ln \left(\frac{X_{PP}}{Y_P^2} \right) + n_{FeP} \ln \left(\frac{X_{FeP}}{2Y_{Fe}Y_P} \right) \right] \quad (3.9)$$

here n_{FeFe} , n_{PP} and n_{FeP} are the numbers of moles of (Fe-Fe), (P-P) and (Fe-P) pairs, and X_{FeFe} , X_{FeP} and X_{PP} are the pair fraction of the corresponding atom pairs. X_{Fe} and X_P are the mole fraction of Fe and P atoms and Y_{Fe} and Y_P are the coordination equivalent fractions of components Fe and P. The pair fractions X_{FeFe} , X_{FeP} , X_{PP} and coordination equivalent fractions Y_{Fe} , Y_P can be calculated as follows:

$$X_{FeFe} = n_{FeFe} / (n_{FeFe} + n_{FeP} + n_{PP}) \quad (3.10)$$

$$X_{FeP} = n_{FeP} / (n_{FeFe} + n_{FeP} + n_{PP}) \quad (3.11)$$

$$X_{PP} = n_{PP} / (n_{FeFe} + n_{FeP} + n_{PP}) \quad (3.12)$$

$$Y_{Fe} = X_{FeFe} + \frac{1}{2} X_{FeP} \quad (3.13)$$

$$Y_P = X_{PP} + \frac{1}{2} X_{FeP} \quad (3.14)$$

Δg_{FeP} is the model parameter for reproducing the Gibbs energy of the binary Fe-P solution, which can be expanded as a polynomial in terms of the atomic pair fractions X_{FeFe} and X_{PP} as follows:

$$\Delta g_{FeP} = \Delta g_{FeP}^{\circ} + \sum_{i \geq 1} g_{FeP}^{i0} X_{FeFe}^i + \sum_{j \geq 1} g_{FeP}^{0j} X_{PP}^j \quad (3.15)$$

where Δg_{FeP}° , g_{FeP}^{i0} and g_{FeP}^{0j} are the adjustable model parameters that can be functions of the temperature. In the MQM, the coordination numbers of atoms Fe and P, Z_{Fe} and Z_P , are allowed

to vary with composition to reproduce the short-range ordering of the liquid phase and expand to higher-order systems using proper geometric interpolation technique.

$$\frac{1}{Z_{Fe}} = \frac{1}{Z_{FeFe}^{Fe}} \left(\frac{2n_{FeFe}}{2n_{FeFe} + n_{FeP}} \right) + \frac{1}{Z_{FeP}^{Fe}} \left(\frac{n_{FeP}}{2n_{FeFe} + n_{FeP}} \right) \quad (3.16)$$

$$\frac{1}{Z_P} = \frac{1}{Z_{PP}^P} \left(\frac{2n_{PP}}{2n_{PP} + n_{FeP}} \right) + \frac{1}{Z_{PFe}^P} \left(\frac{n_{FeP}}{2n_{PP} + n_{FeP}} \right) \quad (3.17)$$

where Z_{FeFe}^{Fe} is the value Z_{Fe} when all nearest neighbors of the Fe atom are Fe atoms, and Z_{FeP}^{Fe} is the value of Z_{Fe} when all nearest neighbors are P atoms. Z_{PP}^P and Z_{PFe}^P are defined in an analogous manner. In the present study, $Z_{FeFe}^{Fe} = Z_{PP}^P = Z_{PFe}^P = 6$ and $Z_{FeP}^{Fe} = 3$ were taken for the liquid Fe-P solution, aiming at describing the short-range ordering of liquid Fe-P solution.

3.2.3 Solid Solutions

The Gibbs energies of the solid solutions were described using the Compound Energy Formalism (CEF)[13] considering crystallographic structures. In the present study, the FCC_A1 and BCC_A2 solid solutions were described with a one-sublattice (Fe, P) model. The molar Gibbs energies of the solid solutions can be expressed as follows:

$$G_S^{sol.} = (y_{Fe} G_{Fe}^o + y_P G_P^o) + RT(y_{Fe} \ln y_{Fe} + y_P \ln y_P) + \sum_{m=0,1,2,\dots} L_{Fe,P}^m y_{Fe} y_P + G^{mg} \quad (3.18)$$

where y_{Fe} and y_P are the site fraction of Fe and P species in the sublattice, respectively. G_{Fe}^o and G_P^o are molar Gibbs energies of pure solid Fe and P. R and T are the gas constant (8.314 J/mol-K) and the temperature in Kelvin (K); $L_{Fe,P}^m$ is the adjustable interaction parameters between Fe and P in the sublattice; G^{mg} is the magnetic contribution to the Gibbs energy.

3.3 Critical Evaluation and Thermodynamic Optimization

3.3.1 Phase Diagram

In the Fe-P system with suppression of gas phase, three solutions (liquid, FCC_A1 and BCC_A2) and four stoichiometric compounds (Fe_3P , Fe_2P , FeP and FeP_2) are considered stable in the present study. Though existence of FeP_4 between 900 K and 1200 K was reported by Jeitschko and Braun [18], its stability is very controversial and available experimental information of this phase is very scarce, so it is treated as unstable in the present study. The crystal structure information of all solid phases in the Fe-P system is summarized in **Table 3.1**, and the optimized model parameters are summarized in **Table 3.2**. The calculated phase diagram of the Fe-P system is compared with experimental data [19-38] in **Fig. 3.1**. As shown in **Fig. 3.1(a)**, all phase diagram data are concentrated within the composition $x_P < 0.5$, because high vaporization pressure of phosphorus greatly limits the reliability of experimental results at the higher P concentration region. The present calculation is in fairly good agreement with the majority of experimental data. In **Fig. 3.1(b)**, the presently calculated Fe-P phase diagram is compared with previously assessed diagrams. It is shown that all modeled phase diagrams are basically consistent with each other at $x_P < 0.4$ but differ largely at $x_P > 0.4$. In the assessment by Gustafson [5] and Shim et al. [6], the phase diagram was not given for the region of $x_P > 0.5$. A two-phase liquid miscibility gap is calculated in the high P region, if the parameters of Gustafson [5] are used. In contrast, thermodynamic descriptions of the Fe-P system were made for the full composition region by Ohtani et al. [7] and Cao et al. [8,9]. In both studies, high-order phosphides FeP_2 and FeP_4 were considered stable till at least 1544 °C. Although there is no experimental evidence, such a high congruent melting of FeP_2 and FeP_4 seem to be unreliable considering the short-range ordering of liquid phase at around $x_P = 0.33$. The present liquidus plotted in solid black lines show the

peritectic melting of FeP₂. All invariant reactions of the Fe-P system in the present study are summarized in **Table 3.3**.

Table 3.1 Summary of crystal structure information of all solid phases in the Fe-P system

Phase	Structure	Prototype	Space group	Pearson symbol
FCC_A1	Cubic	Cu	$\bar{F}m\bar{3}m$	<i>cF4</i>
BCC_A2	Cubic	W	$Im\bar{3}m$	<i>cI2</i>
Fe ₃ P	Tetragonal	Ni ₃ P	$I\bar{4}$	<i>tI32</i>
Fe ₂ P	Hexagonal	Fe ₂ P	$P\bar{6}2m$	<i>hP9</i>
FeP	Orthorhombic	MnP	<i>Pnma</i>	<i>oP8</i>
FeP ₂	Orthorhombic	FeS ₂	<i>Pnmm</i>	<i>oP6</i>
White P	Cubic	P ₄	$I\bar{4}3m$	<i>C*8</i>
Red P	---	P	---	<i>C*66</i>

Table 3.2 Optimized model parameters for the Fe-P system (J/mol, J/mol-K)

Phase	Model parameters
Liquid (Fe, P)	$Z_{FeFe}^{Fe} = Z_{PP}^P = 6, Z_{PFe}^P = 6, Z_{FeP}^{Fe} = 3$ [*] $\Delta g_{FeP} = -56902.4 + 6.56888T + (5481.04 + 3.0334T)X_{FeFe} +$ $(-11966.24 + 2.5104T)X_{FeFe}^2 - 9623.2X_{PP}$ [*]
FCC_A1 (Fe, P) ₁ (Va) ₁	$G_{Fe:Va}^{FCC} = G_{Fe(FCC)}^\circ$ [*] $G_{P:Va}^{FCC} = G_{P(FCC)}^\circ$ [*] $L_{Fe,P:Va}^{FCC} = -139787.44 + 6.4852T$ [*] $T_{CFe:Va} = -201, \beta_{Fe:Va} = -2.1$ [39]

	$G_{Fe:Va}^{BCC} = G_{Fe(BCC)}^{\circ} [*]$
BCC_A2	$G_{P:Va}^{BCC} = G_{P(BCC)}^{\circ} [*]$
(Fe, P) ₁ (Va) ₃	$L_{Fe,P:Va}^{BCC} = -203476.288 + 15.4808T - 33472(y_P - y_{Fe}) [*]$
	$T_{CFe:Va} = 1043, \beta_{Fe:Va} = 2.22 [39]$
	$T_{CFe,P:Va} = -285 [*]$
LT-Fe₃P:	
	$\Delta H_{298.15K}^{\circ} = -164830, S_{298.15K}^{\circ} = 110.15$
	$298.15 \text{ K} < T < 727 \text{ K}: C_p = 106.76 + 0.0108T - 780000T^{-2}$
	$727 \text{ K} < T < 2000 \text{ K}: C_p = 109.84 + 0.0287T - 8000000T^{-2}$
Fe ₃ P [*]	
(Fe) ₃ (P) ₁	HT-Fe₃P:
	$\Delta H_{trans.}^{L \rightarrow H} = 1000, T_{trans.}^{L \rightarrow H} = 698 \text{ K}$
	$298.15 \text{ K} < T < 727 \text{ K}: C_p = 106.76 + 0.0108T - 780000T^{-2}$
	$727 \text{ K} < T < 2000 \text{ K}: C_p = 109.84 + 0.0287T - 8000000T^{-2}$
	$\beta = 0.6, T_C = 713 \text{ K}, P = 0.28$
Fe ₂ P [*]	$\Delta H_{298.15K}^{\circ} = -157643, S_{298.15K}^{\circ} = 83.12$
(Fe) ₂ (P) ₁	$C_p = 71.555 + 0.02375T - 370000T^{-2}$
FeP [*]	$\Delta H_{298.15K}^{\circ} = -126100, S_{298.15K}^{\circ} = 47.77$
(Fe) ₁ (P) ₁	$C_p = 43.7878 + 0.01985T - 232000T^{-2}$
FeP ₂ [*]	$\Delta H_{298.15K}^{\circ} = -191100, S_{298.15K}^{\circ} = 51.05$
(Fe) ₁ (P) ₂	$C_p = 77.52563 + 0.009348T - 443846T^{-2} - 1.1 \times 10^{-6}T^2$

* Optimized in the present study

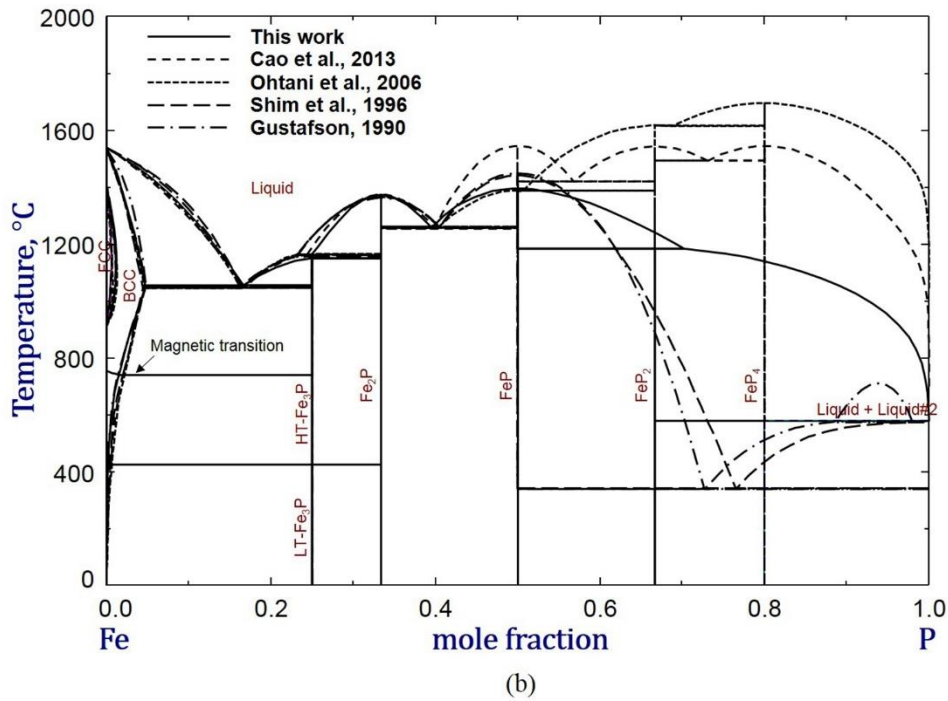
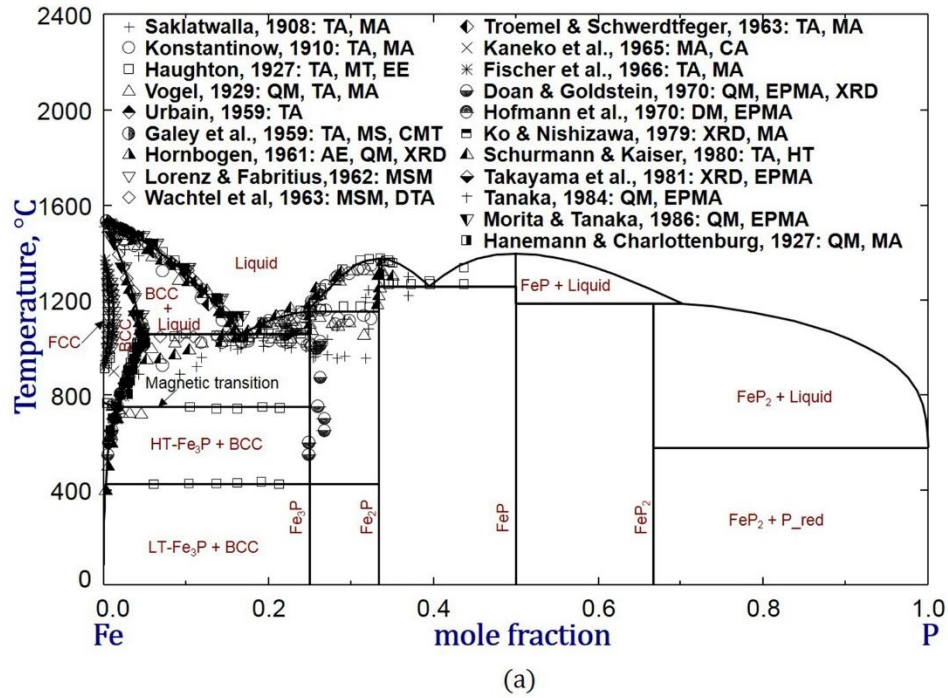


Figure 3.1 Present optimized phase diagram of the Fe-P system (a) compared with experimental data, and (b) compared with previous assessments [5-7,9]

Table 3.3 Invariant reactions of the Fe-P system in the present study

Type	Reactions	Temperature, °C
Eutectic	$L(x_P = 0.166) = \text{BCC}(x_P = 0.0466) + \text{Fe}_3\text{P}(x_P = 0.25)$	1055
Incongruent	$L(x_P = 0.246) + \text{Fe}_2\text{P}(x_P = 0.333) = \text{Fe}_3\text{P}(x_P = 0.25)$	1151
Congruent	$L(x_P = 0.333) = \text{Fe}_2\text{P}(x_P = 0.333)$	1374
Eutectic	$L(x_P = 0.395) = \text{Fe}_2\text{P}(x_P = 0.333) + \text{FeP}(x_P = 0.50)$	1257
Congruent	$\text{FeP}(x_P = 0.50) = \text{FeP}(x_P = 0.50)$	1395
Incongruent	$L(x_P = 0.702) + \text{FeP}(x_P = 0.50) = \text{FeP}_2(x_P = 0.667)$	1184
Eutectic	$L(x_P = 0.166) = \text{FeP}_2(x_P = 0.6667) + \text{Red}_P(x_P = 1)$	579

Fig. 3.2 presents the partial Fe-P phase diagram within the composition of $x_P < 0.2$ compared with the experimental data. Most of the experimental data are consistent except those measured by Saklatwalla [19], Konstantinow [20], Schurmann and Kaiser [35]. The eutectic reaction liquid = BCC_A2 + Fe₃P occurring at around $x_P = 0.166$ and $T = 1055$ °C was accepted in all assessments. A maximum solubility ($x_P = 0.0466$) of P in BCC_A2 phase at eutectic temperature was obtained in the present study, as summarized in **Table 3.3**. Above the eutectic temperature, the calculated boundary of BCC_A2 phase by Gustafson [5] deviates positively from the experimental data. This is probably due to the overestimated temperature-dependent parameters used for the liquid or BCC_A2 phase. Below the eutectic temperature, experimental data were well reproduced in the present and Gustafson's studies, whereas Shim et al. [6], Ohtani et al. [7] and Cao et al. [9] overestimated the solubility of P in BCC_A2 phase, and the overestimation increases especially with decreasing temperature. In FCC_A1 solution, the data

by Haughton [21], Lorenz and Fabritius [27], and Fischer et al. [31] were reasonably reproduced in all assessments except that by Ohtani et al. [7].

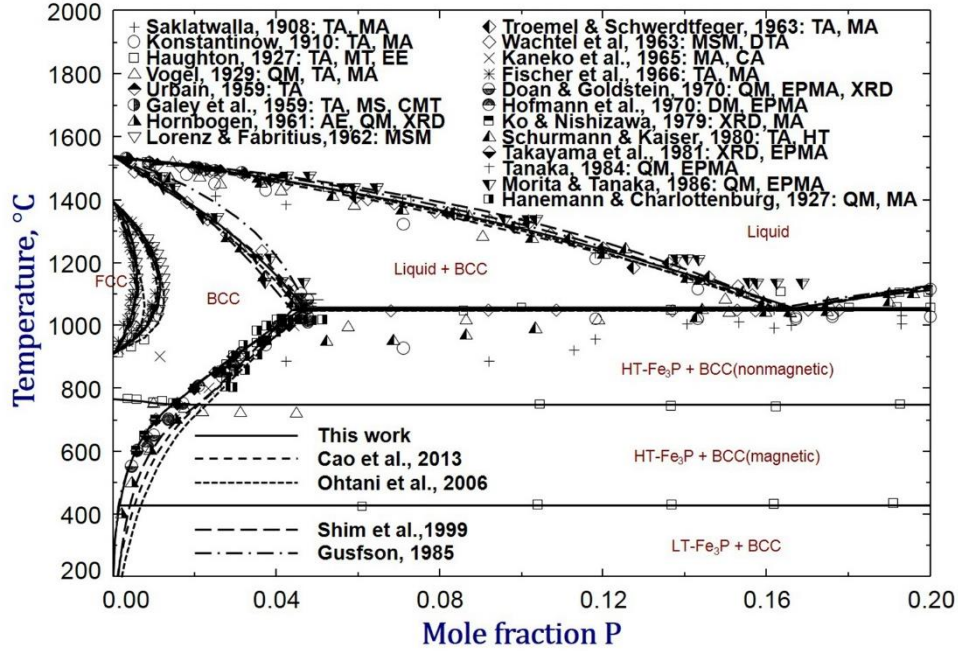


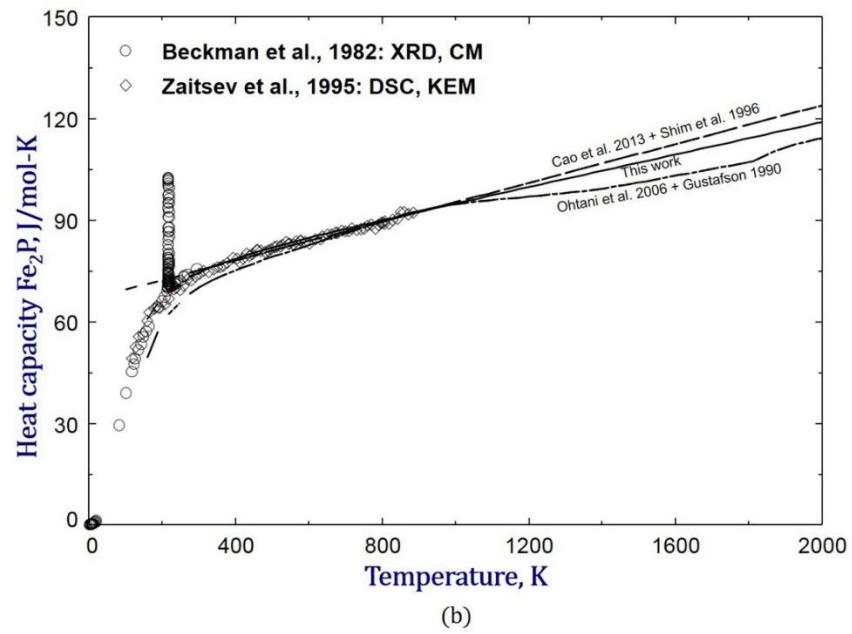
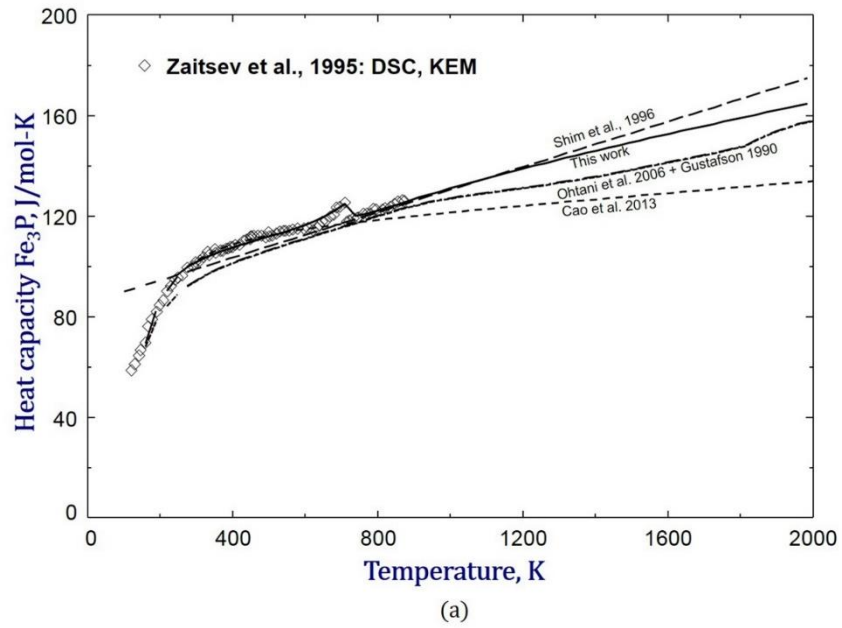
Figure 3.2 Phase diagram of the Fe-P system in the Fe-rich region

3.3.2 Thermodynamic Properties of Iron Phosphides

The thermodynamic properties including heat capacity, enthalpy, entropy, Gibbs energy, and relative stability of intermediate compounds of the Fe-P system were critically evaluated and optimized. Though red P is thermodynamically more stable than white P at room temperature, the standard enthalpy of white P is set to be 0 J/mol at 25 °C, which is thermodynamically more consistent for calculating the Gibbs energies of solid phases. Therefore, α -Fe (BCC_A2) and white P were taken as standard states for evaluating the formation enthalpy and Gibbs energy of the solid phases, and pure liquid Fe and liquid P as reference state for the liquid Fe-P solution. In the present

study, experimental data in the reference of red P have been converted to corresponding values in the reference of white P for consistency.

Zaitsev et al. [10] carried out experiments using differential scanning calorimetry (DSC) and Knudsen effusion method (KEM) with mass-spectrometric analysis of the gaseous phase to investigate the thermodynamic properties of iron phosphides, BCC_A2 and liquid phases. The DSC experiments were performed in the temperature range of 113 K to 873 K. The stoichiometric compounds including Fe₃P, Fe₂P and FeP were synthesized from high purity of iron and red phosphorus in dry Ar atmosphere. **Fig. 3.3** shows the calculated heat capacity of Fe₃P, Fe₂P and FeP together with the experimental data, and the C_p function of each compound is summarized in **Table 3.2**. A magnetic transition at around 713 K was observed in the sample Fe₃P, which was adopted in the present study. Another sudden strong Curie transit peak for Fe₂P at 217 K was suggested by Beckman et al. [40] The C_p functions by Gustafson [5] and Ohtani et al. [7], derived from α -Fe and red P using the Neumann-Kopp (NK) rule,[41] deviate slightly from experimental data particularly at low temperatures. In the assessment by Shim et al. [6], linear C_p functions were proposed for reproducing the data above room temperature.



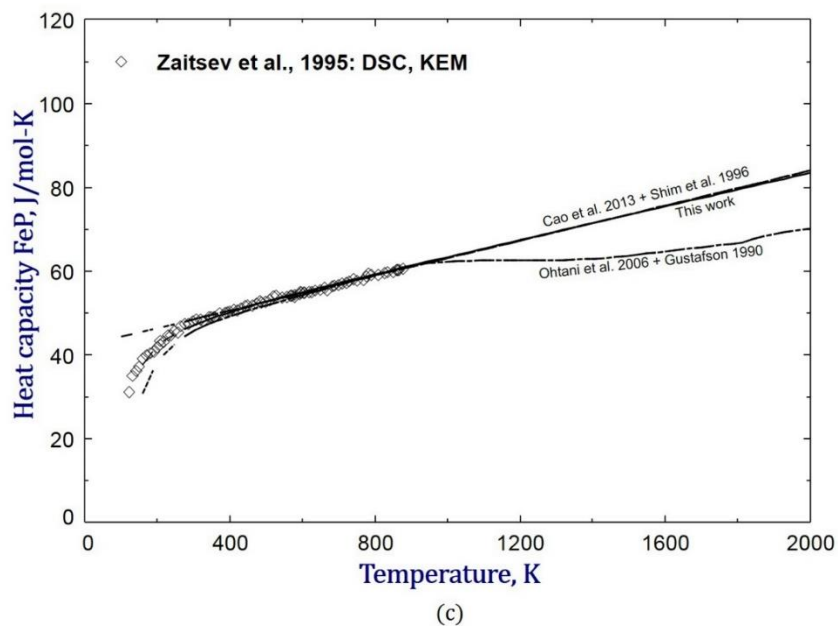
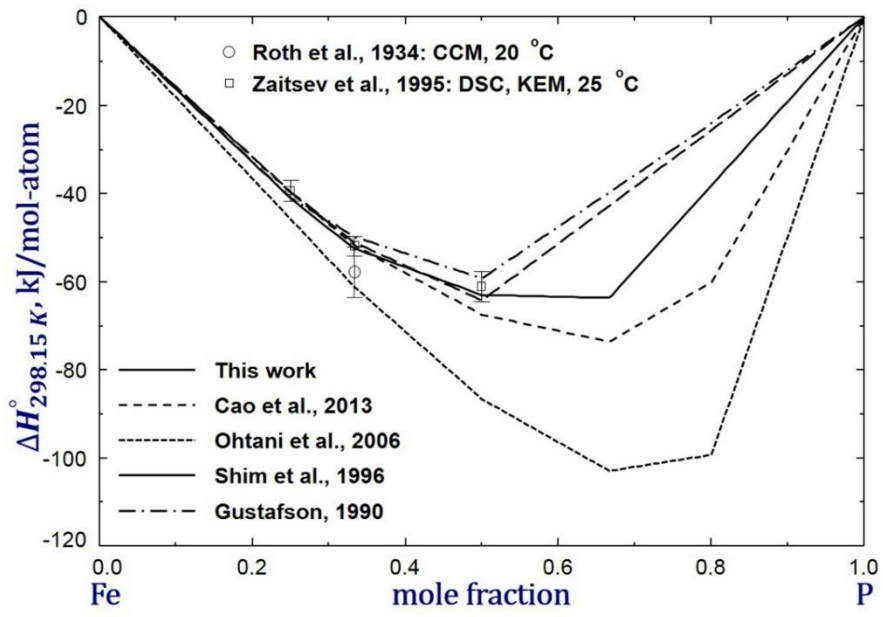


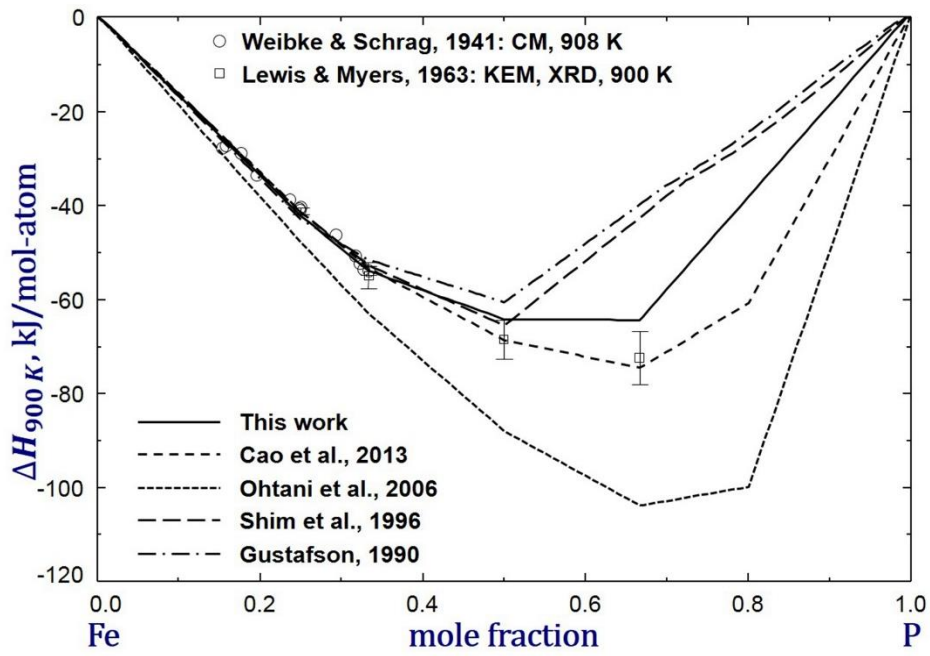
Figure 3.3 Heat capacities C_p of stoichiometric compounds (a) Fe_3P , (b) Fe_2P , and (c) FeP

The standard entropy ($S_{298.15\text{ K}}^\circ$) of iron phosphides (Fe_3P , Fe_2P , FeP) according to Zaitsev et al. [10] was determined from low temperature heat capacity data and high temperature Knudsen effusion experimental data. **Fig. 3.4(c)** shows that $S_{298.15\text{ K}}^\circ$ data from these two experiments are basically consistent and reproduced in all assessments excluding that of FeP underestimated by Ohtani et al. [7] Similar discrepancies also exist in Ohtani et al.'s calculations of enthalpy at 298.15 K and 900 K, as shown in **Fig. 3.4(a)** and **(b)**. The $\Delta H_{298.15\text{ K}}^\circ$ data of Fe_3P , Fe_2P , and FeP obtained by Zaitsev et al. [10] from Knudsen effusion experiments are favored in the present study. Roth et al. [42] also measured the $\Delta H_{298.15\text{ K}}^\circ$ of Fe_2P using a combustion calorimeter. In their experiments, three series of experiments were carried out to measure the enthalpy, and the results of all experiments were very inconsistent. For example, despite an average $\Delta H_{298.15\text{ K}}^\circ(\text{Fe}_2\text{P}) = -188.99\text{ kJ/mol}$ by the authors, $\Delta H_{298.15\text{ K}}^\circ(\text{Fe}_2\text{P}) = -173.51 \pm 15.6\text{ kJ/mol}$ was obtained from one series of experiments. Considering the large error range of the data, the optimized $\Delta H_{298.15\text{ K}}^\circ$

of Fe₂P in the present study is still in fair agreement with the results of Roth et al. [42] At the higher temperature (about 900 K), the formation enthalpy of the Fe-P samples were measured by Weibke and Schrag [43] in the composition range of $0.15 < x_P < 0.33$. $\Delta H_{900\text{ K}}^\circ = -164.78 \pm 2.95$ kJ/mol for Fe₃P and $\Delta H_{900\text{ K}}^\circ = -161.85 \pm 2.89$ kJ/mol for Fe₂P were proposed in the reference of α -Fe (BCC_A2) and white P. These data were favored in the present and previous studies [5,6,9]. However, the present enthalpy for Fe₂P, FeP and FeP₂ is slightly more positive than the data suggested by Lewis and Myers [44], who determined the enthalpy of Fe₂P from Knudsen effusion experiments. The P₂(g) gas pressure for the reaction $6\text{Fe}_2\text{P}(\text{s}) = 4\text{Fe}_3\text{P}(\text{s}) + \text{P}_2(\text{g})$ was determined first based on the known data of Fe₃P. However, they mentioned that P₂(g) gas pressure of this reaction was less reliable. That is, the enthalpy of Fe₂P derived from this chemical reaction might be less accurate. Using a similar method, the enthalpy of FeP and FeP₂ were also derived and the error in the enthalpy values could be accumulated. Therefore, the data by Lewis and Myers were not highly considered. Nevertheless, the enthalpy calculated from the present study is still in fair agreement with their results.



(a)



(b)

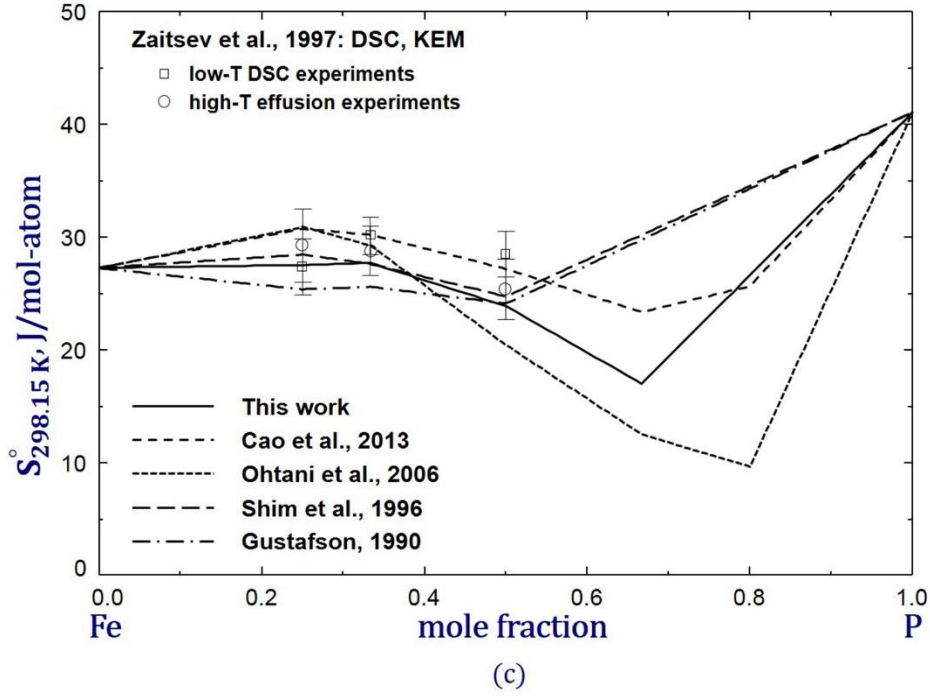
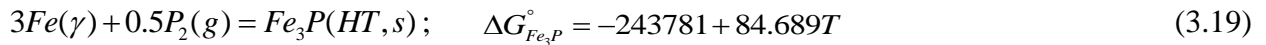


Figure 3.4 Thermodynamic properties of iron phosphides in the Fe-P system (a) $\Delta H_{298.15\text{ K}}^\circ$, (b)

$\Delta H_{900\text{ K}}$, and (c) $S_{298.15\text{ K}}^\circ$

Zaitsev et al. [10] measured the equilibrium partial pressures of Fe(g) and P₂(g) in equilibrium with Fe₃P and Fe₂P using the high-temperature Knudsen effusion method (KEM). From these pressures, they determined the Gibbs energy of formation of Fe₃P and Fe₂P, as expressed in Eqs.(3.19) and (3.20).



As can be seen in **Fig. 3.5**, the experimental Gibbs energy data of Fe₃P and Fe₂P are well reproduced in the present study.

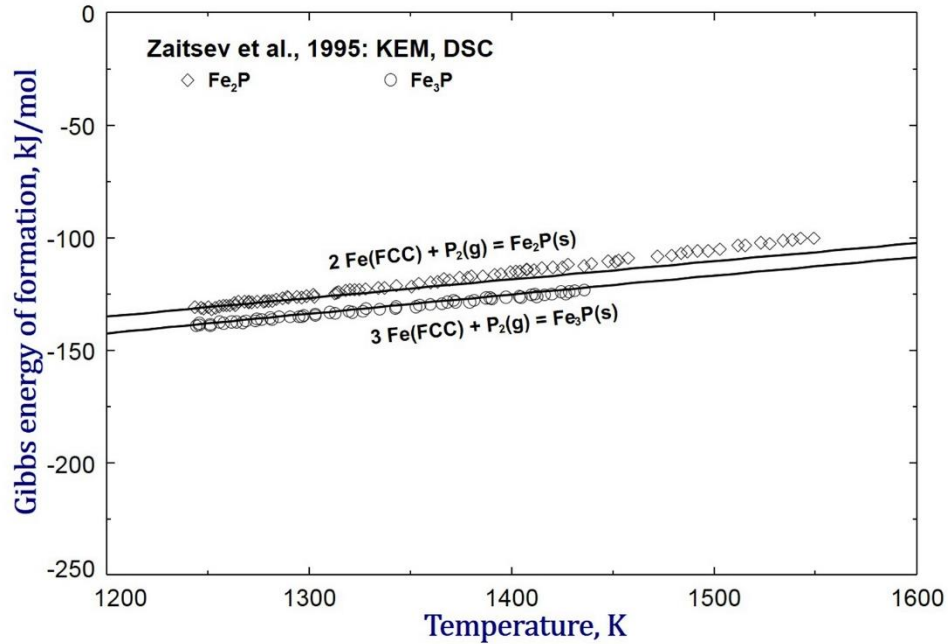
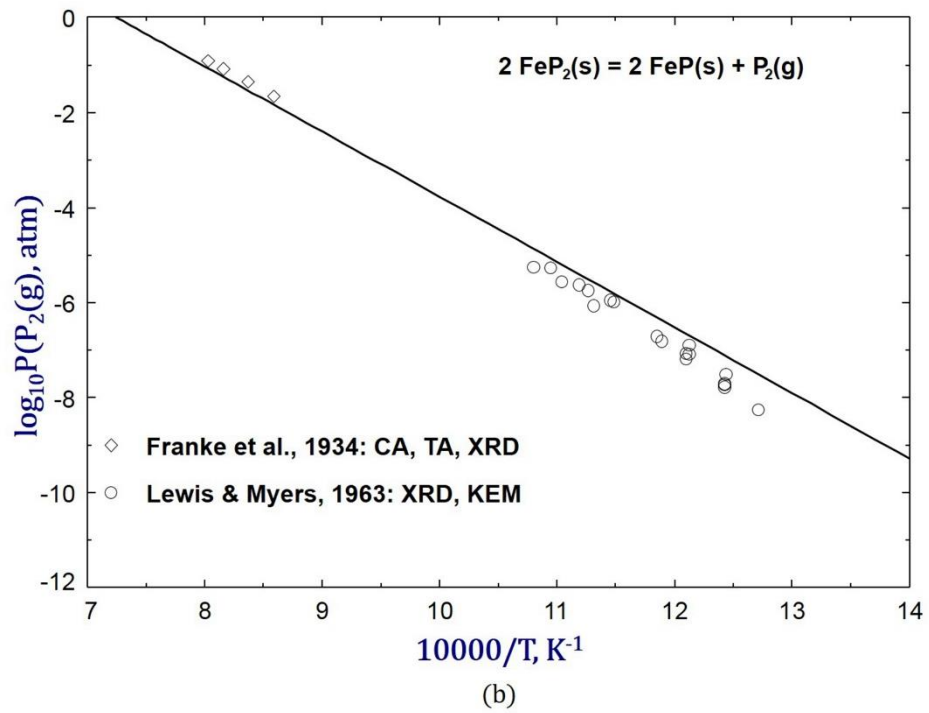
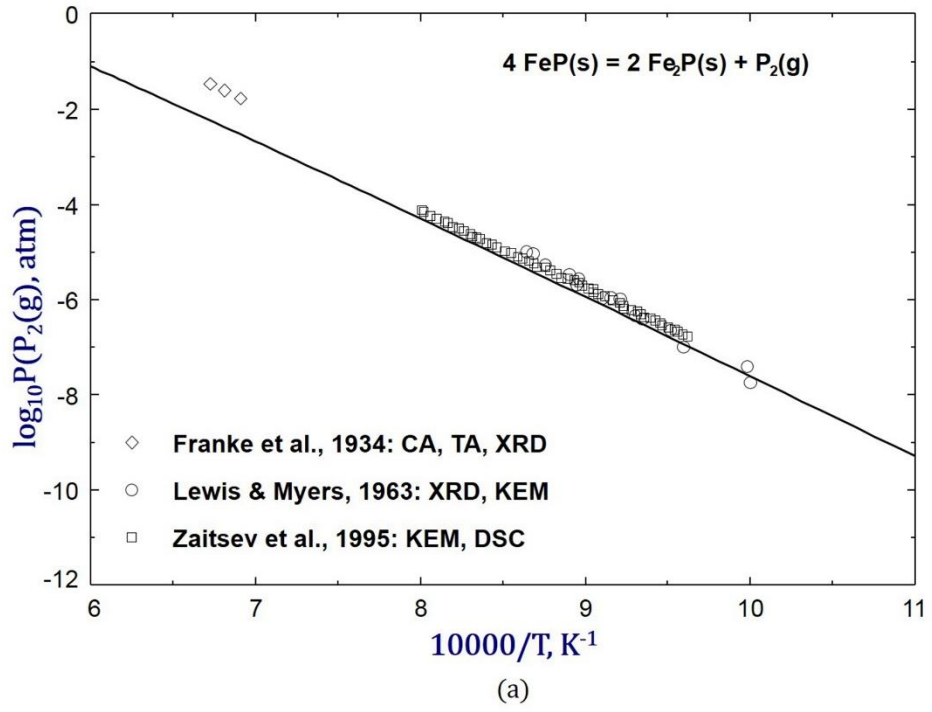


Figure 3.5 Gibbs energies of formations of Fe₃P and Fe₂P from γ -Fe and P₂(g)

Experimental investigation of the stability of phosphides Fe₂P, FeP and FeP₂ was carried out by Franke et al. [45], Lewis and Myers [44], and Zaitsev et al. [10]. The experimental results are compared with present calculations in **Fig. 3.6**. In the experiments by Franke et al. [45], existence of FeP₂ between 892 °C to 973 °C was confirmed with the XRD technique. The partial pressure of P₂(g) above Fe₂P-FeP mixture and P₂(g) and P₄(g) above FeP₂-FeP mixture were measured using tension analysis (TA) technique. Lewis and Myers [44] and Zaitsev et al. [10] measured the P₂(g) pressure from Knudsen effusion experiments. Overall, the experimental data are reproduced within reasonable accuracy as shown in **Fig. 3.6**.



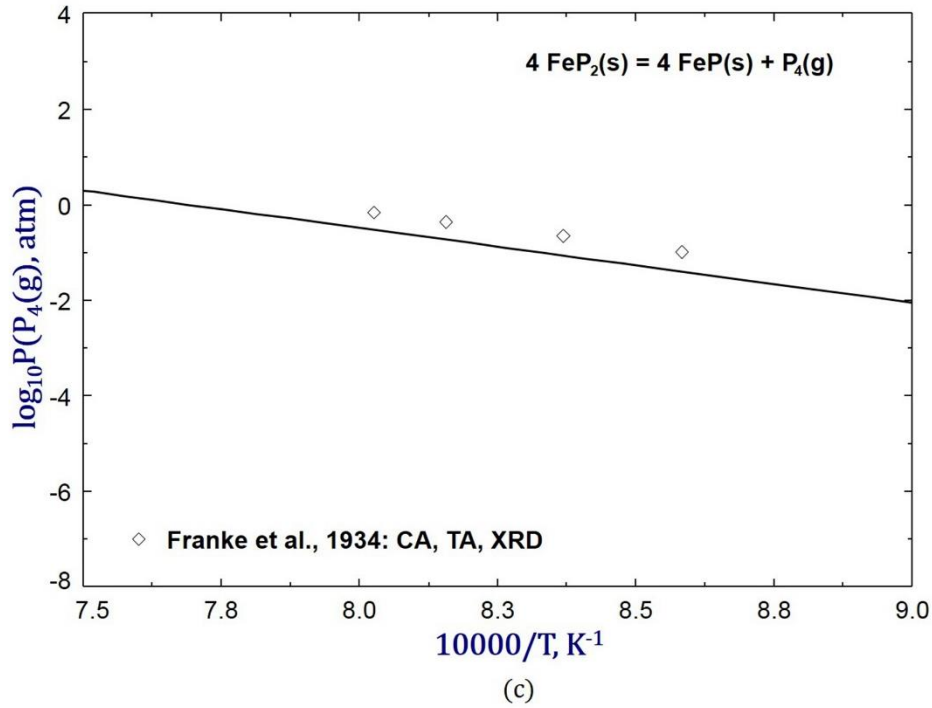


Figure 3.6 Equilibrium partial pressures of phosphorus vapor of reactions (a) $4\text{FeP}(s) = 4\text{Fe}_2\text{P}(s) + \text{P}_2(g)$, (b) $2\text{FeP}_2(s) = 2\text{FeP}(s) + \text{P}_2(g)$, and (c) $4\text{FeP}_2(s) = 4\text{FeP}(s) + \text{P}_4(g)$, depending on the temperature

3.3.3 Thermodynamic Properties of Liquid Solution

To understand the behavior of P in liquid Fe, many experimental studies have been conducted to determine the thermodynamic properties of liquid Fe-P solution. Due to the high vapor pressure of phosphorus, especially at high temperatures and high P concentration region, most of the experimental studies are concentrated in Fe-rich region. In previous thermodynamic assessments [5-9], less emphasis was put on the behavior of P in liquid Fe. Zhang [46] and Yang et al. [47] calculated the thermodynamic properties of Fe and P of the Fe-P melts in different standard states based on the Atom-Molecule Coexistence Theory (AMCT) [48]. However, their assessments were limited only to liquid Fe-P solution, and no phase diagram data including solid phases were taken

into account. The activity of P in liquid Fe is the most important data to evaluate the dephosphorization in the steelmaking process. For calculation convenience, the activities of various steel components are usually defined based on three different standard states (Raoultian standard state related to pure substances, infinite dilute Henrian standard state, 1 wt.% standard state), and conversions of the activity between three standard states are expressed as follows:

Henrian standard state to Raoultian standard state:

$$a_P^R = \gamma_P^0 a_P^H \quad (3.21)$$

Raoultian standard state to 1 wt.% standard state:

$$a_P^{wt.\%} = \frac{100M_P}{\gamma_P^0 M_{Fe}} a_P^R \quad (3.22)$$

1 wt.% standard state to Henrian standard state:

$$a_P^H = \frac{M_{Fe}}{100M_P} a_P^{wt.\%} \quad (3.23)$$

where M_P and M_{Fe} are the atomic weight of P and Fe, respectively. γ_P^0 is the Henrian activity coefficient of P in the liquid Fe-P solution. In the present study, the Henrian activity coefficient γ_P^0 of P(l) is optimized as below:

$$\ln \gamma_{P(l)}^0 = -22871/T + 4.3704 \quad (3.24)$$

where T is the temperature in Kelvin (K).

3.3.3.1 Dissolution of Phosphorus in Liquid Fe from Gas Phase

Dissolution of phosphorus in molten Fe depends on the equilibrium partial pressure of phosphorus above the liquid Fe-P alloys. Gaseous phosphorus has three different allotropes in the form of P(g), P₂(g) and P₄(g). At steelmaking temperatures, gaseous phosphorus exists mainly as P₂(g) and P(g),

because $P_4(g)$ gas becomes unstable and decomposes into $P_2(g)$ and $P(g)$. In most previous studies, $P_2(g)$ was assumed to be the only species in the gas phase. According to reported data [10,49], the partial pressure of $P(g)$ is comparable to that of $P_2(g)$ above the dilute Fe-P melts. Therefore, all experimental data in the literature should be evaluated very carefully. In the present study, all possible gas species were considered simultaneously. To deal with practical steelmaking conditions, 1 wt.% standard state is conveniently defined for such dissolution reaction. In the present study, the Gibbs energy changes for the dissolution of $P(g)$ and $P_2(g)$ in liquid Fe (1 wt.% standard state) are determined as follows, based on $\gamma_{P(l)}^0$ in **Eq. (3.24)**.

$$P(g) = P_{Fe-P}(wt. \%); \quad \Delta G_{P(g)}^\circ = -497803 + 113.26T \quad (3.25)$$

$$0.5P_2(g) = P_{Fe-P}(wt. \%); \quad \Delta G_{P_2(g)}^\circ = -249378 + 53.768T \quad (3.26)$$

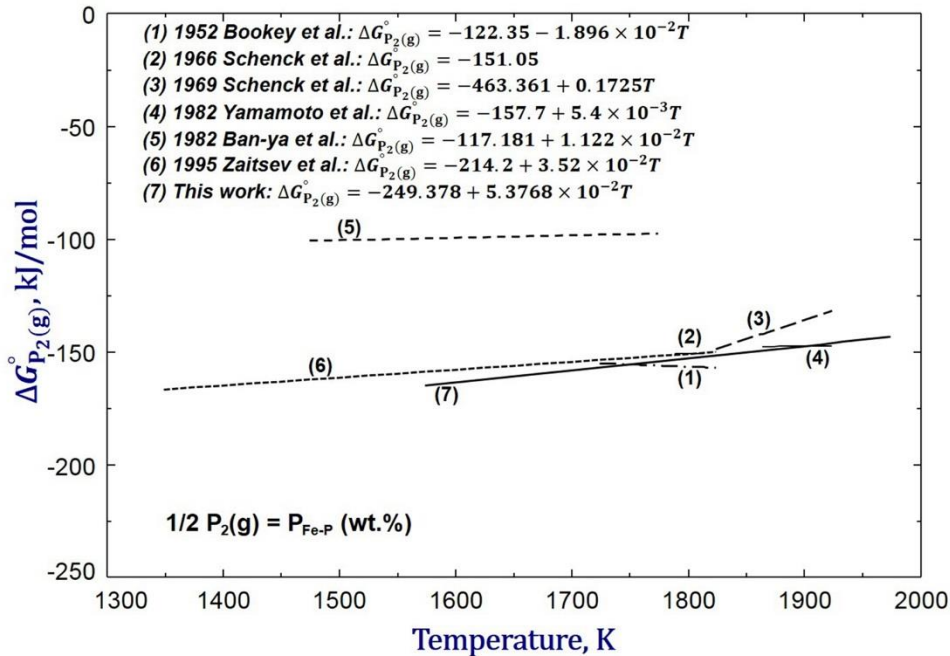


Figure 3.7 Standard Gibbs energy change for the reaction of P_2 dissolution in liquid Fe

The calculated Gibbs energy of $P_2(g)$ dissolution in molten Fe is plotted in **Fig. 3.7** and compared with the available data in the literature. Bookey and Bookey et al. [50,51] studied the equilibration between liquid Fe (wt. %P = 0.008~1.0) and a mixture of tetracalcium phosphate ($Ca_4P_2O_9$) and calcium oxide (CaO) under the controlled O_2 atmosphere by the mixture of $H_2O(g)$ and $H_2(g)$. The Gibbs energy change $\Delta G_{P_2(g)}^\circ = -122.35 - 1.896 \times 10^{-2}T$ kJ/mol for the reaction $0.5P_2(g) = P(\text{wt. \%})$ was derived. Though the values of $\Delta G_{P_2(g)}^\circ$ at the considered low temperatures are close to other results, the negative temperature dependence seems to be unreasonable. Schenck et al. [52,53] conducted experiments on the Fe-P melts in the composition of $x_P = 0.15 - 0.43$. The vapor above the liquid was suggested to be composed of $P_2(g)$ and $P_4(g)$, whereas the partial pressure of $P_2(g)$ was assumed to far exceed that of $P_4(g)$. $\Delta G_{P_2(g)}^\circ = -151.05$ kJ/mol at 1528 ± 13 °C and $\Delta G_{P_2(g)}^\circ = -463.361 + 0.1725T$ kJ/mol at 1550 °C to 1650 °C were proposed as the Gibbs energy change of $P_2(g)$ dissolution in molten Fe. However, as the concentration of P is far from its diluted region, the accuracy of $\Delta G_{P_2(g)}^\circ$ can not be guaranteed. In the experiments by Ban-ya et al. [54], the vapor pressures of phosphorus species at 1200 °C to 1500 °C are measured using the gas transportation method (TM). They proposed that $P_2(g)$ was dominant among three gaseous phosphorus species ($P(g)$, $P_2(g)$ and $P_4(g)$) especially when the P concentration is high in the liquid solution. As shown in **Fig. 3.7**, the $\Delta G_{P_2(g)}^\circ$ by Ban-ya et al. [54] deviates significantly from the others. In the experiments by Yamamoto et al. [49] and Zaitsev et al. [10], both $P_2(g)$ and $P(g)$ were considered simultaneously in equilibrium with the liquid Fe-P solution, and the corresponding partial pressures were measured using the Knudsen effusion method (KEM). The advantage of this is the accuracy of the measured partial pressures of $P(g)$ and $P_2(g)$ can be self-tested. As indicated in both experiments, the activity of phosphorus (a_P) in liquid Fe-P calculated from $P(g)$ is consistent with that from $P_2(g)$. Besides, in the Knudsen effusion experiments by

Yamamoto et al. ($x_P = 0.017 - 0.051$) and Zaitsev et al. ($x_P = 0.015 - 0.30$), the dilute Fe-P alloys was analyzed for the proper determination of the Henrian activity coefficient (γ_P^0) of P in liquid Fe. As shown in the figure, reasonable agreement is achieved between the present optimization and the results proposed by Yamamoto et al. [49] and Zaitsev et al. [10].

3.3.3.2 Activity of Fe and P in Liquid Solution

The activity of Fe(l) in Raoultian standard state (a_{Fe}^R) in liquid Fe-P solution at 1550 °C is calculated in **Fig. 3.8** and compared with experimental data [10,56,57]. Polyakov et al. [56] measured mass loss of the molten Fe-P alloys in the vacuum furnace at 1550 °C. The activity of Fe, a_{Fe}^R , was determined from mass loss amount of the Fe-P alloys relative to that of pure Fe. The obtained experimental data deviate from the other two sets of data because of the limitation of the experimental technique with high vaporization of phosphorus in the experiments. Ban-ya and Suzuki [57] conducted equilibration experiments between liquid Fe-P and Ag at the temperatures of 1300 °C to 1600 °C. The activity of Fe at 1550 °C was calculated from measured activity of P using the Gibbs-Duhem equation. Comparing to a_{Fe}^R obtained by Polyakov et al. [56], the reported a_{Fe}^R by Ban-ya and Suzuki [57] and Zaitsev et al. [10] were more favored in the present study. It should be noted that the activity of Fe(l) decreases rapidly at around $x_P = 0.333$, which indicates the strong short-range ordering of the liquid solution.

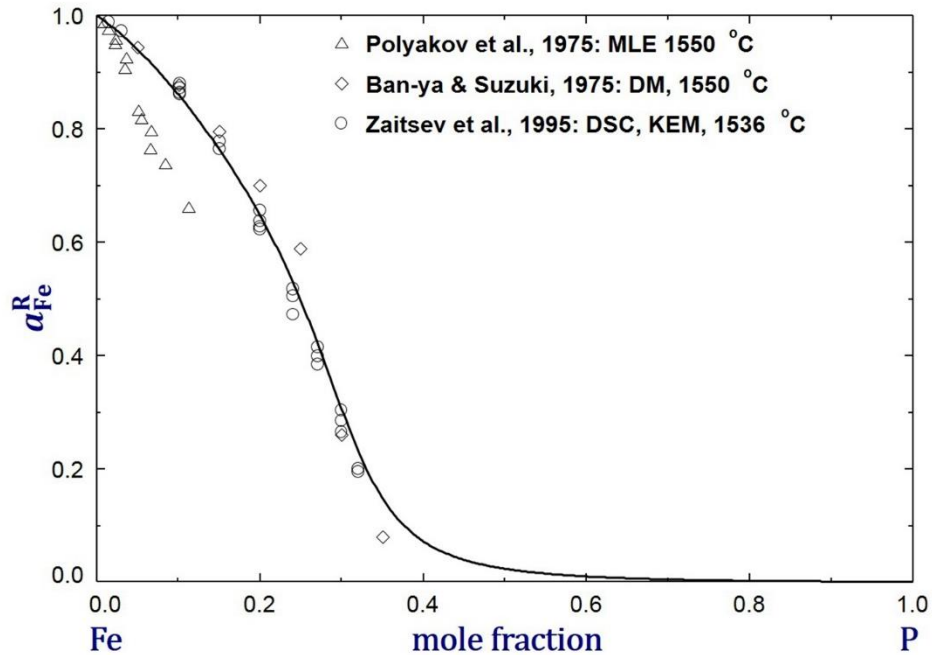


Figure 3.8 Activity of Fe in the liquid Fe-P solution at 1550 °C, along with experimental data [10,56,57]

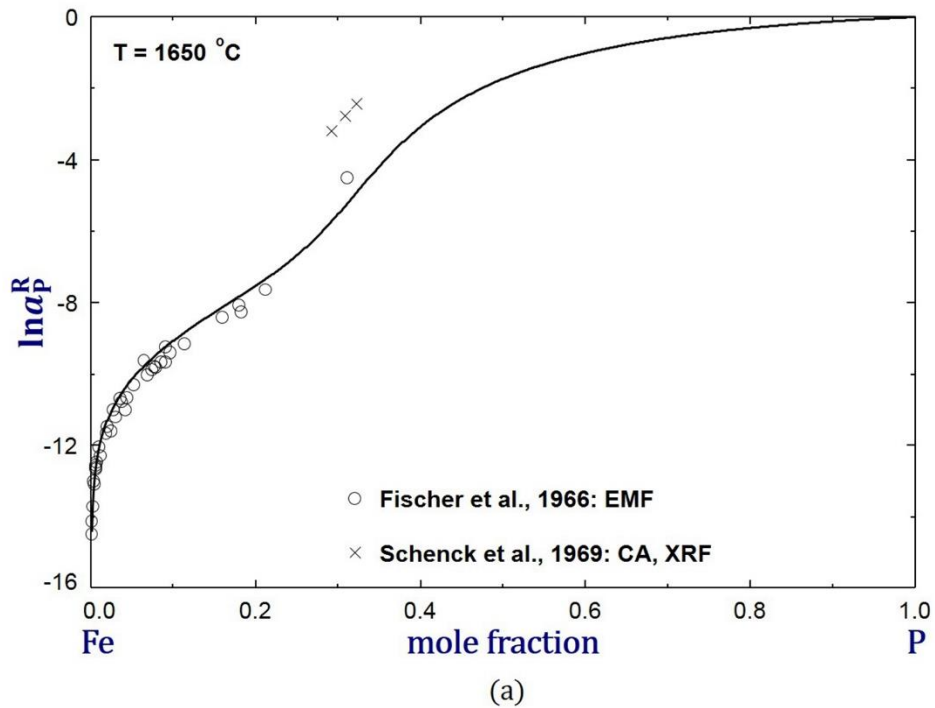
The activity of P in liquid Fe is critically important for describing the behavior of P during the steelmaking process and ferroalloy refining. Numerous experimental studies [10,24,31,49,52-54, 57-62] have been performed to investigate the activity of P in molten Fe-P alloys at different temperatures. The activity data of P in the Fe-P liquid solution are available in the literature in various forms: (i) the activity ($a_P^H, a_P^R, a_P^{wt.\%}$) or activity coefficient ($f_P^H, \gamma_P^R, f_P^{wt.\%}$) in three different standard states (infinite dilute Henrian standard state, Raoultian standard state and 1 wt.% standard state), and (ii) equilibrium vapor pressures of $P_2(g)$ and $P(g)$. All these data available in the literature were converted into the activity of P(l) in Raoultian standard state scale a_P^R (pure P(l) as reference state) to compare with existing data in consistent manner. All data are compared in

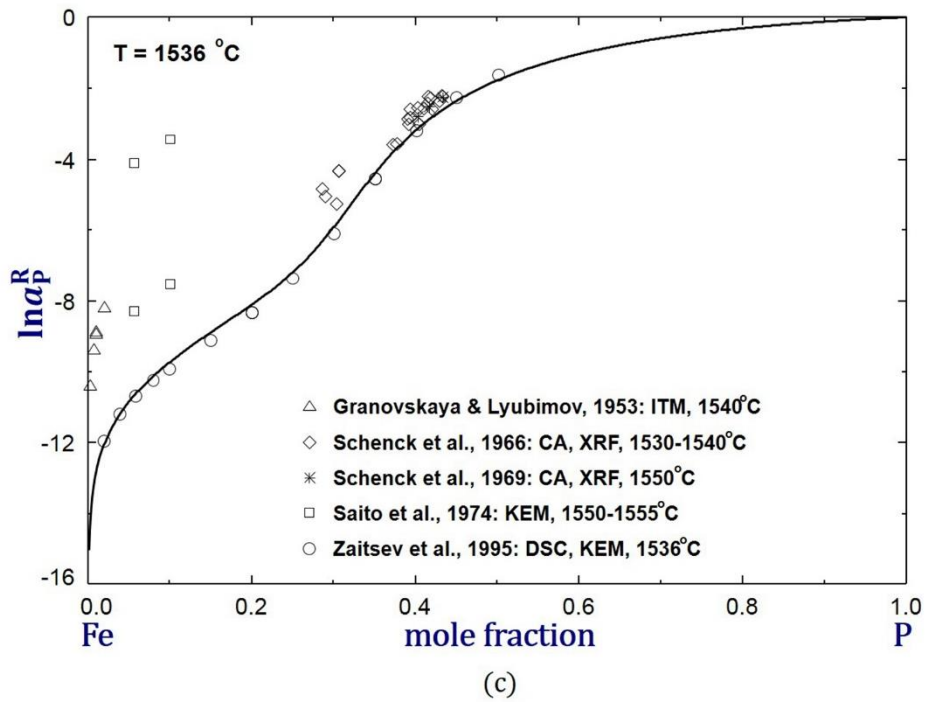
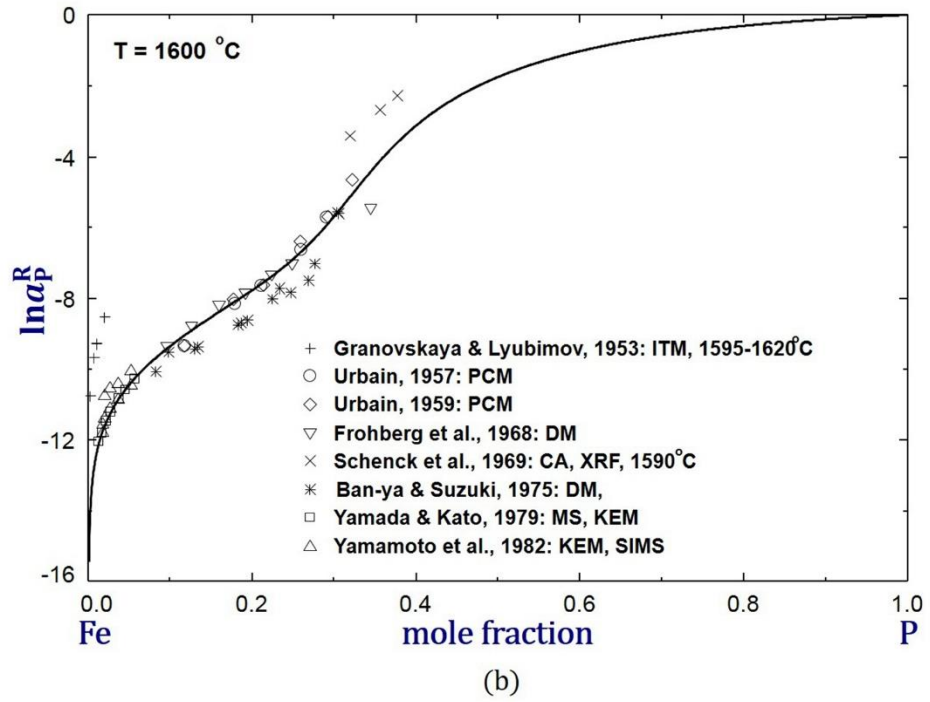
Fig. 3.9. In the calculation, the solid FCC_A1, BCC_A2 and intermediate compounds were also considered.

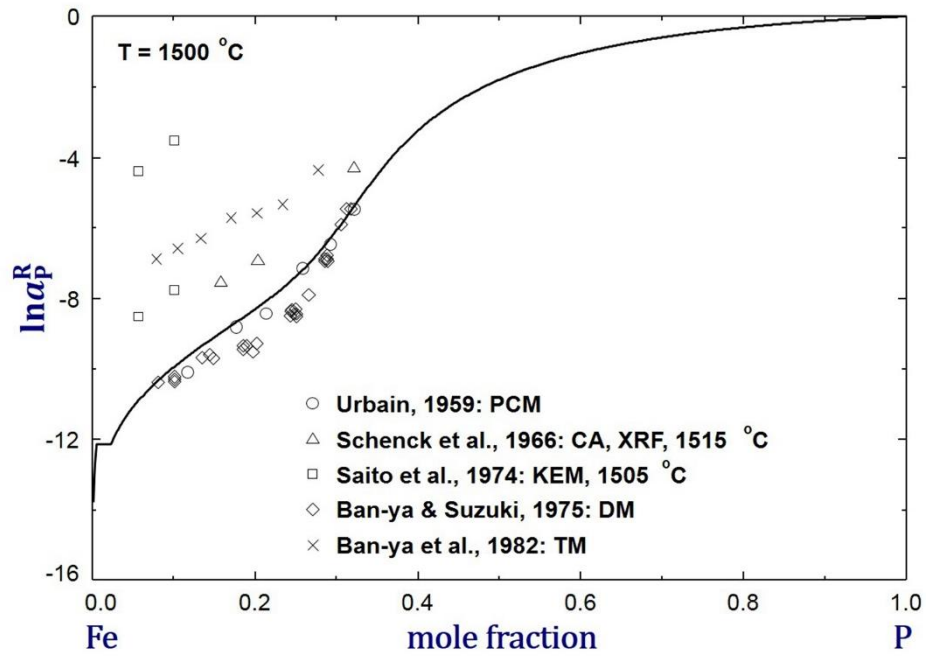
Granovskaya and Lyubimov [58] measured the partial pressures of phosphorus and Fe above the Fe-P melts in the composition of $x_P = 0 - 0.02$ at 1540 °C, 1595 °C and 1620 °C using the isotopic tracer method (ITM). Since different allotropes cannot be distinguished from each other by this technique, gaseous phosphorus was assumed to exist entirely as P(g). That is why the activity of P converted from partial P(g) pressure deviates positively from most other data sets. Moreover, it is contradictory that measured partial pressures of Fe(g) are even higher than those of pure liquid Fe. The Knudsen effusion method (KEM) was adopted in the experiments by Saito et al. [62], Yamada and Kato [61], Yamamoto et al. [49], and Zaitsev et al. [10]. Vapor pressures of P₂(g) and P(g) were determined simultaneously from the intensities of P₂⁺ and P⁺ ions. All KEM data are consistent and fairly well reproduced in the present optimization, with the exception of those by Saito et al. [62]. As shown in **Fig. 3.9(c)** and **(d)**, the activity of P by Saito et al. [62] converted from both P₂(g) and P(g), is apparently inconsistent and deviates greatly from the other data, so their data are not considered reliable and are neglected in this optimization. **Fig. 3.9(b)**, **(c)** and **(d)** also shows that the experimental data by Schenck et al. [52,53] are off compared to the other data, because they assumed P₂(g) as the only phosphorus species in the calculation of a_P of the liquid phase. Ban-ya and Suzuki [57] and Ban-ya et al. [54] measured a_P in molten Fe using the distribution method (DM) and gas transportation method (TM), respectively. The reported earlier a_P data are slightly smaller than the present calculated lines, while the latter data converted from P₂(g) vapor pressure (P(g) and P₄(g) were taken into account to determine the apparent vapor pressure of P₂(g)) deviates greatly from the other data. This is probably due to the influence of the

carrier gas flow rate and gas condensation on the measurement of phosphorus partial pressure. As tested by Ban-ya et al. [54], the $P_2(g)$ partial pressure fluctuated with the gas flow rate, so it might be hard to determine the appropriate carrier gas flow rate and condensing time to achieve equilibrium $P_2(g)$ partial pressure above the Fe-P melts. Other data by Urban [24,59] using the partition coefficient method (PCM), Fischer et al. [31] using electromotive force (EMF), Froberg et al. [60] using the distribution method (DM) are reasonable.

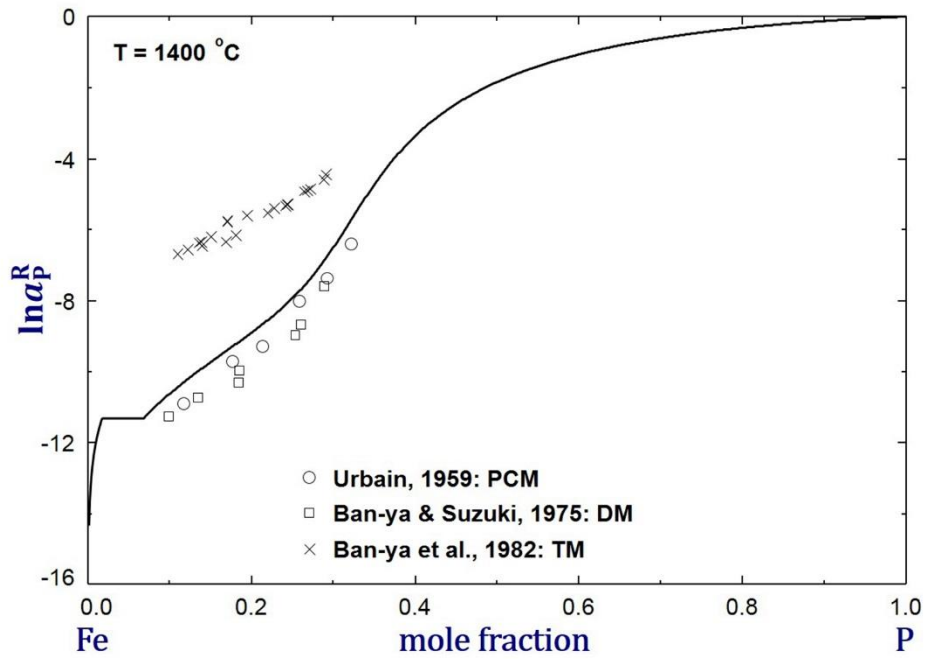
It should be noted that the slope of a_P^R is changing at $x_P \approx 0.333$. This also indicates the strong short range ordering at $x_P \approx 0.333$ composition.







(d)



(e)

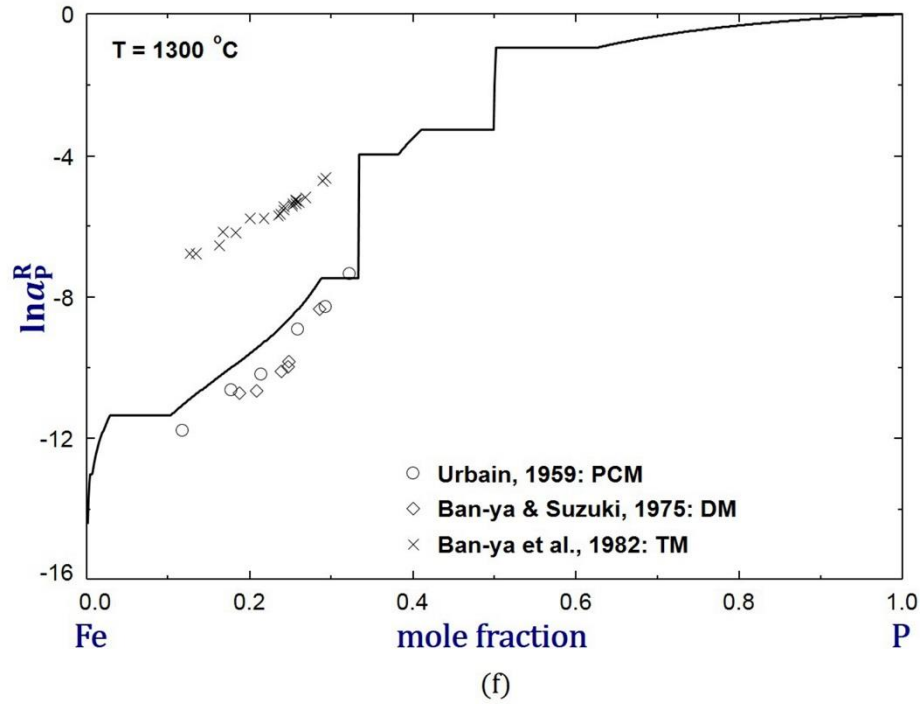


Figure 3.9 Activity of P(l) in the liquid Fe-P solution with reference to pure P(l) as a standard state at (a) 1650 °C, (b) 1600 °C, (c) 1536 °C, (d) 1500 °C, (e) 1400 °C, and (f) 1300 °C

3.3.3.3 Enthalpy and Gibbs Energy of Mixing

Enthalpy of mixing is one of most important thermodynamic properties for evaluating the interaction between the components of the liquid phase. Schurmann et al. [55] measured the enthalpy of mixing (ΔH_{mix}) of liquid Fe-P alloys for a composition up to $x_P = 0.34$ at 1550 °C, using the calorimetry method (CM) and thermal analysis (TA). Correspondingly, the Gibbs energy of mixing (ΔG_{mix}) was also derived. The enthalpy and Gibbs energy of mixing at 1550 °C are calculated and compared with the experimental data [55] in **Fig. 3.10**. As shown in the figure, the enthalpy of mixing has a minimum value of -47.98 kJ/mol at $x_P \approx 0.35$. The slope of mixing enthalpy is nearly constant up to the minimum enthalpy region. This is a typical feature for the

liquid solution which has a very strong short-range ordering. The present calculation results are in excellent agreement with the experimental data, as shown in **Fig. 3.10**.

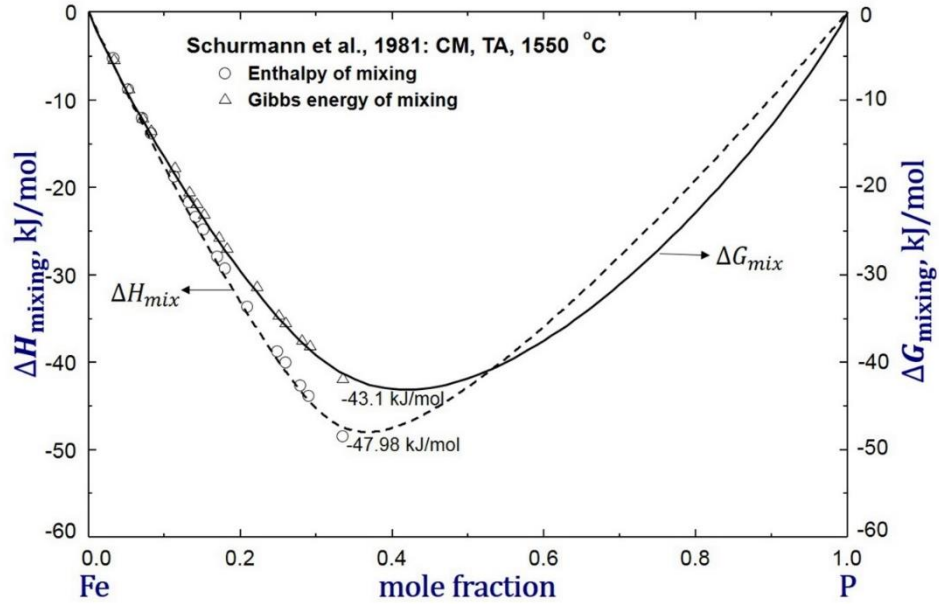
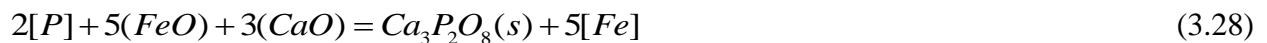


Figure 3.10 Enthalpy and Gibbs energy of mixing of the Fe-P liquid solution at 1550 °C optimized in the present study in comparison with experimental data [55]

3.4 Application of Optimized Database to Dephosphorization Calculation for Liquid Fe

Depending on the basicity (CaO) and oxidizing (Fe₂O) conditions, phosphorus in liquid steels and ferroalloys can be removed from liquid metal and transferred into slag in the form of P₂O₅ [1]. In high CaO slag, the formed P₂O₅ can further react with CaO to generate stoichiometric tricalcium phosphate (Ca₃P₂O₈) or tetracalcium phosphate (Ca₄P₂O₉) depending on the basicity (CaO/P₂O₅) of the slag. Dephosphorization reactions typically occur under high basicity and oxidizing condition, as expressed by the following reactions:



where [i] and (i) represents the component in molten steel and slag, respectively. Since dephosphorization occurs at the interface of the metal and slag, the distribution of P depends on the properties of P in molten steel and that of P₂O₅ in slag. The distribution coefficient L_P of P is calculated from the ratio of the P concentration in molten slag to that in metal, as expressed below:

$$L_P = \frac{wt.\%(P)_{slag}}{wt.\%[P]_{metal}} \quad (3.26)$$

where $wt.\%(P)_{slag}$ is the weight percent of P (in the form of P₂O₅) in molten slag, and $wt.\%[P]_{metal}$ is the weight percent of P in liquid metal.

Recently, the Gibbs energies of pure solid and liquid P₂O₅ were reevaluated by Jung and Hudon [63] and a thermodynamic database of the molten Fe₂O-CaO containing P₂O₅ slag system has been optimized.[1] for the dephosphorization treatment in the steelmaking process, which is now stored as the FToxid database in FactSage 7.3 [14]. The database has been proved to be accurate in reproducing the dephosphorization capacity of various multicomponent slag systems. Here, dephosphorization calculations were performed using the FToxid database for slag and thermodynamic database of the Fe-P system optimized in the present study.

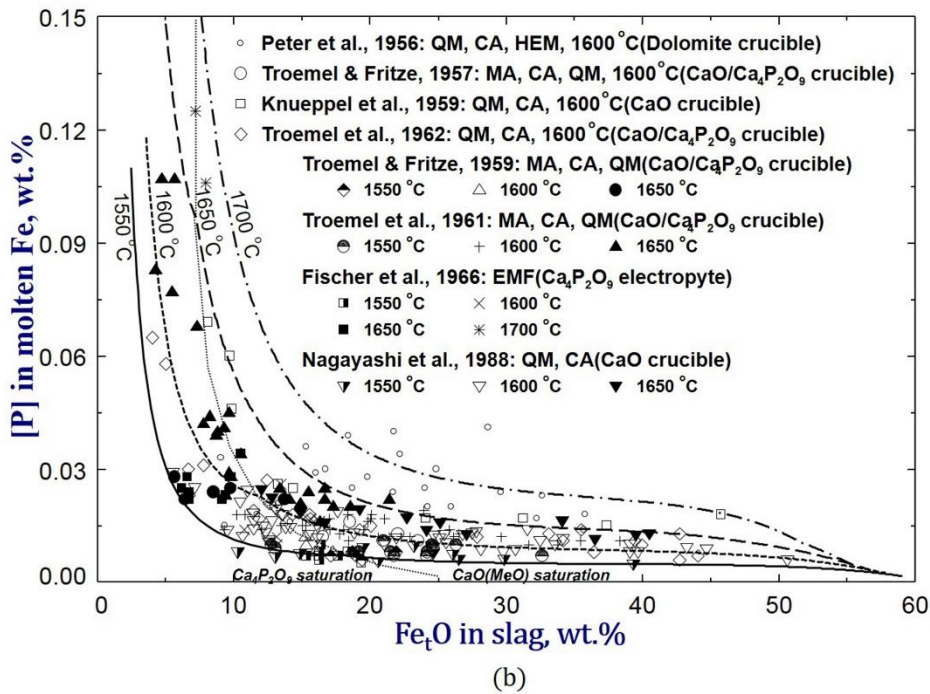
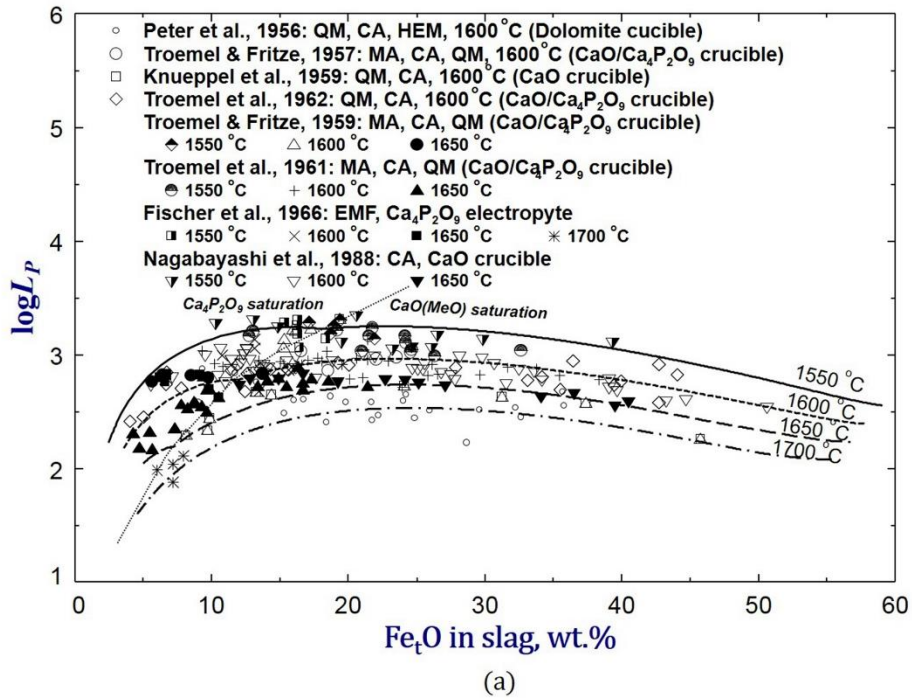


Figure 3.11 (a) Distribution coefficient of P, and (b) dissolved [P] content in molten Fe after dephosphorization of the liquid Fe-P solution with molten slag at 1550 °C to 1700 °C

Many experimental investigation [31,64-70] have been performed to determine the P distribution between molten steel and slag at various compositions and temperatures. Peter et al. [64] conducted equilibrium experiments between molten iron and phosphorus containing slag in the dolomite crucible (co-saturation of CaO and MgO) at 1550 °C to 1700 °C. Troemel et al. [65,67-69], Knueppel et al. [66], and Nagabayashi et al. [70] also studied the dephosphorization of molten steels in the saturation of CaO or Ca₄P₂O₉ at 1550 °C to 1650 °C. Fischer et al. [31] measured the activity of P in the Fe-P melts from 1550 °C to 1700 °C through electromagnetic force (EMF) experiments with Ca₄P₂O₉ electrolyte, and the P distribution coefficient L_P was also determined in the experiments. The literature data [31,64-70] of L_P between liquid Fe and CaO or Ca₄P₂O₉ saturated CaO-FeO-P₂O₅ slag at 1550 °C to 1700 °C are compared with the present calculations in **Fig. 3.11(a)**. The L_P data, despite some scattering, are reasonably reproduced in a wide temperature and composition range. As shown in the figure, L_P varies with the temperature and slag composition. In particular, L_P has a maximum value when wt. %FeO \approx 20 in slag, and higher L_P values can be achieved at lower temperatures. **Fig. 3.11(b)** shows variations of the P content in liquid Fe with slag composition (wt.%Fe_tO). The P content decreases dramatically with increasing Fe_tO content of slag up to about 10~20 in weight percent. Then, it remains almost constant even if the Fe_tO content was further increased. As shown in **Fig. 3.11(b)**, the measured concentration of dissolved P in molten Fe is very well reproduced based on the liquid Fe-P database optimized in the present study.

3.5 Summary

A critical evaluation and optimization of all available experimental data of the Fe-P system have been performed to obtain a set of Gibbs energies of all the phases of this system. The liquid Fe-P

solution was described using the Modified Quasichemical Model (MQM), and solid solutions such as BCC_A2 and FCC_A1 solutions were described using the Compound Energy Formalism (CEF). The discrepancies of the phase diagram and thermodynamic data left in previous assessments were resolved in the present study. The present Fe-P thermodynamic optimization results are proved to be reliable in describing the dephosphorization process between steels and slags.

Acknowledgments

We gratefully acknowledge the Steelmaking Consortium Members, Hyundai Steel, Tata Steel Europe, Posco, Doosan Heavy Industry and Construction, Nucor Steel, RioTinto Iron and Titanium, JFE Steel, Nippon Steel Corp., RHI-Magnesita, Voestalpine, SeAh Besteel, and Natural Science and Engineering Research Council of Canada for supporting the present project. This work was also supported by the National Research Foundation of Korea (NRF) grant funded by the Korean government (MSIT) (No. 2020R1A5A6017701).

References

1. I. H. Jung, P. Hudon, W. Y. Kim, M. A. van Ende, M. Rahman, and G. G. Curiel, Thermodynamic Database of P₂O₅-containing Oxide Systems for the Dephosphorization Process in Steelmaking, *High Temp. Mater. Proc.*, 2013, 32(3), p 247-254.
2. H. Okamoto, The Fe-P (iron-phosphorus) System, *Bull. Alloy Phase Diagram*, 1990, 11(4), p 404-412.
3. M. E. Schlesinger, The Thermodynamic Properties of Phosphorus and Solid Binary Phosphides, *Chem. Reviews*, 2002, 102(11), p 4267-4302.

4. P. Spencer and O. Kubaschewski, A Thermodynamic Assessment of the Iron-Phosphorus System, *Arch. Eisen.*, 1978, 49(5), p 225-228.
5. P. Gustafson, Internal Report IM-2549, *Swedish Institute for Metals Research*, Stockholm, Sweden, 1990.
6. J. H. Shim, C. S. Oh, and D. N. Lee, Thermodynamic Properties and Calculation of Phase Diagram of the Fe-P System, *J. Korean. Inst. Met. Mater.*, 1996, 34(11), p 1385-1393.
7. H. Ohtani, N. Hanaya, M. Hasebe, S. I. Teraoka, and M. Abe, Thermodynamic Analysis of the Fe-Ti-P Ternary System by Incorporating First-principles Calculations into the CALPHAD Approach, *CALPHAD*, 2006, 30(2), p 147-158.
8. Z. M. Cao, K. P. Wang, Z. Y. Qiao, and G. W. Du, Thermodynamic Reoptimization of the Fe-P System, *Acta Phys. Chim. Sinica*, 2012, 28(1), p 37-43.
9. Z. M. Cao, W. Xie, K. P. Wang, C. J. Niu, G. W. Du, and Z. Y. Qiao, Thermodynamic Optimization of the Al-Fe-P Ternary System, *Acta Phys. Chim. Sinica*, 2013, 29(10), p 2148-2156.
10. A. I. Zaitsev, Z. V. Dobrokhotova, A. D. Litvina, and B. M. Mogutnov, Thermodynamic Properties and Phase Equilibria in the Fe-P System, *J. CSFT*, 1995, 91(4), p 703-712.
11. A. D. Pelton, S. A. Degterov, G. Eriksson, C. Robelin, and Y. Dessureault, The Modified Quasichemical Model I-Binary Solutions, *Metall. Mater. Trans. B*, 2000, 31(4), p 651-659.
12. A. D. Pelton and P. Chartrand, The Modified Quasi-chemical Model: Part II. Multicomponent Solutions, *Metall. Mater. Trans. A*, 2001, 32(6), p 1355-1360.
13. M. Hillert, The Compound Energy Formalism, *J. Alloys Compound*, 2001, 320(2), p 161-176.
14. W. Bale, P. Chartrand, S. A. Degterov, G. Eriksson, K. Hack, R. B. Mahfoud, and S. Petersen, FactSage Thermochemical Software and Databases, *CALPHAD*, 2002, 26(2), p 189-228.

15. A. T. Dinsdale, SGTE Data for Pure Elements, *CALPHAD*, 1991, 15(4), p 317-425.
16. G. Inden, Project Meeting CALPHAD V, Max-Planck-Inst, *Eisenforschung*, Dusseldorf, Germany, 1976, p 111.
17. M. Hillert and M. Jarl, A Model for Alloying in Ferromagnetic Metals, *CALPHAD*, 1978, 2(3), p 227-238.
18. W. Jeitschko and D. J. Braun, Synthesis and Crystal Structure of the Iron Polyphosphide FeP₄, *Acta Crystall. Section B: Struc. Crystall. Crys. Chem.*, 1978, 34(11), p 3196-3201.
19. D. Saklatwalla, Constitution of Iron and Phosphorus Compounds, *J. Iron Steel Inst.*, 1908, 77, p 92-103.
20. N. Konstantinov, Compounds of Iron with Phosphorus, *Zeitsch. Anorg. Chem.*, 1910, 66(1), p 209-228.
21. J. L. Haughton, Alloys of Iron Research. Part VIII. The Constitution of Alloys of Iron and Phosphorus, *J. Iron Steel Inst*, 1927, 115, p 417-433.
22. H. Hanemann and H. Voss, The System Iron-Phosphorus, Iron-Silicon, and Iron-Phosphorus-Silicon. I. New Investigations of Iron-Phosphorus Solid Solution in the Binary System: Iron-Phosphorus, *Zentr. Hutten. Walzwerke*, 1927, 31(19), p 245-248.
23. R. Vogel, The Iron-Phosphorus-Carbon System, *Arch. Eisen.*, 1929, 3(4), p 369-381.
24. G. Urbain, Activity of Phosphorus Dissolved in Molten Iron. *Mem. Sci. Rev. Metall.*, 1959, 56, p 529-544.
25. J. Galey, L. Beaujard, P. Vallet, G. Urbain, J. Tordeux, P. Villette, and J. Foulard, Measurement and Recording of the Bath Temperature in Basic Bessemer Converter by Sighting through the Neck. Applications to Study of Basic Converters, *Rev. Métall.*, 1959, 56(7), p 69-99.

26. E. Hornbogen, Precipitation of Phosphorus from Alpha Iron and Its Effect on Plastic Deformation, *Trans. ASM*, 1961, 53, p 569-589.
27. K. Lorenz and H. Fabritius, Use of a Magnetic Balance for Determination of Phase Diagrams in the Solid State Region of Iron-Rich Systems. Investigation of the System Iron-Phosphorus, *Arch. Eisen.*, 1962, 33(4), p 269-275.
28. E. Wachtel, G. Urbain, and E. Ubelacker, Study on the Iron-Phosphorus Diagram by Magnetic and Thermal Analyses, *Compt. Rend.*, 1963, 257, p 2470-2472.
29. G. Troemel and K. Schwerdtfeger, A Study of the System Iron-Phosphorus-Oxygen, *Arch. Eisen.*, 1963, 34(1), p 55-59.
30. H. Kaneko, T. Nishizawa, K. Tamaki, and A. Tanifuji, Solubility of Phosphorus in α and γ -Iron, *Nippon Kinzoku Gakkai-Si*, 1965, 29, p 166-170.
31. W. A. Fischer, K. Lorenz, H. Fabritius, A. Hoffmann, and G. Kalwa, Magnetic-Balance Investigations of Phase Transformations in Pure Fe Alloys, *Arch. Eisen.*, 1966, 37(1), p 79-86.
32. A. S. Doan and J. I. Goldstein, The Ternary Phase Diagram, Fe-Ni-P, *Metall. Trans.*, 1970, 1(6), p 1759-1767.
33. P. Hofmann, K. Lohberg, and W. Reif, On the Solubility of Phosphorus in Iron and Iron-Carbon Alloys, *Arch. Eisen.*, 1970, 41(10), p 975-982.
34. M. Ko and T. Nishizawa, Effect of Magnetic Transition on the Solubility of Alloying Elements in Alpha Iron, *J. JIM*, 1979, 43(2), p 118-126.
35. E. Schurmann and H. P. Kaiser, Melting Equilibria of Iron-Aluminium and Iron-Phosphorus Alloys, *Arch. Eisen.*, 1980, 51(8), p 325-327.
36. T. Takayama, M. Y. Wey, and T. Nishizawa, Effect of Magnetic Transition on the Solubility of Alloying Elements in bcc Iron and fcc Cobalt, *Trans. JIM*, 1981, 22(5), p 315-325.

37. T. Tanaka, Thermodynamic Studies on the Equilibrium Distribution of Solute Elements between Solid and Liquid Phases in Iron Alloys, *Doctoral Dissertation*, Osaka University, Japan, 1985.
38. Z. I. Morita and T. Tanaka, Equilibrium Distribution Coefficient of Phosphorus in Iron Alloys, *Trans. ISIJ*, 1986, 26(2), p 114-120.
39. W. Huang, An Assessment of the Fe-Mn System, *CALPHAD*, 1989, 13(3), p 243-252.
40. O. Beckman, L. Lundgren, P. Nordblad, P. Svedlindh, A. Törne, Y. Andersson, and S. Rundqvist, Specific Heat of the Ferromagnet Fe₂P, *Physica Scripta*, 1982, 25(6A), p 679-681.
41. J. Leitner, P. Voňka, D. Sedmidubsky, and P. Svoboda, Application of Neumann-Kopp Rule for the Estimation of Heat Capacity of Mixed Oxides, *Thermo. Acta*, 2010, 497(1-2), p 7-13.
42. W. A. Roth, A. Meichsner, and H. Richter, An Approximation Value for the Heat of Formation of Fe₂P, *Arch. Eisen.*, 1934, 8, p 239-241.
43. F. Weibke, and G. Schrag, Heats of Formation of the Lower Phosphides of Several Heavy Metals, *Z. Elektrochem.*, 1941, 47, p 222-238.
44. G. Lewis and C. E. Myers, Vaporization Properties of Iron Phosphides, *J. Phys. Chem.*, 1963, 67(6), p 1289-1292.
45. W. Franke, K. Meisel, and R. Juza, The relationship of Phosphorus to Iron, *Z. Anorg. Chem.* 1934, 218(4), p 346-359.
46. J. Zhang, Calculating Models of Mass Action Concentrations for Fe-P and Cr-P Melts and Optimization of Their Thermodynamic Parameters, *J. Uni. Sci. Tech. Beijing*, 1999, 6(3), p 174-177.
47. X. M. Yang, P. C. Li, J. Y. Li, M. Zhang, J. L. Zhang, and J. Zhang, Representation Reaction Abilities of Structural Units and Related Thermodynamic Properties in Fe-P Binary Melts

Based on the Atom-Molecule Coexistence Theory, *Steel Research International*, 2014, 85(3), p 426-460.

48. J. Zhang, Computational Thermodynamics of Metallurgical Melts and Solutions, *Metallurgical Industry Press*, Beijing, China, 2007, p 40-70.
49. M. Yamamoto, K. Yamada, L. L. Meshkov, and E. Kato, The Standard Free Energies of Dissolution of Phosphorus Gases in Liquid Iron, *Trans. ISIJ*, 1982, 22(4), p 262-268.
50. B. Bookey, The Free Energies of Formation of Tricalcium and Tetracalcium Phosphates, *J. Iron Steel Inst., London*, 1952, 172, p 61-66.
51. B. Bookey, F. D. Richardson, and A. J. E. Welch, Phosphorus-Oxygen Equilibria in Liquid Iron, *J. Iron Steel Inst.*, 1952, 171, p 404-412.
52. H. Schenck, E. Steinmetz, and R. Gohlke, Activity of Phosphorus in Molten Iron, *Arch. Eisen.*, 1966, 37(10), p 775-778.
53. H. Schenck, E. Steinmetz, and H. Gitizad, Activity of Phosphorus in Molten Iron and Its Control by Nickel, Manganese and Chromium, *Arch. Eisen.*, 1969, 40(8), p 597-602.
54. S. Ban-ya, N. Maruyama, and S. Fujino, Vapor Pressure of Phosphorus in Liquid Fe-P Alloys, *Tetsu-to-Hagané*, 1982, 68(2), p 269-276.
55. E. Schurmann, H. P. Kaiser, and U. Hensgen, Calorimetry and Thermodynamics of the System Iron-Phosphorus, *Arch. Eisen.*, 1981, 52(2), p 51-55.
56. A. Y. Polyakov, Y. D. Pyshkin, V. T. Vovk, and K. Grigorov, Activity of Phosphorus in Liquid Phosphorus Solutions in Iron, *Zhurnal Fizicheskoi Khimii*, 1975, 49(1), p 126-129.
57. S. Ban-ya and M. Suzuki, Activity of Phosphorus in Liquid Fe-P and Fe-P-C Alloys, *Tetsu-to-Hagané*, 1975, 61(14), p 2933-2942.

58. A. A. Granovskaya and A. P. Lyubimov, Measurements of Low Vapor Pressures at High Temperatures. V. Partial Vapor Pressures of Components of the Iron-Phosphorus System, *Zh. Fiz. Khim.*, 1953, 27, p 1443-1445.
59. G. Urbain, Thermodynamic Activity of Phosphorus in Liquid Iron-Phosphorus Alloys at 1600°, *Compt. Rend*, 1957, 244(8), p 1036-1039.
60. M. Froberg, J. Elliott, and H. Hadrys, Contribution to Study of Thermodynamics of Complex Solutions Shown by Example Homogeneous Iron-Chromium-Phosphorus-Carbon Melts, *Arch. Eisen.*, 1968, 39(8), p 587-593.
61. K. Yamada and E. Kato, Mass Spectrometric Determination of Activity of Phosphorus in Liquid Fe-P Alloy, *Tetsu-to-Hagané*, 1979, 65(2), p 264-272.
62. T. Saito, Y. Shiraishi, and M. Ismail, Mass Spectrometric Study of the Gaseous Phase in Equilibrium with Molten Iron-Phosphorus Alloys. *Proceedings of the Fourth International Conference on Vacuum Metallurgy, Tokyo, June 4-8, 1973, Under the Auspices of the Iron and Steel Institute of Japan, the Japan Institute of Metals [and] the Vacuum Society of Japan. Iron and Steel Institute of Japan, Japan Institute of Metals [and] Vacuum Society of Japan.*
63. H. Jung and P. Hudon, Thermodynamic Assessment of P₂O₅, *J. Amer. Ceram. Soc.*, 2012, 95(11), p 3665-3672.
64. W. Peter, O. W. vor dem Esche, and W. Willy, Reactions between Iron Bath and Phosphate Slag, *Arch. Eisen.*, 1956, 27, p 219-230.
65. G. Troemel and H. W. Fritze, Further Investigation of the Dephosphorization of the Iron with Lime-rich Slags, *Arch. Eisen.*, 1957, 28(8), p 489-495.
66. H. Knueppel, F. Oeters and H. G. Dortmund, The Phosphorus-Oxygen Equilibrium between Liquid Iron and Lime-Saturated Phosphate Slags, *Arch. Eisen.*, 1959, 30(5), p 253-265.

67. G. Troemel and W. Fix, The Equilibrium between an Iron Melt and Lime-containing Phosphate Slags in the Presence of Silica and Manganese Oxide, *Arch. Eisen.*, 1962, 33(11), p 745-755.
68. G. Troemel and W. Fritze, Equilibriums between Iron and Lime-containing Phosphate Slags, *Arch. Eisen.*, 1959, 30(8), p 461-472.
69. G. Troemel, W. Fix, and H. W. Fritze, Equilibrium between Iron and Lime-containing Phosphate Slags, *Arch. Eisen.*, 1961, 32(6), p 353-359.
70. R. Nagabayashi, M. Hino and S. Ban-ya, Solubilities of Calcium Oxide, Magnesium Oxide, Silicon Dioxide and $2\text{CaO}\cdot\text{SiO}_2$, and Ferric-ferrous Equilibrium in $\text{Fe}_x\text{O}-(\text{CaO} + \text{MgO})-(\text{SiO}_2 + \text{P}_2\text{O}_5)$ Phosphate Slags, *Tetsu-to-Hagané*, 1988, 74(8), p 1577-1584.

Chapter 4: Thermodynamic Optimization of the Mn-P and Fe-Mn-P Systems

Zhimin You¹, In-Ho Jung²

1. Department of Mining and Materials Engineering, McGill University, 3610 University Street, Montreal, QC, H3A 0C5, Canada

2. Department of Materials Science and Engineering, and Research Institute of Advanced Materials (RIAM), Seoul National University, 1 Gwanak-ro, Gwanak-gu, Seoul, 08826, South Korea

(On revision to be published CALPHAD, 2020)

Abstract

Thermodynamic modeling of the Mn-P and Fe-Mn-P systems in the full composition was carried out using the CALculation of PHase Diagrams (CALPHAD) method based on the critical evaluation of all available phase equilibria and thermodynamic data. The liquid and solid solutions were described using the Modified Quasichemical Model and Compound Energy Formalism, respectively. The Gibbs energies of the binary stoichiometric iron and manganese phosphides were determined based on reliable experimental data. The ternary (Fe,Mn)₃P, (Fe,Mn)₂P and (Fe,Mn)P phosphides were modeled as solid solutions with mutual substitution between Fe and Mn atoms. The Gibbs energy of the liquid solution was predicted using the Toop interpolation technique with P as an asymmetric component, without any ternary parameters. The thermodynamic properties of P in the entire composition region and the liquidus of the ternary system were well reproduced. Based on the thermodynamic models with optimized parameters, unexplored phase diagrams and thermodynamic properties of the Fe-Mn-P system were predicted.

Keywords: Thermodynamic modeling, Mn-P system, Fe-Mn-P system, CALPHAD, Phase diagrams, Thermodynamic properties

4.1. Introduction

Manganese (Mn), as the fifth most abundant metallic element in the earth, has valuable significance in the metallurgical industry as an alloying additive in high Mn steels, in which Mn can be up to 30 wt.% for improving mechanical properties including hardenability, tensile strength, toughness. Besides, Mn is always used as a deoxidizer or a sulphide former in the steelmaking process [1]. The Mn in steels mostly originates from raw materials such as iron ore, flux, FeMn alloy agents, etc., which also contain certain amount of impurity elements like phosphorus. In most cases, P is a detrimental element in steels when exceeding allowed level because it can cause irreversible steel defects such as embrittlement and inner cracks. However, it is difficult to get rid of P during the steelmaking process especially at the presence of Mn because of high affinity between Mn and P.

In the past decades, various experimental and computational studies have been performed to investigate the behavior of P in Fe, Mn, and Fe-Mn alloys. Experimental studies on the Fe-P, Mn-P and Fe-Mn-P systems were reviewed by Okamoto [2], Schlesinger [3], Hansen and Anderko [4], Raghavan [5], and Korniyenko [6]. Thermodynamic assessments of the binary Fe-P, Mn-P and Fe-Mn systems have been performed by many researchers [7-21]. Previous assessments of the Fe-P system were discussed by present authors [22]. The Mn-P system was assessed by Lee et al. [12] based on reported data, including the partial Mn-P phase diagram up to $x_P = 0.5$ and thermodynamic properties of intermediate manganese phosphides Mn_3P , Mn_2P , Mn_3P_2 , MnP and MnP_3 . Miettinen [13,23] also calculated the Mn-P phase diagram of the composition up to $x_P = 0.5$. Tokunaga et al. [14] calculated the Mn-P diagram of the full composition range considering Mn_3P , Mn_2P , Mn_3P_2 , MnP and MnP_4 phosphides. Thermodynamic optimization of the Fe-Mn

system was performed by many researchers [15-21], in which the parameters proposed by Huang [17] were widely accepted. The ternary Fe-Mn-P system was thermodynamically modeled by Miettinen et al. [23], and Tokunaga et al. [14]. In the former, the descriptions were given only in the composition of $x_p \leq 0.5$ while the discrepancies in liquid and solid solutions were not resolved despite excessive model parameters used. In the latter, the Gibbs energy of MnP_4 was calculated based on the assumed formation enthalpy of FeP_4 . The uncertainty resulted from the assumptions in the binary Fe-P and Mn-P systems can be accumulated in the ternary Fe-Mn-P system. Besides, some phase diagram and thermodynamic data of previous experiments were ignored in the work by Tokunaga et al. [14].

Thermodynamic database based on the CALculation of PHAse Diagrams (CALPHAD) method is a powerful tool for new materials design and process optimization. The database of a target system is developed by means of thermodynamic modeling (optimization), aiming at obtaining one set of the consistent Gibbs energies of all phases as functions of temperature and composition. In the optimization, all available phase equilibria and thermodynamic data such as activity, entropy, enthalpy, and Gibbs energy, etc are critically evaluated simultaneously. The discrepancies between available data are resolved in the critical evaluation process, and the Gibbs energy functions for all related phases in the target system are derived. Prediction on unexplored thermodynamic properties and phase equilibria can be possible by interpolations and extrapolations in a thermodynamically correct manner.

In the present study, the liquid and solid solutions will be described using the Modified Quasichemical Model (MQM) [24,25] and Compound Energy Formalism (CEF) [26], respectively.

The optimized Fe-Mn system by Huang [17] with modification of the liquid phase by Paek et al. [27] and the recently optimized Fe-P system by present authors [22] have been adopted in this work. Phase equilibria and thermodynamic properties of the Mn-P and Fe-Mn-P systems were optimized for the entire composition range, based on critical evaluation of all available experimental data. The present description of the Fe-Mn-P system will be included in the new high-alloy steel Fe-Mn-Al-Si-Cr-Ni-Ti-Nb-C-O-N-S-P FSstel 8.0 database. All the calculations were performed using FactSage software [28].

4.2. Thermodynamic Models

4.2.1 Pure Elements and Stoichiometric Compounds

The Gibbs energies of all elemental Fe, Mn and P were taken from Scientific Group Thermodata Europe (SGTE) database compiled by Dinsdale [29]. The Gibbs energies of stoichiometric compounds were determined based on available thermodynamic data including heat capacity, standard enthalpy and entropy of formation at 298.15 K. In the present study, stoichiometric iron phosphides Fe₃P, Fe₂P, FeP and FeP₂ of the Fe-P system and manganese phosphides Mn₃P, Mn₂P, Mn₃P₂, MnP and MnP₃ of the Mn-P system were taken into account, and their Gibbs energies were determined using the equation below:

$$G_T^\circ = \left(\Delta H_{298.15K}^\circ + \int_{298.15K}^T C_P dT \right) - T \left(S_{298.15K}^\circ + \int_{298.15K}^T \frac{C_P}{T} dT \right) \quad (4.1)$$

here G_T° is the Gibbs energy at temperature T (J/mol), $\Delta H_{298.15K}^\circ$ and $S_{298.15K}^\circ$ are standard enthalpy of formation (J/mol) and standard entropy (J/mol/K) at 298.15 K, and C_P is the heat capacity (J/mol/K). The heat capacity of each stoichiometric compound was expressed as a function of temperature by fitting experimental C_P data. In the case of compounds without

available experimental C_p data, their C_p were estimated using Neumann-Kopp (NK) rule [30] or C_p functions of neighboring compounds.

When a pure element or stoichiometric compound exhibits magnetic behavior, an additional magnetic contribution term G^{mg} will be added to describe the Gibbs energies of corresponding phases using the empirical expression proposed by Inden [31] and modified by Hillert and Jarl [32].

$$G^{mg} = RT \ln(\beta + 1) g(\tau) \quad (4.2)$$

where τ is given by T/T^* and T^* is the critical temperature of magnetic transition associated with Curie temperature T_C for ferromagnetic materials or Neel temperature T_N for antiferromagnetic materials. β is the average magnetic moment per mole of atoms expressed in Bohr magnetons. $g(\tau)$ is a polynomial function derived by Hillert and Jarl [32]. In the Fe-Mn-P system, the magnetic contribution terms was applied to Fe (BCC_A2, FCC_A1), Mn (CBCC_A12, BCC_A2, FCC_A1), Fe₃P and MnP.

4.2.2 Solid Solutions

The Gibbs energies of solid solutions were described using the Compound Energy Formalism (CEF) [26] considering crystallographic structures. In the ternary Fe-Mn-P system, the solid (Fe,Mn)₃P, (Fe,Mn)₂P and (Fe,Mn)P solutions in the formulas of Me₃P, Me₂P and MeP were taken into account through mutual substitution of Fe and Mn atoms between isomorphous Fe₃P and Mn₃P, Fe₂P and Mn₂P, FeP and MnP, respectively. Besides, the solid FCC_A1, BCC_A2, CBCC_A12 and CUB_A13 solutions were also considered.

The FCC_A1, BCC_A2, CBCC_A12 and CUB_A13 phases were described using the CEF with the substitutional one-sublattice (Fe, Mn, P) approach. The molar Gibbs energies of these solid solutions were calculated as follows:

$$G_S^{sol.} = \sum_{i=Fe,Mn,P} x_i G_i^o + RT \sum_{i=Fe,Mn,P} x_i \ln x_i + \sum_{m=0,1,2,\dots} x_{Fe} x_P L_{Fe,P}^m + \sum_{k=0,1,2,\dots} x_{Mn} x_P L_{Mn,P}^k + \sum_{p=0,1,2,\dots} x_{Fe} x_{Mn} L_{Fe,Mn}^p + \sum_{q=0,1,2,\dots} x_{Fe} x_{Mn} x_P L_{Fe,Mn,P}^q + G^{mg} \quad (4.3)$$

where x_i is the mole fraction of component i and G_i^o is the molar Gibbs energy (J/mol) of the pure solid i ($i = Fe, Mn, P$); R and T are the gas constant (8.314 J/mol-K) and the temperature in Kelvin (K); $L_{Fe,P}^m$, $L_{Mn,P}^k$, $L_{Fe,Mn}^p$ and $L_{Fe,Mn,P}^q$ are the adjustable interaction parameters of corresponding binary and ternary systems; G^{mg} is the magnetic contribution to the Gibbs energy (J/mol).

The solid Me_3P , Me_2P and MeP solutions were also described with a two-sublattice (Fe, Mn)_n(P) model. In the substitutional site, Fe and Mn atoms substitute each other to form the solutions in different compositions. Their molar Gibbs energies can be expressed as:

$$G_S^{sol.} = y_{Fe} G_{Fe_nP}^o + y_{Mn} G_{Mn_nP}^o + nRT (y_{Fe} \ln y_{Fe} + y_{Mn} \ln y_{Mn}) + \sum_{m=0,1,2,\dots} y_{Fe} y_{Mn} L_{Fe,Mn:P}^m + G^{mg} \quad (4.4)$$

here $G_{Fe_nP}^o$ and $G_{Mn_nP}^o$ are Gibbs energies (J/mol) of pure stoichiometric compounds Fe_nP and Mn_nP , respectively. n ($n = 3, 2, 1$) is the number of molar substitutional sites of the two-sublattice formula. y_{Fe} and y_{Mn} are site fractions of Fe and Mn in the substitutional site. $L_{Fe,Mn:P}^m$ is the adjustable parameter describing the interaction between Fe and Mn in the substitutional lattice.

4.2.3 Liquid Solution

The Modified Quasichemical Model (MQM) [24,25] considering the short-range ordering of the nearest-neighbor atoms was used to describe the liquid solutions. Compared to the conventional

Bragg-Williams Random Mixing Model (BWRMM), the MQM gives a more realistic description of the entropy of solution. In the MQM, the Gibbs energy of pair formation can be expanded as a polynomial in the pair fraction rather than the component fraction and coordination numbers of the components are allowed to vary with composition for reproducing the short-range ordering of the liquid solution with less parameters, providing greater flexibility in reproducing experimental data of the binary liquids and combining the binary parameters in higher-order systems.

In the case of the binary A - B liquid solution, the atoms A and B are distributed over the quasilattice sites. The atom pair exchanging reaction of the A - B liquid solution can be expressed as follows:



where $(i-j)$ represents the nearest-neighbor pair between components i and j , and Δg_{AB} is the Gibbs energy change (J/mol) of forming 2 moles (A-B) pairs. The Gibbs energy of the liquid solution is given by the following equation:

$$G_{AB}^L = (n_A G_A^\circ + n_B G_B^\circ) - T \Delta S_{AB}^{conf.} + n_{AB} (\Delta g_{AB} / 2) \quad (4.6)$$

where n_A and n_B are the numbers of moles of A atoms and B atoms, and G_A° and G_B° are the molar Gibbs energies of pure A and B components. $\Delta S_{AB}^{conf.}$ is the configurational entropy of mixing given by random distribution of the (A-A), (B-B) and (A-B) pairs as follows:

$$\Delta S_{AB}^{conf.} = -R(n_A \ln X_A + n_B \ln X_B) - R \left[n_{AA} \ln \left(\frac{X_{AA}}{Y_A^2} \right) + n_{BB} \ln \left(\frac{X_{BB}}{Y_B^2} \right) + n_{AB} \ln \left(\frac{X_{AB}}{2Y_A Y_B} \right) \right] \quad (4.7)$$

here n_{AA} , n_{BB} and n_{AB} are the numbers of moles of the (A-A), (B-B) and (A-B) pairs; X_{AA} , X_{AB} and X_{BB} are the pair fractions of corresponding atom pairs; X_A and X_B are the mole fractions of A and B atoms and Y_A and Y_B are the coordination equivalent fractions of A and B atoms. The pair fractions X_{AA} , X_{AB} , X_{BB} and coordination equivalent fractions Y_A and Y_B are calculated as:

$$X_{AA} = n_{AA} / (n_{AA} + n_{AB} + n_{BB}) \quad (4.8)$$

$$X_{AB} = n_{AB} / (n_{AA} + n_{AB} + n_{BB}) \quad (4.9)$$

$$X_{BB} = n_{BB} / (n_{AA} + n_{AB} + n_{BB}) \quad (4.10)$$

$$Y_A = X_{AA} + \frac{1}{2} X_{AB} \quad (4.11)$$

$$Y_B = X_{BB} + \frac{1}{2} X_{AB} \quad (4.12)$$

The Δg_{AB} in **Eq. (4.5)**, the model parameter for reproducing the Gibbs energy of the binary *A-B* solution, can be expanded as a polynomial based on the atomic pair fractions X_{AA} and X_{BB} :

$$\Delta g_{AB} = \Delta g_{AB}^{\circ} + \sum_{i \geq 1} g_{AB}^{i0} X_{AA}^i + \sum_{j \geq 1} g_{AB}^{0j} X_{BB}^j \quad (4.13)$$

where Δg_{AB}° , g_{AB}^{i0} and g_{AB}^{0j} are the adjustable model parameters that can be functions of the temperature. In the MQM, the coordination numbers of A and B, Z_A and Z_B , can be varied with the composition to reproduce the short-range ordering of the solution:

$$\frac{1}{Z_A} = \frac{1}{Z_{AA}^A} \left(\frac{2n_{AA}}{2n_{AA} + n_{AB}} \right) + \frac{1}{Z_{AB}^A} \left(\frac{n_{AB}}{2n_{AA} + n_{AB}} \right) \quad (4.14)$$

$$\frac{1}{Z_B} = \frac{1}{Z_{BB}^B} \left(\frac{2n_{BB}}{2n_{BB} + n_{AB}} \right) + \frac{1}{Z_{BA}^B} \left(\frac{n_{AB}}{2n_{BB} + n_{AB}} \right) \quad (4.15)$$

here Z_{AA}^A is the value Z_A when all nearest neighbors of a A atom are A atoms, and Z_{AB}^A is the value of Z_A when all nearest neighbors of the A atom are B atoms. Z_{BB}^B and Z_{BA}^B are defined in an analogous manner.

When extending from the binary systems to the ternary system, the Gibbs energy of the ternary liquid solution can be predicted using the proper interpolation technique based on the nature of all

involved binary systems. If necessary, ternary correction terms can also be further introduced to give a more precise description of the Gibbs energy of the ternary liquid solution. In the Fe-Mn-P system, the liquid Fe-P and Mn-P solutions behave very negative deviation from ideal mixing while the liquid Fe-Mn solution is almost in ideal mixing. Therefore, the Toop-type geometric interpolation technique [25] with P as the asymmetric component was adopted for the Fe-Mn-P system. The configurational entropy of mixing and Gibbs energy of the liquid Fe-Mn-P solution was calculated using the following equations:

$$\Delta S_{FeMnP}^{conf.} = -R \sum_{i=Fe,Mn,P} n_i \ln X_i - R \left[\sum_{j=Fe,Mn,P} n_{jj} \left(\frac{X_{jj}}{Y_j^2} \right) + \sum_{k,m=Fe,Mn,P}^{k \neq m} n_{km} \ln \left(\frac{X_{km}}{2Y_k Y_m} \right) \right] \quad (4.16)$$

$$G_{FeMnP}^L = \sum_{i=Fe,Mn,P} n_i G_i^\circ - T \Delta S_{FeMnP}^{conf.} + \sum_{j,k=Fe,Mn,P}^{j \neq k} (n_{jk} / 2) \Delta g_{jk} \quad (4.17)$$

here each pair formation Gibbs energy Δg_{FeP} , Δg_{MnP} and Δg_{FeMn} depends on the symmetry of each component (Fe, Mn, P) in the ternary system. Therefore, Δg_{FeP} and Δg_{MnP} between asymmetric components (Fe and P, Mn and P) are expressed as below:

$$\Delta g_{FeP} = \Delta g_{FeP}^\circ + \sum_{(i+j) \geq 1} g_{FeP}^{ij} x_{PP}^i (x_{FeFe} + x_{FeMn} + x_{MnMn})^j + \sum_{i \geq 0, j \geq 0, k \geq 1} g_{FeP(Mn)}^{ijk} x_{PP}^i (x_{FeFe} + x_{FeMn} + x_{PP})^j \left(\frac{Y_{Mn}}{Y_{Fe} + Y_{Mn}} \right)^k \quad (4.18)$$

$$\Delta g_{MnP} = \Delta g_{MnP}^\circ + \sum_{(i+j) \geq 1} g_{MnP}^{ij} x_{PP}^i (x_{FeFe} + x_{FeMn} + x_{MnMn})^j + \sum_{i \geq 0, j \geq 0, k \geq 1} g_{MnP(Fe)}^{ijk} x_{PP}^i (x_{FeFe} + x_{FeMn} + x_{PP})^j \left(\frac{Y_{Fe}}{Y_{Fe} + Y_{Mn}} \right)^k \quad (4.19)$$

and Δg_{FeMn} between symmetric Fe and Mn is expressed as:

$$\Delta g_{FeMn} = \Delta g_{FeMn}^\circ + \sum_{(i+j) \geq 1} g_{FeMn}^{ij} \left(\frac{x_{FeFe}}{x_{FeFe} + x_{FeMn} + x_{MnMn}} \right)^i \left(\frac{x_{MnMn}}{x_{FeFe} + x_{FeMn} + x_{MnMn}} \right)^j + \sum_{i \geq 0, j \geq 0, k \geq 1} g_{FeMn(P)}^{ijk} \left(\frac{x_{FeFe}}{x_{FeFe} + x_{FeMn} + x_{MnMn}} \right)^i \left(\frac{x_{MnMn}}{x_{FeFe} + x_{FeMn} + x_{MnMn}} \right)^j Y_P^k \quad (4.20)$$

where g_{FeP}^{ij} , g_{MnP}^{ij} , g_{FeMn}^{ij} are the binary liquid parameters; $g_{\text{FeP(Mn)}}^{ijk}$, $g_{\text{MnP(Fe)}}^{ijk}$ and $g_{\text{FeMn(P)}}^{ijk}$ are the ternary liquid parameters.

4.3 Critical Evaluation and Thermodynamic Optimization

Thermodynamic optimization of the Fe-Mn-P system was performed using the CALPHAD approach based on the critical evaluation of all available phase equilibria and thermodynamic data. The liquid and solid solutions of all sub-systems were described using the MQM [24,25] and CEF [26], respectively. White P were selected as the standard state for the solid phases. The crystal structure information of all solid phases in the Fe-Mn-P system is summarized in **Table 4.1**. The optimized model parameters of the Fe-Mn-P system are summarized in **Table 4.2**.

Table 4.1 Summary of crystal structure information of all solid phases in the Fe-Mn-P system

Phase	Structure	Prototype	Space group	Pearson symbol
FCC_A1	Cubic	Cu	$\bar{F}m\bar{3}m$	<i>cF4</i>
BCC_A2	Cubic	W	$Im\bar{3}m$	<i>cI2</i>
CBCC_A12	Cubic	α Mn	$I\bar{4}3m$	<i>cI58</i>
CUB_A13	Cubic	β Mn	$P4_132$	<i>cP20</i>
Me ₃ P	Tetragonal	Ni ₃ P	$I\bar{4}$	<i>tI32</i>
Me ₂ P	Hexagonal	Fe ₂ P	$P\bar{6}2m$	<i>hP9</i>
MeP	Orthorhombic	MnP	<i>Pnma</i>	<i>oP8</i>
FeP ₂	Orthorhombic	FeS ₂	<i>Pnnm</i>	<i>oP6</i>
Mn ₃ P ₂	Tetragonal	Zn ₃ P ₂	$P4_2/nmc$	<i>tP40</i>
MnP ₃	---	---	---	---

White P	Cubic	P ₄	$\bar{I}43m$	C*8
Red P	---	P	---	C*66

Table 4.2 Optimized model parameters for the Fe-Mn-P system (J/mol, J/mol-K)

Phase	Model parameters
	$Z_{FeFe}^{Fe} = Z_{MnMn}^{Mn} = Z_{PP}^P = 6$ [27, *]
	$Z_{PFe}^P = Z_{PMn}^P = Z_{FeMn}^{Fe} = Z_{MnFe}^{Fe} = 6$ [27, *], $Z_{FeP}^{Fe} = Z_{MnP}^{Mn} = 3$ [*]
Liquid (Fe, Mn, P)	$\Delta g_{FeP} = -56902 + 6.569T + (5481 + 3.0334T)X_{FeFe} + (-11966 + 2.5104T)X_{FeFe}^2 - 9623.2X_{PP}$ [*] $\Delta g_{MnP} = -57279 + 4.6024T + (7113 + 4.6024T)X_{MnMn} + (-18326 + 4.184T)X_{MnMn}^2 - 17656.5X_{PP}$ [*] $\Delta g_{FeMn} = -1338.88 + 0.16736T + 418.4X_{FeFe} - 334.72X_{MnMn}$ [27] “Toop-type” interpolation with P as an asymmetric component [*]
FCC_A1 (Fe, Mn, P) ₁ (Va) ₁	$G_{Fe:Va}^{FCC} = G_{Fe(FCC)}^\circ, G_{Mn:Va}^{FCC} = G_{Mn(FCC)}^\circ, G_{P:Va}^{FCC} = G_{P(FCC)}^\circ$ [*] $L_{Fe,P:Va}^{FCC} = -139787.44 + 6.4852T$ [22] $L_{Mn,P:Va}^{FCC} = -33472$ [*] $L_{Fe,Mn:Va}^{FCC} = -7762 + 3.865T - 259(x_{Fe} - x_{Mn})$ [17] $L_{CFe,Mn:Va}^{FCC} = -2282 - 2068(y_{Fe} - y_{Mn})$ [17] $T_{CFe:Va} = -201, \beta_{Fe:Va} = -2.1$ [17] $T_{CMn:Va} = -1620, \beta_{Mn:Va} = -1.86$ [17]

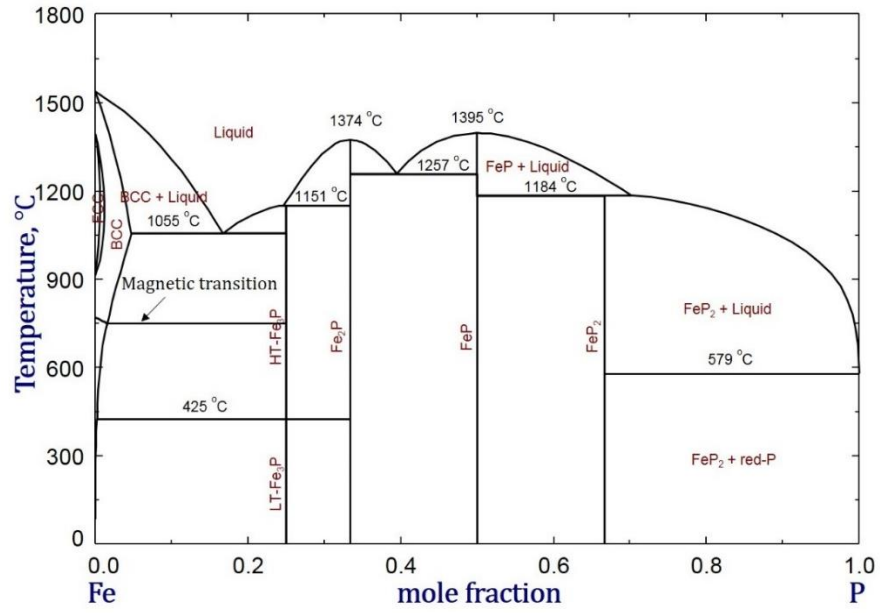
	$G_{Fe:Va}^{BCC} = G_{Fe(BCC)}^{\circ}, G_{Mn:Va}^{BCC} = G_{Mn(BCC)}^{\circ}, G_{P:Va}^{BCC} = G_{P(BCC)}^{\circ} \quad [*]$
	$L_{Fe,P:Va}^{BCC} = -203476.3 + 15.4808T + 33472(y_{Fe} - y_P) \quad [22]$
	$L_{Mn,P:Va}^{BCC} = -30543.2 \quad [*]$
BCC_A2	
(Fe, Mn, P) ₁ (Va) ₃	$L_{Fe,Mn:Va}^{BCC} = -2759 + 1.237T \quad [17]$
	$T_{CFe,P:Va} = -285, T_{CFe,Mn:Va} = 123 \quad [17]$
	$T_{CFe:Va} = 1043, \beta_{Fe:Va} = 2.22 \quad [17]$
	$T_{CMn:Va} = -580, \beta_{Mn:Va} = -0.27 \quad [17]$
	$G_{Fe:Va}^{CBCC} = G_{Fe(CBCC)}^{\circ}, G_{Mn:Va}^{CBCC} = G_{Mn(CBCC)}^{\circ}, G_{P:Va}^{CBCC} = G_{P(white)}^{\circ} + 30000 \quad [*]$
CBCC_A12	
(Fe, Mn, P) ₁ (Va) ₁	$L_{Mn,P:Va}^{CBCC} = -34308.8 \quad [*]$
	$L_{Fe,Mn:Va}^{CBCC} = -10184 \quad [17]$
	$G_{Fe:Va}^{CUB} = G_{Fe(CUB)}^{\circ}, G_{Mn:Va}^{CUB} = G_{Mn(CUB)}^{\circ}, G_{P:Va}^{CUB} = G_{P(white)}^{\circ} + 25000 \quad [*]$
CUB_A13	
(Fe, Mn, P) ₁ (Va) ₁	$L_{Mn,P:Va}^{CUB} = -34308.8 \quad [*]$
	$L_{Fe,Mn:Va}^{CUB} = -11518 + 2.819T \quad [17]$
	$G_{Fe:P}^{Me_3P} = G_{Fe_3P}^{\circ} \quad [22]$
Me ₃ P	
(Fe, Mn) ₃ (P) ₁	$G_{Mn:P}^{Me_3P} = -224543 + 629.2778T - 108.95T \ln T - 0.0136T^2 + 6.583 \times 10^{-7}T^3 + 212500T^{-1} \quad [*]$
	$L_{Fe,Mn:P}^{Me_3P} = 47446.56 - 29.288T + (-7041.67 + 10.46T)(x_{Fe} - x_{Mn}) \quad [*]$
	$G_{Fe:P}^{Me_2P} = G_{Fe_2P}^{\circ} \quad [22]$
Me ₂ P	
(Fe, Mn) ₂ (P) ₁	$G_{Mn:P}^{Me_2P} = -195270 + 374.927T - 67.4032T \ln T - 0.01865T^2 + 4.675 \times 10^{-7}T^3 + 234827T^{-1} \quad [*]$
	$L_{Fe,Mn:P}^{Me_2P} = -39886.1 - 20.92T + (-26359.2 + 16.736T)(y_{Fe} - y_{Mn}) \quad [*]$

MeP	$G_{Fe:P}^{MeP} = G_{FeP}^{\circ}$ [22]
(Fe, Mn) ₁ (P) ₁	$G_{Mn:P}^{MeP} = -137881 + 246.546T - 43.945T \ln T - 0.0113T^2 + 4.675 \times 10^{-7}T^3 + 165000T^{-1}$ [*]
	$I_{Fe,Mn:P}^{MeP} = 0$ [*]
FeP ₂ [22]	$\Delta H_{298.15K}^{\circ} = -191100, S_{298.15K}^{\circ} = 51.05$
(Fe) ₁ (P) ₂	$C_p = 77.52563 + 0.009348T - 443846T^{-2} - 1.1 \times 10^{-6}T^2$
Mn ₃ P ₂ [*]	$\Delta H_{298.15K}^{\circ} = -288185, S_{298.15K}^{\circ} = 151.5$
(Mn) ₃ (P) ₂	$C_p = 111.3482 + 0.0599T - 799654T^{-2} - 5.61 \times 10^{-6}T^2$
MnP ₃ [*]	$\Delta H_{298.15K}^{\circ} = -201880, S_{298.15K}^{\circ} = 82.0$
(Mn) ₁ (P) ₃	$C_p = 84.9186 + 0.03840928T - 710692T^{-2} - 8.415 \times 10^{-6}T^2$

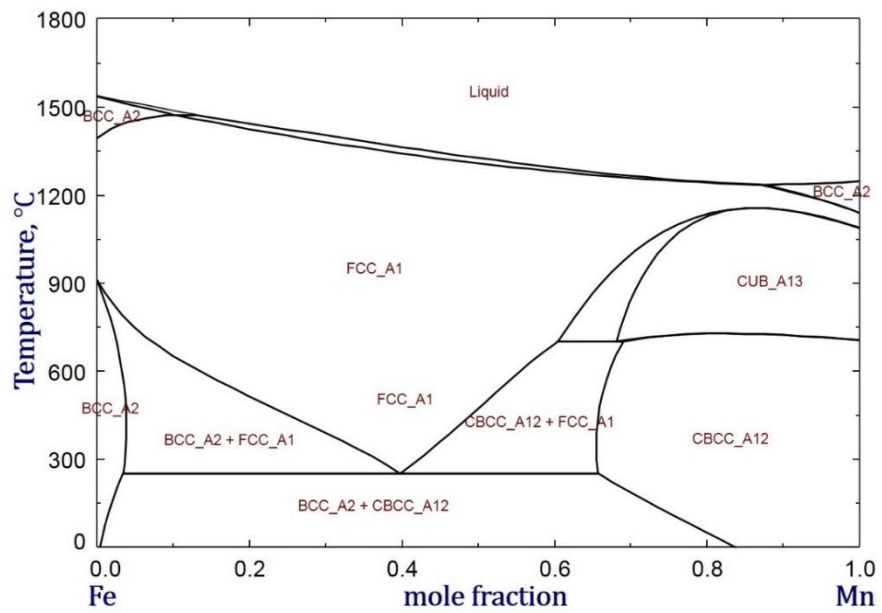
* optimized in the present study

4.3.1 The Fe-P and Fe-Mn System

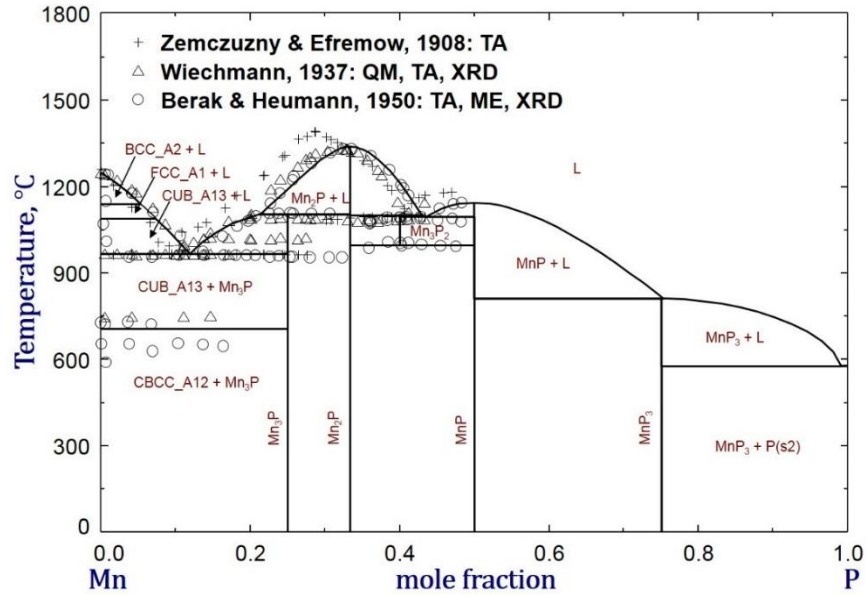
The Fe-P system optimized by present authors [22] and the Fe-Mn system optimized by Huang [17] with the modification of the liquid phase by Paek et al. [27] were adopted in the present study. The optimized phase diagrams of the Fe-P and Fe-Mn system are plotted in **Fig. 4.1(a)** and **Fig. 4.1(b)**. With suppression of the gas phase, three solutions including the liquid, FCC_A1 and BCC_A2 and four stoichiometric compounds including Fe₃P, Fe₂P, FeP and FeP₂ are stable in the Fe-P system [22]. P is soluble in γ -Fe and α -Fe in the Fe-rich region, as shown in **Fig. 4.1(a)**. In the Fe-Mn system, five solutions including the liquid, BCC_A2, FCC_A1, CBCC_A12 and CUB_A13 were considered.



(a)



(b)



(c)

Figure 4.1 Optimized phase diagrams of the (a) Fe-P (b) Fe-Mn, and (c) Mn-P systems

4.3.2 The Mn-P System

4.3.2.1 Phase Diagram

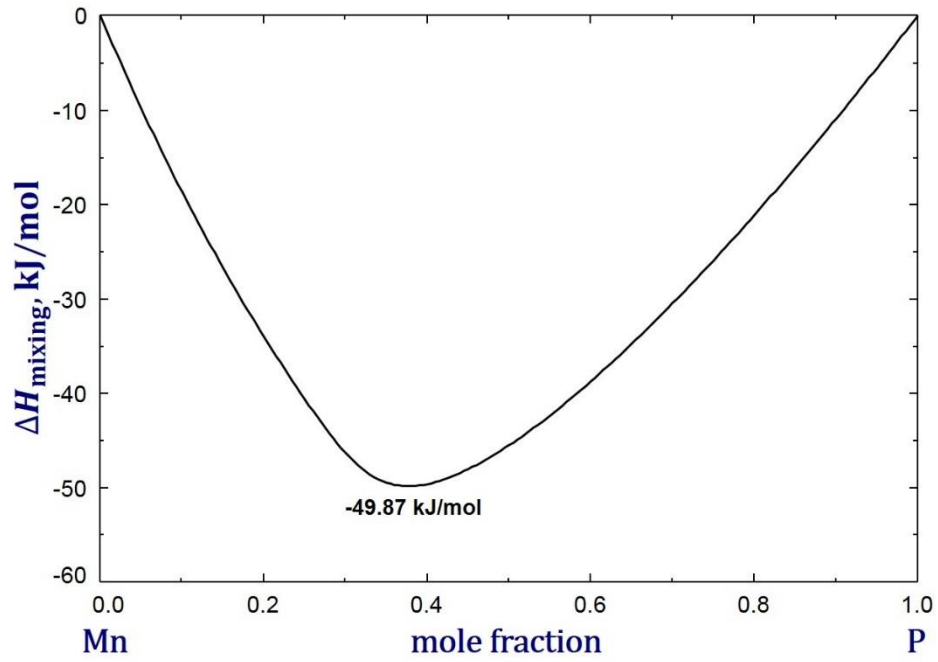
The optimized Mn-P phase diagram was compared with experimental data in **Fig. 4.1(c)**. Five solutions (liquid, BCC_A2, FCC_A1, CUB_A13 and CBCC_A12) and five stoichiometric compounds (Mn₃P, Mn₂P, Mn₃P₂, MnP and MnP₃) were considered in the Mn-P system. There is no evidence of P dissolution in solid Mn, so the solubility of P in the BCC_A2, FCC_A1, CUB_A13 and CBCC_A12 Mn is taken as zero. Invariant reactions of the Mn-P system are summarized in **Table 4.3**.

Table 3.3 Invariant reactions of the Mn-P system optimized in the present study

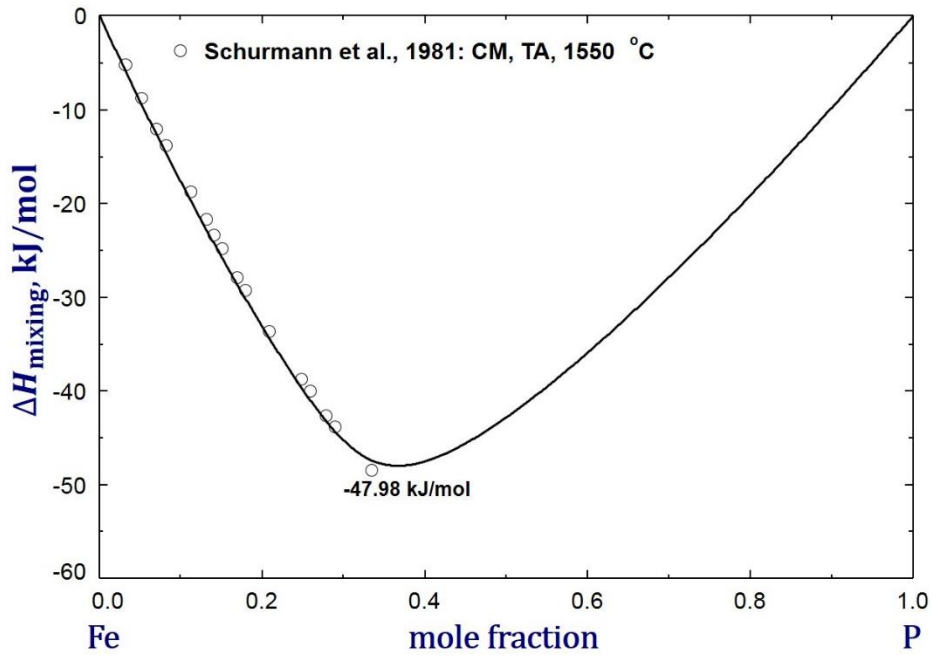
Type	Reactions	Temperature, °C
Eutectic	$L(x_P = 0.119) = \text{CUB_Mn}(x_P = 0) + \text{Mn}_3\text{P}(x_P = 0.25)$	965
Incongruent	$L(x_P = 0.212) + \text{Mn}_2\text{P}(x_P = 0.333) = \text{Mn}_3\text{P}(x_P = 0.25)$	1101
Congruent	$L(x_P = 0.333) = \text{Mn}_2\text{P}(x_P = 0.333)$	1337
Peritectic	$\text{Mn}_2\text{P}(x_P = 0.333) + L(x_P = 0.429) = \text{Mn}_3\text{P}_2(x_P = 0.4)$	1100
Eutectic	$L(x_P = 0.434) = \text{Mn}_3\text{P}_2(x_P = 0.4) + \text{MnP}(x_P = 0.50)$	1094
Congruent	$\text{MnP}(x_P = 0.50) = \text{MnP}(x_P = 0.50)$	1143
Peritectic	$\text{MnP}(x_P = 0.5) + L(x_P = 0.754) = \text{MnP}_3(x_P = 0.75)$	809
Eutectic	$L(x_P = 0.9996) = \text{MnP}_3(x_P = 75) + \text{Red_P}(x_P = 1)$	576

4.3.2.2 Liquid Solution

The thermodynamic properties of P in molten Mn are of metallurgical significance particularly for the P removal in Mn alloys and high Mn steels. Schurmann et al. [33] measured the enthalpy of mixing of the liquid Fe-P solution at 1550 °C using the calorimetry method (CM) and thermal analysis (TA). The optimized enthalpy of mixing of liquid Mn-P and Fe-P solutions are plotted in **Fig. 4.2**. The liquid Mn-P solution shows very negative mixing enthalpy ($\Delta H_{\text{mixing}}^{\text{min}} = -49.87$ kJ/mol), which is slightly more negative than that of the liquid Fe-P solution ($\Delta H_{\text{mixing}}^{\text{min}} = -47.98$ kJ/mol) [22]. Both solutions exhibit apparent short-range ordering at the composition of $0.3 < x_P < 0.4$, which were well described using the MQM.



(a)



(b)

Figure 4.2 Enthalpy of mixing of the liquid solutions in the (a) Fe-P and (b) Mn-P systems

The activities of P and Mn in the Mn-P liquid solution were investigated by Dashevskii et al. [34], Batalin et al. [35,36] and Zaitsev et al. [37]. The calculated Raoltian activities of P (a_P^R) and Mn (a_{Mn}^R) in the reference of pure liquid P and Mn were compared with experimental results in **Fig. 4.3**. As shown in the figure, the data of both a_P^R and a_{Mn}^R from different experiments are very inconsistent. The a_P^R obtained by Dashevskii et al. [34] and Batalin et al. [35] were calculated based on the a_{Mn}^R determined from the Mn vapor over the liquid solution using the Gibbs-Duhem relationship. In their experiments, the measured Mn vapor pressure over the pure liquid Mn, however, as the reference pressure, even deviated from the well-known vapor pressure, so the accuracy of their data is suspicious. Another set of a_P^R data were measured by Batalin et al. [36] using the vacuum calorimetry method (VCM), which seems to be more reliable. Zaitsev et al. [37] carried out Knudsen effusion experiments at 976 °C to 1298 °C to measure the activities of P and Mn, which were determined from the intensities of individual gaseous ion species. As can be seen in **Fig. 4.3**, the experimental data of Zaitsev et al. [37] at lower temperatures ($976\text{ °C} \leq T \leq 1175\text{ °C}$) are reasonably reproduced in the present modeling. However, the data at higher temperatures ($1243\text{ °C} \leq T \leq 1298\text{ °C}$) deviate from the calculated results, because vaporization of the liquid Mn into the gas phase cannot be neglected at higher temperatures, which resulted in positive deviation in a_{Mn}^R in terms of the analytical technique (KEM). The behaviors of a_P^R and a_{Mn}^R in **Fig. 4.3** for the Mn-P system are very similar to those of a_P^R and a_{Fe}^R for the Fe-P system [22].

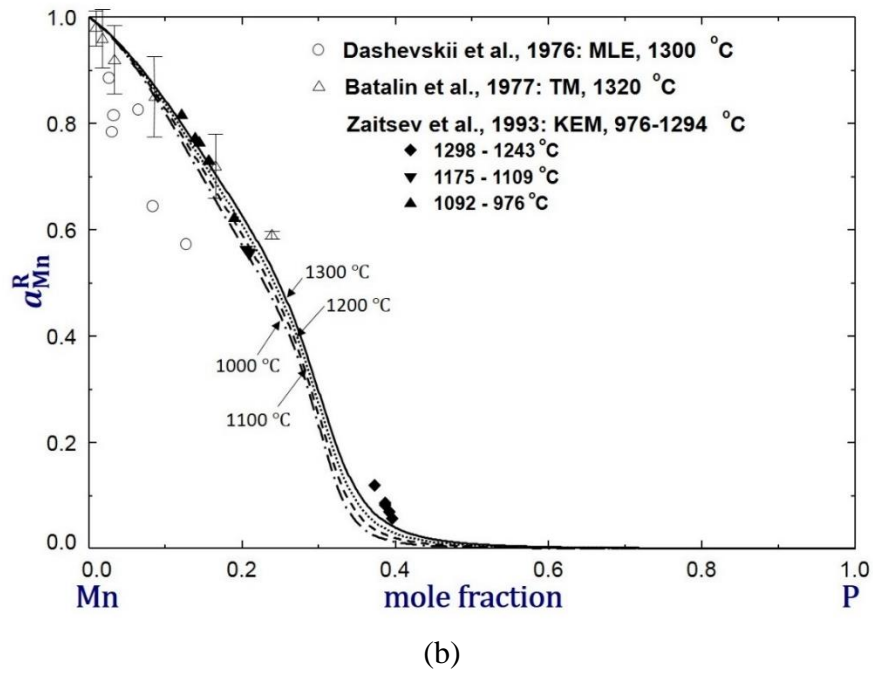
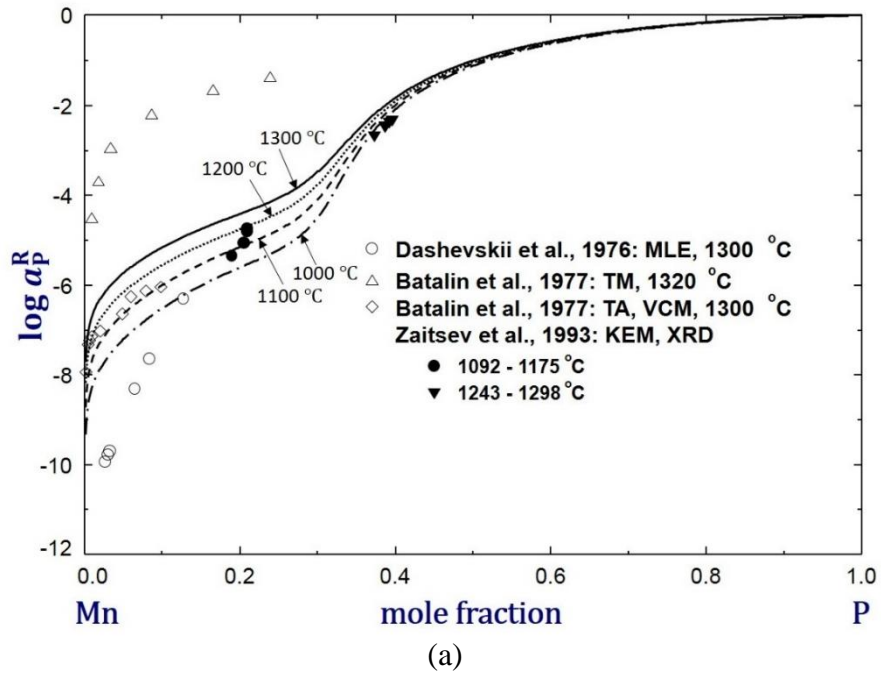


Figure 4.3 Calculated activities (a) a_P^R , and (b) a_{Mn}^R of the liquid Mn-P solution in the references of pure liquid P and Mn, compared to experimental data [34-37]

In the dilute solution of P in liquid Mn, the Henrian activity coefficient γ_P^0 of P is a very important parameter to calculate the P distribution between the liquid Mn and slag or gas phase. The calculated γ_P^0 and the Gibbs energy of $P_2(g)$ dissolution in liquid Mn are:

$$\ln \gamma_P^0 = -24713 / T + 4.8307 \quad (4.21)$$

$$0.5P_2(g) = P_{in\ liquid\ Mn} (wt.\%); \quad \Delta G_{P_2(g)}^\circ = -265250 + 57.779T \quad (4.22)$$

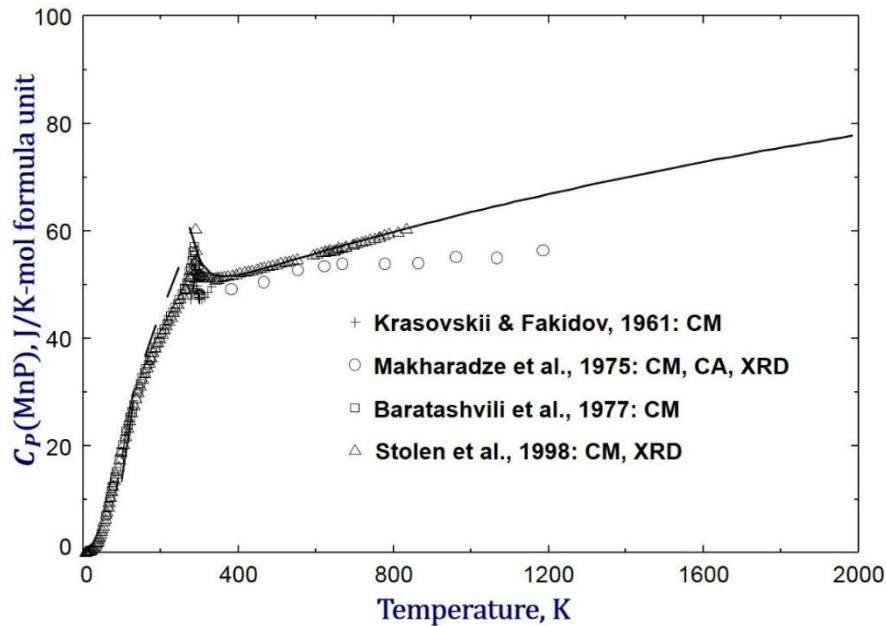
here T is the temperature in Kelvin (K).

4.3.2.3 Stoichiometric Manganese Phosphides

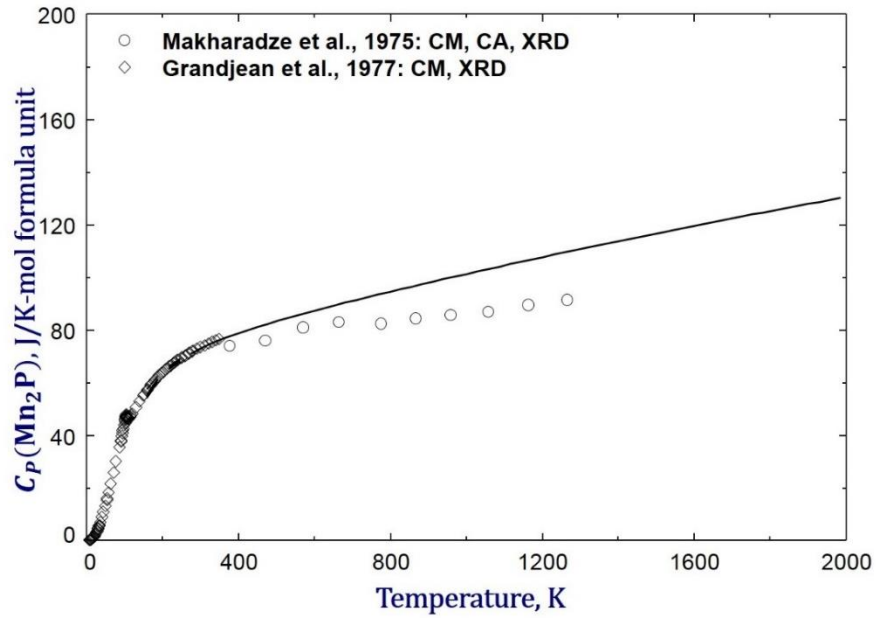
Stoichiometric Mn_3P , Mn_2P and MnP compounds are undoubtedly stable in the Mn-P system at 1 atm total pressure. Mn_3P_2 , however, was not confirmed in the early experiments [38,39] but was detected between around 1002 °C and 1090 °C in more recent experiments [37,40-42]. The stabilities of stoichiometric MnP_3 and MnP_4 compounds are very controversial. Biltz and Wiechmann [43] measured the vapor pressure of $P_4(g)$ in equilibrium with the Mn and red P mixture in the composition of $n_P:n_{Mn} = 1.0 - 4.2$ at 610 °C to 720 °C. In their experiments, stoichiometric MnP and MnP_3 compounds, instead of MnP_2 and MnP_4 , were detected in the samples. According to other researchers, various polymorphs of manganese tetrphosphides (2-, 6-, 8- and γ - MnP_4) synthesized either at very high pressure (30-55 kbar) or in tin flux experiments [44-46]. Interestingly, MnP_3 can always be detected in the tin flux experiments [45,46] In the investigation by Henge et al. [47], the stabilities of the above four polymorphs of MnP_4 were evaluated based on their electronic structures and phonon calculations. The new γ - MnP_4 turned out to be metastable, and the other three modifications exist only in very limited conditions. Since no reliable clue of thermodynamic properties is available for MnP_4 , so it was assumed to be metastable

in the present optimization. Instead, MnP_3 was considered as the stable phase in favor of experimental results by Biltz and Wiechmann [43].

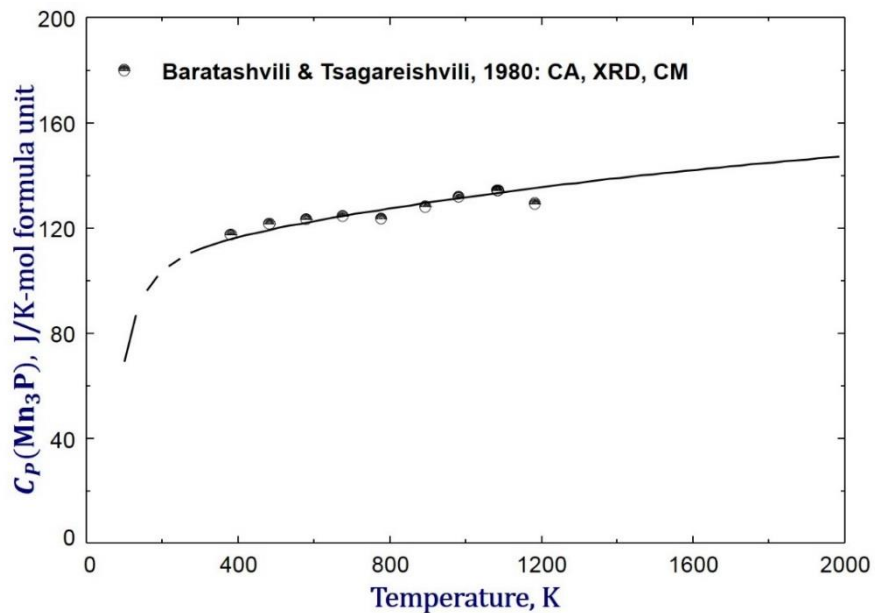
The calculated heat capacities of Mn_3P , Mn_2P , and MnP were compared with experimental data in **Fig. 4.4**. With no available experimental data in the literature, the heat capacities of Mn_3P_2 and MnP_3 were determined based on those of Mn_2P and MnP , $C_p(\text{Mn}_3\text{P}_2) = C_p(\text{MnP}) + C_p(\text{Mn}_2\text{P})$ and $C_p(\text{MnP}_3) = 3C_p(\text{MnP}) - 2C_p(\text{Mn}_{\text{CBCC}})$, as expressed in **Table 4.2**. The heat capacities of MnP and Mn_2P obtained by Makharadze et al. [48] using the calorimetry technique are inconsistent with other experimental results [49-51]. Makharadze et al. [48] extrapolated the heat capacities of MnP and Mn_2P from the C_p data of the Mn_2P - MnP mixture. The C_p data of Mn_2P obtained by Grandjean [52] and those of MnP obtained by Krasovskii and Fakidov [49], Baratashvili et al. [50] and Stolen et al. [51] were consistent and favored in the present optimization.



(a)



(b)

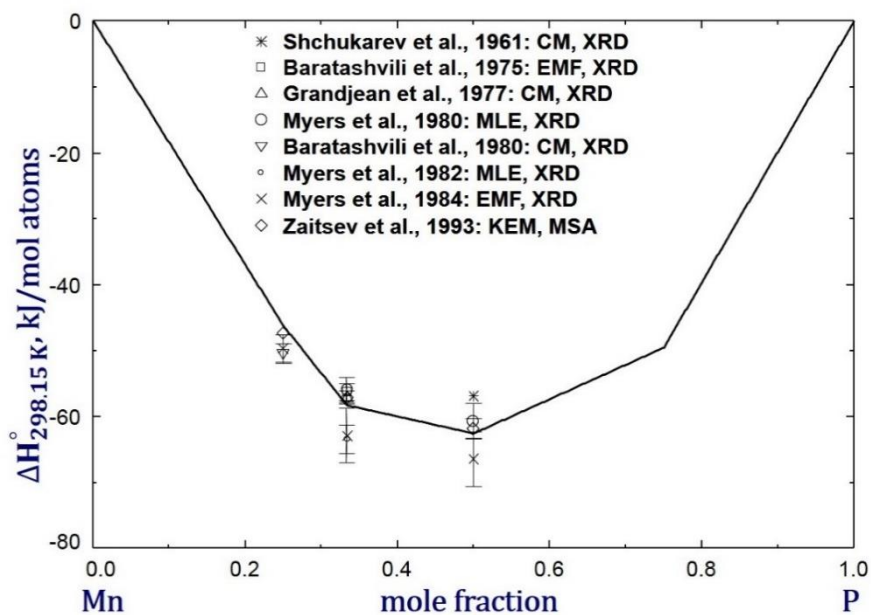


(c)

Figure 4.4 Heat capacities of (a) MnP, (b) Mn₂P, and (c) Mn₃P in the Mn-P system

Fig. 4.5 shows the standard formation enthalpy and standard entropy of stoichiometric manganese phosphides in the references of CBCC_A12 Mn(α) and white P at 298.15 K. The standard enthalpy

of formation was measured using the calorimetry method (CM) [52-54], Electromotive Force (EMF) technique [55,56], Mass-loss effusion (MLE) technique [57,58] and Knudsen effusion method (KEM) [37]. The results reported by Grandjean et al. [52] and Zaitsev et al. [37] are in good consistency but deviated from those of Mn₃P by Baratashvili et al. [54], Mn₂P and MnP by Myers et al. [56,58] and Shchukarev et al. [53]. Baratashvili et al. [54] obtained the standard enthalpy of Mn₃P based on their previous result of Mn₂P [55] and estimated C_p of Mn₃P. Therefore, the experimental errors and estimation uncertainties are probably accumulated in the standard enthalpy of Mn₃P. In addition, the standard enthalpies of Mn₂P and MnP suggested by Myers et al. [56,58] deviate largely from other data including their own earlier results [57]. Hence, these two sets of data are not considered reliable. Shchukarev et al. [53] synthesised MnP with solid Mn and phosphorus vapor. However, the MnP formed on the surface of Mn probably prevented further formation of MnP, and condensation of gaseous phosphorus mixing with the solid MnP was observed during the experiments. These phenomena cause inaccuracy in the measured enthalpy of MnP, as shown Fig. 4.5(a).



(a) $\Delta H_{298.15\text{ K}}^{\circ}$

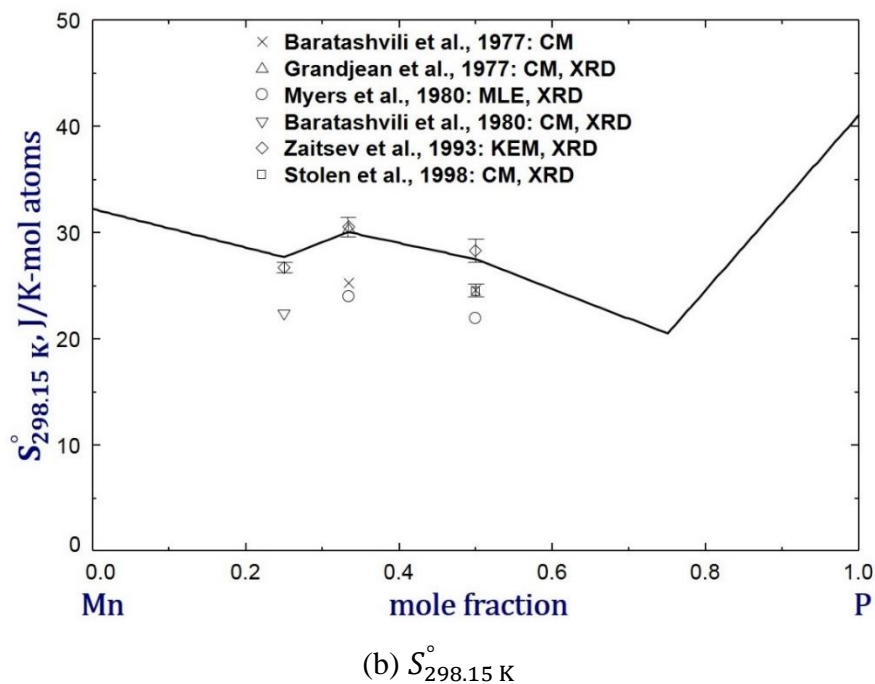
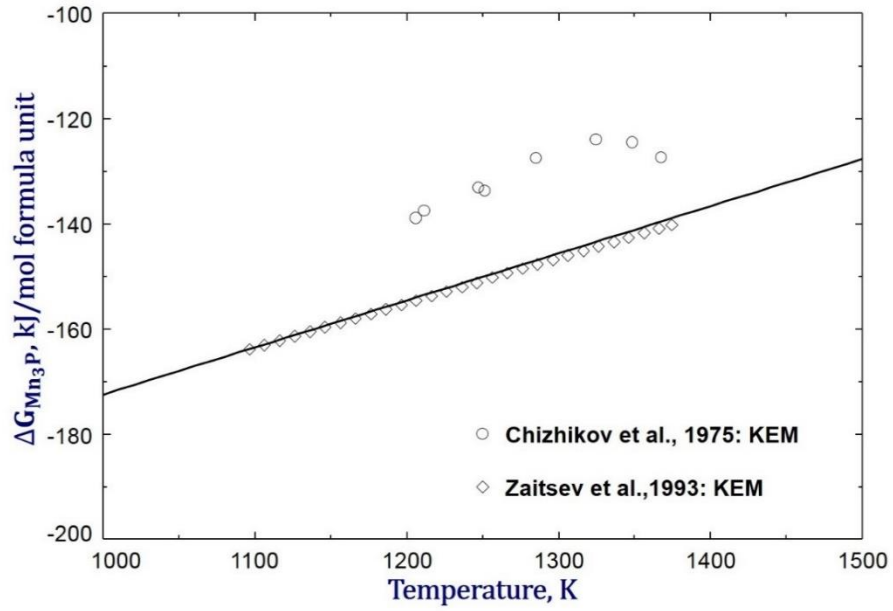


Figure 4.5 Standard enthalpy of formation $\Delta H_{298.15 K}^{\circ}$ and entropy $S_{298.15 K}^{\circ}$ of stoichiometric manganese phosphides at 298.15 K

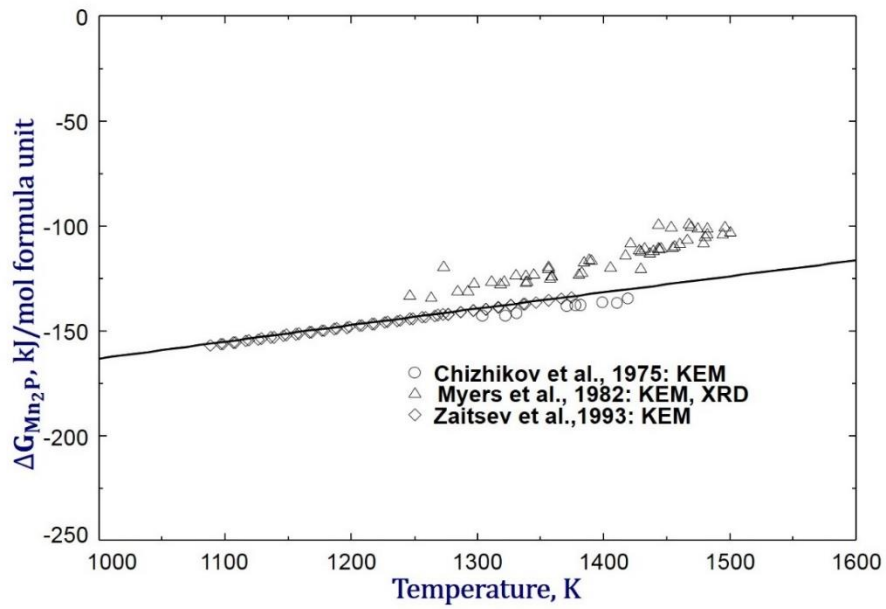
In the Mn-P system, experimental data [37,50-52,54,57] of the standard entropy at 298.15 K are only available for Mn_3P , Mn_2P and MnP . However, significant scattering exists among available experimental results, as can be seen in **Fig. 4.5(b)**. Baratashvili et al. [54] obtained a value of $S_{298.15 K}^{\circ} = 22.385$ J/K-mol atoms for Mn_3P using the calorimetry method (CM), based on their earlier $S_{298.15 K}^{\circ} = 25.243$ J/K-mol atoms [50] for Mn_2P . Myers et al. [57] measured the vapor pressure of $P_2(g)$ in equilibrium with the Mn_2P - MnP mixture using the mass-loss effusion (MLE) technique to determine the enthalpies of Mn_2P and MnP . They also assessed the standard entropies $S_{298.15 K}^{\circ}$ of Mn_2P and MnP based on the entropies of manganese silicides. Grandjean et al. [52] measured the heat capacity of Mn_2P at 5 to 350 K using an adiabatic calorimeter and determined $S_{298.15 K}^{\circ}$ of Mn_2P by integrating experimental C_p data of Mn_2P . Zaitsev et al. [37] conducted

Knudsen effusion experiments to measure the intensities of all ion species in the gas phase. The obtained entropies of Mn_3P , Mn_2P and MnP were determined based on their Gibbs energy and heat capacity data. Stolen et al. [51] obtained a value of $S_{298.15\text{ K}}^\circ = 24.48\text{ J/K-mol atoms}$ for MnP from the heat capacity data of MnP at 5 to 840 K using the adiabatic calorimetry method (ACM). As can be seen in **Fig. 4.5(b)**, the entropies of Mn_3P by Baratashvili et al. [54], Mn_2P and MnP by Baratashvili et al. [50], Myers et al. [57] and Stolen et al. [51] are apparently underestimated compared to the results by Grandjean et al. [52] and Zaitsev et al. [37], which are in reasonable agreement with the present calculations.

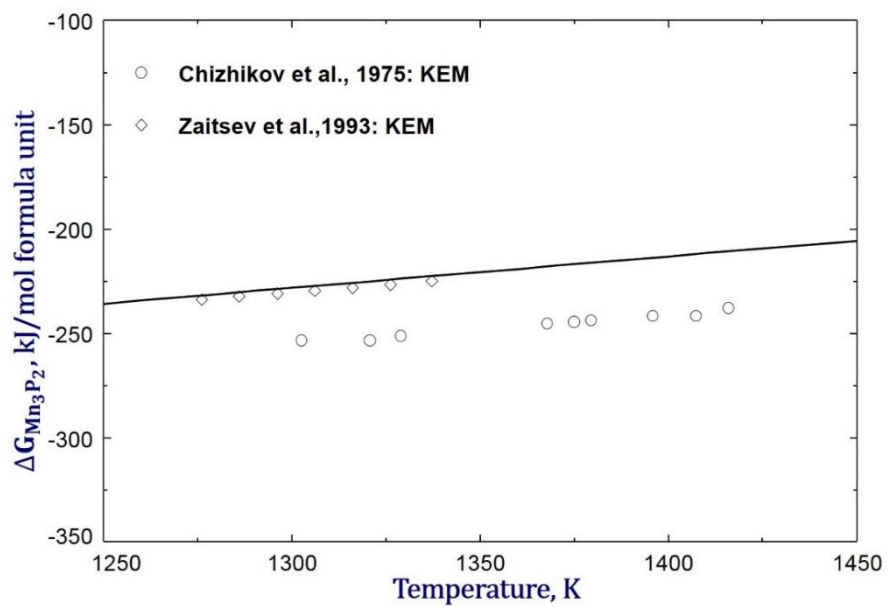
Fig. 4.6 shows variations of the Gibbs energy of formations of per mole of Mn_3P , Mn_2P , Mn_3P_2 and MnP with the temperature. Experimental studies on the Gibbs energy of manganese phosphides were performed by Chizhikov et al. [59], Myers et al. [58] and Zaitsev et al. [37] using the Knudsen effusion method (KEM). A maximum difference of about 27 kJ per mole formula unit exists between the Gibbs energy data for Mn_3P . Among all these data, those obtained from Knudsen effusion experiments by Zaitsev et al. [37] are favored in the present study.



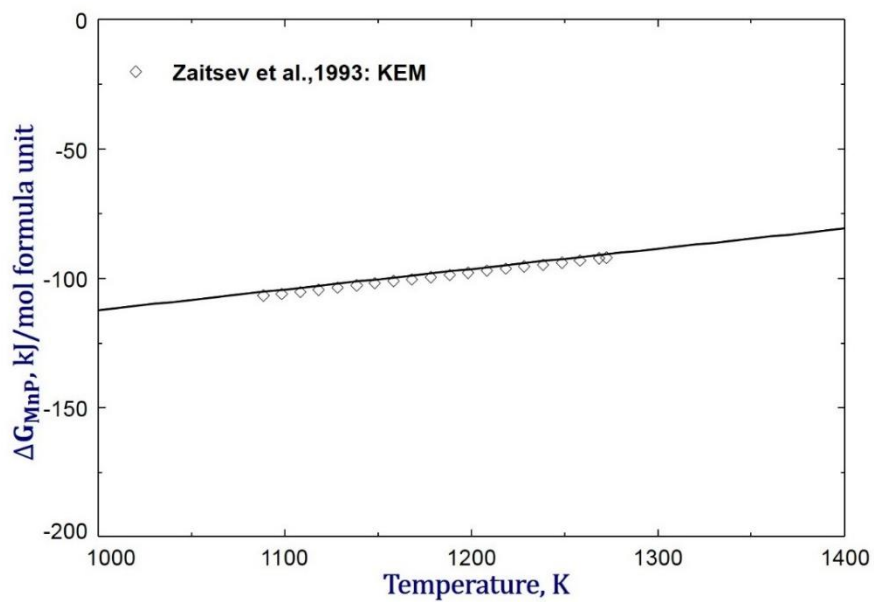
(a)



(b)



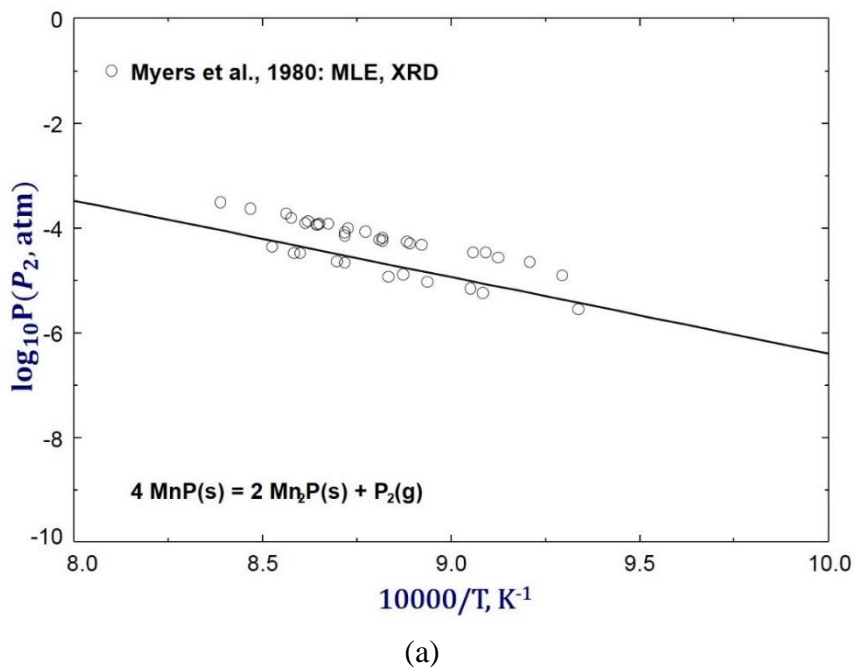
(c)

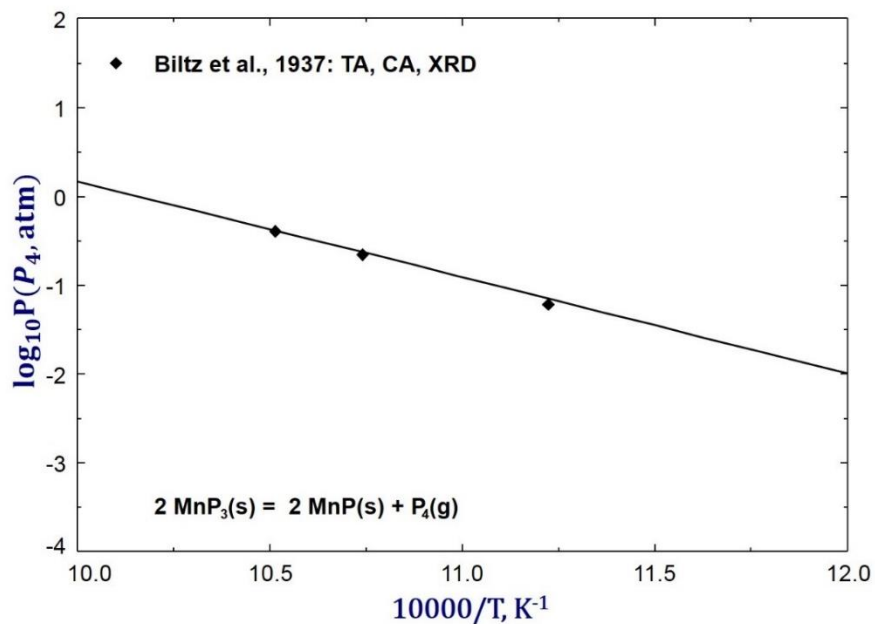


(d)

Figure 4.6 Gibbs energy of formations of (a) Mn_3P , (b) Mn_2P , (c) Mn_3P_2 , and (d) MnP from CUB-Mn and $\text{P}_2(\text{g})$

Myers et al. [57] carried out Mass-loss effusion (MLE) experiments on the reaction $4\text{MnP(s)} = 2\text{Mn}_2\text{P(s)} + \text{P}_2\text{(g)}$ in the temperature range of 1071 K to 1192 K. The variation of the equilibrium P_2 pressure with the temperature is plotted in **Fig. 4.7(a)** along with experimental data. The only available thermodynamic data for MnP_3 was reported by Biltz and Wiechmann [43] who synthesized MnP_3 from a mixture of Mn and red P. In the equilibrated specimen, a mixture of MnP_3 and MnP was detected and the partial pressure of P_4 gas above this solid mixture was measured. The obtained experimental results are compared with present calculation in **Fig. 4.7(b)**.





(b)

Figure 4.7 Calculated equilibrium vapor pressures of P₂ and P₄ gas of the reactions (a) 4MnP(s) = 2Mn₂P(s) + P₂(g) and (b) 2MnP₃(s) = 2MnP(s) + P₄(g), compared to experimental data [43,57]

In the present study, all the data [37,43,48-59] in **Fig. 4.4** to **4.7** were simultaneously optimized to obtain one set of parameters for all solid manganese phosphides.

4.3.3 The Fe-Mn-P System

In the ternary Fe-Mn-P system, solution phases including the liquid, BCC_A2, FCC_A1, CBCC_A12, CUB_A13 and mutually substitutional (Fe, Mn)₃P, (Fe, Mn)₂P, (Fe, Mn)P solid solutions, and stoichiometric compounds including FeP₂, Mn₃P₂ and MnP₃ were considered in the present study. Specially, the (Fe, Mn)₃P solid solution is formed with mutual dissolution of the isomorphous (Ni₃P type) Fe₃P and Mn₃P phases. Goto et al. [60] proposed the occurrence of an

ordered orthorhombic phase (τ_3) in the composition range of $0.3 < x_{Mn} < 0.7$ between tetragonal Fe_3P - and Mn_3P -based solid solution, which has not yet confirmed. In this work, partial dissolution between the isomorphous Fe_3P and Mn_3P in each other to form the discontinuous tetragonal $(Fe, Mn)_3P$ solution, instead of the ordered orthorhombic τ_3 phase, was taken into account to reproduce the available experimental data [61-63]. Likewise, the hexagonal $(Fe, Mn)_2P$ solid solution is formed with mutual dissolution between the isomorphous (Fe_2P -type) Fe_2P and Mn_2P in each other. Some researchers [64-71] reported an orthorhombic $FeMnP$ (τ_2) phase that demonstrates antiferromagnetic behavior in the composition between Fe_2P side and Mn_2P side of the $(Fe, Mn)_2P$ solution. According to the experiments conducted by Nowotny and Henglein [61] and Vogel and Berak [62], however, a continuous $(Fe, Mn)_2P$ solid solution throughout the composition from Fe_2P side to Mn_2P side was observed, which was favored in the present optimization. And also, the orthorhombic MnP -type $(Fe, Mn)P$ phase was also modeled as a continuous ideal solution in the present study, based on reported data [72-74].

4.3.3.1 Phase Diagram

Vogel and Berak [62] undertook the experimental investigation on the phase equilibria of the Fe-Mn-P system by means of the thermal analysis (TA), microscopic analysis (MA) and X-ray diffraction (XRD), including a series of vertical sections, an isothermal section at 20 °C as well as the liquidus surface projection. The experimental results of isopleths of $Fe_2P - Mn_2P$, wt. %Fe: wt. %Mn = 1: 9, 5: 5, 9: 1, 19: 1, and wt. %P = 1, 6, 12 are compared with the present calculations in **Fig. 4.8, 4.9, 4.10**, respectively. In the previous experiments, a full composition range of various FeMn alloys containing up to 25 wt.%P were used. As can be seen in the figure, all the experimental results are very well reproduced in this study.

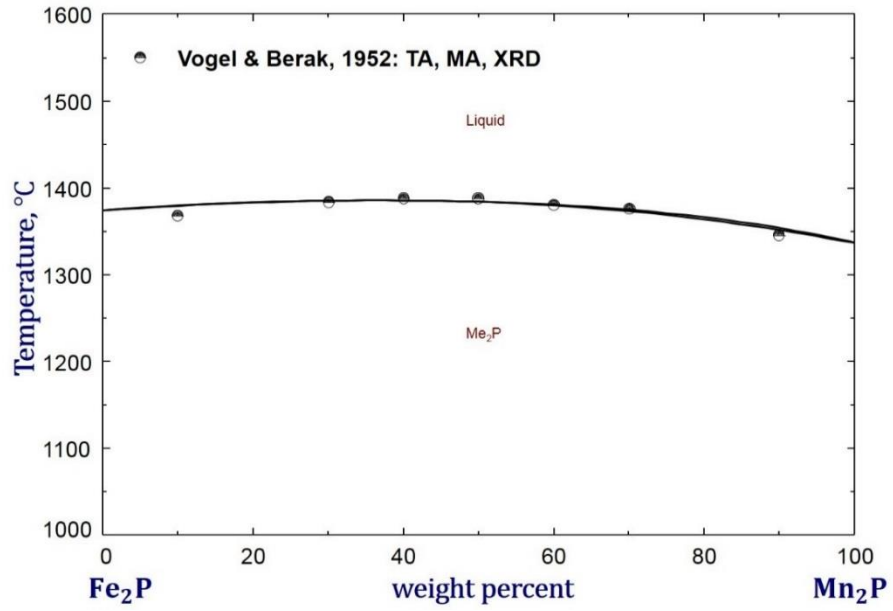
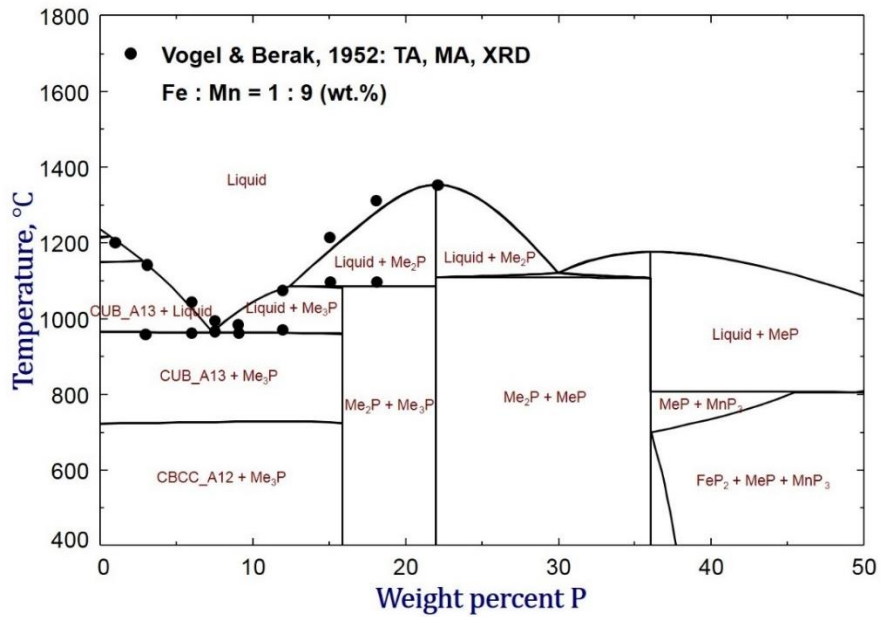
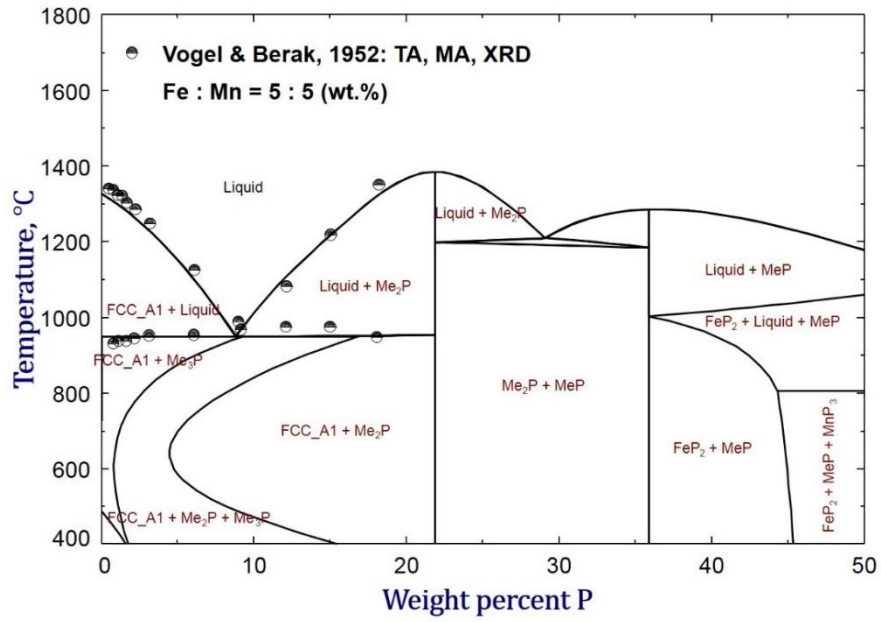


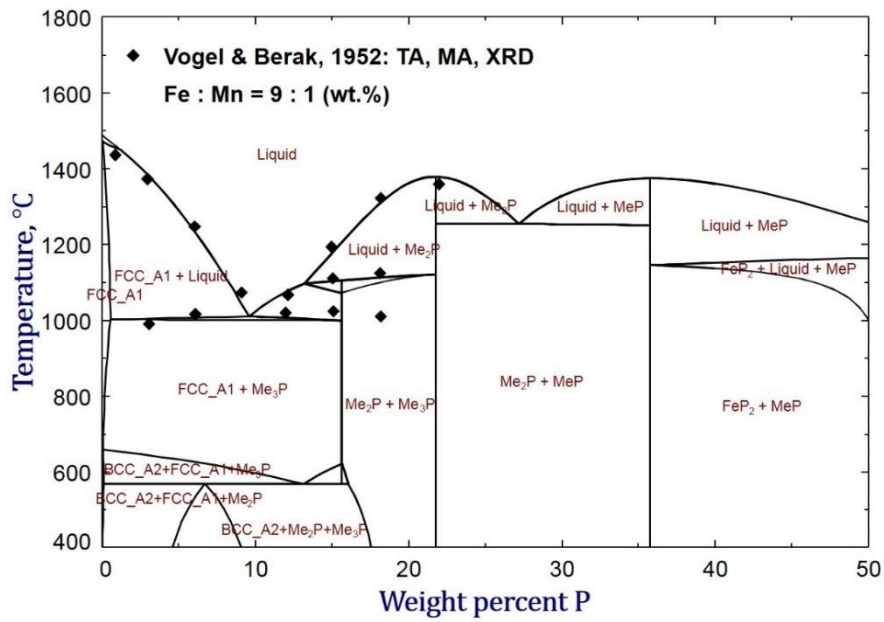
Figure 4.8 Calculated phase diagram of the Fe_2P - Mn_2P system, compared to experimental data[62]



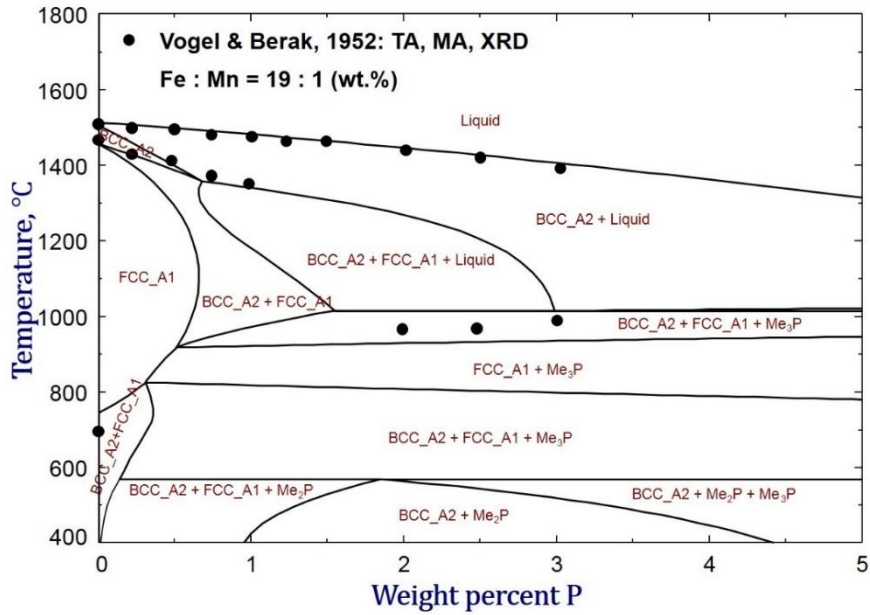
(a)



(b)

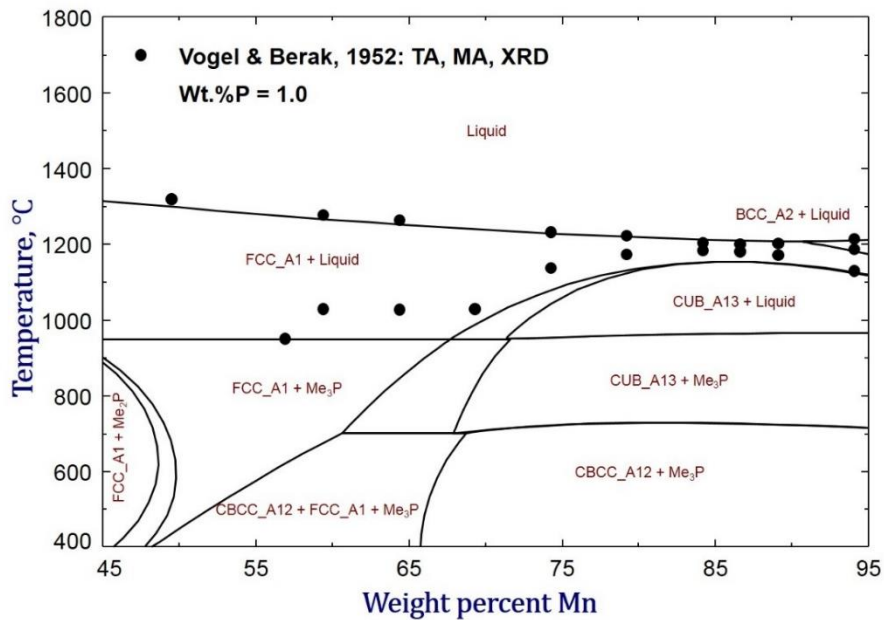


(c)

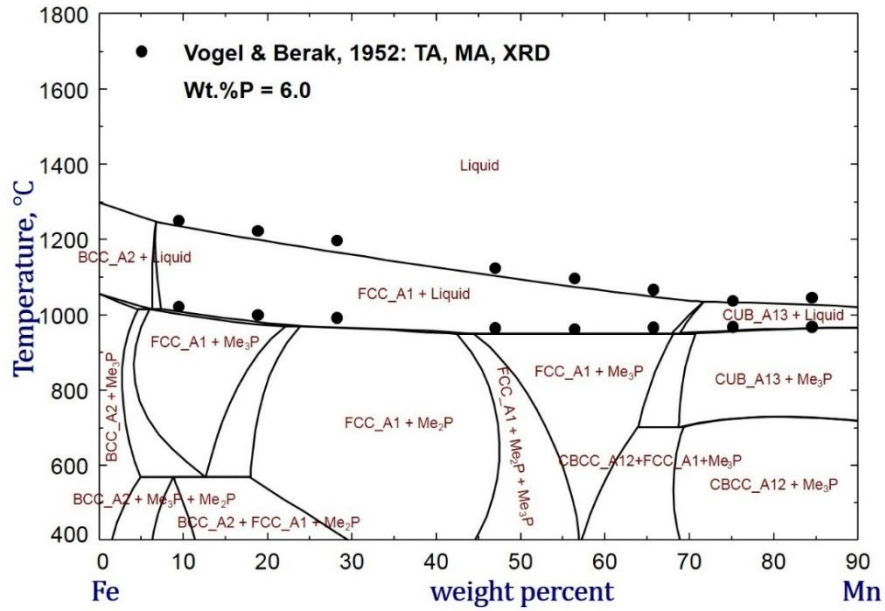


(d)

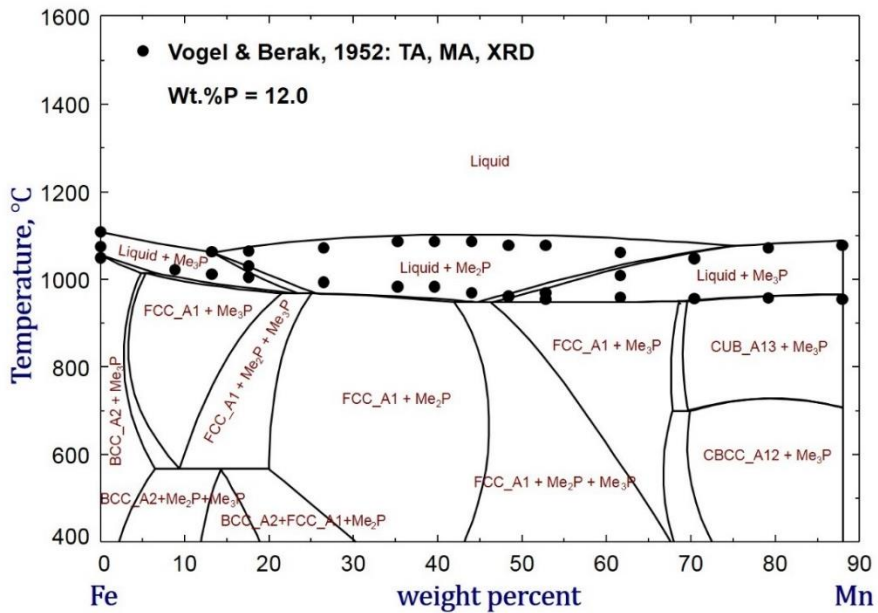
Figure 4.9 Calculated isopleths of the Fe-Mn-P system at mass ratios of (a) Fe: Mn = 1: 9, (b) Fe: Mn = 5: 5, (c) Fe: Mn = 9: 1, and (d) Fe: Mn = 19: 1, compared to experimental data [62]



(a)



(b)



(c)

Figure 4.10 Calculated phase diagrams of the Fe-Mn-P system at (a) wt. %P = 1, (b) wt. %P = 6, and (c) wt. %P = 12, compared to experimental data [62]

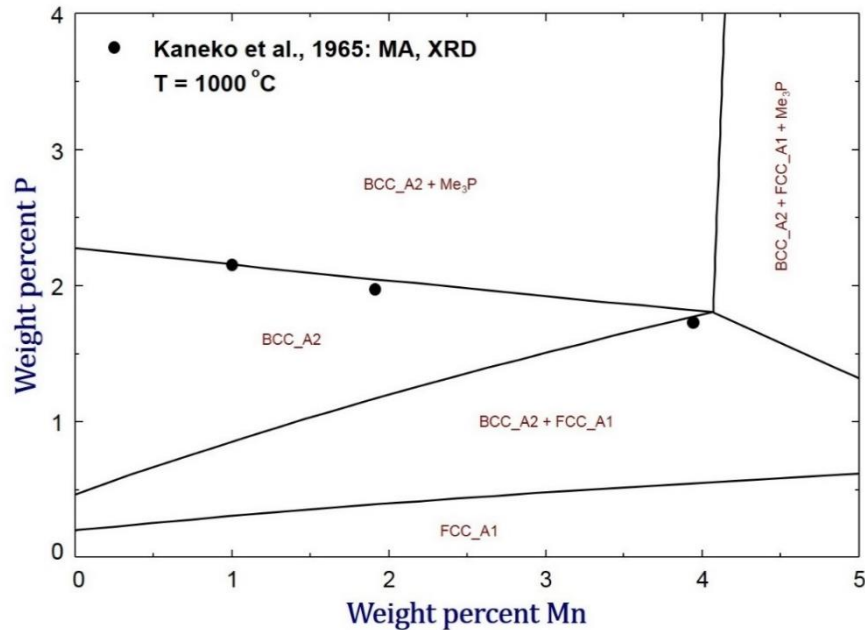


Figure 4.11 Calculated isothermal section in the Fe-rich region of the Fe-Mn-P system at 1000 °C, compared to experimental data [30]

Kaneko et al. [75] measured the solubility of P in ferrite Fe-Mn alloys, which are in equilibrium with the ternary phosphide Me₃P at 1000 °C. **Fig. 4.11** shows the isothermal phase diagram in the Fe-rich region at 1000 °C, compared to experimental data [75]. As can be seen in the figure, fairly good agreement was achieved between the present calculation and experimental results. The solubility of P in ferrite Fe decreases gradually from 2.28 to 1.80 in weight percent with the increase of Mn up to 4.0 in weight percent.

Kaneko et al. [63] studied the homogeneous range of Fe₃P with additional Mn. They found that the Fe₃P phase can dissolve at least 13.3 wt.% of Mn to form the Ni₃P-type (Fe, Mn)₃P solid solution at 800 °C. **Fig. 4.12** shows the calculated isothermal phase diagram of the Fe-Mn-P system at 800 °C, compared to the experimental data [63]. As can be seen in the diagram, the Me₃P solid

solution exhibits a miscibility gap, and the Me_2P solid solution appears as the primary crystalline phase at $\text{wt. \%Mn} = 10 - 75$ while the Me_3P solid solution is stable on the rest Fe-rich and Mn-rich sides, as also indicated in **Fig. 4.10(c)**. According to the present modeling, a maximum solubility of $\text{wt. \%Mn} = 13.37$ in Fe_3P and $\text{wt. \%Fe} = 28.80$ in Mn_3P at $800\text{ }^\circ\text{C}$ were calculated. However, no experimental data are available on the site of the miscibility gap of the Me_3P solid solution so far. On the other hand, the Me_2P and MeP are complete solid solutions. This is consistent with observations in the previous studies [61,63].

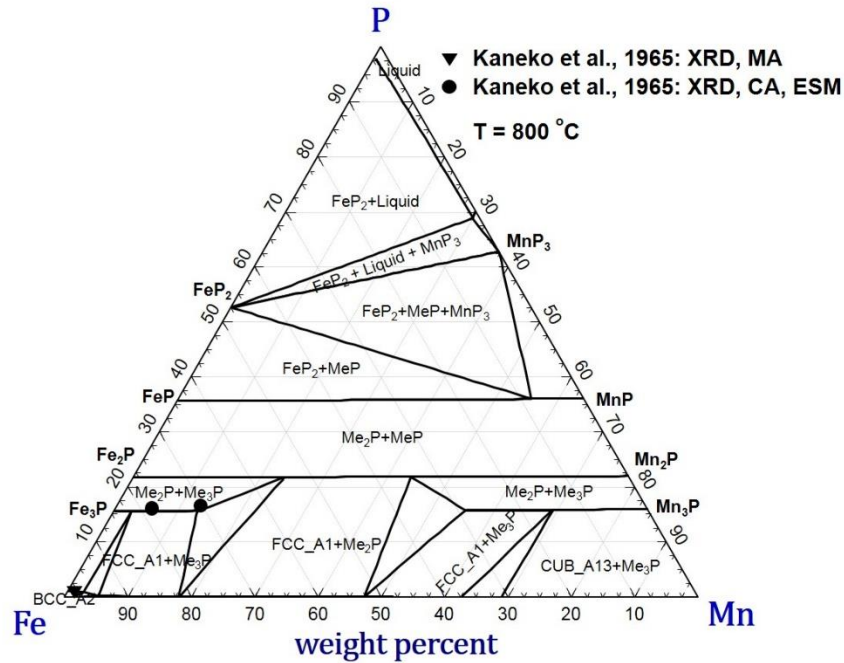


Figure 4.12 Isothermal phase diagram of the Fe-Mn-P system at $800\text{ }^\circ\text{C}$

The liquidus surface projection of the Fe-Mn-P system between $1000\text{ }^\circ\text{C}$ and $1500\text{ }^\circ\text{C}$ was predicted together with experimental results by Vogel and Berak [62] in **Fig 4.13**. The invariant reactions were summarized in **Table 4.4**. The calculated invariant points **U1**, **U2** and **U3** are well matching the data [62] within experimental errors. The calculated reaction $\text{L} + \text{CUB_A13} =$

$\text{Me}_2\text{P} + \text{FCC_A1}$ at point **U4** deviates from the reported experimental data [62]. The discrepancy in the CUB_A13 phase is accepted in the present study because the suggested experimental data for this reaction cannot be reproduced without sacrificing the accuracy of the binary Fe-Mn diagram or adding unreasonable ternary parameters. And also, another invariant point **Ux** representing the reaction $\text{L} + \text{FCC_Mn} = \text{CUB_A13} + \text{FCC_Fe}$ was reported by Vogel and Berak [62]. Occurrence of this reaction (**Ux**) can only be resulted from incomplete dissolution of FCC_A1 Fe-Mn solution, that is, FCC_Fe phase on the Fe-rich side is isolated from FCC_Mn phase on the Mn-rich side, which is apparently contradictory with the well-known Fe-Mn phase diagram. Therefore, the **Ux** point is not considered in the present study.

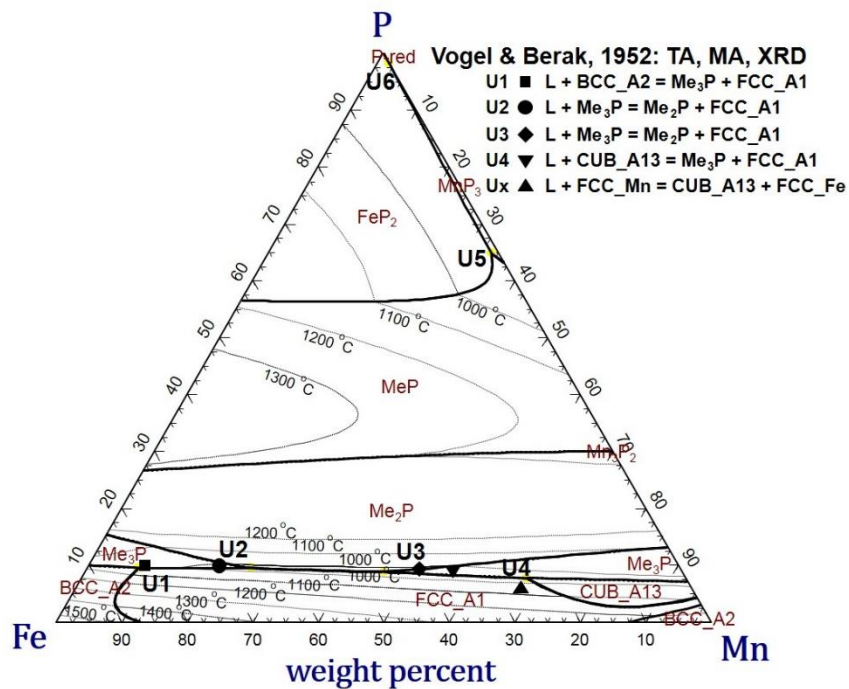


Figure 4.13 Liquidus surface projection of the Fe-Mn-P system between 1000 °C and 1500 °C, compared to experimental data [62]

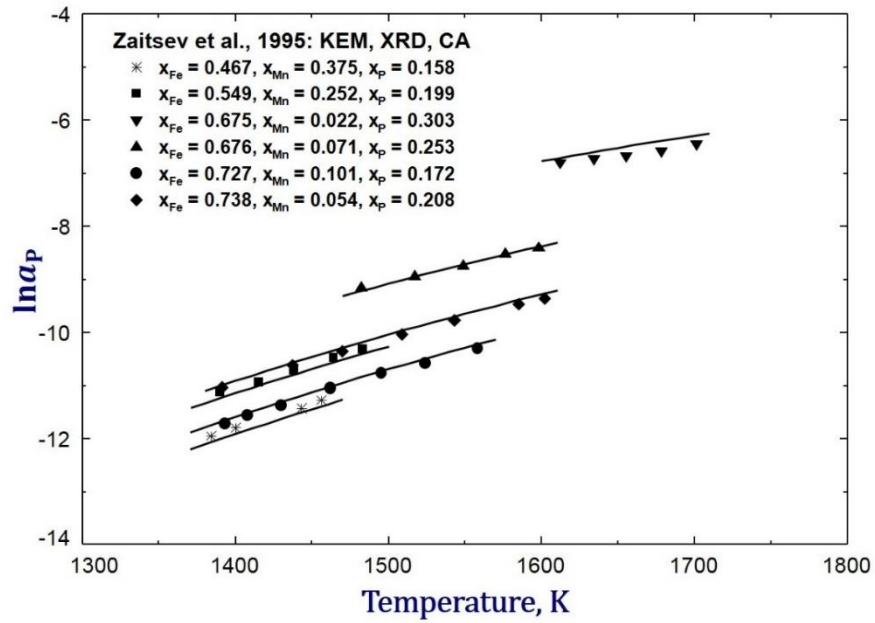
Table 4.4 Invariant reactions of the Fe-Mn-P system with experimental data [62]

Code	Reactions	Wt.%Fe	Wt%Mn	Wt.%P	T, °C
U1	L + BCC = Me ₃ P + FCC	82.64	7.79	9.57	1014
		~81.60	~8.5	~9.9	1025[62]
U2	L + Me ₃ P = Me ₂ P + FCC	65.49	25.05	9.46	968
		~70.1	~20	~9.9	1008[62]
U3	L + Me ₃ P = Me ₂ P + FCC	45.53	45.67	8.80	949
		~39.9	~50.8	~9.3	955[62]
U4	L + CUB_A13 = Me ₂ P + FCC	24.31	67.98	7.71	950
		~35	~56	~9.0	958[62]
Ux	L + FCC_Mn = CUB_A13 + FCC_Fe	26	68	6.0	1050[62]
U5	L + MnP ₃ = FeP ₂ + MeP	1.17	33.97	64.86	806
E6	L = Red_P + MnP ₃ + FeP ₂	0.07	1.58	98.35	576

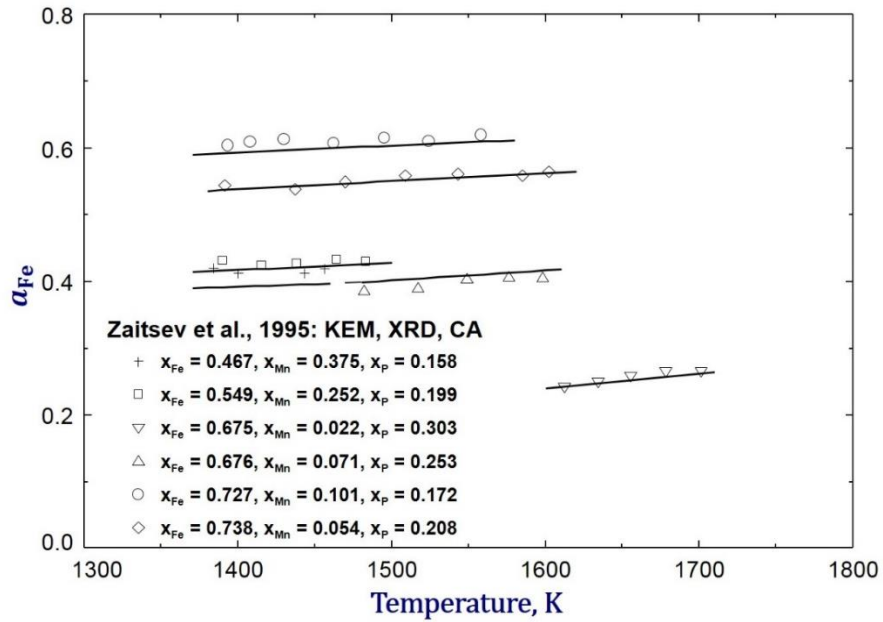
4.3.3.2 Thermodynamic Property of Liquid Solution

The binary parameters of liquid Fe-P, Mn-P and Fe-Mn solutions were combined to predict the ternary liquid Fe-Mn-P solution using the Toop-type interpolation technique [25] (P as an asymmetric component), without any additional ternary parameters, as presented in **section 4.3**. All available thermodynamic properties of the liquid solution are very well calculated.

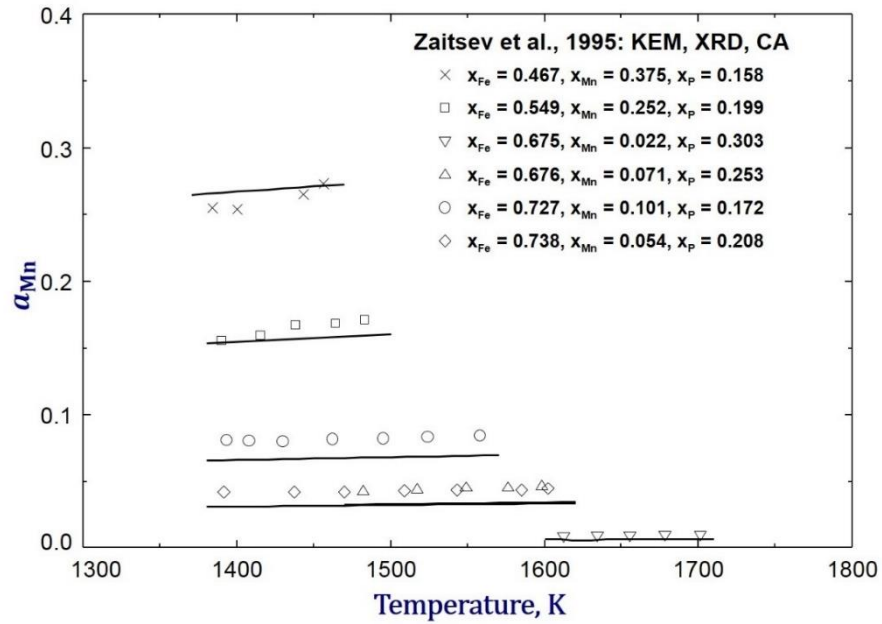
The activities of P, Fe and Mn in various compositions of the liquid solutions were measured by Zaitsev et al. [76,77] using the Knudsen effusion method (KEM). As shown in **Fig. 4.14**, the experimental data are predicted very accurately using the MQM in this study.



(a)

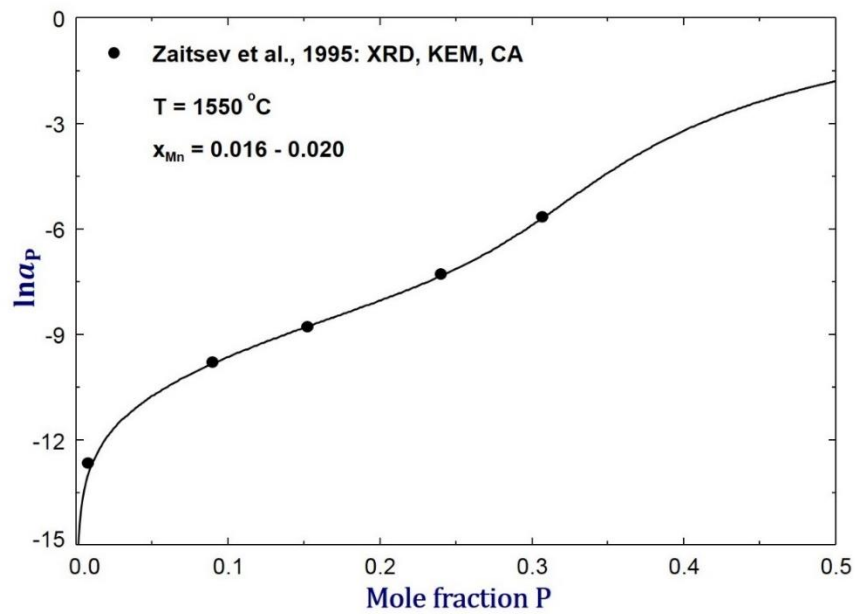


(b) Fe



(c)

Figure 4.14 Calculated activities (a) a_P^R , (b) a_{Fe}^R , and (c) a_{Mn}^R in various liquid Fe-Mn-P solutions, compared to experimental data [76]



(a)

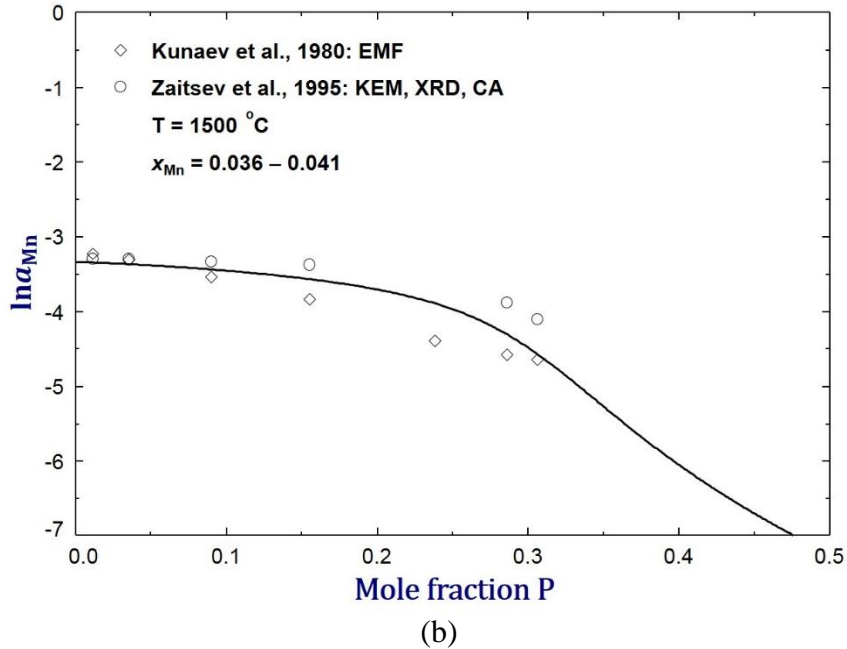


Figure 4.15 Calculated activities of (a) P(l) at $x_{\text{Mn}} = 0.016 - 0.20$ and $1550\text{ }^{\circ}\text{C}$, and (b) Mn(l) at $x_{\text{Mn}} = 0.036 - 0.041$ and $1500\text{ }^{\circ}\text{C}$ of the liquid Fe-Mn-P, compared to experimental data[76,78]

Fig 4.15 shows the variations of the activity of P(l) at $x_{\text{Mn}} = 0.016 - 0.02$ and $1550\text{ }^{\circ}\text{C}$, and Mn(l) at $x_{\text{Mn}} = 0.036 - 0.041$ and $1500\text{ }^{\circ}\text{C}$ respectively with the content of P. Both sets of experimental data [76,78] are well reproduced by the present calculations.

Schenck et al. [79] conducted experiments to measure the activity coefficient of P in the Fe melts with the added Mn up to $x_{\text{Mn}} = 0.167$ at $1550\text{ }^{\circ}\text{C}$ using X-ray fluorescence (XRF) and chemical analysis (CA). Ban-ya et al. [80] measured the partial pressure of P_2 in equilibrium with the liquid Fe-Mn-P at $1400\text{ }^{\circ}\text{C}$ using the transportation method (TM). According to the experimental results, effect of Mn on the activity coefficient of P(l) are presented in **Fig. 4.16**. A significant deviation exhibits between two data sets. Only the data by Schenck et al. [79] were well reproduced and an

interaction parameter $\varepsilon_P^{\text{Mn}} = -0.287$ at 1550 °C was calculated based on the present database. The results of Ban-ya et al. [80] were not favored because they assumed only $\text{P}_2(\text{g})$ in the gas phase. However, high vaporization of Mn ($P_{\text{Mn}(\text{g})} = 1.706 \times 10^{-3}$ atm above the Fe – Mn alloys at $x_{\text{Mn}} = 0.2$ and 1400 °C) can occur and other gaseous P species, such as $\text{P}(\text{g})$ and $\text{P}_4(\text{g})$, can be formed as well. According to the present calculations, the partial pressures of $\text{P}(\text{g})$ and $\text{P}_4(\text{g})$ are 1.951×10^{-8} atm and 1.091×10^{-14} atm respectively at $x_P = 0.2$ and 1400 °C. In addition, their results [81,82] for the binary Fe-P liquid solution were also not reliable, as discussed in the previously published paper [22].

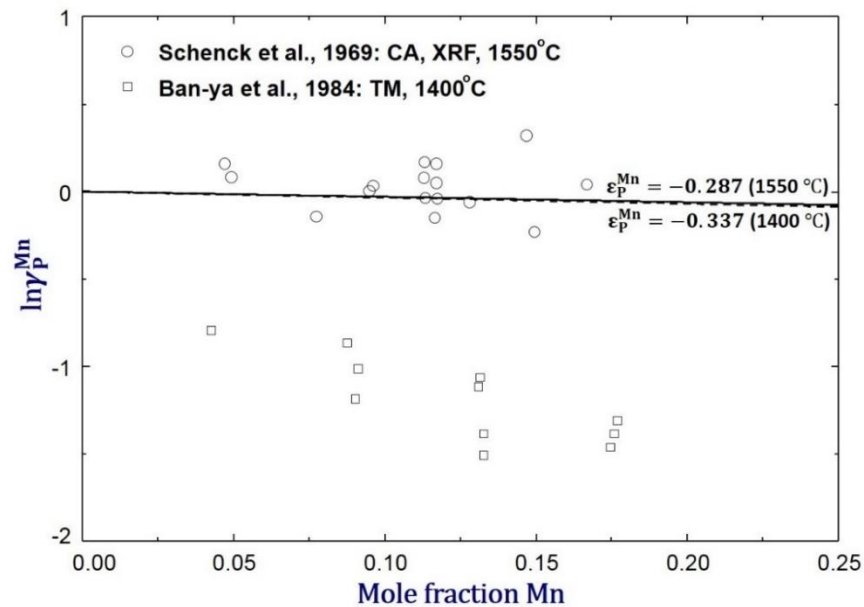


Figure 4.16 Effect of Mn on the activity coefficient of P in the liquid Fe-Mn-P solution at 1400 °C and 1550 °C, compared to experimental data [79,80]

The thermodynamic properties of P in the liquid Fe-Mn is of great importance for understanding the behavior of P in high Mn steels as well as ferromanganese (FeMn) alloys. With the increasing demand for high quality steel, tight control of P becomes very critical. Since P is always very dilute

in both high Mn steels and Mn alloys, so the Henrian activity coefficient of P, γ_P^0 , is a key parameter for the dephosphorization calculations. The γ_P^0 in the binary Fe-P [22] and Mn-P liquids have been discussed previously. The γ_P^0 in the ternary liquid Fe-Mn-P solution was calculated in the temperature range of 1400 °C to 1700 °C and plotted in **Fig. 4.17**. As shown in the figure, the γ_P^0 decreases with the increase of the Mn content. The difference between γ_P^0 in Fe and γ_P^0 in Mn is about 0.5 in logarithmic scale, and it becomes bigger with the decrease of the temperature.

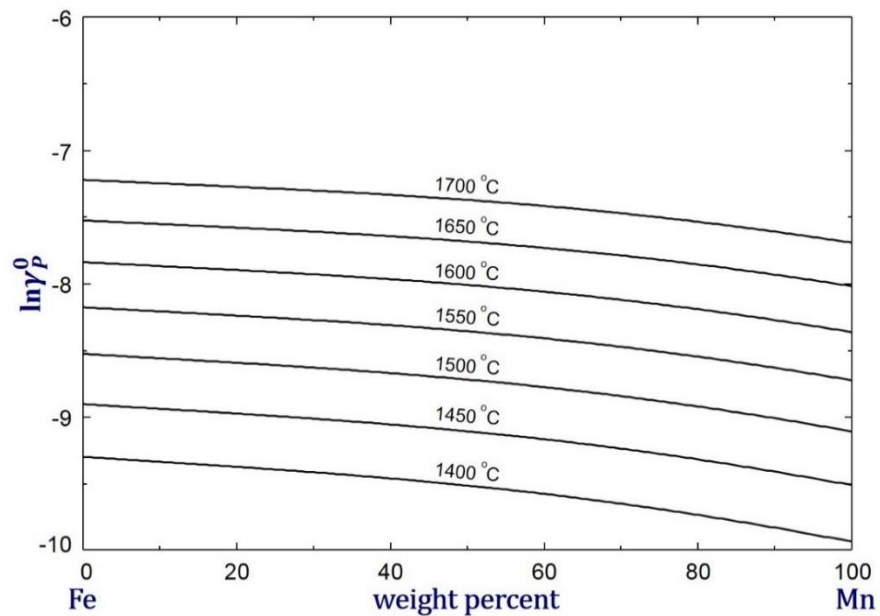
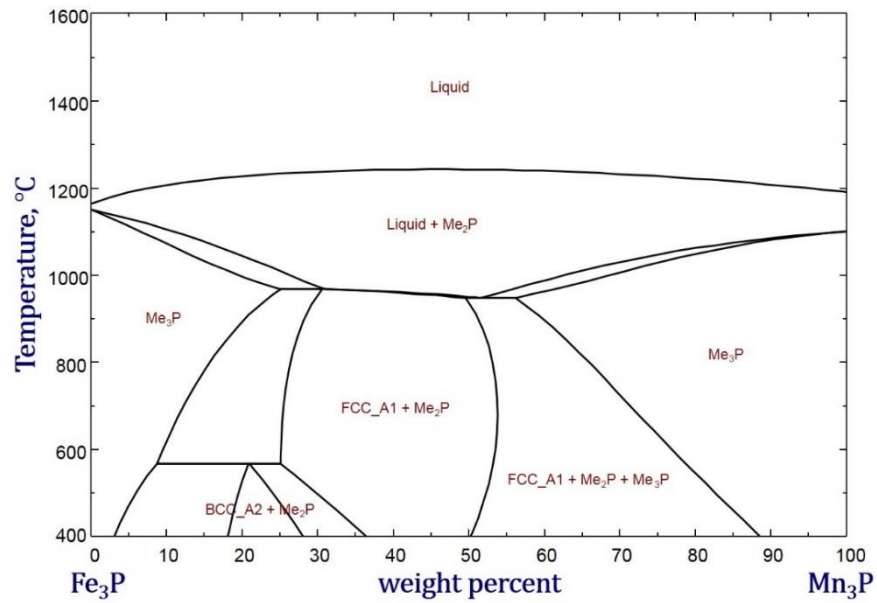


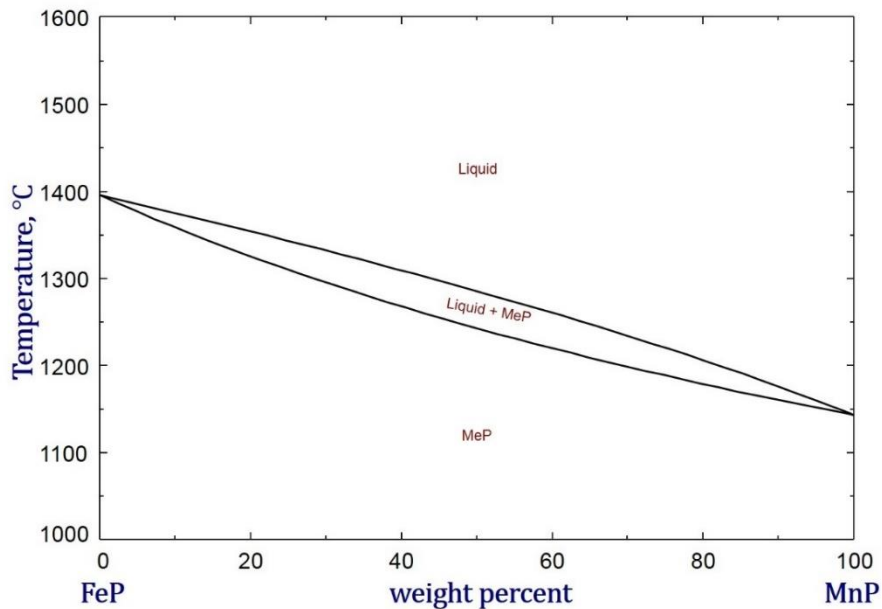
Figure 4.17 Predicted Henrian activity coefficient of P in the Fe-Mn melts at 1400 °C to 1700 °C

4.3.3.3 Predicted Phase Diagrams of the Fe-Mn-P System

According to the thermodynamic modeling with optimized model parameters, the phase diagrams of the Fe₃P – Mn₃P system and the FeP – MnP system with gas phase suppression are predicted in **Fig. 4.18**. As can be seen in the figure, Fe₃P and Mn₃P are partially soluble in each other while FeP and MnP are completely soluble in each other below the melting point of MnP (1143 °C).



(a)

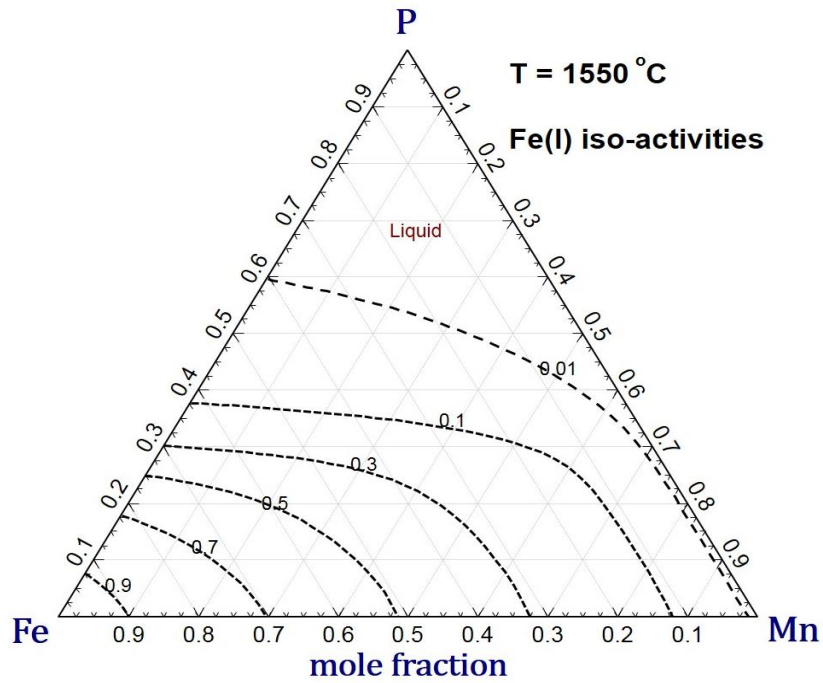


(b)

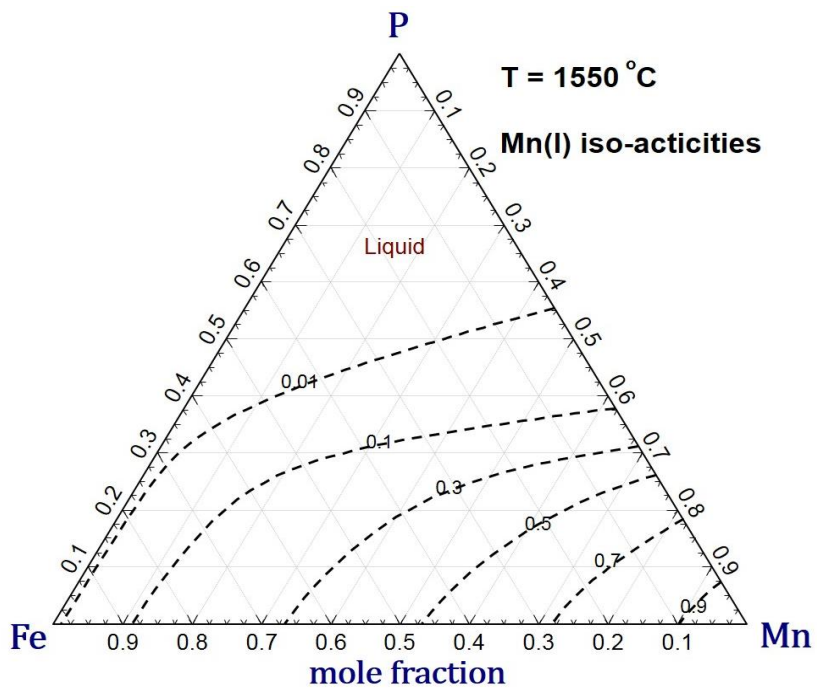
Figure 4.18 Predicted phase diagrams of the (a) Fe₃P-Mn₃P system and (b) FeP-MnP system

The iso-activity contours of Fe, Mn and P in pure liquid standard state at 1550 °C are predicted in **Fig. 4.19**. As shown in the figure, the iso-activities at 0.01, 0.1, 0.3, 0.5, 0.7 and 0.9 are plotted for

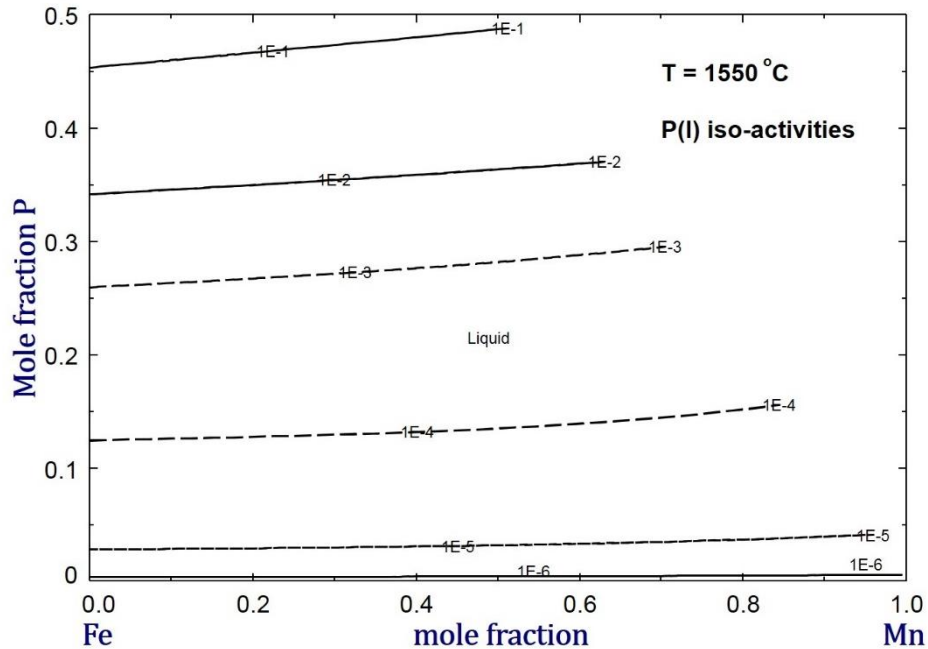
Fe(l) and Mn(l), and the iso-activities at 1×10^{-6} , 1×10^{-5} , 1×10^{-4} , 1×10^{-3} , 1×10^{-2} and 1×10^{-1} are plotted for P(l).



(a)



(b)



(c)

Figure 4.19 Predicted iso-activity contours of (a) Fe(l), (b) Mn(l), and (c) P(l) of the liquid Fe-Mn-P solution at 1550 °C

4.3.3.4 Improvements of Present Optimization Compared to Previous Assessments

Compared to previous assessments on the Mn-P system [12,13,23] and Fe-Mn-P system [14,23], some improvements have been achieved in the present thermodynamic optimization. In the Mn-P system, the phase diagram of the composition range over $x_P > 0.5$ were calculated based on consistent descriptions of the liquid solution and thermodynamic properties of all stoichiometric compounds (Mn_3P , Mn_2P , Mn_3P_2 , MnP and MnP_3). In the assessments of the Fe-Mn-P system by Tokunaga et al. [14] and Miettinen and Vassilev [23], many big parameters have to be added for the liquid solution to reproduce available experimental data in the literature. However, thermodynamic properties of each component in the liquid Fe-Mn-P solution and various isopleths

and isothermal phase diagrams were accurately predicted without any parameters based on the present database, compared to experimental results.

4.4 Summary

The binary Mn-P system and ternary Fe-Mn-P system in the full composition range were thermodynamically optimized based on the critical evaluation of available thermodynamic and phase equilibria data. The Modified Quasichemical Model (MQM) and Compound Energy Formalism (CEF) were used to model the liquid and solid solutions, respectively. The activities of P, Fe and Mn in the liquid solution and various phase diagrams were accurately predicted by combining the binary parameters and the Toop-type interpolation technique (P as an asymmetric component), without any ternary liquid parameters. Besides, the discrepancies left in the Mn-P system and Fe-Mn-P system were resolved with very few model parameters. In the present study, a more accurate and consistent thermodynamic database has been developed for describing the behavior of the Fe-Mn-P system.

Acknowledgments

We gratefully acknowledge the Steelmaking Consortium Members, Hyundai Steel, Tata Steel Europe, Posco, Doosan Heavy Industry and Construction, Nucor Steel, RioTinto Iron and Titanium, JFE Steel, Nippon Steel Corp., RHI-Magnesita, Voestapine, SeAH Besteel, and Natural Science and Engineering Research Council of Canada for supporting the present project. This work was also supported by the National Research Foundation of Korea (NRF) grant funded by the Korean government (MSIT) (No. NRF-2020R1A5A6017701). We would also like to thank the McGill Engineering Doctorate Award (MEDA) program.

References

1. J. Safarian and L. Kolbeinsen, Purity Requirements for Mn-alloys for Producing High Manganese Trip and Twip Steels, *Infacon XIII, Thirteenth International Ferroalloys Congress, Almaty, Kazakhstan, 9-12 June 2013*, p 175-184.
2. H. Okamoto, The Fe-P (Iron-Phosphorus) System, *Bull. Alloy Phase Dia.*, 1990, 11(4), p 404-412.
3. M. E. Schlesinger, The Thermodynamic Properties of Phosphorus and Solid Binary Phosphides, *Chemical Reviews*, 2002, 102(11), p 4267-4302.
4. M. Hansen. and K. Anderko, Constitution of Binary Alloys. Mn-P Manganese-Phosphorus, *McGraw-Hill Book Company, Inc., New York Toronto, London*, 1958, p 941-943.
5. V. Raghavan, Phase Diagrams for Ternary Iron Alloys, Part 3, *Indian Institute of Metals, Calcutta*, 1988, p 91-99.
6. K. Korniyenko, Ternary Alloy System, Phase Diagrams, Crystallographic and Thermodynamic Data: Iron-Manganese-Phosphorus, *Group IV Physical Chemistry*, 2017, 11, p 200-219.
7. P. Gustafson, Internal Report IM-2549, *Swedish Institute for Metals Research*, Stockholm, Sweden, 1990.
8. J. H. Shim, C. S. Oh, and D. N. Lee, Thermodynamic Properties and Calculation of Phase Diagram of the Fe-P System, *J. Korean. Inst. Met. Mater.*, 1996, 34(11), p 1385-1393.
9. H. Ohtani, N. Hanaya, M. Hasebe, S. I. Teraoka, and M. Abe, Thermodynamic Analysis of the Fe-Ti-P Ternary System by Incorporating First-principles Calculations into the CALPHAD Approach, *CALPAHD*, 2006, 30(2), p 147-158.

10. Z. M. Cao, K. P. Wang, Z. Y. Qiao, and G. W. Du, Thermodynamic Reoptimization of the Fe-P System, *Acta Phys. Chim. Sinica*, 2012, 28(1), p 37-43.
11. Z. M. Cao, W. Xie, K. P. Wang, C. J. Niu, G. W. Du, and Z. Y. Qiao, Thermodynamic Optimization of the Al-Fe-P Ternary System, *Acta Phys. Chim. Sinica*, 2013, 29(10), p 2148-2156.
12. Y. E. Lee, Thermodynamics of the Mn-P System, *Metall. Trans. B*, 1986, 17(4), p 777-783.
13. J. Miettinen, Thermodynamic Solution Phase Data for Binary Mn-based Systems, *CALPHAD*, 2001, 25(1), p 43-58.
14. T. Tokunaga, N. Hanaya, H. Ohtani, and M. Hasebe, Thermodynamic Analysis of the Fe-Mn-P Ternary Phase Diagram by Combining the First-Principles and CALPHAD Methods, *Materials Science Forum*, 2007, 561-565, p 1899-1902.
15. L. Kaufman, Coupled Phase Diagrams and Thermochemical Data for Transition Metal Binary Systems-III, *CALPHAD*, 1978, 2(2), p 117-146.
16. W. Huang, An Assessment of the Fe-Mn System, *CALPHAD*, 1987, 11(2), p 183-186.
17. W. Huang, An Assessment of the Fe-Mn System, *CALPHAD*, 1989, 13(3), p 243-252.
18. B. J. Lee and D. N. Lee, A Thermodynamic Study on the Mn-C and Fe-Mn Systems, *CALPHAD*, 1989, 13(4), p 345-354.
19. V. T. Witusiewicz, F. Sommer, and E. J. Mittemeijer, Reevaluation of the Fe-Mn Phase Diagram, *J. Phase Equilib. Diffu.*, 2004, 25(4), p 346-354.
20. D. Djurovic, B. Hallstedt, J. Von Appen, and R. Dronskowski, Thermodynamic Assessment of the Fe-Mn-C System, *CALPHAD*, 2001, 35(4), p 479-491.
21. S. Bigdeli and M. Selleby, A Thermodynamic Assessment of the Binary Fe-Mn System for the Third Generation of Calphad Databases, *CALPHAD*, 2019, 64, p 185-195.

22. Z. M. You and I. H. Jung, Critical Evaluation and Optimization of the Fe-P System, *Metall. Mater. Trans. B*, 2020. (published DOI: <https://doi.org/10.1007/s11663-020-01939-0>).
23. J. Miettinen and G. Vassilev, Thermodynamic Description of Ternary Fe-X-P Systems. Part 3: Fe-Mn-P, *J. Phase Equilib. Diffu.*, 2014, 35(4), p 587-594.
24. D. Pelton, S. A. Degterov, G. Eriksson, C. Robelin, and Y. Dessureault, The Modified Quasichemical Model I-Binary Solutions, *Metall. Mater. Trans. B*, 2000, 31(4), p 651-659.
25. D. Pelton and P. Chartrand, The Modified Quasi-chemical Model: Part II. Multicomponent Solutions, *Metall. Mater. Trans. A*, 2001, 32(6), p 1355-1360.
26. M. Hillert, The Compound Energy Formalism, *J. Alloys Compound*, 2001, 320(2), p 161-176.
27. M. K. Paek, S. Chatterjee, J. J. Pak, and I. H. Jung, Thermodynamics of Nitrogen in Fe-Mn-Al-Si-C Alloy Melts, *Metall. Mater. Trans. B*, 2016, 47(2), p 1243-1262.
28. W. Bale, P. Chartrand, S. A. Degterov, G. Eriksson, K. Hack, R. B. Mahfoud, and S. Petersen, FactSage Thermochemical Software and Databases, *CALPHAHD*, 2002, 26(2), p 189-228.
29. T. Dinsdale, SGTE Data for Pure Elements, *CALPHAD*, 1991, 15(4), p 317-425.
30. J. Leitner, P. Vončka, D. Sedmidubsky, and P. Svoboda, Application of Neumann-Kopp Rule for the Estimation of Heat Capacity of Mixed Oxides, *Thermoch. Acta*, 2010, 497(1-2), p 7-13.
31. G. Inden, Project Meeting CALPHAD V, Max-Planck-Inst, *Eisenforschung*, Dusseldorf, Germany, 1976, p 111.
32. M. Hillert and M. Jarl, A Model for Alloying in Ferromagnetic Metals, *CALPHAHD*, 1978, 2(3), p 227-238.

33. E. Schurmann, H. P. Kaiser, and U. Hensgen, Calorimetry and Thermodynamics of the System Iron-Phosphorus, *Arch. Eisen.*, 1981, 52(2), p 51-55.
34. V. Ya. Dashevskii, V. I. Kashin, N. I. Rakitina, and M. S. Ageev, Study of the Thermodynamic Properties of Solutions of Phosphorus in Molten Manganese, *Zakonomern. Vzaimodeistviya Zhidk. Met. Gazami Shlakami*, Nauka, 1976, p 109-113.
35. G. I. Batalin, V. A. Stukalo, and N. Ya. Neshchimenko, Thermodynamic Activity of Phosphorus in Molten Alloys of Manganese with Phosphorus, *Ukrainskii Khimicheskii Zhurnal*, 1977, 43(6), p 602-604.
36. G. I. Batalin, V. A. Stukalo, N. Ya. Neshchimenko, V. A. Lizogub, and V. S. Ignat'ev, Study of Thermodynamic Activity of Phosphorus in Manganese-base Molten Alloys, *Vosstanovit. Protsessy v Proiz-ve Ferrosplavov*, 1977, p 45-48.
37. A. I. Zaitsev, M. A. Zemchenko, A. D. Litvina, and B. M. Mogutnov, Thermodynamic Properties of Mn-P Alloys, *Z. Metall.*, 1993, 84(3), p 178-184.
38. S. Žemčuzny and N. Eefremow, Phosphide des Mangans, *Z. Anorg. Chem.*, 1908, 57(1), p 241-252.
39. F. Wiechmann, The Systematic Study of Affinity. LXXVII. The Lower Phosphides of Manganese. Thermal Analysis of the System Manganese-Manganese Monophosphide, *Z. Anorg. Allgem. Chem.*, 1937, 234, p 130-141.
40. J. Berak and T. Heumann, The System Manganese-Phosphorus, *Z. Metallkd.*, 1950, 41(1), p 19-23.
41. C. Sugiura, Phosphorus K β X-Ray Emission Spectra and Valence-Band Structures of Transition-Metal Phosphides and GaAs_{1-x}P_x, *J. Phys. Soc. Japan*, 1996, 65(7), p 2170-2177.

42. G. Z. Shen, Y. Bando, C. H. Ye, X. L. Yuan, T. Sekiguchi, and D. Golberg, Single-Crystal Nanotubes of II3-V2 Semiconductors, *Ang. Chem. Int. Edition*, 2006, 45(45), p 7568-7572.
43. W. Biltz, F. Wiechmann, and K. Meisel, The Systematic Study of Affinity. LXXVI. Tensiometric Analysis of the Higher Phosphides of Manganese, *Z. Anorg. Allgem. Chem.*, 1937, 234(2), p 117-129.
44. W. Jeitschko and P. C. Donohue, High-pressure MnP_4 , a Polyphosphide with Mn-Mn Pairs, *Acta Crystall. Section B: Struc. Crystall. Crystal Chem.*, 1975, 31(2), p 574-580.
45. D. J. Braun and W. Jeitschko, Polyphosphides of Chromium, Manganese, Ruthenium, and Osmium. Synthesis and Crystal Structure of Ruthenium Phosphide (RuP_4) and Osmium Phosphide (OsP_4), *Z. Anorg. Allgem. Chem.*, 1978, 445, p 157-66.
46. R. Rühl and W. Jeitschko, Stacking Variants of MnP_4 : Preparation and Structure of 6- MnP_4 , *Acta Crystall. Section B: Struc. Crystall. Crystal Chem.*, 1981, 37(1), p 39-44.
47. D. B. Henge, M. Hermus, C. F. Litterscheid, N. Wagner, J. Beck, B. Albert, and J. Brgoch, Discovery of $\gamma\text{-MnP}_4$ and the Polymorphism of Manganese Tetrphosphide, *Inorg. Chem.*, 2015, 54(17), p 8761-8768.
48. I. A. Makharadze, I. B. Baratashvili, D. Sh. Tsagareishvili, and G. G. Gvelesiani, Enthalpy and Specific Heat of Manganese Phosphides at High Temperatures, *Izvestiya Akademii Nauk SSSR, Neorganicheskie Materialy*, 1975, 11(4), p 599-601.
49. V. P. Krasovskii and I. G. Fakidov, Heat Capacity of the Manganese Monophosphide, MnP , *Fizika Metallov i Metallovedenie*, 1961, 11, p 477-479.
50. I. B. Baratashvili, I. A. Makharadze, V. S. Varazashvili, M. S. Tsarakhov, D. Sh. Tsagareishvili, Standard Entropies of Manganese Phosphides MnP and Mn_2P , *Soobshcheniya Akademii Nauk Gruzinskoi SSR*, 1977, 85(3), p 625-628.

51. S. Stølen, F. Grønvold, H. O. Haakonsen, J. T. Sipowska, and Jr. E. F. Westrum, Heat Capacity and Thermodynamic Properties of Manganese Monophosphide at Temperatures from 5 K to 840 K: Transitions, *J. Chem. Thermody.*, 1998, 30(1), p 117-127.
52. F. Grandjean, D. W. Osborne, W. G. Lyon, and H. E. Flotow, Dimanganese Phosphide, Mn_2P : Heat Capacity from 5 to 350 K, Magnetic Entropy, and Thermodynamic Functions to 1300 K, *J. Chem. Thermody.*, 1977, 9(6), p 549-559.
53. S. Shchukarev, T. A. Stolyarova, and M. P. Morozova, Enthalpy of Formation of Compounds by Manganese with Elements of Main Sub-group Of V Group, *Zhurnal Obshchei Khimii*, 1961, 31(6), p 1773-1777.
54. I. B. Baratashvili, D. Sh. Tsagareishvili, and I. N. Dashniani, Gibbs Free Energy of Formation of Manganese Phosphide (Mn_3P), *Soobshcheniya Akademii Nauk Gruzinskoi SSR*, 1980, 99(1), p 121-123.
55. I. B. Baratashvili, A. A. Nadiradze, I. A. Makharadze, and L. A. Shvartsman, Investigation of Thermodynamic Properties of Manganese Phosphide, Mn_2P , *Doklady Akademii Nauk SSSR*, 1975, 224(4), p 844-846.
56. C. E. Myers and D. J. Simpson, Thermodynamic Stability of Manganese Phosphides from High Temperature Solid-State Galvanic Cells, *J. Electrochem. Soc.*, 1984, 131(5), p 1179-1181.
57. C. E. Myers, E. D. Jung, and E. L. Patterson, Vaporization Behavior of $MnP(s)$ and the Thermodynamics of the Mn-P System, *Inorg. Chem.*, 1980, 19(2), p 532-534.
58. C. E. Myers, G. A. Kisacky, E. L. Patterson, and R. A. Mevorach, The Congruent Vaporization of $Mn_2P(s)$, *J. Electrochem. Soc.*, 1982, 129(10), p 2343-2346.

59. D. M. Chizhikov, V. I. Kashin, E. Kazenas, V. K. Tagirov, V. Ya. Dashevskii, N. I. Rokitina, High-Temperature Mass-Spectrometric Study of the Vaporization of Manganese-Phosphorus Alloys, *Izvestiya Akademii Nauk SSSR, Metally*, 1975, (5), p 64-68.
60. M. Goto, H. Tange, T. Tokunaga, H. Fujii, and T. Okamoto, Magnetic Properties of the $(\text{Fe}_{1-x}\text{M}_x)_3\text{P}$ Compounds, *Japan. J. Applied Phys.*, 1977, 16(12), p 2175-2179.
61. H. Nowotny and E. Henglein, Ternary Phosphorus Alloys, *Monatsh. Chem.*, 1948, 79, p 385-393.
62. R. Vogel and J. Berak, The System Iron-Phosphorus-Manganese, *Arch. Eisen.*, 1952, 23(5-6), p 217-223.
63. H. Kaneko, Phosphide-Phases in Ternary Alloys of Iron, Phosphorus and Other Elements, *J. Japan Inst. Metals*, 1965, 29, p 159-165.
64. R. Fruchart, A. Roger, and J. P. Senateur, Crystallographic and Magnetic Properties of Solid Solutions of the Phosphides M_2P , $\text{M} = \text{Cr}, \text{Mn}, \text{Fe}, \text{Co}, \text{and Ni}$, *J. Applied Phys.*, 1969, 40(3), p 1250-1257.
65. A. Roger, J. P. Senateur, and R. Fruchart, Crystallographic and Magnetic Properties of Solid Solutions Among the Phosphides $\text{Ni}_2\text{P}-\text{Co}_2\text{P}-\text{Fe}_2\text{P}-\text{Mn}_2\text{P}$ and Cr_2P , *Ann. Chim.*, 1969, 4(2), p 79-91.
66. A. Nylund, A. Roger, J. P. Senateur, and R. Fruchart, R. Structural Transitions between Phosphorus, Arsenides and Arsenophosphides of Composition M_2P , M_2As and $\text{M}_2(\text{P}_{1-x}\text{As}_x)$, *Monatshefte fur Chemie*, 1971, 102(5), p 1631-1642.
67. S. Nagase, H. Watanabe, and T. Shinohara, Magnetic Properties of the System $\text{Fe}_2\text{P}-\text{Mn}_2\text{P}$, *J. Phys. Soc. Japan*, 1973, 34(4), p 908-910.

68. T. Suzuki, Y. Yamaguchi, H. Yamamoto, and H. Watanabe, Magnetic Structure of FeMnP. *J. Phys. Soc. Japan*, 1973, 34(4), p 911-916.
69. B. Chenevier, J. L. Soubeyroux, M. Bacmann, D. Fruchart, and R. Fruchart, The High Temperature Orthorhombic \rightleftharpoons Hexagonal Phase Transformation of FeMnP, *Solid State Communications*, 1987, 64(1), p 57-61.
70. B. K. Srivastava, T. Ericsson, L. Haggstrom, H. R. Verma, Y. Andersson, and S. Rundqvist, A Mossbauer Study of the $(\text{Fe}_{1-x}\text{Mn}_x)_2\text{P}$ System, *J. Phys. C: Solid State Phys.*, 1987, 20(3), p 463-472.
71. B. Chenevier, D. Fruchart, M. Bacmann, D. Boursier, and R. Fruchart, The High-temperature Paramagnetic Susceptibility of the System $(\text{Fe}_{1-x}\text{Mn}_x)_2\text{P}$, *J. Phys.: Condensed Matter*, 1989, 1(48), p 9599-9607.
72. Y. Maeda and Y. Takashima, Mossbauer Studies of Solid Solution Systems of Fe(P, As), (Fe, Co)P, (Fe, Mn)P and (Fe, W)P, *J. Inorg. Nucl. Chem.*, 1973, 35(4), p 1219-1225.
73. J. Bonnerot, B. Fruchart, and A. Roger, Magnetic and Thermodynamic Properties of Iron Phosphide and Magnetic Properties of $\text{Mn}_{1-x}\text{Fe}_x\text{P}$ Solid Solutions, *Physics Letters A*, 1968, 26A(11), p 536-537.
74. H. Fjellvag, A. Kjekshus, and A. F. Andresen, Magnetic and Structural Properties of Transition Metal Substituted MnP. III. $\text{Mn}_{1-t}\text{Fe}_t\text{P}$ ($0.00 \leq t \leq 0.30$), *Acta Chemica Scandinavica A*, 1984, 38(7), p 711-717.
75. H. Kaneko, T. Nishizawa, K. Tamaki, and A. Tanifuji, Solubility of Phosphorus in α and γ -Iron, *Nippon Kinzoku Gakkai-Si*, 1965, 29, p 166-170.
76. A. I. Zaitsev, Z. V. Dobrokhotova, A. D. Litvina, and B. M. Mogutnov, Thermodynamic Properties of Iron-Manganese-Phosphorus Melts, *Inorg. Mater.*, 1995, 31(9), p 1064-1072.

77. A. I. Zaitsev, A. D. Litvina, N. E. Shelkova, and B. M. Mogutnov, Association in Ternary Metallic Melts Fe-Mn-Si, Fe-Cr-P and Fe-Mn-P, *Thermoch. Acta*, 1998, 314(1-2), p 307-315.
78. A. M. Kunaev, B. A. Shabdenov, and B. B. Beisembaev, Study of Thermodynamic Behavior of Manganese in Melts of the System Iron-Phosphorus-Manganese, *Vestnik Akademi Nauk Kazakhskoi SSR*, 1980, (7), p 43-46.
79. H. Schenck, E. Steinmetz, and H. Gitizad, Activity of Phosphorus in Molten Iron and Its Control by Ni, Mn, and Cr, *Arch. Eisen.*, 1969, 40(8), p 597-602.
80. S. Ban-ya, N. Maruyama, and Y. Kawase, Effects of Ti, V, Cr, Mn, Co, Ni, Cu, Nb, Mo, and W on the Activity of Phosphorus in Liquid Iron, *Tetsu-to-Hagané*, 1984, 70(1), p 65-72.
81. S. Ban-ya and M. Suzuki, Activity of Phosphorus in Liquid Fe-P and Fe-P-C Alloys, *Tetsu-to-Hagané*, 1975, 61(14), p 2933-2942.
82. S. Ban-Ya, N. Maruyama, and S. Fujono, Vapor Pressure of Phosphorus in Liquid Fe-P Alloys, *Tetsu-to-Hagané*, 1982, 68(2), p 269-276.

Chapter 5: Critical Evaluation and Thermodynamic Optimization of the Al-P and Fe-Al-P Systems

Zhimin You¹, In-Ho Jung²

1. Department of Mining and Materials Engineering, McGill University, 3610 University Street,
Montreal, QC, H3A 0C5, Canada

2. Department of Materials Science and Engineering, and Research Institute of Advanced
Materials (RIAM), Seoul National University, 1 Gwanak-ro, Gwanak-gu, Seoul, 08826, South
Korea

(Published in the Journal of Phase Equilibria and Diffusion, July 2020)

Abstract

The Al-P system and Fe-Al-P system have been thermodynamically optimized using the CALculation of PHase Diagrams (CALPHAD) method based on the critical evaluation of all available experimental data. The liquid phases and solid solutions were modeled using the Modified Quasichemical Model and Compound Energy Formalism, respectively. The Gibbs energies of stoichiometric AlP compound and liquid Al-P solution were critically optimized to reproduce the melting point of AlP and the liquidus of the Al-P system on the Al-rich corner. In the ternary Fe-Al-P system, the behavior of P in the liquid was also well optimized with introduction of Toop interpolation technique (Al as an asymmetric component). In addition, various phase equilibria of Fe-Al-P alloys containing up to 30 wt.%Al and 15 wt.%P, isothermal sections at 450 °C, 650 °C and 800 °C, and the solubility of P in BCC_A2 Fe-Al alloys were excellently described, compared to experimental data. According to the present optimization, an accurate and consistent thermodynamic database of the Fe-Al-P system has been developed.

Keywords: Al-P system, Fe-Al-P system, CALPHAD, AlP, Thermodynamic descriptions

5.1 Introduction

With increasingly high demand for the safety and energy-efficiency of automotive, light alloy such as Al is often added into the new generation automotive steels for reducing the weight and improving the mechanical properties simultaneously. To further enhance the corrosion resistance, paintability and also the weldability of steels, the galvannealing coatings were always applied on the steel plate surface [1]. In high Al steels, phosphorus on one hand plays a positive role in solid solution strengthening and corrosion resistance of the steels, but on the other hand, enrichment of P in the grain boundary inhibits formation of coating layers [2]. Besides, the galvannealing coating layer pulverization and flaking off the substrate are very challenging difficulties during the stamping process, which largely increase the defective and repairing rate. Moreover, P, as the typical metalloid impurity of steels, can also cause unexpected steel defects like brittleness and inner cracks. Therefore, it is very necessary to tightly control the P impurity of the steels below the allowed level. In the Fe-Al alloys containing high concentration of P, formation of aluminum phosphide AlP and various iron phosphides depends on the temperature and composition. As is well known, AlP is highly toxic compound widely used as rodenticide, insecticide, fumigant [3]. Hence, very cautious attention needs to be paid to the application of high Al and high P materials. Nevertheless, aluminum phosphide and iron phosphides are also widely applied in high power and high frequency manufacturing, such as semiconductor diodes [4,5]. To explore as much application potential as possible without sacrificing their mechanical properties, it is very essential to understand the thermodynamic behaviors of the Fe-Al-P system in terms of service conditions.

Previously, many experimental and computational studies have been conducted to investigate the sub-systems of the Fe-Al-P system. Besides, reviews on the Fe-P system were given by Okamoto

[6] and Schlesinger [7], the Al-P system by McAlister [8] and Okamoto [9], and the Fe-Al-P system by Raghavan [10-12], Schmid-Fetzer [13]. The Fe-P system was thermodynamically assessed in many studies [14-18] and by the present authors [19]. The Al-P system and the Fe-Al-P system was optimized by Ansara et al. [20], Tu et al. [21], Wu et al. [22], Liang and Schmid-Fetzer [23,24], Cao et al. [17], and Miettinen et al. [25]. Although the Al-P system is a simple system containing the only stoichiometric compound AlP, inconsistency among available experimental data has not been resolved in the previous optimizations [17,20-24]. In the recent assessment by Miettinen et al. [25], experimental data of the binary Al-P system was reasonably reproduced, but the accuracy was not maintained when extending to the ternary Fe-Al-P system, compared with available experimental data [25]. Therefore, it is necessary to resolve the discrepancies left in previous modeling by reoptimizing the Fe-Al-P system.

Thermodynamic database based on the CALculation of PHase Diagrams (CALPHAD) method is a powerful tool for new materials design and process optimization. The database of a target system is developed by means of thermodynamic modeling (optimization), aiming at obtaining one set of consistent Gibbs energies of all phases as functions of temperature and composition. In the optimization, all available phase equilibria and thermodynamic data such as activity, entropy, enthalpy, and Gibbs energy, etc are critically evaluated simultaneously. The discrepancies between available data are resolved in the critical evaluation process, and the Gibbs energy functions for all related phases in the target system are derived. Prediction on unexplored thermodynamic properties and phase equilibria can be possible by interpolations and extrapolations in a thermodynamically correct manner.

In the present study, the liquid phases and solid solutions of the binary Al-P and ternary Fe-Al-P systems were described using the Modified Quasichemical Model (MQM) [26,27] and Compound Energy Formalism (CEF) [28], respectively. The Fe-Al system originally optimized by Sundman et al. [29] with recent modification by Phan et al. [30], and the Fe-P system reassessed by present authors [19] were adopted in the present study. The solubility of P in liquid Al, thermodynamic properties of stoichiometric AlP compound, various isopleth diagrams, isothermal diagrams, liquidus surface projection and the activity of P in molten Fe-Al-P alloys will be optimized to reproduce reliable experimental data. All the thermodynamic calculations were performed using FactSage software [31].

5.2. Thermodynamic Models

5.2.1 Pure Elements and Stoichiometric Compounds

The Gibbs energies of elemental Fe, Al and P were taken from the Scientific Group Thermodata Europe (SGTE) database [32]. The Gibbs energies of stoichiometric compounds involved in the Fe-Al-P system were determined based on available thermodynamic data including the heat capacity, standard enthalpy of formation and standard entropy at 298.15 K. In the present study, the Gibbs energies of stoichiometric compounds were calculated as follows:

$$G_T^\circ = \left(\Delta H_{298.15K}^\circ + \int_{298.15K}^T C_P dT \right) - T \left(S_{298.15K}^\circ + \int_{298.15K}^T \frac{C_P}{T} dT \right) \quad (5.1)$$

where G_T° is the Gibbs energy (J/mol) at temperature $T(K)$, $\Delta H_{298.15K}^\circ$ and $S_{298.15K}^\circ$ are standard enthalpy of formation (J/mol) and standard entropy (J/mol/K) at 298.15 K, and C_P is the heat capacity (J/mol/K). The heat capacity of each stoichiometric compound was expressed as a function of temperature by fitting experimental data. For the compounds with no available

experimental data, their C_p functions were estimated using Neumann-Kopp (NK) rule [33] or based on determined C_p of neighboring compounds in the same system.

When a pure element or stoichiometric compound exhibits magnetic behavior, an additional Gibbs energy of magnetic contribution term G^{mg} will be applied. In the Fe-Al-P system, the magnetic contribution terms for Fe (BCC_A2, FCC_A1) and Fe₃P were determined using the empirical expression proposed by Inden [34] and modified by Hillert and Jarl [35]:

$$G^{mg} = RT \ln(\beta + 1) g(\tau) \quad (5.2)$$

where τ is expressed as T/T^* and T^* is the critical temperature of magnetic transition associated with Curie temperature T_C for ferromagnetic materials or Neel temperature T_N for antiferromagnetic materials. β is the average magnetic moment per mole of atoms in Bohr magnetons. $g(\tau)$ is a polynomial function derived by Hillert and Jarl [35], as expressed below:

$$g(\tau) = 1 - \left[\frac{79\tau^{-1}}{140P} + \frac{474}{497} \left(\frac{1}{P} - 1 \right) \left(\frac{\tau^3}{6} + \frac{\tau^9}{135} + \frac{\tau^{15}}{600} \right) \right] / D \quad \dots \tau \leq 1 \quad (5.3)$$

$$g(\tau) = - \left(\frac{\tau^{-5}}{10} + \frac{\tau^{-15}}{315} + \frac{\tau^{-25}}{1500} \right) / D \quad \dots \tau > 1 \quad (5.4)$$

where $D = \frac{518}{1125} + \frac{11692}{15975} \left(\frac{1}{P} - 1 \right)$, and the value of P can be considered as the fraction of the magnetic enthalpy absorbed above the critical temperature depending on the structure. P is 0.40 for the simple BCC_A2 phase while P is 0.28 for other common phases.

5.2.2 Solid Solutions

In the binary Fe-P system, solid solutions including disordered FCC_A1 and BCC_A2 were considered in the present study [19]. As is well known, P is not soluble in solid Al, so no stable

solid solution in the binary Al-P system. In the binary Fe-Al system, the BCC phase undergoes a long-range ordering from disordered BCC_A2 to ordered BCC_B2 transition. Another ordered DO₃ phase [29] in maximized Fe₃Al composition was not considered in this work for keeping the consistency in extending to multicomponent systems. Besides, disordered FCC_A1, Al₈Fe₅ and Al₁₃Fe₄ are also taken into account. In the ternary Fe-Al-P system, Al can substitute the Fe atoms of Fe₃P and Fe₂P to form Me₃P and Me₂P solid solutions in the formulas (Fe, Al)₃P and (Fe, Al)₂P, respectively. The Gibbs energies of all solid solutions in the sub-systems of the Fe-Al-P system were described using the Compound Energy Formalism (CEF) [28] considering their crystallographic structures.

5.2.2.1 FCC_A1 Solid Solutions

The disordered FCC_A1 solid solution was modeled with the formula (Fe, Al, P)₁(Va)₁, and its Gibbs energy was calculated using the following equation:

$$G_S^{disorder} = \sum_{i=Fe,Al,P} x_i G_i^o + RT \sum_{i=Fe,Al,P} x_i \ln x_i + \sum_{m=0,1,2,\dots} x_{Fe} x_P L_{Fe,P}^m + \sum_{k=0,1,2,\dots} x_{Al} x_P L_{Al,P}^k + \sum_{p=0,1,2,\dots} x_{Fe} x_{Al} L_{Fe,Al}^p + \sum_{q=0,1,2,\dots} x_{Fe} x_{Al} x_P L_{Fe,Al,P}^q + G^{mg} \quad (5.5)$$

where x_i is the mole fraction of component i and G_i^o is the molar Gibbs energy (J/mol) of pure solid i ($i = Fe, Al, P$); R and T are the gas constant (8.314 J/mol-K) and the temperature in Kelvin (K); $L_{Fe,P}^m$, $L_{Al,P}^k$, $L_{Fe,Al}^p$ and $L_{Fe,Al,P}^q$ are the adjustable interaction parameters of the related binary and ternary systems; G^{mg} is the magnetic contribution to the Gibbs energy (J/mol).

5.2.2.2 Disordered/Ordered BCC Solid Solutions

The BCC phase exhibits a transition from disordered to ordered crystallographic structure. The Gibbs energy of BCC solution was modeled combining the disordered part with the model (Fe, Al, P)(Va)₃ and the ordered part with the model (Fe, Al, P)_{0.5}(Fe, Al, P)_{0.5}(Va)₃. The Gibbs energy of the disordered part was calculated using **Eq. (5.5)**, which is the same as that for disordered FCC_A1 phase. The Gibbs energy contribution from the ordered part was calculated as follows:

$$\Delta G_{BCC}^{order} = G_{BCC}^{order}(y'_i, y''_j) - G_{BCC}^{order}(y'_i, y''_j)_{y'_k=y''_k} \quad (5.6)$$

$$\begin{aligned} G_{BCC}^{order}(y'_i, y''_j) = & y'_{Fe} y'_{Fe} G_{Fe:Fe} + y'_{Al} y''_{Al} G_{Al:Al} + y'_P y''_P G_{P:P} \\ & + y'_{Fe} y''_{Al} G_{Fe:Al} + y'_{Al} y''_{Fe} G_{Al:Fe} + y'_{Fe} y''_P G_{Fe:P} \\ & + y'_{Al} y''_P G_{Al:P} + y'_P y''_{Fe} G_{P:Fe} + y'_P y''_{Al} G_{P:Al} \\ & + 0.5RT \left(y'_{Fe} \ln y'_{Fe} + y'_{Al} \ln y'_{Al} + y'_P \ln y'_P \right) \\ & + 0.5RT \left(y''_{Fe} \ln y''_{Fe} + y''_{Al} \ln y''_{Al} + y''_P \ln y''_P \right) \\ & + \sum_{i,j,k} y'_i y'_j y'_k L_{i,j:k} + \sum_{i,j,k} y'_k y'_i y'_j L_{k:i,j} + G^{mg} \end{aligned} \quad (5.7)$$

here i, j, k are the component symbols of Fe, Al, P. y'_i, y'_j, y'_k and y''_i, y''_j, y''_k are site fractions of component i, j, k in the first and second lattice of the formula (Fe, Al, P)_{0.5}(Fe, Al, P)_{0.5}(Va)₃. The total Gibbs energy of the BCC solid solution combining contribution from both disordered and ordered parts was determined from **Eq. (5.8)**:

$$G_{BCC}^{sol.} = G_S^{disorder} + \Delta G_{BCC}^{order} \quad (5.8)$$

When the site fractions of i in the first sublattice equals to that in the second sublattice ($y'_i = y''_i$), then the ordering contribution ΔG_{BCC}^{order} is nil and the Gibbs energy of BCC phase can be calculated by **Eq. (5.5)**. However, in the case of $y'_i \neq y''_i$, then ordering contribution ΔG_{BCC}^{order} becomes negative and the Gibbs energy of BCC_B2 phase can be described with **Eq. (5.8)**.

5.2.2.3 Other Solid Solutions (Al_8Fe_5 , $Al_{13}Fe_4$, Me_3P , Me_2P)

The solid solutions including Al_8Fe_5 , $Al_{13}Fe_4$, Me_3P and Me_2P were also modeled using the formulas $(Al, Fe)_8(Al, Fe)_5$, $(Al)_{32}(Fe)_{12}(Al, Va)_7$, $(Fe, Al)_3P$, and $(Fe, Al)_2P$, respectively. The

Gibbs energy of Al_8Fe_5 was calculated with the equation below:

$$G_{Al_8Fe_5}^{sol.} = y'_{Al}y''_{Al}G_{Al:Al} + y'_{Fe}y''_{Fe}G_{Fe:Fe} + y'_{Al}y''_{Fe}G_{Al:Fe} + y'_{Fe}y''_{Al}G_{Fe:Al} \\ + 8RT(y'_{Al} \ln y'_{Al} + y'_{Fe} \ln y'_{Fe}) + 5RT(y''_{Al} \ln y''_{Al} + y''_{Fe} \ln y''_{Fe}) \\ + \sum_{m=0,1,2...}^{i=Al,Fe} y'_{Al}y'_{Fe}y''_i L_{Al,Fe:i}^m + \sum_{n=0,1,2...}^{j=Al,Fe} y'_j y''_{Al} y''_{Fe} L_{j:Al,Fe}^n \quad (5.9)$$

where $G_{Al:Al}$, $G_{Fe:Fe}$, $G_{Al:Fe}$, $G_{Fe:Al}$ are the end-member Gibbs energies (J/mol); y'_{Al} , y''_{Al} , y'_{Fe} , y''_{Fe} are the site fractions of Al and Fe in corresponding lattice; $L_{Al,Fe:i}^m$, $L_{j:Al,Fe}^n$ are the adjustable interaction parameters. The Gibbs energy of $Al_{13}Fe_4$ was calculated as follows:

$$G_{Al_{13}Fe_4}^{sol.} = y_{Al}G_{Al:Fe:Al} + y_{Va}G_{Al:Fe:Va} + 7RT(y_{Al} \ln y_{Al} + y_{Va} \ln y_{Va}) + \sum_{m=0,1,2...} y_{Al}y_{Va}L_{Al:Fe:Al,Va}^m \quad (5.10)$$

where $G_{Al:Fe:Al}$ and $G_{Al:Fe:Va}$ are end-member Gibbs energies (J/mol); y_{Al} and y_{Va} are site fractions of Al and vacancies in the third sublattice; $L_{Al:Fe:Al,Va}^m$ is the adjustable interaction parameter. The Gibbs energies of Me_3P and Me_2P are expressed by as follows:

$$G_{Me_nP}^{sol.} = y_{Fe}G_{Fe_nP}^{\circ} + y_{Al}G_{Al_nP} + nRT(y_{Fe} \ln y_{Fe} + y_{Al} \ln y_{Al}) + \sum_{m=0,1,2...} y_{Fe}y_{Al}L_{Fe,Al:P}^m + G^{mg} \quad (5.11)$$

where n is the number of substitutional site within the formulas Me_3P ($n = 3$) and Me_2P ($n = 2$); $G_{Fe_3P}^{\circ}$ and $G_{Fe_2P}^{\circ}$ are optimized Gibbs energies (J/mol) of stoichiometric Fe_3P and Fe_2P compounds respectively in the Fe-P system [19]; G_{Al_3P} and G_{Al_2P} are Gibbs energies (J/mol) of the end-members Al_3P and Al_2P respectively in the substitutional sublattice; y_{Fe} , y_{Al} are site fractions in the substitutional sublattice; $L_{Fe,Al:P}^m$ is the adjustable interaction parameter; G^{mg} is the magnetic contribution to the Gibbs energy (J/mol).

5.2.3 Liquid Solution

The liquid solution was described using the Modified Quasichemical Model (MQM) [26,27] accounting for the short-range ordering of the nearest-neighbor atoms explicitly. Comparing to the conventional Bragg-Williams Random Mixing Model (BWRMM), the MQM gives a more realistic description of the entropy of liquid solution. In the MQM, the Gibbs energy of pair formation can be expanded as a polynomial in the pair fraction rather than the component fraction, and the coordination number of each component is allowed to vary with composition for reproducing the short-range ordering of liquid solution with less parameters, providing greater flexibility in reproducing experimental data of the binary liquids and higher-order systems.

In the case of the binary A - B liquid solution, the atoms A and B are distributed over the quasilattice sites. The atom pair exchanging reaction of liquid A - B solution can be expressed as follows:



here, $(i-j)$ represents the nearest-neighbor pair between components i and j , and Δg_{AB} is the Gibbs energy change (J/mol) of forming 2 moles $(A-B)$ pairs. The Gibbs energy of liquid solution was calculated:

$$G_{AB}^L = (n_A G_A^\circ + n_B G_B^\circ) - T \Delta S_{AB}^{conf.} + n_{AB} (\Delta g_{AB} / 2) \quad (5.13)$$

where n_A and n_B are the numbers of moles of A atoms and B atoms, and G_A° and G_B° are the molar Gibbs energies (J/mol) of pure liquid A and B . $\Delta S_{AB}^{conf.}$ is the configurational entropy (J/mol) of mixing given by random distribution of the $(A-A)$, $(B-B)$ and $(A-B)$ pairs as follows:

$$\Delta S_{AB}^{conf.} = -R(n_A \ln X_A + n_B \ln X_B) - R \left[n_{AA} \ln \left(\frac{X_{AA}}{Y_A^2} \right) + n_{BB} \ln \left(\frac{X_{BB}}{Y_B^2} \right) + n_{AB} \ln \left(\frac{X_{AB}}{2Y_A Y_B} \right) \right] \quad (5.14)$$

here n_{AA} , n_{BB} and n_{AB} are the numbers of moles of (A-A), (B-B) and (A-B) pairs; X_{AA} , X_{AB} and X_{BB} are the pair fraction of the corresponding atom pairs; Y_A and Y_B are the coordination equivalent fractions of atoms A and B. The pair fractions X_{AA} , X_{AB} , X_{BB} and coordination equivalent fractions Y_A , Y_B were calculated as follows:

$$X_{AA} = n_{AA} / (n_{AA} + n_{AB} + n_{BB}) \quad (5.15)$$

$$X_{AB} = n_{AB} / (n_{AA} + n_{AB} + n_{BB}) \quad (5.16)$$

$$X_{BB} = n_{BB} / (n_{AA} + n_{AB} + n_{BB}) \quad (5.17)$$

$$Y_A = X_{AA} + \frac{1}{2} X_{AB} \quad (5.18)$$

$$Y_B = X_{BB} + \frac{1}{2} X_{AB} \quad (5.19)$$

Δg_{AB} in **Eqs. (5.12)** and **(5.13)** is the model parameter for reproducing the Gibbs energy of the binary A-B solution, which can be expanded as a polynomial based on the atomic pair fractions X_{AA} and X_{BB} as follows:

$$\Delta g_{AB} = \Delta g_{AB}^{\circ} + \sum_{i \geq 1} g_{AB}^{i0} X_{AA}^i + \sum_{j \geq 1} g_{AB}^{0j} X_{BB}^j \quad (5.20)$$

where Δg_{AB}° , g_{AB}^{i0} and g_{AB}^{0j} are the adjustable model parameters that can be functions of the temperature. In the MQM, the coordination numbers of A and B, Z_A and Z_B , can be varied with composition to reproduce the short-range ordering of the solution:

$$\frac{1}{Z_A} = \frac{1}{Z_{AA}^A} \left(\frac{2n_{AA}}{2n_{AA} + n_{AB}} \right) + \frac{1}{Z_{AB}^A} \left(\frac{n_{AB}}{2n_{AA} + n_{AB}} \right) \quad (5.21)$$

$$\frac{1}{Z_B} = \frac{1}{Z_{BB}^B} \left(\frac{2n_{BB}}{2n_{BB} + n_{AB}} \right) + \frac{1}{Z_{BA}^B} \left(\frac{n_{AB}}{2n_{BB} + n_{AB}} \right) \quad (5.22)$$

here, Z_{AA}^A is the value Z_A when all nearest neighbors of an A atom are A atoms and Z_{AB}^A is the value of Z_A when all nearest neighbors of an A atom are B atoms. Z_{BB}^B and Z_{BA}^B are defined in an analogous manner. When extending from the binary systems to the ternary system, the Gibbs energy of ternary liquid solution can be predicted using a proper geometric interpolation technique based on the nature of all involved binary liquid solutions. If necessary, ternary correction terms can also be introduced to give more precise description of phase equilibria and thermodynamic properties of the ternary liquid solution. In the Fe-Al-P system, the liquid Fe-P exhibits much more negative deviation from ideal mixing, compared to liquid Al-P and Fe-Al solutions. Therefore, the Toop-type interpolation technique [27] with Al as the asymmetric component was applied to the liquid Fe-Al-P solution. The Gibbs energy and configurational entropy of mixing of liquid Fe-Al-P solution were calculated as follows:

$$G_{FeAlP}^L = \sum_{i=Fe,Al,P} n_i G_i^\circ - T \Delta S_{FeAlP}^{conf.} + \sum_{j,k=Fe,Al,P}^{j \neq k} (n_{jk} / 2) \Delta g_{jk} \quad (5.23)$$

$$\Delta S_{FeAlP}^{conf.} = -R \sum_{i=Fe,Al,P} n_i \ln X_i - R \left[\sum_{j=Fe,Al,P} n_{jj} \left(\frac{X_{jj}}{Y_j^2} \right) + \sum_{k,m=Fe,Al,P}^{k \neq m} n_{km} \ln \left(\frac{X_{km}}{2Y_k Y_m} \right) \right] \quad (5.24)$$

where each pair formation Gibbs energy Δg_{FeP} , Δg_{AlP} and Δg_{FeAl} depends on the symmetry of each component (Fe, Al, P) in the ternary system. Therefore, Δg_{AlP} and Δg_{AlFe} between asymmetric components are described as follows:

$$\Delta g_{FeAl} = \Delta g_{FeAl}^\circ + \sum_{(i+j) \geq 1} g_{FeAl}^{ij} x_{AlAl}^i (x_{FeFe} + x_{FeP} + x_{PP})^j + \sum_{i \geq 0, j \geq 0, k \geq 1} g_{FeAl(P)}^{ijk} x_{AlAl}^i (x_{FeFe} + x_{FeP} + x_{AlAl})^j \left(\frac{Y_P}{Y_{Fe} + Y_P} \right)^k \quad (5.25)$$

$$\Delta g_{AlP} = \Delta g_{AlP}^\circ + \sum_{(i+j) \geq 1} g_{AlP}^{ij} x_{AlAl}^i (x_{FeFe} + x_{FeP} + x_{PP})^j + \sum_{i \geq 0, j \geq 0, k \geq 1} g_{AlP(Fe)}^{ijk} x_{AlAl}^i (x_{FeFe} + x_{FeP} + x_{AlAl})^j \left(\frac{Y_{Fe}}{Y_{Fe} + Y_P} \right)^k \quad (5.26)$$

and Δg_{FeP} between symmetric Fe and P was calculated as follows:

$$\Delta g_{FeP} = \Delta g_{FeP}^{\circ} + \sum_{(i+j) \geq 1} g_{FeP}^{ij} \left(\frac{x_{FeFe}}{x_{FeFe} + x_{FeP} + x_{PP}} \right)^i \left(\frac{x_{PP}}{x_{FeFe} + x_{FeP} + x_{PP}} \right)^j$$

$$+ \sum_{i \geq 0, j \geq 0, k \geq 1} g_{FeP(Al)}^{ijk} \left(\frac{x_{FeFe}}{x_{FeFe} + x_{FeP} + x_{PP}} \right)^i \left(\frac{x_{PP}}{x_{FeFe} + x_{FeP} + x_{PP}} \right)^j Y_{Al}^k \quad (5.27)$$

where g_{AlP}^{ij} , g_{FeAl}^{ij} , g_{FeP}^{ij} are the binary liquid parameters; $g_{FeAl(P)}^{ijk}$, $g_{AlP(Fe)}^{ijk}$ and $g_{FeP(Al)}^{ijk}$ are the ternary liquid parameters.

5.3 Critical Evaluation and Thermodynamic Optimization

Thermodynamic optimization of the Fe-Al-P system was performed using the CALPHAD approach based on critical evaluation of all available phase equilibria and thermodynamic data. The liquid and solid solutions of all sub-systems were described using MQM [26,27] and CEF [28], respectively. White P was selected as the reference state of P in the solid phases. The crystal structure information of all solid phases in the Fe-Al-P system is summarized in **Table 5.1**. The optimized model parameters of the Fe-Al-P system are summarized in **Table 5.2**.

Table 5.1 Summary of crystal structure information of all solid phases in the Fe-Al-P system

Phase	Structure	Prototype	Space group	Pearson symbol
FCC_A1	Cubic	Cu	$\bar{F}m\bar{3}m$	<i>cF4</i>
BCC_A2	Cubic	W	$Im\bar{3}m$	<i>cI2</i>
BCC_B2	Cubic	CsCl	$Pm\bar{3}m$	<i>cP8</i>
Fe ₃ Al	Cubic	BiF ₃	$Fm\bar{3}m$	<i>cF16</i>
Me ₃ P	Tetragonal	Ni ₃ P	$I\bar{4}$	<i>tI32</i>
Me ₂ P	Hexagonal	Fe ₂ P	$P\bar{6}2m$	<i>hP9</i>
FeP	Orthorhombic	MnP	$Pnma$	<i>oP8</i>

FeP ₂	Orthorhombic	FeS ₂	<i>Pnmm</i>	<i>oP6</i>
AlP	Hexagonal	ZnS	<i>F$\bar{4}3m$</i>	<i>cF8</i>
Al ₂ Fe	Rhombohedral	FeAl ₂	<i>P1</i>	<i>aP18</i>
Al ₅ Fe ₂	Orthorhombic	Al ₅ Fe ₂	<i>Cmcm</i>	<i>oC16</i>
Al ₈ Fe ₅	Cubic	Zn ₈ Cu ₅	<i>I$\bar{4}3m$</i>	<i>cI52</i>
Al ₁₃ Fe ₄	Monoclinic	Al ₁₃ Fe ₄	<i>C2/m</i>	<i>mC102</i>
White P	Cubic	P ₄	<i>I$\bar{4}3m$</i>	<i>C*8</i>
Red P	---	P	---	<i>C*66</i>

Table 5.2 Optimized model parameters for the Fe-Al-P system (J/mol, J/mol-K)

Phase	Model parameters
	$Z_{FeFe}^{Fe} = Z_{AlAl}^{Al} = Z_{PP}^P = 6$ [30,*]
	$Z_{PFe}^P = Z_{PAI}^P = Z_{FeAl}^{Fe} = Z_{AlFe}^{Al} = Z_{AlP}^{Al} = 6$ [19,30,*], $Z_{FeP}^{Fe} = 3$ [19]
Liquid (Fe,Al,P)	$\Delta g_{FeP} = -56902 + 6.569T + (5481 + 3.033T)X_{FeFe} + (-11966 + 2.510T)X_{FeFe}^2 - 9623X_{PP}$ [19]
	$\Delta g_{AlP} = -21443 + 6.9036T$ [*]
	$\Delta g_{FeAl} = -20292 + 3.347T - (1674 + 1.255T)X_{FeFe} - 1046X_{FeFe}^2 - (10460 - 4.184T)X_{AlAl}$ [30]
	$g_{FeP(Al)}^{101} = -20920 + 5.6484T$, $g_{FeP(Al)}^{011} = -104600$
	“Toop-type” interpolation with Al as an asymmetric component [*]
FCC_A1 (Fe,Al,P) ₁ (Va) ₁	$G_{FeVa}^{FCC} = G_{Fe(FCC)}^\circ$, $G_{AlVa}^{FCC} = G_{Al(FCC)}^\circ$, $G_{P,Va}^{FCC} = G_{P(FCC)}^\circ$ [*]
	$L_{Fe,P,Va}^{FCC} = -139787.44 + 6.4852T$ [19]
	$L_{Al,P,Va}^{FCC} = -18828$ [*]
	$L_{Fe,Al,Va}^{FCC} = -105855 + 30.65T - (29017 - 4.91T)(x_{Fe} - x_{Al}) + (32200 - 17T)(x_{Fe} - x_{Al})^2$ [30]

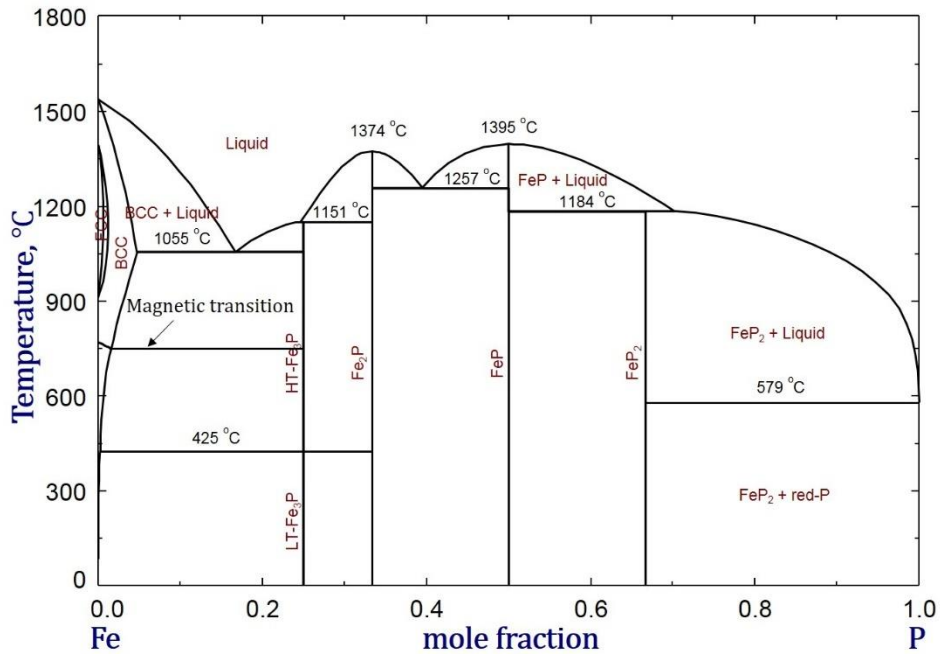
	$T_{CFeVa} = -201, \beta_{FeVa} = -2.1$ [36]
	$G_{FeVa}^{BCC_A2} = G_{Fe(BCC)}^\circ, G_{AlVa}^{BCC_A2} = G_{Al(BCC)}^\circ, G_{P_Va}^{BCC_A2} = G_{P(BCC)}^\circ$ [*]
	$L_{Fe,P_Va}^{BCC_A2} = -203476.3 + 15.4808T + 33472(y_{Fe} - y_P)$ [19]
BCC_A2	$L_{Al,P_Va}^{BCC_A2} = -6276$ [*]
(Fe,Al,P) ₁ (Va) ₃	$L_{Fe,AlVa}^{BCC_A2} = -123044 + 31.99T - 2945(x_{Fe} - x_{Al}) - 3347(x_{Fe} - x_{Al})^2$ [30]
	$T_{CFe,P_Va} = -285$ [19], $T_{CFe,AlVa} = -438 + 1720(y_{Fe} - y_{Al})$ [30]
	$T_{CFeVa} = 1043, \beta_{FeVa} = 2.22$ [36]
	$G_{FeAlVa}^{BCC_B2} = G_{AlFeVa}^{BCC_B2} = -14462 - 3.973T$ [29,30]
	$G_{FeFeVa}^{BCC_B2} = G_{AlAlVa}^{BCC_B2} = 0$ [30]
	$G_{P_P_Va}^{BCC_B2} = G_{FeP_Va}^{BCC_B2} = G_{AlP_Va}^{BCC_B2} = G_{P_FeVa}^{BCC_B2} = G_{P_AlVa}^{BCC_B2} = 0$ [*]
	$T_{CFeAlVa} = T_{CaAlFeVa} = -250$ [29], $\beta_{FeAlVa} = \beta_{AlFeVa} = -2.72$ [29]
	$L_{FeAlAl}^{BCC_B2} = 1665.37 - 4T + 524(y_{Fe} - y_{Al}) - 1560(y_{Fe} - y_{Al})^2$ [29]
BCC_B2	$L_{AlFeAl}^{BCC_B2} = 1665.37 - 4T + 524(y_{Fe} - y_{Al}) - 1560(y_{Fe} - y_{Al})^2$ [29]
(Fe,Al,P) _{0.5} (Fe,Al,P) _{0.5}	$L_{FeAlFe}^{BCC_B2} = -5346 - 1.6T + 524(y_{Fe} - y_{Al}) - 1560(y_{Fe} - y_{Al})^2$ [29]
(Va) ₃	$L_{FeFeAl}^{BCC_B2} = -5346 - 1.6T + 524(y_{Fe} - y_{Al}) - 1560(y_{Fe} - y_{Al})^2$ [29]
	$T_{CFeAlAlVa} = T_{CFeAlFeVa} = T_{CFeFeAlVa} = T_{CaAlFeAlVa} = -250$ [29]
	$\beta_{FeAlAlVa} = \beta_{FeAlFeVa} = -0.6 + 1.6(y_{Fe} - y_{Al}) + 0.4(y_{Fe} - y_{Al})^2$ [29]
	$\beta_{FeFeAlVa} = \beta_{AlFeAlVa} = -0.6 + 1.6(y_{Fe} - y_{Al}) + 0.4(y_{Fe} - y_{Al})^2$ [29]
	$L_{FeAlFeAlVa}^{BCC_B2} = -16800 - 3.6T$ [29,30]
Al ₈ Fe ₅	$G_{AlAl} = 13G_{Al(BCC)}^\circ$ [29], $G_{FeFe} = 13G_{Fe(BCC)}^\circ + 13000$ [29]
(Al, Fe) ₈ (Al, Fe) ₅	$G_{AlFe} = 8G_{Al(BCC)}^\circ + 5G_{Fe(BCC)}^\circ - 384500 + 30T$ [29,30]

	$G_{Fe:Al} = 8G_{Fe(BCC)}^{\circ} + 5G_{Al(BCC)}^{\circ} + 200000 + 30T$ [29,30]
	$L_{Al:Al,Fe}^{Al_8Fe_5} = -133888$ [30], $L_{Al,Fe:Fe}^{Al_8Fe_5} = -174000$ [29]
Al ₁₃ Fe ₄	$G_{Al:Fe:Al} = 39G_{Al(FCC)}^{\circ} + 12G_{Fe(BCC)}^{\circ} - 1564680 + 377T$ [29]
(Al) ₃₂ (Fe) ₁₂ (Al,Va) ₇	$G_{Al:Fe:Va} = 32G_{Al(FCC)}^{\circ} + 12G_{Fe(BCC)}^{\circ} - 1433100 + 377T$ [29]
Me ₃ P	$G_{Fe:P}^{Me_3P} = G_{Fe_3P}^{\circ}$ [19]
(Fe, Al) ₃ (P) ₁	$G_{Al:P}^{Me_3P} = 3G_{Al(FCC)}^{\circ} + G_{P(White)}^{\circ} - 14830 + 85T$ [*]
	$L_{Fe,Al:P}^{Me_3P} = -346025 + 50T$ [*]
Me ₂ P	$G_{Fe:P}^{Me_2P} = G_{Fe_2P}^{\circ}$ [19]
(Fe, Al) ₂ (P) ₁	$G_{Al:P}^{Me_2P} = 2G_{Al(FCC)}^{\circ} + G_{P(White)}^{\circ} + 50000$ [*]
	$L_{Fe,Al:P}^{Me_2P} = -175728$ [*]
FeP [19]	$\Delta H_{298.15K}^{\circ} = -126100, S_{298.15K}^{\circ} = 47.77$
(Fe) ₁ (P) ₁	$C_p = 43.7878 + 0.01985T - 232000T^{-2}$
FeP ₂ [19]	$\Delta H_{298.15K}^{\circ} = -191100, S_{298.15K}^{\circ} = 51.05$
(Fe) ₁ (P) ₂	$C_p = 77.52563 + 0.009348T - 443846T^{-2} - 1.1 \times 10^{-6}T^2$
AlP [*]	$\Delta H_{298.15K}^{\circ} = -163000, S_{298.15K}^{\circ} = 40.34$
(Al) ₁ (P) ₁	$C_p = 48.53 + 0.00457T - 690000T^{-2}$
Al ₂ Fe [30]	$G_{Al_2Fe}^{\circ} = 2G_{Al(FCC)}^{\circ} + G_{Fe(BCC)}^{\circ} - 94850 + 13.42T$
(Al) ₂ (Fe) ₁	
Al ₅ Fe ₂ [30]	$G_{Al_5Fe_2}^{\circ} = 5G_{Al(FCC)}^{\circ} + 2G_{Fe(BCC)}^{\circ} - 217301 + 34.83T$
(Al) ₅ (Fe) ₂	

* optimized in the present study

5.3.1 The Fe-P and Fe-Al Systems

The Fe-P system was optimized by present authors [19] using the CALPHAD approach. The Fe-Al system assessed by Sundman et al. [29] was modified by Phan et al. [30]. In particular, they applied MQM to the liquid phase. The optimized parameters of the above Fe-P and Fe-Al systems were adopted in the present study. The calculated phase diagrams of the Fe-P and Fe-Al systems are plotted in **Fig. 5.1**. With suppression of gas phase, 3 solutions including liquid, FCC_A1 and BCC_A2 and 4 stoichiometric compounds including Fe₃P, Fe₂P, FeP and FeP₂ are considered in the Fe-P system [19]. P is soluble in γ -Fe and α -Fe of the Fe-rich region, as shown in **Fig. 5.1(a)**. In the Fe-Al system, 5 solutions including liquid, FCC_A1, BCC_A2, BCC_B2, Al₈Fe₅, Al₁₃Fe₄ and stoichiometric compounds Al₂Fe, and Al₅Fe₂ are taken into account.



(a)

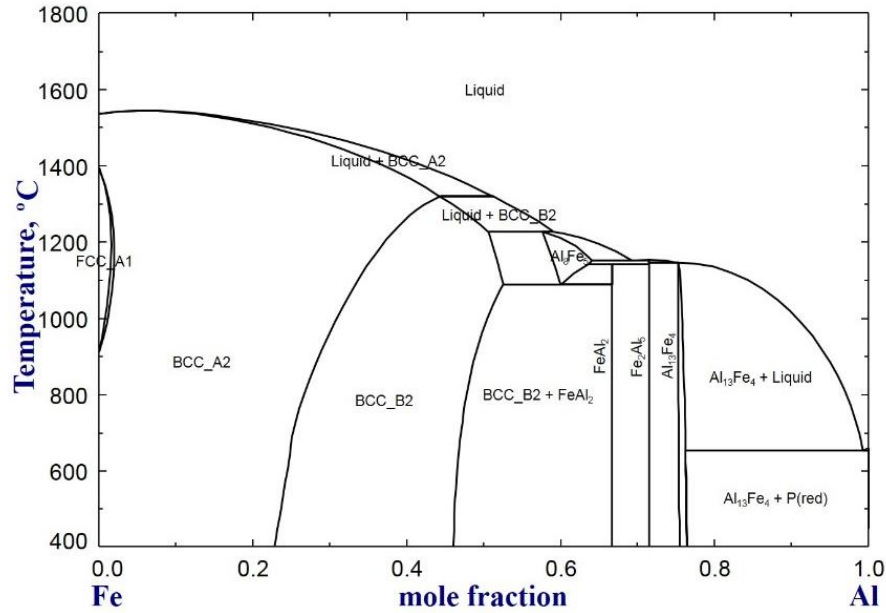
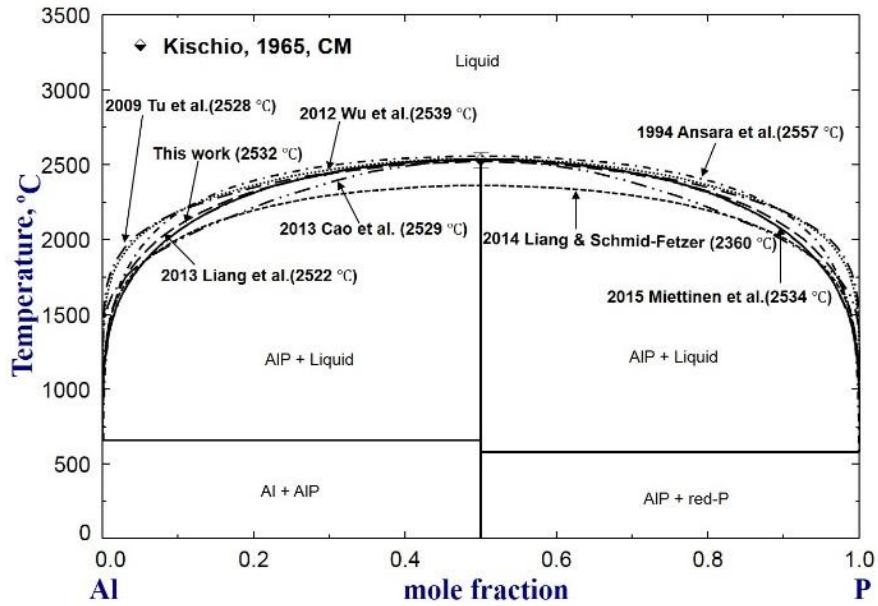


Figure 5.1 Optimized phase diagrams of the (a) Fe-P system [19] and (b) Fe-Al system [30]

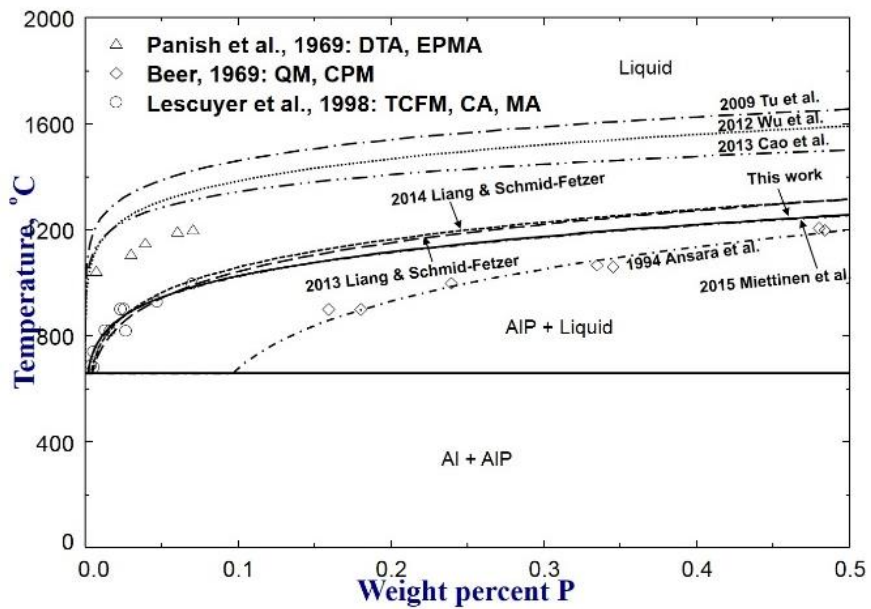
5.3.2 The Al-P System

In the Al-P system, AlP is well known as the only stable stoichiometric compound. White and Bushey [37] adopted a few approaches to produce AlP and eventually confirmed AlP as the only stable intermediate stoichiometric aluminum phosphide in the Al-P system, which was also supported by Panish and Ilegems [38], and Ilegems and Panish [39,40]. The crystal structure of AlP was characterized as ZnS-blende cubic type [37,41,42]. The melting point of AlP was experimentally determined as 2530 ± 30 °C by Kischio [43]. The liquidus of the Al-rich region was investigated experimentally by Panish et al. [44], Beer [45], and Lescuyer et al. [46]. The present Al-P phase diagram is compared with previous one in **Fig. 5.2** along with experimental data. According to the present optimization, the melting temperature of AlP is calculated to be 2532 °C, compared to 2557 °C by Ansara et al. [20], 2528 °C by Tu et al. [21], 2539 °C by Wu et

al. [22], 2529 °C by Cao et al. [18], 2522 °C by Liang et al. [23], 2360 °C by Liang and Schmid-Fetzer [24], and 2534 °C by Miettinen et al. [25]. That is, the melting point of AlP reported by Kischio [43] was basically favored in all the assessments except in the recent one by Liang and Schmid-Fetzer [24]. However, the liquidus of the Al-rich and P-rich regions are very scattering among the assessments. As indicated in **Fig. 5.2(b)**, the experimental data of P dissolution in molten Al were neglected by Tu et al. [21], Wu et al. [22], and Cao et al. [18]. Liang and Schmid-Fetzer [24] modified their earlier result [23] with respect to the experiments conducted by Lescuyer et al. [46], but at the sacrifice of accuracy in reproducing the melting point of AlP. Beer [45] equilibrated AlP with molten Al at 900 to 1200 °C to measure the solubility of P in quenched samples using colorimetric phosphovanadomolybdate method (CPM). The accuracy of his experimental data relies too much on the dissolution and reprecipitation of AlP crystals in the liquid. Panish et al. [44] estimated the solubility of P in liquid Al based on the solubility of P in Ga-rich Ga-Al liquid solution with assumption of ideal mixing of Ga and Al. This assumption can result in big errors in the solubility of P in pure Al despite small interaction between Ga and Al. Lescuyer et al. [46] measured the concentration of P in two types of samples: a few hundred grams of isothermally filtered liquid Al-P alloy and isolated isothermally filtered liquid Al-P drops. The accuracy of their experimental results can be ensured by two analyses. As can be seen in **Fig. 5.2(b)**, the data by Lescuyer et al. [46] are favored in the present study and by Miettinen et al. [25]. No experimental data are available in the P-rich region due to high vaporization of P.



(a) full composition range



(b) Al-rich side

Figure 5.2 The Al-P phase diagram in the (a) full composition and (b) Al-rich region

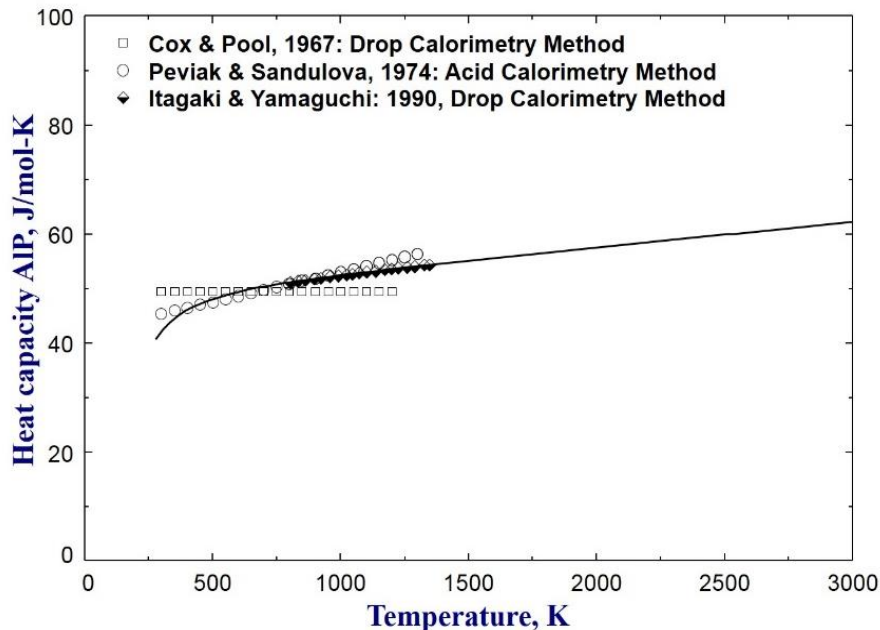


Figure 5.3 Heat capacity of AlP against the temperature

The heat capacity of AlP compound is plotted in **Fig. 5.3** along with a few sets of data obtained from calorimetry experiments [47-49]. The constant heat capacity from 300 K to 1200 K by Cox and Pool [47] is less likely. In contrast, the data by Peviak and Sandulova [48] and Itagaki and Yamaguchi [49] are more favored in this work to obtain the C_p of stoichiometric AlP compound.

The standard enthalpy of formation $\Delta H_{298.15 K}^\circ$ and standard entropy $S_{298.15 K}^\circ$ of AlP are summarized in **Table 5.3** and **5.4**, respectively. As listed in **Table 5.3**, Wang et al. [42] obtained a value of $\Delta H_{298.15 K}^\circ = -138.80 \pm 8.37$ kJ/mol as the standard enthalpy of AlP by means of oxygen bomb calorimetry. Peviak and Sandulova [48] determined a much more negative value ($\Delta H_{298.15 K}^\circ = -180.33 \pm 9.62$ kJ/mol) from the heat of reaction $3\text{H}_2\text{SO}_4 + \text{AlP} = \text{Al}_2(\text{SO}_4)_3 + 2\text{PH}_3$. In comparison, $\Delta H_{298.15 K}^\circ = -165.27 \pm 2.09$ kJ/mol by Kischio [43] using HCl solution

calorimetry method and 163.15 ± 1.72 kJ/mol by Martosudirdjo and Pratt [50] using precipitation calorimetry method are more favored in the present optimization ($\Delta H_{298.15 K}^{\circ} = -163.15$ kJ/mol).

There was no available experimental data on the standard entropy ($S_{298.15 K}^{\circ}$) of stoichiometric AlP compound. Various estimations [52-55] and assessments [18,21-25] of $S_{298.15 K}^{\circ}$ of AlP range from 36.00 to 57.39 J/mol/K, excluding an incredibly high value (175.32 J/mol/K) given by Ansara et al. [20]. In the present study, the standard entropy ($S_{298.15 K}^{\circ}$) of AlP was determined as 40.34 J/mol/K, as listed in **Table 5.4**. According to the currently optimized $\Delta H_{298.15 K}^{\circ}$, $S_{298.15 K}^{\circ}$ and C_P of AlP, the partial pressures of Al(g) and P₂(g) in equilibrium with solid AlP, which were obtained from Knudsen effusion experiments by Maria et al. [56], were well reproduced along with a wide temperature range, as shown in **Fig. 5.4**.

Table 5.3 Standard enthalpy of formation ($\Delta H_{298.15 K}^{\circ}$) of AlP in the Al-P system

$\Delta H_{298.15 K}^{\circ}$, kJ/mol	Methods	References
-138.80 ± 8.37	Oxygen Bomb Calorimetry	Wang et al. [42]
-165.27 ± 2.09	Acid Solution Calorimetry	Kischio [43]
-180.33 ± 9.62	Acid Solution Calorimetry	Peviak & Sandulova [48]
-163.15 ± 1.72	Precipitation Calorimetry	Martosudirdjo & Pratt [50]
-148.56	Assessment	Ansara et al. [20]
-102.00	Assessment	Tu et al. [21]
-166.52	Assessment	Wu et al. [22]
-148.00	Assessment	Cao et al. [18]
-163.20	Assessment	Liang et al. [23]

-163.20	Assessment	Liang & Schmid-Fetzer [24]
-163.69	Assessment	Miettinen et al. [25]
-163.15	Assessment	This work

Table 5.4 Standard entropy ($S_{298.15 K}^{\circ}$) of AlP in the Al-P system

$S_{298.15 K}^{\circ}$, J/mol/K	Methods	References
38.06	Estimation	Sharifov [51]
39.36	Estimation	Karapet'yants & Karapet'yants [52]
46.89 ± 2.51	Estimation	Marina et al. [53]
47.28	Estimation	Voronin & Nashelskii [54]
47.30	Estimation	Kubaschewski & Alcock [55]
175.32	Assessment	Ansara et al. [20]
57.39	Assessment	Tu et al. [21]
47.28	Assessment	Wu et al. [22]
55.11	Assessment	Cao et al. [18]
40.39	Assessment	Liang et al. [23]
36.00	Assessment	Liang & Schmid-Fetzer [24]
42.11	Assessment	Miettinen et al. [25]
40.34	Assessment	This work

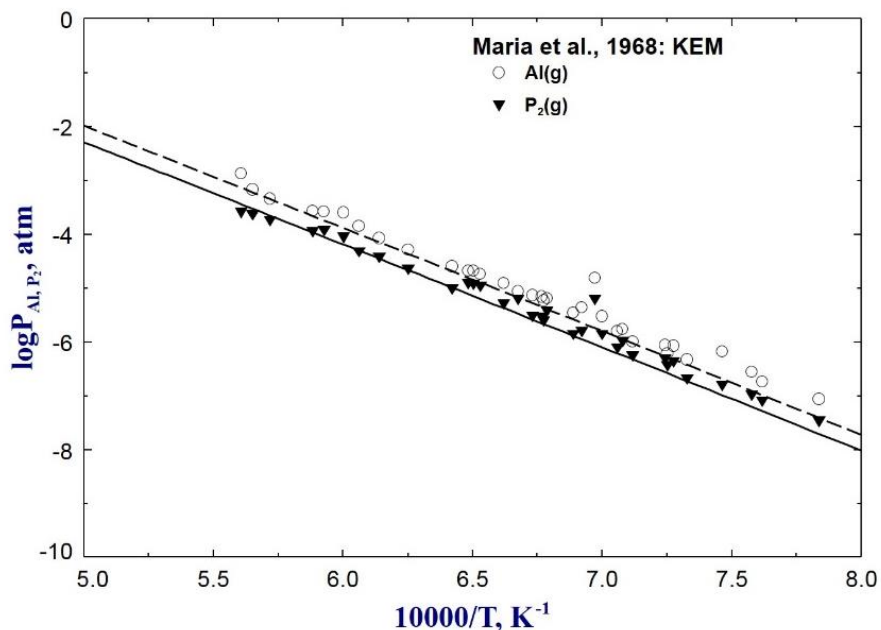


Figure 5.4 Vaporization pressures of Al(g) and P₂(g) above solid AlP phase

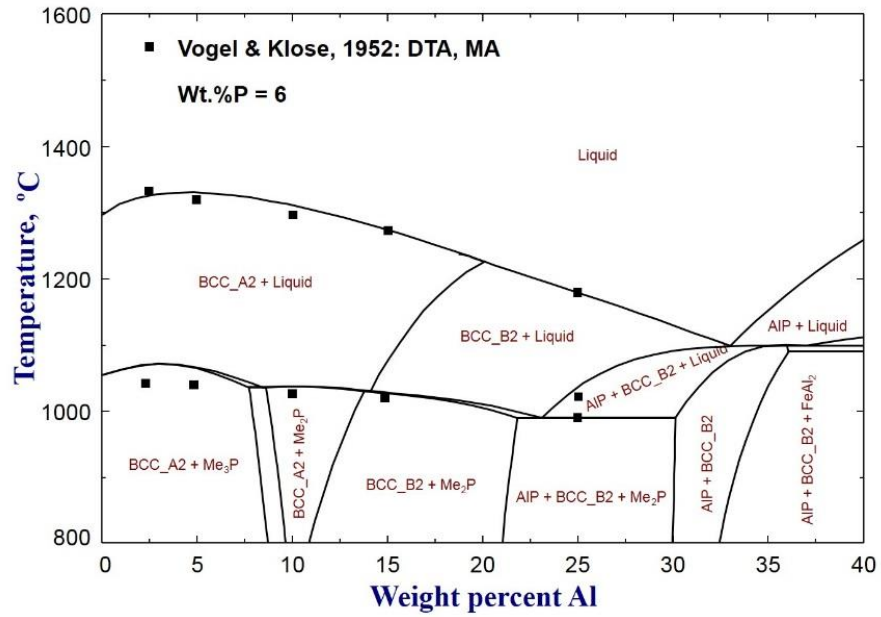
5.3.3 The Fe-Al-P System

In the ternary Fe-Al-P system, the liquid phase, solid solutions including BCC_A2, BCC_B2, FCC_A1, Al₈Fe₅, Al₁₃Fe₄, Me₃P and Me₂P, and stoichiometric compounds including FeP, FeP₂, AlP, Al₂Fe, Al₅Fe₂ were taken into account. The parameters of FCC_A1, BCC_A2 and BCC_B2 phases in the Al-P system were optimized to reproduce phase equilibria of the ternary Fe-Al-P system. In addition, the solubility of Al in Fe₃P and Fe₂P were also calculated. It should be noted that no ternary parameter was necessary for FCC_A1, BCC_A2 and BCC_B2 solid solutions.

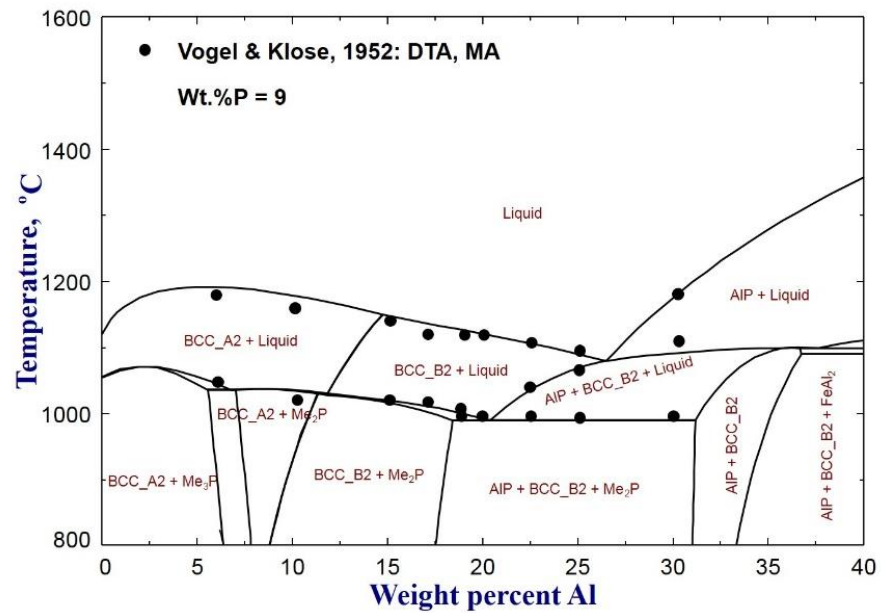
5.3.3.1 Phase Diagram

Vogel and Klose [57] carried out a series of experiments to study the liquidus and solidus of the ternary Fe-Al-P system by means of differential thermal analysis (DTA) and microscopic analysis (MA). Experimental results of the Fe-Al-P isopleths at the composition of wt. %P = 6 and 9 and

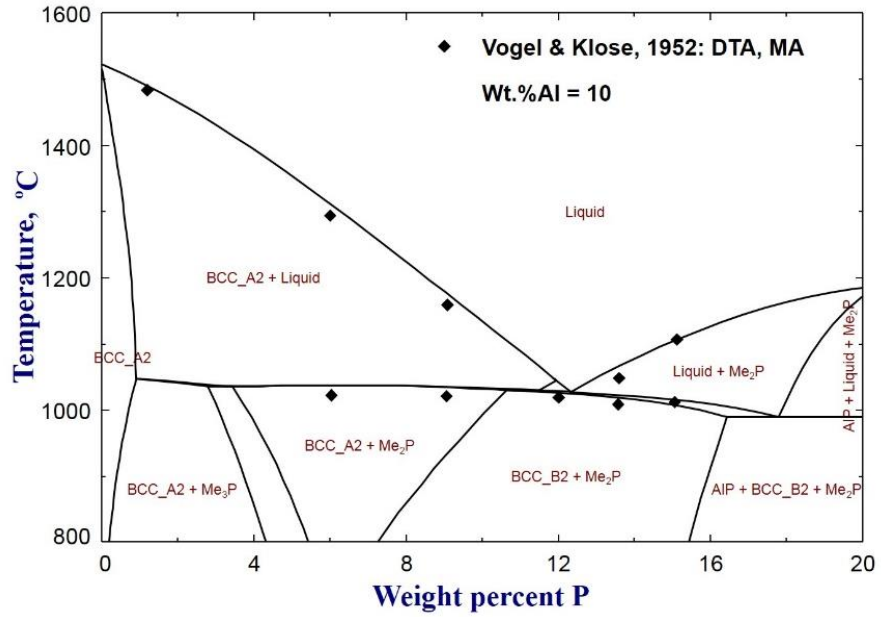
wt. %Al = 10 and 25 were compared with present calculations in **Fig. 5.5**. As can be seen in the figure, experimental data up to 30 wt. %Al and 15 wt. %P were excellently reproduced.



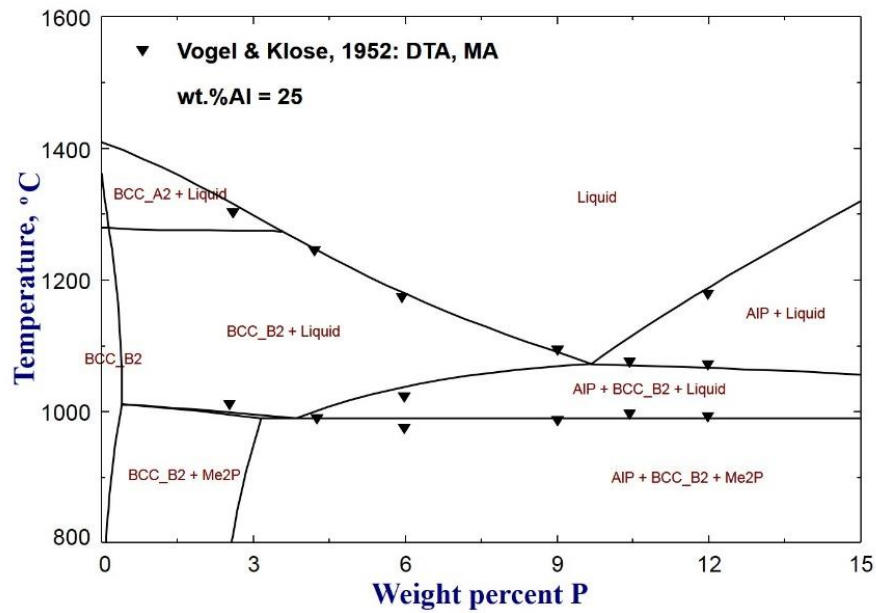
(a)



(b)



(c)



(d)

Figure 5.5 Calculated isopleths of the Fe-Al-P system at (a) wt. %P = 6, (b) wt. %P = 9, (c) wt. %Al = 10, and (d) wt. %Al = 25, compared to the experimental data [57]

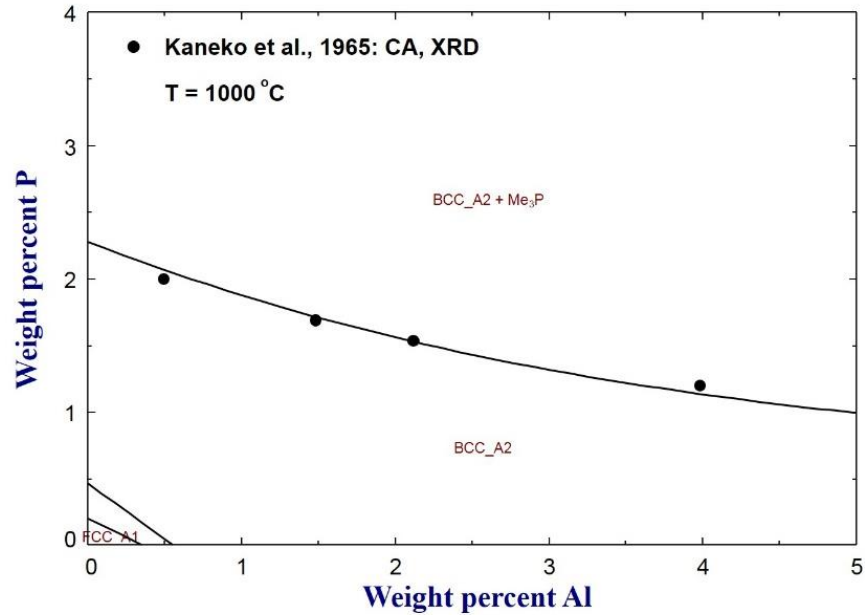
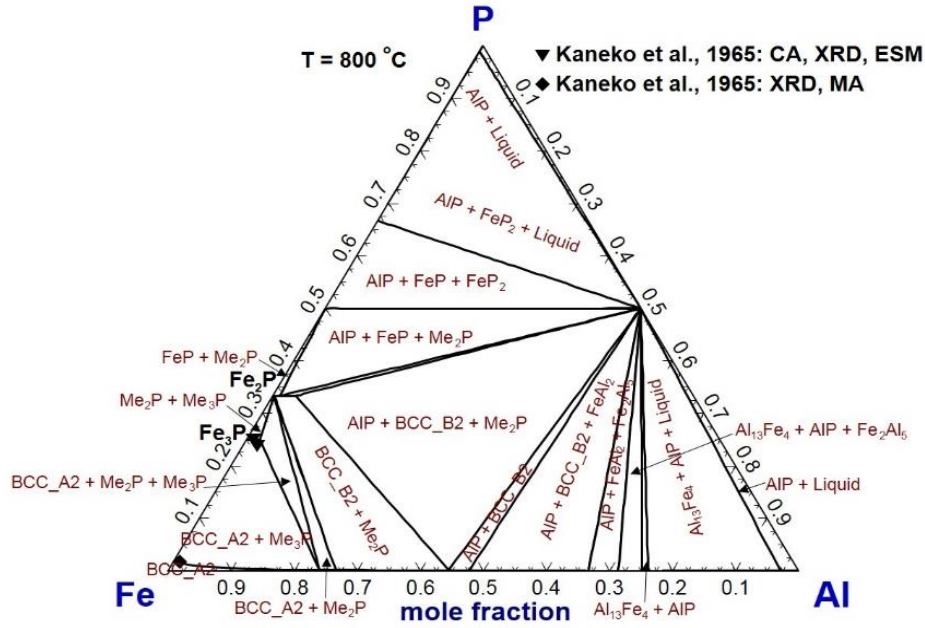


Figure 5.6 Isothermal phase diagram of the Fe-Al-P system on the Fe-rich corner at 1000 °C, compared to experimental data [58]

The solubility of P in α -Fe (BCC_A2) with addition of Al at 1000 °C was investigated by Kaneko et al. [58] using chemical analysis (CA) and X-ray diffraction (XRD) techniques. It was found that saturation of P in BCC_A2 solution results in precipitation of the ternary phosphide Me_3P , which is in the Ni_3P prototype crystal structure. In this work, the isothermal section of the Fe-Al-P system at 1000 °C on the Fe-rich corner was calculated and compared with experimental results in **Fig. 5.6**. As shown in the figure, the solubility of P in ferrite Fe-Al alloys decreases from 2.28 to 1.0 in weight percent with the added Al increasing up to 5 in weight percent, and the present calculation is in good agreement with experimental data.



(c)

Figure 5.7 Isothermal diagrams of the Fe-Al-P system at (a) 450 °C, (b) 650 °C, and (c) 800 °C

Fig. 5.7 shows the isothermal phase diagrams of the Fe-Al-P system at the temperatures of 450 °C, 650 °C and 800 °C. The phase equilibria of the Fe-Al-P system was studied by Wu et al. [22] and Huang [1] by annealing various compositions of alloys within 20 at.%P at 450 °C and 650 °C for 60 days. The equilibrated specimens were analyzed using scanning electron microscopy (SEM) coupled with energy dispersive X-ray spectroscopy (EDS) and X-ray diffraction (XRD). In their experiments [1,22], the Al_2Fe , Al_5Fe_2 , $\text{Al}_{13}\text{Fe}_4$, Me_3P , Me_2P , AIP, disordered BCC_A2 and ordered BCC_B2 phases were observed, which has also been verified by the present database, as shown in **Fig. 5.7(a)** and **(b)**. Kaneko et al. [58,59] found that Fe_3P containing 1.1 wt.%Al was in equilibrium with the ferrite alloy in the composition of Fe – 0.49 wt. %Al – 0.96 wt. %P at 800 °C. In order to reproduce this data, the Gibbs energy of Al_3P in Me_3P was optimized.

5.3.3.2 Liquid Surface Projection

The liquid projection of the Fe-Al-P system is predicted in **Fig. 5.8**. All predicted invariant reactions are summarized in **Table 5.5**. Besides, the available experimental data [57] representing quasi-peritectic reaction $L + \text{Me}_3\text{P} = \text{Me}_2\text{P} + \text{BCC_A2}$ and eutectic reaction $L = \text{AlP} + \text{Me}_2\text{P} + \text{BCC_B2}$ were imposed for comparison. As can be seen in the figure, the calculated eutectic reaction ($L = \text{AlP} + \text{Me}_2\text{P} + \text{BCC_B2}$) is in satisfactory agreement with the experimental datapoint **E1**. However, the prediction of the quasi-peritectic reaction at point **U1** is deviated from the experimental result. This is mainly ascribed to the stability of Me_3P phase relative to Me_2P and BCC_A2 phases. This discrepancy cannot be avoided unless sacrificing the accuracy of phase equilibria presented in **Fig. 5.5** and **Fig. 5.6**. In addition, other invariant reactions at points **U2**, **U3**, **U4**, **U5**, **U6**, **U7**, **U8**, **U9** and **E2** involved in the Fe-Al-P system are also predicted based on the optimized thermodynamic database, as shown in **Fig. 5.8** and **Table 5.5**. To validate these predictions, further experimental studies are still necessary.

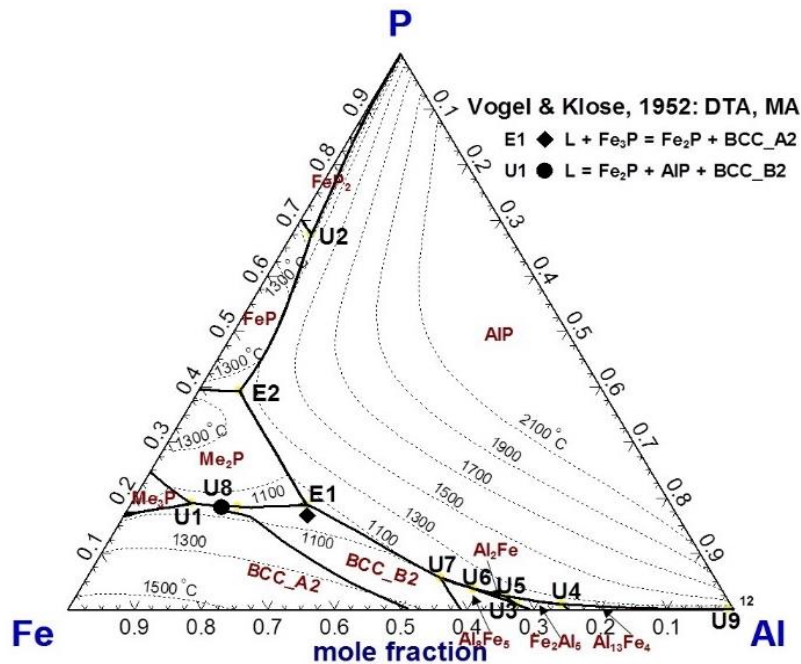


Figure 5.8 Liquid projection of the Fe-Al-P system together with experimental data [57]

Table 5.5 Invariant reactions of the Fe-Al-P system with experimental data [57]

Code	Invariant reactions	x_{Fe}	x_{Al}	x_{P}	$T, ^\circ\text{C}$
U1	$L + \text{Me}_3\text{P} = \text{Me}_2\text{P} + \text{BCC_A2}$	0.720	0.089	0.191	1035
		0.677	0.140	0.183	1020[57]
E1	$L = \text{AlP} + \text{Me}_2\text{P} + \text{BCC_B2}$	0.547	0.264	0.189	989
		0.556	0.275	0.169	995[57]
E2	$L = \text{FeP} + \text{Me}_2\text{P} + \text{AlP}$	0.546	0.061	0.393	1208
U2	$L + \text{FeP} = \text{FeP}_2 + \text{AlP}$	0.297	0.028	0.675	1170
U3	$L + \text{Fe}_2\text{Al}_5 = \text{Al}_8\text{Fe}_5 + \text{Fe}_2\text{Al}$	0.322	0.668	0.01	1142
U4	$L + \text{Fe}_2\text{Al}_5 = \text{Al}_{13}\text{Fe}_4 + \text{AlP}$	0.253	0.737	0.01	1139
U5	$L + \text{Fe}_2\text{Al}_5 = \text{Fe}_2\text{Al} + \text{AlP}$	0.331	0.646	0.023	1130
U6	$L + \text{Fe}_2\text{Al} = \text{Al}_8\text{Fe}_5 + \text{AlP}$	0.372	0.591	0.037	1118
U7	$L + \text{Al}_8\text{Fe}_5 = \text{BCC_B2} + \text{AlP}$	0.412	0.531	0.057	1099
U8	$L + \text{BCC_A2} = \text{Me}_2\text{P} + \text{BCC_B2}$	0.653	0.162	0.185	1030
U9	$L + \text{Al} = \text{Al}_{13}\text{Fe}_4 + \text{AlP}$	0.008	0.992	0	1099

5.3.3.3 Activity of P in Liquid Fe-Al-P Solution

Yamada and Kato [60,61] investigated the influence of Al on the activity coefficient of P in molten Fe at 1600 °C using Knudsen effusion method (KEM). In their experiments, the concentration of P in the samples was maintained at 1 wt.% while that of Al was increased up to 5 wt.%. They calculated $\varepsilon_{\text{Al}}^{\text{P}} = 4.6 \pm 0.7$ at 1600 °C based on their experimental results. In comparison, Ban-ya et al. [62] measured the vapor pressure of phosphorus above the Fe-Al-P melts containing 2.46 to

2.97 wt.% Al at 1400 °C using transportation method (TM), and derived $\epsilon_{Al}^P = 3.57 \pm 0.33$ at 1400 °C. These experimental results are compared with present calculations in **Fig. 5.9**. As shown in the figure, the present calculations are in reasonable agreement with the experimental data [60-62]. According to present optimization, the activity coefficient interaction parameters are determined as $\epsilon_{Al}^P = 2.878$ at 1600 °C and $\epsilon_{Al}^P = 2.655$ at 1400 °C.

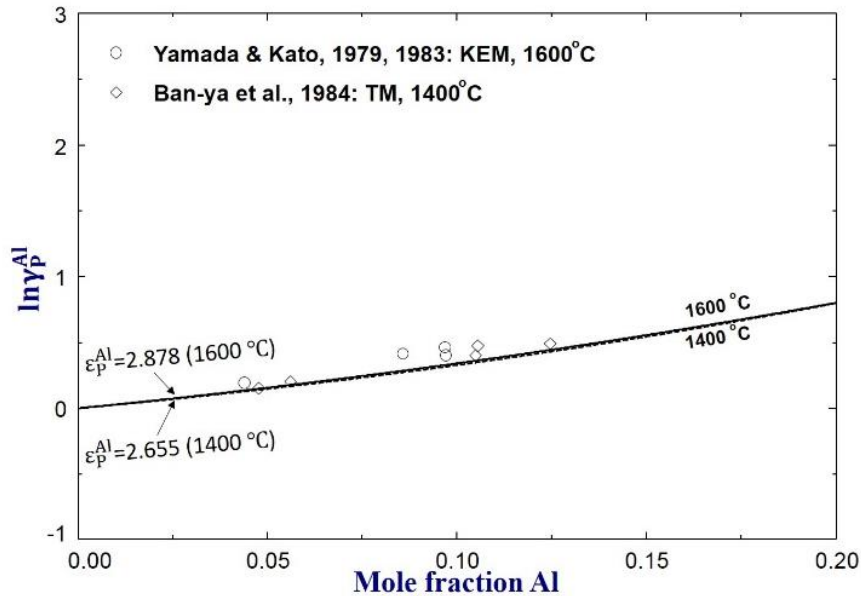


Figure 5.9 Effect of Al on the activity coefficient of P in the liquid Fe-Al-P solution at 1400 °C and 1600 °C, compared to experimental data [60-62]

5.4 Summary

The binary Al-P and ternary Fe-Al-P systems have been thermodynamically optimized in the full composition range based on critical evaluation of available thermodynamic and phase equilibria data. The Modified Quasichemical Model (MQM) and Compound Energy Formalism (CEF) were used to model the liquid and solid solutions, respectively. Dissolution of P in liquid Al, the melting point of stoichiometric AlP compound, and thermodynamic properties of AlP compound in the

binary Al-P system were accurately described. The optimized parameters of binary Al-P system and recently optimized Fe-Al and Fe-P system were combined to describe the ternary Fe-Al-P system. The Gibbs energy of liquid solution was determined with very few parameters by adopting the Toop-type interpolation technique. Besides, the thermodynamic properties and phase equilibria of the Fe-Al-P system have been accurately and consistently reproduced, compared to available experimental data. The thermodynamic database of the Fe-Al-P system developed in the present study will be used as part of new FSstel database in FactSage 8.0 version.

Acknowledgments

We gratefully acknowledge the Steelmaking Consortium Members, Hyundai Steel, Tata Steel Europe, Posco, Doosan Heavy Industry and Construction, SeAh Besteel, Nucor Steel, RioTinto, JFE Steel, Nippon Steel, RHI, Voestalpine, and Natural Science and Engineering Research Council of Canada for supporting the present project. This work was also supported by the National Research Foundation of Korea (NRF) grant funded by the Korean government (MSIT) (No. NRF-2020R1A5A6017701). We would also like to thank the McGill Engineering Doctorate Award (MEDA) program.

References

1. W. M. Huang, The Phase Relations of the Fe-Al-P Ternary System and the Galvannealed Process of Zn-Coating, *Master Dissertation*, Xiangtan University, China, 2011.
2. P. D. Mercer, Factors Which Affect the Alloy Growth Rate in Galvannealed Coatings, *In Galvatech'92: 2nd International Conference on Zinc and Zinc Alloy Coated Steel Sheet*, Dusseldorf, Germany, 1992, p 204-208.

3. Y. Singh, S. C. Joshi, V. Satyawali, and A. Gupta, Acute Aluminium Phosphide Poisoning, What is New?, *The Egyptian Journal of Internal Medicine*, 2014, 26(3), p 99-103.
4. S. W. Fan, L. Yang, and G. Y. Gao, The Electronic Structures and Properties for Carbon Doped Aluminum Phosphide, *Phys. Letters A*, 2019, 383(25), p 3138-3142.
5. M. Sharon and G. Tamizhmani, Transition Metal Phosphide Semiconductors for Their Possible Use in Photoelectrochemical Cells and Solar Chargeable Battery (Saur Vidyut Kosh V), *J. Mater., Science*, 1986, 21(6), p 2193-2201.
6. H. Okamoto, The Fe-P (Iron-Phosphorus) System, *Bull. Alloy Phase Dia.*, 1990, 11(4), p 404-412.
7. M. E. Schlesinger, The Thermodynamic Properties of Phosphorus and Solid Binary Phosphides, *Chem. Reviews*, 2002, 102(11), p 4267-4302.
8. A. J. McAlister, The Al-P (Aluminum-Phosphorus) System, *Bulletin of Alloy Phase Diagrams*, 1985, 6(3), p 222-224.
9. H. Okamoto, Supplemental Literature Review of Binary Phase Diagrams: Al-P, B-Ga, B-Nd, Ba-Ga, Bi-Cs, Ca-Ga, Cd-Gd, Cr-Mo, Gd-Ni, Ni-Pb, Ni-Sc, and Sc-Sn, *J. Phase Equilib. Diffus.*, 2015, 36(5), p 518-530.
10. V. Raghavan, The Al-Fe-P(Aluminium-Iron-Phosphorus) System, *Phase Diagrams of Ternary Iron Alloys*, 1988, 3, p 9-16.
11. V. Raghavan, The Al-Fe-P(Aluminium-Iron-Phosphorus) System, *J. Alloy Phase Dia.*, 1989, 5(1), p 32-39.
12. V. Raghavan, Phase Diagram Updates and Evaluations of the Al-Fe-P, B-Fe-U, Bi-Fe-Zn, Cu-Fe-Zn, Fe-Si-Zn and Fe-Ti-V Systems, *J. Phase Equilib. Diffu.*, 2013, 34(3), p 230-243.

13. R. Schmid-Fetzer and V. Tomashik, Aluminium-Iron-Phosphorus, *Iron Systems, Part 1*, Springer, Berlin, Heidelberg, 2008, p 172-183.
14. P. Gustafson, Internal Report IM-2549, *Swedish Institute for Metals Research*, Stockholm, Sweden, 1990.
15. J. H. Shim, C. S. Oh, and D. N. Lee, Thermodynamic Properties and Calculation of Phase Diagram of the Fe-P System, *J. Korean. Inst. Met. Mater.*, 1996, 34(11), p 1385-1393.
16. H. Ohtani, N. Hanaya, M. Hasebe, S. I. Teraoka, and M. Abe, Thermodynamic Analysis of the Fe-Ti-P Ternary System by Incorporating First-principles Calculations into the CALPHAD Approach, *CALPHAD*, 2006, 30(2), p 147-158.
17. Z. M. Cao, K. P. Wang, Z. Y. Qiao, and G. W. Du, Thermodynamic Reoptimization of the Fe-P System, *Acta Phys. Chim. Sinica*, 2012, 28(1), p 37-43.
18. Z. M. Cao, W. Xie, K. P. Wang, C. J. Niu, G. W. Du, and Z. Y. Qiao, Thermodynamic Optimization of the Al-Fe-P Ternary System, *Acta Phys. Chim. Sinica*, 2013, 29(10), p 2148-2156.
19. Z. M. You and I. H. Jung, Critical Evaluation and Optimization of the Fe-P System, *Metall. Mater. Trans. B*, 2020. (published DOI: <https://doi.org/10.1007/s11663-020-01939-0>)
20. I. Ansara, C. Chatillon, H. L. Lukas, T. Nishizawa, H. Ohtani, K. Ishida, and T. G. Chart, A Binary Database for III-V Compound Semiconductor Systems, *CALPHAD*, 1994, 18(2), p 177-222.
21. H. Tu, F. Yin, X. Su, Y. Liu, and X. Wang, Experimental Investigation and Thermodynamic Modeling of the Al-P-Zn Ternary System, *CALPHAD* 2009, 33(4), p 755-760.

22. C. Wu, W. Huang, X. Su, H. Peng, J. Wang, and Y. Liu, Experimental Investigation and Thermodynamic Calculation of the Al-Fe-P System at Low Phosphorus Contents, *CALPHAD*, 2012, 38, p 1-6.
23. S. M. Liang and R. Schmid-Fetzer, Thermodynamic Assessment of the Al-P System Based on Original Experimental Data, *CALPHAD*, 2013, 42, p 76-85.
24. S. M. Liang and R. Schmid-Fetzer, Corrigendum to “Thermodynamic Assessment of the Al-P System Based on Original Experimental Data”[*CALPHAD* 42 (2013) 76-85], *CALPHAD*, 2014, 100(45), p 251-253.
25. J. Miettinen, S. Louhenkilpi, and G. Vassilev, Thermodynamic Description of Ternary Fe-X-P Systems. Part 9: Fe-Al-P, *J. Phase Equilib. Diffu.*, 2015, 36(4), p 317-326.
26. D. Pelton, S. A. Degterov, G. Eriksson, C. Robelin, and Y. Dessureault, The Modified Quasichemical Model I-Binary Solutions, *Metall. Mater. Trans. B*, 2000, 31(4), p 651-659.
27. D. Pelton and P. Chartrand, The Modified Quasi-chemical Model: Part II. Multicomponent Solutions, *Metall. Mater. Trans. A*, 2001, 32(6), p 1355-1360.
28. M. Hillert, The Compound Energy Formalism, *J. Alloys Compounds*, 2001, 320(2), p 161-176.
29. B. Sundman, I. Ohnuma, N. Dupin, U. R. Kattner, and S. G. Fries, An Assessment of the Entire Al-Fe System Including D03 Ordering, *Acta Mater.*, 2009, 57(10), p 2896-2908.
30. A. T. Phan, M. K. Paek, and Y. B. Kang, Phase Equilibria and Thermodynamics of the Fe-Al-C System: Critical Evaluation, Experiment and Thermodynamic Optimization, *Acta Mater.*, 2014, 79, p 1-15.
31. W. Bale, P. Chartrand, S. A. Degterov, G. Eriksson, K. Hack, R. B. Mahfoud, and S. Petersen, FactSage Thermochemical Software and Databases, *CALPHAD*, 2002, 26(2), p 189-228.

32. T. Dinsdale, SGTE Data for Pure Elements, *CALPHAD*, 1991, 15(4), p 317-425.
33. P. Vončka Leitner, D. Sedmidubský, and P. Svoboda, Application of Neumann-Kopp Rule for the Estimation of Heat Capacity of Mixed Oxides, *Thermoch. Acta*, 2010, 497(1-2), p 7-13.
34. G. Inden, Project Meeting CALPHAD V, Max-Planck-Inst, *Eisenforschung*, Dusseldorf, Germany, 1976, p 111.
35. M. Hillert and M. Jarl, A Model for Alloying in Ferromagnetic Metals, *CALPHAD*, 1978, 2(3), p 227-238.
36. W. Huang, An Assessment of the Fe-Mn System, *CALPHAD*, 1989, 13(3), p 243-252.
37. W. E. White and A. H. Bushey, Aluminum Phosphide-Preparation and Composition, *J. American Chem. Soc.*, 1944, 66(10), p 1666-1672.
38. B. Panish and M. Ilegems, Phase Equilibria in Ternary III-V Systems, *Progress in Solid State Chemistry*, 1972, 7, p 39-83.
39. M. Ilegems and M. B. Panish, Phase Diagram of the System Al-Ga-P, *J. Crystal Growth*, 1973, 20(2), p 77-81.
40. M. Ilegems and M. B. Panish, Phase Equilibria in III-V Quaternary Systems-Application to Al-Ga-P-As, *J. Phys. Chem. Solids*, 1974, 35(3), p 409-420.
41. V. M. Goldschmidt, Geochemical Distribution Laws of the Elements. VIII. Researches on the Structure and Properties of Crystals, *Skr. Akad. Oslo*, 1927, 1926(8), p 7-156.
42. C. Wang, M. Zaheeruddin, and L. H. Spinar, Preparation and Properties of Aluminum Phosphide, *J. Inorg. Nuclear Chem.*, 1963, 25(3), p 326-327.
43. W. Kischio, Formation Enthalpy of Aluminum Phosphide, *J. Inorg. Nuclear Chem.*, 1965, 27(3), p 750-751.

44. M. B. Panish, R. T. Lynch, and S. Sumski, Phase and Thermodynamic Properties of the Ga-Al-P System-Solution Epitaxy of Ga_xAl_{1-x}P and AlP AND, *Trans. Met. Soc. AIME*, 1969, 245(3), p 559-563.
45. S. Z. Beer, The Solution of Aluminum Phosphide in Aluminum, *J. Electrochem. Soc.*, 1969, 116(2), p 263-265.
46. H. Lescuyer, M. Allibert, and G. Laslaz, Solubility and Precipitation of AlP in Al-Si Melts Studied with a Temperature Controlled Filtration Technique, *J. Alloys Compounds*, 1998, 279(2), p 237-244.
47. R. H. Cox and M. J. Pool, Heat Contents and Heats of Fusion of III-V Compounds, *J. Chem. Engineer. Data*, 1967, 12(2), p 247-248.
48. S. Peviak and A. Sandulova, Thermodynamic Characteristics of Aluminum Phosphide, *Izv. Akad. Nauk SSSR Neorg. Mater.*, 1974, 10, p 146-147.
49. K. Itagaki and K. Yamaguchi, High Temperature Heat Contents of III-V Semiconductor Systems, *Thermochimica Acta*, 1990, 163, p 1-12.
50. S. Martosudirdjo and J. N. Pratt, Calorimetric Studies of the Heats of Formation of IIIB-VB Adamantine Phases, *Thermochimica Acta*, 1974, 10(1), p 23-31.
51. K. A. Sharifov, Calculation of Entropy of Solids, *Russ. J. Phys. Chem., USSR*, 1966, 40(1), p 113.
52. M. K. Karapetyants and M. L. Karapetyants, Tables of Some Thermodynamic Properties of Various Substances, *Khim. Tekh. Inst., Moscow*, 1961, (34), p 166.
53. L. I. Marina, A. Y. Nashel'skii, and B. A. Sakharov, Heats of Atomization and Some Thermochemical Constants of A III B V Compounds, *Chem. Bonds in Solids, Springer, Boston, MA*, 1972, p 124-129.

54. G. F. Voronin, Estimation of the Standard Entropies of Chemical Compounds, *Zhur Fiz Khim*, 1970, 44(12), p 3013-3017.
55. O. Kubaschewski and C. B. Alcock, Metallurgical Thermochemistry, 5th Edition, *Pergamon Press*, Elmsford, NY, 1979, p 360.
56. G. D. Maria, K. A. Gingerich, and V. Piacente, Vaporization of Aluminum Phosphide, *J. Chem. Phys.*, 1968, 49(10), p 4705-4710.
57. R. Vogel, The Diagram of State Iron-Iron Phosphide-Aluminum Phosphide-Aluminum, *Arch. Eisen.*, 1952, 23, p 287-291.
58. H. Kaneko, T. Nishizawa, K. Tamaki, and A. Tanifuji, Solubility of Phosphorus in α and γ -Iron, *Nippon Kinzoku Gakkai-Si*, 1965, 29, p 166-170.
59. H. Kaneko, Phosphide-Phases in Ternary Alloys of Iron, Phosphorus and Other Elements, *J. Japan Inst. Metals*, 1965, 29, p 159-165.
60. K. Yamada and E. Kato, Mass Spectrometric Determination of Activities of Phosphorus in Liquid Fe-P-Si, Al, Ti, V, Cr, Co, Ni, Nb, and Mo Alloys, *Tetsu-to-Hagané*, 1979, 65(2), p 273-280.
61. K. Yamada and E. Kato, Effect of Dilute Concentrations of Si, Al, Ti, V, Cr, Co, Ni, Nb and Mo on the Activity Coefficient of P in Liquid Iron, *Trans. Iron Steel Ins. Japan*, 1983, 23(1), p 51-55.
62. S. Ban-ya, N. Maruyama, and S. Fujino, The Effects of C, Si, Al, and B on the Activity of Phosphorus in Liquid Iron, *Tetsu-to-Hagané*, 1983, 69(8), p 921-928.

Chapter 6: Critical Thermodynamic Modeling of the Fe-Si-P and Fe-C-P Systems

Zhimin You¹, In-Ho Jung²

1. Department of Mining and Materials Engineering, McGill University, 3610 University Street,
Montreal, QC, H3A 0C5, Canada

2. Department of Materials Science and Engineering, and Research Institute of Advanced
Materials (RIAM), Seoul National University, 1 Gwanak-ro, Gwanak-gu, Seoul, 08826, South
Korea

(To be submitted)

Abstract

Critical evaluation and optimization of all available thermodynamic and phase diagram data of the Fe-Si-P system and Fe-C-P system has been performed using the CALculation of PHase Diagrams (CALPHAD) method to obtain a set of Gibbs energy functions of all the phases in the systems. The liquid phases and solid solutions were modeled using the Modified Quasichemical Model employing short-range ordering in the pair fraction approximation and Compound Energy Formalism considering crystallographic structures, respectively. Accurate descriptions on the thermodynamic properties of liquid solutions and phase equilibria of the Fe-Si-P and Fe-C-P systems have been achieved by resolving the discrepancies among the experimental data. The developed thermodynamic database can be used to predict the behavior of P in the Fe-Si and Fe-C alloys at any compositions and temperatures.

Keywords: Optimization, Fe-Si-P system, Fe-C-P system, Thermodynamic properties, Phase equilibria

6.1 Introduction

Silicon electrical steels (or silicon steels) with excellent magnetic properties have aroused much attention among researchers. As typical soft magnetic materials combining high saturation magnetization and low magneto-striation, silicon steels are usually used to produce electric motors in the industry of green energy generation and vehicles. Besides, Advanced High Strength Steels (AHSS) such as TWIP, TRIP steels containing 1-3 wt.% Si are always applied in the automotive industry. The mechanical and electromagnetic properties of these silicon steels are highly depending on their compositions and microstructure features. On the other hand, production of ferrosilicon alloys needs tight control of impurities such as carbon, phosphorus etc.

Many thermodynamic assessments and reviews [1-8] and assessments [9-35] were performed to describe the thermodynamic behaviors of the sub-systems of the Fe-Si-P and Fe-C-P systems. However, some discrepancies such as thermodynamic stability of Fe phosphides and activity of P in molten Fe, Gibbs energy of P₂ dissolution in molten Si, stability of BCC phase at high-temperature of the Fe-C region, liquidus and solidus boundaries of the Fe-C-P system, etc. left in previous assessments degrade the reliability of currently available thermodynamic database. To resolve the above discrepancies, development of a new thermodynamic database of the Fe-Si-C-P system with more accuracy and consistency will very necessary for producing the materials with required properties.

Thermodynamic database based on the CALculation of PHase Diagrams (CALPHAD) method is a powerful tool for new materials design and process optimization. The database of a target system is developed by means of thermodynamic modeling (optimization), aiming at obtaining one set of

consistent Gibbs energies of all phases as functions of temperature and composition. In the optimization, all available phase equilibria and thermodynamic data such as activity, entropy, enthalpy, and Gibbs energy, etc are critically evaluated simultaneously. The discrepancies between available data are resolved in the critical evaluation process, and the Gibbs energy functions for all related phases in the target system are derived. Prediction on unexplored thermodynamic properties and phase equilibria can be possible by interpolations and extrapolations in a thermodynamically correct manner.

In the present study, all sub-systems of the Fe-Si-P and Fe-C-P systems were modeled using the Modified Quasichemical Model (MQM) [36,37] and Compound Energy Formalism (CEF) [38] for the liquid phases and solid solutions, respectively. The optimized thermodynamic database of the Fe-Si-P and Fe-C-P systems, as the basis of the quaternary Fe-Si-C-P system, will be included in the new high alloy steel Fe-Mn-Al-Si-Cr-Ni-Ti-Nb-C-N-O-P database. The recently optimized Fe-P [14], Si-P [26], and Fe-Si [24], and Fe-C [32] systems using CALculation of PHase Diagrams (CALPHAD) approach were adopted in the present optimization. The optimized thermodynamic properties of liquid solutions, various vertical section diagrams, isothermal phase diagrams, and liquid surface projections of ternary Fe-Si-P and Fe-C-P systems will be presented. All the calculations were carried out using FactSage software [39].

6.2. Thermodynamic Models

6.2.1 Pure Elements and Stoichiometric Compounds

The Gibbs energies of elemental solid and liquid Fe, Si, C, P were taken from the Scientific Group Thermodata Europe (SGTE) database [40]. The Gibbs energies of all involved stoichiometric

compounds in the Fe-Si-P and Fe-C-P systems were optimized based on their heat capacity, standard enthalpy of formation and standard entropy at 298.15 K. In the present study, Gibbs energies of stoichiometric iron phosphides Fe₃P, Fe₂P, FeP and FeP₂ in the Fe-P system, silicon phosphides SiP and SiP₂ in the Si-P system, ferrosilicides Fe₂Si, Fe₅Si₃, FeSi, FeSi₂ and Fe₃Si₇ in the Fe-Si system, cementite Fe₃C in the Fe-C system, and iron phosphosilicides FeSi₄P₄ in the ternary Fe-Si-P system were calculated using the following equation:

$$G_T^\circ = \left(\Delta H_{298.15K}^\circ + \int_{298.15}^T C_P dT \right) - T \left(S_{298.15K}^\circ + \int_{298.15}^T \frac{C_P}{T} dT \right) \quad (6.1)$$

here G_T° is the Gibbs energy at temperature T , $\Delta H_{298.15K}^\circ$ and $S_{298.15K}^\circ$ are standard enthalpy of formation and standard entropy at 298.15 K, and C_P is the heat capacity. The heat capacity of each stoichiometric compound was expressed as a function of temperature by fitting experimental data. For the compounds with no available experimental data, C_P was estimated using Neumann-Kopp (NK) rule [41] or determined C_P functions of other relevant compounds in the same system.

In the cases of pure elements or stoichiometric compounds exhibiting magnetic behavior, an additional Gibbs energy of magnetic contribution term G^{mg} will be applied. In the Fe-Si-P system, magnetic contribution terms apply to Fe(BCC_A2, FCC_A1), Fe₃P and Fe₅Si₃ were determined using the empirical expression proposed by Inden [42] and modified by Hillert and Jarl [43]:

$$G^{mg} = RT \ln(\beta + 1) g(\tau) \quad (6.2)$$

here, τ is expressed as T/T^* and T^* is the critical temperature of magnetic transition associated with Curie temperature T_C for ferromagnetic materials or Neel temperature T_N for antiferromagnetic materials. β is the average magnetic moment per mole of atoms in Bohr magnetons. $g(\tau)$ is a polynomial function derived by Hillert and Jarl [43], as expressed below:

$$g(\tau) = 1 - \left[\frac{79\tau^{-1}}{140P} + \frac{474}{497} \left(\frac{1}{P} - 1 \right) \left(\frac{\tau^3}{6} + \frac{\tau^9}{135} + \frac{\tau^{15}}{600} \right) \right] / D \quad \dots \tau \leq 1 \quad (6.3)$$

$$g(\tau) = - \left(\frac{\tau^{-5}}{10} + \frac{\tau^{-15}}{315} + \frac{\tau^{-25}}{1500} \right) / D \quad \dots \tau > 1 \quad (6.4)$$

where $D = \frac{518}{1125} + \frac{11692}{15975} \left(\frac{1}{P} - 1 \right)$, and the value of P can be considered as the fraction of the

magnetic enthalpy absorbed above the critical temperature depending on the structure. P is 0.40 for the simple BCC_A2 phase while P is 0.28 for other common phases.

6.2.2 Solid Solutions

In the present study, the disordered solid solutions including FCC_A1, BCC_A2, Diamond_A4, Me₃P, Me₂P, MeP and ordered BCC_B2 solid solution in the Fe-Si-P system and all disordered solid solutions including FCC_A1, BCC_A2 in the Fe-C-P system were modeled using Compound Energy Formalism with consideration of their crystallographic structures [38].

6.2.2.1 Disordered FCC_A1, BCC_A2, Diamond_A4 Solid Solutions

In the Fe-Si-P system, FCC_A1, BCC_A2 and diamond_A4 solid solutions were described with the substitutional model (Fe, Si, P)₁(Va)_n, where $n = 1$ for FCC_A1 and diamond_A4 phases and $n = 3$ for BCC_A2 solid solution. The Gibbs energy per formula unit were calculated using the following equation:

$$G_S^{disorder} = \sum_{i=Fe, Si, P} x_i G_i^o + RT \sum_{i=Fe, Si, P} x_i \ln x_i + \sum_{m=0,1,2,\dots} x_{Fe} x_P L_{Fe,P}^m + \sum_{k=0,1,2,\dots} x_{Si} x_P L_{Si,P}^k + \sum_{p=0,1,2,\dots} x_{Fe} x_{Si} L_{Fe,Si}^p + \sum_{q=0,1,2,\dots} x_{Fe} x_{Si} x_P L_{Fe,Si,P}^q + G^{mg} \quad (6.5)$$

where x_i is the mole fraction of component i and G_i° is the molar Gibbs energy of pure solid i ($i = \text{Fe, Si, P}$); R is the gas constant (8.314 J/mol-K) and T is the temperature in Kelvin (K); $L_{Fe,P}^m$, $L_{Si,P}^k$, $L_{Fe,Si}^p$ and $L_{Fe,Si,P}^q$ are the adjustable interaction parameters of relevant binary and ternary systems; G^{mg} is the magnetic contribution to the Gibbs energy.

In the Fe-C-P system, FCC_A1 and BCC_A2 phases were modeled using two sublattice formula $(\text{Fe, P})_1(\text{C, Va})_q$, in which Fe, P atoms are in the substitutional lattice and C, vacancies(Va) are in the interstitial lattice. The Gibbs energy per formula unit were described using CEF as follows:

$$G_S^{sol.} = y_{Fe}y_C G_{Fe:C} + y_{Fe}y_{Va} G_{Fe:Va} + y_P y_C G_{P:C} + y_P y_{Va} G_{P:Va} + RT(y_{Fe} \ln y_{Fe} + y_P \ln y_P) + qRT(y_C \ln y_C + y_{Va} \ln y_{Va}) + \sum_{i=0,1,2,\dots} \left(\sum_{m=C,Va} y_{Fe}y_P y_m L_{Fe,P:m}^i + \sum_{n=Fe,P} y_n y_C y_{Va} L_{n:C,Va}^i \right) + G^{mg} \quad (6.6)$$

here, $q = 1$ for FCC_A1 phase and $q = 3$ for BCC_A2 phase. $L_{Fe,P:m}^i$ and $L_{n:C,Va}^i$ are adjustable interaction parameters between the species in the same sublattice.

6.2.2.2 Ordered BCC_B2 Solid Solution

The BCC solid solution of the Fe-Si-P system exhibits the transition from disordered to ordered crystal structures. The Gibbs energy of BCC solution was modeled considering disordered part described with the model $(\text{Fe, Si, P})(\text{Va})_3$ and ordered part described with the model $(\text{Fe, Si, P})_{0.5}(\text{Fe, Si, P})_{0.5}(\text{Va})_3$. The Gibbs energy contribution of ordered part was calculated as follows:

$$\Delta G_{BCC}^{order} = G_{BCC}^{order}(y_i', y_j'') - G_{BCC}^{order}(y_i', y_j'')_{y_k' = y_k''} \quad (6.7)$$

and,

$$\begin{aligned}
G_{BCC}^{order}(y'_i, y''_j) = & y'_{Fe} y''_{Fe} G_{Fe:Fe} + y'_{Si} y''_{Si} G_{Si:Si} + y'_P y''_P G_{P:P} \\
& + y'_{Fe} y''_{Si} G_{Fe:Si} + y'_{Si} y''_{Fe} G_{Si:Fe} + y'_{Fe} y''_P G_{Fe:P} \\
& + y'_{Si} y''_P G_{Si:P} + y'_P y''_{Fe} G_{P:Fe} + y'_P y''_{Si} G_{P:Si} \\
& + 0.5RT \left(y'_{Fe} \ln y'_{Fe} + y'_{Si} \ln y'_{Si} + y'_P \ln y'_P \right) \\
& + 0.5RT \left(y''_{Fe} \ln y''_{Fe} + y''_{Si} \ln y''_{Si} + y''_P \ln y''_P \right) \\
& + \sum_{i,j,k} y'_i y'_j y''_k L_{i,j,k} + \sum_{i,j,k} y'_k y''_i y''_j L_{k:i,j} + G^{mg}
\end{aligned} \tag{6.8}$$

here i, j, k represent Fe, Si, P. y'_i, y'_j, y'_k and y''_i, y''_j, y''_k are site fractions of component i, j, k in the first and second lattice of the formula $(Fe, Si, P)_{0.5}(Fe, Si, P)_{0.5}(Va)_3$. The Gibbs energy of BCC solid solution with consideration of disorder/order transit was determined from **Eq. (6.9)**:

$$G_{BCC}^{sol.} = G_S^{disorder} + \Delta G_{BCC}^{order} \tag{6.9}$$

In the composition of site fractions of component i in the first sublattice equals to that in the second sublattice ($y'_i = y''_i$), then the ordering contribution ΔG_{BCC}^{order} is nil and the Gibbs energy of BCC is the same as the Gibbs energy of disordered BCC_A2 ($G_S^{disorder}$) calculated in **Eq. (6.5)**. In the case of $y'_i \neq y''_i$, then ordering contribution ΔG_{BCC}^{order} becomes negative and the Gibbs energy of BCC_B2 phase can be calculated using **Eq. (6.9)**.

6.2.2.3 Other Solid Solutions (Me_3P, Me_2P, MeP)

The solid solutions Me_3P, Me_2P and MeP were described using the model $(Fe)_n(P, Si)$, where $n = 3, 2, 1$ for Me_3P, Me_2P and MeP , respectively. The Gibbs energies per formula unit of these three phases calculated based on CEF as follows:

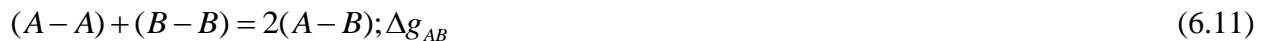
$$G_{Me_nP}^{sol.} = y_P G_{Fe_nP}^\circ + y_{Si} G_{Fe_nSi} + RT \left(y_P \ln y_P + y_{Si} \ln y_{Si} \right) + \sum_{m=0,1,2,\dots} y_P y_{Si} L_{Fe:P,Si}^m + G^{mg} \tag{6.10}$$

here, $G_{\text{Fe}_3\text{P}}^\circ$, $G_{\text{Fe}_2\text{P}}^\circ$ and G_{FeP}° are end-member Gibbs energies, corresponding to the optimized Gibbs energies of stoichiometric Fe_3P , Fe_2P and FeP compounds in the binary Fe-P system [14]. Likewise, $G_{\text{Fe}_3\text{Si}}$, $G_{\text{Fe}_2\text{Si}}$ and G_{FeSi} are end-member Gibbs energies based on BCC_A2 Fe, diamond_A4 Si and additional model parameters; y_P , y_{Si} are site fractions of P and Si in the second sublattice; $L_{\text{Fe:P,Si}}^m$ is the adjustable interaction parameter between P and Si of the second sublattice; G^{mg} is the magnetic contribution to the Gibbs energy.

6.2.3 Liquid Solution

The liquid solutions of all involved sub-systems of the Fe-Si-P and Fe-C-P systems were described using the Modified Quasichemical Model (MQM) [36,37] considering the short-range ordering of the nearest-neighbor atoms. Comparing to the conventional Bragg-Williams Random Mixing Model (BWRMM), the MQM gives a more realistic description of the entropy of liquid solution. In the MQM, the Gibbs energy of pair formation can be expanded as a polynomial in the pair fraction rather than the component fraction and coordination numbers of the components are allowed to vary with composition for reproducing the short-range ordering in liquid solution with less parameters, providing greater flexibility in reproducing experimental data of the binary liquid phases and combining the binary parameters to higher-order systems.

In the case of the binary A - B liquid solution, the atoms A and B are distributed over the quasilattice sites. The atom pair exchanging reaction of liquid A - B solution can be expressed:



here, $(i-j)$ represents the nearest-neighbor pair between components i and j , and Δg_{AB} is the Gibbs energy change of forming 2 moles $(A-B)$ pairs. The Gibbs energy of liquid solution was calculated:

$$G_{AB}^L = (n_A G_A^\circ + n_B G_B^\circ) - T \Delta S_{AB}^{conf.} + n_{AB} (\Delta g_{AB} / 2) \quad (6.12)$$

where n_A and n_B are the numbers of moles of A atoms and B atoms, and G_A° and G_B° are the molar Gibbs energies of pure liquid A and B. $\Delta S_{AB}^{conf.}$ is the configurational entropy of mixing given by random distribution of the (A-A), (B-B) and (A-B) pairs as follows:

$$\Delta S_{AB}^{conf.} = -R(n_A \ln X_A + n_B \ln X_B) - R \left[n_{AA} \ln \left(\frac{X_{AA}}{Y_A^2} \right) + n_{BB} \ln \left(\frac{X_{BB}}{Y_B^2} \right) + n_{AB} \ln \left(\frac{X_{AB}}{2Y_A Y_B} \right) \right] \quad (6.13)$$

here n_{AA} , n_{BB} and n_{AB} are the numbers of moles of (A-A), (B-B) and (A-B) pairs; X_{AA} , X_{AB} and X_{BB} are the pair fraction of the corresponding atom pairs; Y_A and Y_B are the coordination equivalent fractions of atoms A and B. The pair fractions X_{AA} , X_{AB} , X_{BB} and coordination equivalent fractions Y_A , Y_B are calculated as:

$$X_{AA} = n_{AA} / (n_{AA} + n_{AB} + n_{BB}) \quad (6.14)$$

$$X_{AB} = n_{AB} / (n_{AA} + n_{AB} + n_{BB}) \quad (6.15)$$

$$X_{BB} = n_{BB} / (n_{AA} + n_{AB} + n_{BB}) \quad (6.16)$$

$$Y_A = X_{AA} + \frac{1}{2} X_{AB} \quad (6.17)$$

$$Y_B = X_{BB} + \frac{1}{2} X_{AB} \quad (6.18)$$

Δg_{AB} in **Eqs. (6.12)** and **(6.13)** is the model parameter for reproducing the Gibbs energy of the binary A-B solution that can be expanded as a polynomial based on the atomic pair fractions X_{AA} and X_{BB} :

$$\Delta g_{AB} = \Delta g_{AB}^\circ + \sum_{i \geq 1} g_{AB}^{i0} X_{AA}^i + \sum_{j \geq 1} g_{AB}^{0j} X_{BB}^j \quad (6.19)$$

where Δg_{AB}° , g_{AB}^{i0} and g_{AB}^{0j} are the adjustable model parameters that can be functions of the temperature. In the MQM, the coordination numbers of A and B, Z_A and Z_B , can be varied with composition to reproduce the short-range ordering of the solution:

$$\frac{1}{Z_A} = \frac{1}{Z_{AA}^A} \left(\frac{2n_{AA}}{2n_{AA} + n_{AB}} \right) + \frac{1}{Z_{AB}^A} \left(\frac{n_{AB}}{2n_{AA} + n_{AB}} \right) \quad (6.20)$$

$$\frac{1}{Z_B} = \frac{1}{Z_{BB}^B} \left(\frac{2n_{BB}}{2n_{BB} + n_{AB}} \right) + \frac{1}{Z_{BA}^B} \left(\frac{n_{AB}}{2n_{BB} + n_{AB}} \right) \quad (6.21)$$

here Z_{AA}^A is the value Z_A when all nearest neighbors of a A atom are A atoms, and Z_{AB}^A is the value of Z_A when all nearest neighbors of the A atom are B atoms. Z_{BB}^B and Z_{BA}^B are defined in an analogous manner. When extending from the binary systems to the ternary systems, Gibbs energy of the ternary liquid solution can be predicted using proper geometric interpolation technique based on the nature of all the binary systems. In the present study, Toop-type geometric interpolation technique [37] with Fe as the asymmetric component in the Fe-Si-P system and with P as the asymmetric component in the Fe-C-P system were adopted to describe the liquid solutions. If necessary, ternary correction terms will also be introduced to the ternary system for giving more precise description of phase equilibria and thermodynamic properties. The configurational entropy of mixing and Gibbs energy of liquid Fe-Si-P and Fe-C-P solutions were calculated as follows:

$$\Delta S_{Fe,P,Si/C}^{conf.} = -R \sum_{i=Fe,P,Si/C} n_i \ln X_i - R \left[\sum_{j=Fe,P,Si/C} n_{jj} \left(\frac{X_{jj}}{Y_j^2} \right) + \sum_{k,m=Fe,P,Si/C}^{k \neq m} n_{km} \ln \left(\frac{X_{km}}{2Y_k Y_m} \right) \right] \quad (6.22)$$

$$G_{Fe,P,Si/C}^L = \sum_{i=Fe,P,Si/C} n_i G_i^\circ - T \Delta S_{Fe,P,Si/C}^{conf.} + \sum_{j,k=Fe,P,Si/C}^{j \neq k} (n_{jk} / 2) \Delta g_{jk} \quad (6.23)$$

here, Δg_{jk} ($j, k = Fe, Si, C, P$) is the pair formation Gibbs energy depending on the symmetry of each component (Fe, Si, C, P) in the ternary Fe-Si-P and Fe-C-P systems. Therefore, the interaction

model parameters between asymmetric components in the Fe-Si-P system (Δg_{FeSi} , Δg_{FeP}) and Fe-C-P system (Δg_{CP} , Δg_{FeP}) are described as follows:

$$\Delta g_{\text{XZ}} = \Delta g_{\text{XZ}}^{\circ} + \sum_{(i+j) \geq 1} g_{\text{XZ}}^{ij} x_{\text{ZZ}}^i (x_{\text{XX}} + x_{\text{XY}} + x_{\text{ZZ}})^j + \sum_{i \geq 0, j \geq 0, k \geq 1} g_{\text{XZ}(Y)}^{ijk} x_{\text{ZZ}}^i (x_{\text{XX}} + x_{\text{XY}} + x_{\text{ZZ}})^j \left(\frac{Y_Y}{Y_X + Y_Y} \right)^k \quad (6.24)$$

$$\Delta g_{\text{YZ}} = \Delta g_{\text{YZ}}^{\circ} + \sum_{(i+j) \geq 1} g_{\text{YZ}}^{ij} x_{\text{ZZ}}^i (x_{\text{XX}} + x_{\text{XY}} + x_{\text{ZZ}})^j + \sum_{i \geq 0, j \geq 0, k \geq 1} g_{\text{YZ}(X)}^{ijk} x_{\text{ZZ}}^i (x_{\text{XX}} + x_{\text{XY}} + x_{\text{ZZ}})^j \left(\frac{Y_X}{Y_X + Y_Z} \right)^k \quad (6.25)$$

The interaction model parameters between symmetric components (Δg_{SiP} in the Fe-Si-P system and Δg_{CP} in the Fe-C-P system) were calculated using the following equation:

$$\Delta g_{\text{XY}} = \Delta g_{\text{XY}}^{\circ} + \sum_{(i+j) \geq 1} g_{\text{XY}}^{ij} \left(\frac{x_{\text{XX}}}{x_{\text{XX}} + x_{\text{XY}} + x_{\text{YY}}} \right)^i \left(\frac{x_{\text{YY}}}{x_{\text{XX}} + x_{\text{XY}} + x_{\text{YY}}} \right)^j + \sum_{i \geq 0, j \geq 0, k \geq 1} g_{\text{XY}(Z)}^{ijk} \left(\frac{x_{\text{XX}}}{x_{\text{XX}} + x_{\text{XY}} + x_{\text{YY}}} \right)^i \left(\frac{x_{\text{YY}}}{x_{\text{XX}} + x_{\text{XY}} + x_{\text{YY}}} \right)^j Y_X^k \quad (6.26)$$

Here, X, Y represent asymmetric components and Z represents the symmetric component in the Fe-Si-P system and Fe-C-P system. g_{XY}^{ij} , g_{XZ}^{ij} , g_{YZ}^{ij} are the binary liquid parameters; $g_{\text{XY}(Z)}^{ijk}$, $g_{\text{XZ}(Y)}^{ijk}$ and $g_{\text{YZ}(X)}^{ijk}$ are the ternary liquid parameters.

6.3. Critical Evaluation and Thermodynamic Optimization

Thermodynamic modeling of the Fe-Si-P and Fe-C-P systems were performed using the CALPHAD approach based on the critical evaluation of all available phase equilibria and thermodynamic data. The liquid and solid solutions of all sub-systems were described using the MQM [36,37] and CEF [38], respectively. White P were selected as the standard state for the solid phases. The crystal structure information of all solid phases in the Fe-Si-P and Fe-C-P systems

were summarized in **Table 6.1** and **Table 6.2**. The optimized model parameters of the Fe-Si-P and Fe-C-P systems were summarized in **Table 6.3** and **Table 6.4**.

Table 6.1 Summary of crystal structure information of all solid phases in the Fe-Si-P system

Phase	Structure	Prototype	Space group	Pearson symbol
FCC_A1	Cubic	Cu	$\bar{F}m\bar{3}m$	<i>cF4</i>
BCC_A2	Cubic	W	$Im\bar{3}m$	<i>cI2</i>
BCC_B2	Cubic	CsCl	$Pm\bar{3}m$	<i>cP8</i>
Diamond_A4	Cubic	C(dia.)	$Fd\bar{3}m$	<i>cF8</i>
Me ₃ P	Tetragonal	Ni ₃ P	$I\bar{4}$	<i>tI32</i>
Me ₂ P	Hexagonal	Fe ₂ P	$P\bar{6}2m$	<i>hP9</i>
MeP	Orthorhombic	MnP	<i>Pnma</i>	<i>oP8</i>
FeP ₂	Orthorhombic	FeS ₂	<i>Pnnm</i>	<i>oP6</i>
SiP	Orthorhombic	SiP	$Cmc2_1$	<i>oS24</i>
SiP ₂	Orthorhombic	GeAs ₂	<i>Pbam</i>	<i>oP24</i>
Fe ₂ Si	Cubic	CsCl	$Pm\bar{3}m$	<i>cP2</i>
Fe ₅ Si ₃	Hexagonal	Mn ₅ Si ₃	$P6_3/mcm$	<i>hP16</i>
FeSi	Cubic	FeSi	$P2_13$	<i>cP8</i>
FeSi ₂	Orthorhombic	FeSi ₂	<i>Cmca</i>	<i>oC48</i>
Fe ₃ Si ₇	Tetragonal	Fe ₃ Si ₇	$P4/mmm$	<i>tP3</i>
FeSi ₄ P ₄	Triclinic	FeSi ₄ P ₄	<i>P1</i>	---
White P	Cubic	P ₄	$I\bar{4}3m$	<i>C*8</i>
Red P	---	P	---	<i>C*66</i>

Table 6.2 Summary of crystal structure information of all solid phases in the Fe-C-P system

Phase	Structure	Prototype	Space group	Pearson symbol
FCC_A1	Cubic	Cu	$\bar{F}m\bar{3}m$	<i>cF4</i>
BCC_A2	Cubic	W	$Im\bar{3}m$	<i>cI2</i>
Fe ₃ P	Tetragonal	Ni ₃ P	$I\bar{4}$	<i>tI32</i>
Fe ₂ P	Hexagonal	Fe ₂ P	$P\bar{6}2m$	<i>hP9</i>
FeP	Orthorhombic	MnP	<i>Pnma</i>	<i>oP8</i>
FeP ₂	Orthorhombic	FeS ₂	<i>Pnnm</i>	<i>oP6</i>
Fe ₃ C	Orthorhombic	Fe ₃ C	<i>Pnma</i>	<i>oP16</i>
White P	Cubic	P ₄	$I\bar{4}3m$	<i>C*8</i>
Red P	---	P	---	<i>C*66</i>
Graphite	Hexagonal	C	<i>P63/mmc</i>	<i>hP4</i>

Table 6.3 Optimized model parameters for the Fe-Si-P system (J/mol, J/mol-K)

Phase	Model parameters
	$Z_{FeFe}^{Fe} = Z_{SiSi}^{Si} = Z_{PP}^P = 6$ [24,*]
	$Z_{PFe}^P = Z_{PSi}^P = Z_{FeSi}^{Fe} = Z_{SiFe}^{Si} = Z_{SiP}^{Si} = 6$ [14,24,26,*] $Z_{FeP}^{Fe} = 3$ [14]
Liquid (Fe,Si,P)	$\Delta g_{FeP} = -56902 + 6.569T + (5481 + 3.033T)X_{FeFe} + (-11966 + 2.510T)X_{FeFe}^2 - 9623X_{PP}$ [14]
	$\Delta g_{SiP} = -5857.6$ [26]
	$\Delta g_{FeSi} = -33710 + 2.26T - (12552 + 5.02T)X_{FeFe} - (8368 - 4.82T)X_{FeFe}^2 - (3054 - 6.49T)X_{SiSi}$ [24]
	$g_{FeSi(P)}^{001} = -6359.68 + 7.1128T$ [*], $g_{FeSi(P)}^{101} = -11953.69 + 3.138T$ [*]

“Toop-type” interpolation with Fe as an asymmetric component [*]

$$G_{FeVa}^{FCC} = G_{Fe(FCC)}^{\circ}, G_{SiVa}^{FCC} = G_{Si(FCC)}^{\circ}, G_{P.Va}^{FCC} = G_{P(FCC)}^{\circ} \quad [*]$$

$$L_{Fe,P.Va}^{FCC} = -139787.44 + 6.4852T \quad [14]$$

FCC_A1

$$L_{Si,P.Va}^{FCC} = 0 \quad [26]$$

(Fe,Si,P)₁(Va)₁

$$L_{Fe,SiVa}^{FCC} = -115254 - 2.19T - (84777 - 44.33T)(x_{Fe} - x_{Si}) + 20007(x_{Fe} - x_{Si})^2 \quad [24]$$

$$T_{CFeVa} = -201, \beta_{FeVa} = -2.1 \quad [44]$$

$$G_{FeVa}^{BCC_A2} = G_{Fe(BCC)}^{\circ}, G_{SiVa}^{BCC_A2} = G_{Si(BCC)}^{\circ}, G_{P.Va}^{BCC_A2} = G_{P(BCC)}^{\circ} \quad [*]$$

$$L_{Fe,P.Va}^{BCC_A2} = -203476.3 + 15.4808T + 33472(y_{Fe} - y_P) \quad [14]$$

BCC_A2

$$L_{Si,P.Va}^{BCC_A2} = -48116 \quad [*]$$

(Fe,Si,P)₁(Va)₃

$$L_{Fe,SiVa}^{BCC_A2} = -154014 + 32.29T - (63511 - 13.25T)(x_{Fe} - x_{Si}) + 35728(x_{Fe} - x_{Si})^2 \quad [24]$$

$$T_{CFe,P.Va} = -285 \quad [14], T_{CFe,SiVa} = 504(y_{Fe} - y_{Si}) \quad [24]$$

$$T_{CFeVa} = 1043, \beta_{FeVa} = 2.22 \quad [44]$$

$$G_{Fe,SiVa}^{BCC_B2} = G_{Si:FeVa}^{BCC_B2} = -20930 \quad [24]$$

$$G_{Fe:FeVa}^{BCC_B2} = G_{Si:SiVa}^{BCC_B2} = 0 \quad [24]$$

BCC_B2

$$G_{P:P.Va}^{BCC_B2} = G_{Fe:P.Va}^{BCC_B2} = G_{P:FeVa}^{BCC_B2} = G_{Si:P.Va}^{BCC_B2} = G_{P:SiVa}^{BCC_B2} = 0 \quad [*]$$

(Fe,Si,P)_{0.5}(Fe,Si,P)_{0.5}

$$L_{Fe,Si:Si}^{BCC_B2} = L_{Fe,Si:Fe}^{BCC_B2} = L_{Fe:Fe,Si}^{BCC_B2} = L_{Si:Fe,Si}^{BCC_B2} = 0 \quad [24]$$

(Va)₃

$$L_{Fe,P:P}^{BCC_B2} = L_{Fe,P:Fe}^{BCC_B2} = L_{Fe:Fe,P}^{BCC_B2} = L_{P:Fe,P}^{BCC_B2} = 0 \quad [24]$$

$$L_{Si,P:P}^{BCC_B2} = L_{Si,P:Fe}^{BCC_B2} = L_{Si:Si,P}^{BCC_B2} = L_{P:Si,P}^{BCC_B2} = 0 \quad [*]$$

Diamond_A4

$$G_{SiVa} = G_{Si(Diamond)}^{\circ} \quad [24], G_{FeVa} = G_{Fe(FCC)}^{\circ} + 1000 \quad [24]$$

(Si, Fe, P)(Va)

$$G_{P.Va} = G_{P(White)}^{\circ} + 5418.4 + 2.092T \quad [26]$$

	$L_{Si,P:Va}^{Diamond} = 25940.8 - 11.1713T$ [26]
	$L_{Si,Fe:Va}^{Diamond} = 113001.5 - 0.5T$ [24]
Me ₃ P (Fe) ₃ (P,Si)	$G_{Fe:P}^{Me_3P} = G_{Fe_3P}^\circ$ [14] $G_{Fe:Si}^{Me_3P} = 3G_{Fe(BCC)}^\circ + G_{Si(Diamond)}^\circ - 92000$ [*] $L_{Fe:P,Si}^{Me_3P} = 0$ [14]
Me ₂ P (Fe) ₂ (P, Si) ₁	$G_{Fe:P}^{Me_2P} = G_{Fe_2P}^\circ$ [14] $G_{Fe:Si}^{Me_2P} = 2G_{Fe(BCC)}^\circ + G_{Si(Diamond)}^\circ - 113050 + 18.0T$ [*] $L_{Fe:P,Si}^{Me_2P} = 0$ [*]
MeP (Fe)(P, Si) ₁	$G_{Fe:P}^{MeP} = G_{FeP}^\circ$ [14] $G_{Fe:Si}^{MeP} = G_{Fe(BCC)}^\circ + G_{Si(Diamond)}^\circ - 85200 + 15T$ [*] $L_{Fe:P,Si}^{MeP} = 0$ [*]
FeP ₂ [14] (Fe) ₁ (P) ₂	$\Delta H_{298.15K}^\circ = -191100, S_{298.15K}^\circ = 51.05$ $C_p = 77.52563 + 0.009348T - 443846T^{-2} - 1.1 \times 10^{-6}T^2$
SiP [26] (Si) ₁ (P) ₁	$\Delta H_{298.15K}^\circ = -63300, S_{298.15K}^\circ = 34.735$ $C_p = 38.343 + 0.010878T - 565000T^{-2}$
SiP ₂ [26] (Si) ₁ (P) ₂	$\Delta H_{298.15K}^\circ = -79300, S_{298.15K}^\circ = 67.0$ $C_p = 67 + 0.0171T$
Fe ₂ Si [24] (Fe) ₂ (Si) ₁	$\Delta H_{298.15K}^\circ = -53889.7, S_{298.15K}^\circ = 106.39$ $C_p(Fe_2Si) = 2C_p(Fe_{BCC}) + C_p(Si_{Diamond})$
Fe ₅ Si ₃ [24] (Fe) ₅ (Si) ₃	$\Delta H_{298.15K}^\circ = -234740, S_{298.15K}^\circ = 209.1$ $C_p = 180.3069 + 0.085912T - 1060722T^{-2} + 2.665 \times 10^{-7}T^2$

$\beta = 2.32, T_C = 360 \text{ K}, P = 0.28$	
FeSi [24]	$\Delta H_{298.15K}^\circ = -76410, S_{298.15K}^\circ = 46.024$
(Fe) ₁ (Si) ₁	$C_P = 48.5666 + 0.01472T - 428220T^{-2} - 1.7511 \times 10^{-6}T^2$
FeSi ₂ [24]	$\Delta H_{298.15K}^\circ = -96940.44, S_{298.15K}^\circ = 55.48$
(Fe) ₁ (Si) ₂	$C_P = 79.02985 - 0.0181469T - 999009T^{-2} - 1.782 \times 10^{-6}T^2$
Fe ₃ Si ₇ [24]	$\Delta H_{298.15K}^\circ = -247842.42, S_{298.15K}^\circ = 207.3$
(Fe) ₃ (Si) ₇	$C_P = 214.2176 + 0.10993T - 2345707T^{-2} - 2.3033 \times 10^{-6}T^2$
FeSi ₄ P ₄ [*]	$\Delta H_{298.15K}^\circ = -343500, S_{298.15K}^\circ = 178$
(Fe) ₁ (Si) ₄ (P) ₄	$C_P(FeSi_4P_4) = C_P(Fe_{BCC}) + 4C_P(Si_{Diamond}) + 4C_P(P_{White})$

* optimized in the present study

Table 6.4 Optimized model parameters for the Fe-C-P system (J/mol, J/mol-K)

Phase	Model parameters
	$Z_{FeFe}^{Fe} = Z_{CC}^C = Z_{PP}^P = 6$ [32, *]
	$Z_{PFe}^P = Z_{PC}^P = Z_{CFe}^C = Z_{CP}^C = 6$ [32,14,*], $Z_{FeP}^{Fe} = Z_{FeC}^{Fe} = 3$ [14,32]
Liquid (Fe, C, P)	$\Delta g_{FeP} = -56902 + 6.569T + (5481 + 3.033T)X_{FeFe} + (-11966 + 2.510T)X_{FeFe}^2 - 9623X_{PP}$ [14]
	$\Delta g_{CP} = 0$ [*]
	$\Delta g_{FeC} = -30459.52 + 3.138T - 1129.68X_{FeFe}$ [32]
	“Toop-type” interpolation with P as an asymmetric component [*]
FCC_A1	$G_{FeVa}^{FCC} = G_{Fe(FCC)}^\circ, G_{P.Va}^{FCC} = G_{P(FCC)}^\circ$ [*]
(Fe, P) ₁ (C, Va) ₁	$G_{Fe:C}^{FCC} = G_{Fe(FCC)}^\circ + G_{C(graphite)}^\circ + 77207 - 15.877T$ [32]

$$G_{P:C}^{FCC} = G_{P(FCC)}^{\circ} + G_{C(graphite)}^{\circ} + 83000 - 15.0T \text{ [*]}$$

$$L_{Fe,P:Va}^{FCC} = -139787.44 + 6.4852T \text{ [14]}$$

$$L_{Fe:C,Va}^{FCC} = -34671 \text{ [32]}, L_{P:C,Va}^{FCC} = 0 \text{ [*]}$$

$$L_{Fe,P:C}^{FCC} = -87864 \text{ [*]}$$

$$T_{CFeVa} = -201, \beta_{FeVa} = -2.1 \text{ [44]}$$

$$G_{FeVa}^{BCC_A2} = G_{Fe(BCC)}^{\circ}, G_{P:Va}^{BCC_A2} = G_{P(BCC)}^{\circ} \text{ [*]}$$

$$G_{Fe:C,Va}^{BCC_A2} = G_{Fe(BCC)}^{\circ} + 3G_{C(Graphite)}^{\circ} + 322050 + 75.667T \text{ [32]}$$

$$G_{P:C,Va}^{BCC_A2} = G_{P(BCC)}^{\circ} + 3G_{C(Graphite)}^{\circ} + 320000 \text{ [*]}$$

BCC_A2

(Fe,P)₁(C, Va)₃

$$L_{Fe,P:Va}^{BCC_A2} = -203476.3 + 15.4808T + 33472(y_{Fe} - y_P) \text{ [14]}$$

$$L_{Fe:C,Va}^{BCC} = -190T \text{ [32]}, L_{P:C,Va}^{BCC} = 0 \text{ [*]}$$

$$T_{CFe,P:Va} = -285 \text{ [14]}$$

$$T_{CFeVa} = 1043, \beta_{FeVa} = 2.22 \text{ [44]}$$

LT-Fe₃P:

$$\Delta H_{298.15K}^{\circ} = -164830, S_{298.15K}^{\circ} = 110.15$$

$$298.15 \text{ K} < T < 727 \text{ K}: C_p = 106.76 + 0.0108T - 780000T^{-2}$$

$$727 \text{ K} < T < 2000 \text{ K}: C_p = 109.84 + 0.0287T - 8000000T^{-2}$$

Fe₃P [14]

HT-Fe₃P:

(Fe)₃(P)₁

$$\Delta H_{trans.}^{L \rightarrow H} = 1000, T_{trans.}^{L \rightarrow H} = 698 \text{ K}$$

$$298.15 \text{ K} < T < 727 \text{ K}: C_p = 106.76 + 0.0108T - 780000T^{-2}$$

$$727 \text{ K} < T < 2000 \text{ K}: C_p = 109.84 + 0.0287T - 8000000T^{-2}$$

$$\beta = 0.6, T_C = 713 \text{ K}, P = 0.28$$

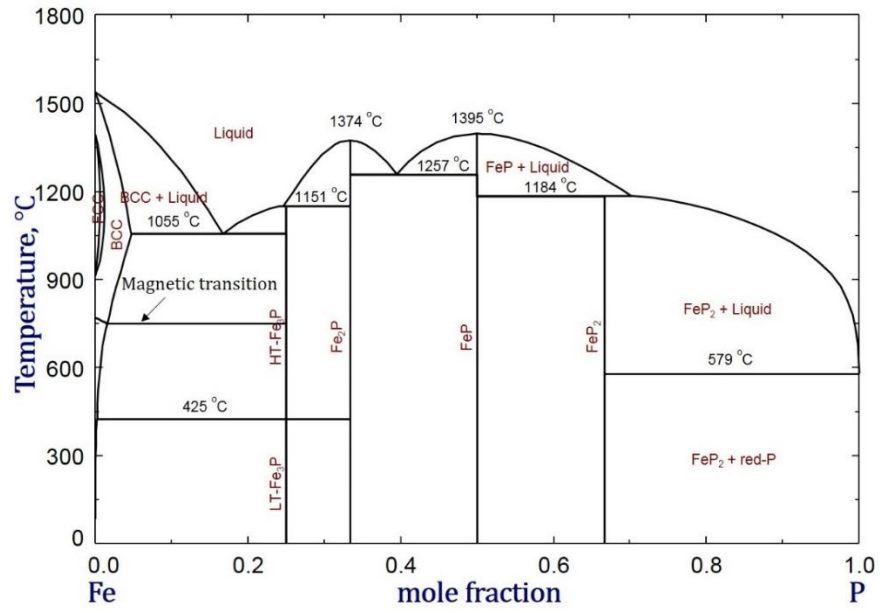
Fe ₂ P [14]	$\Delta H_{298.15K}^{\circ} = -157643, S_{298.15K}^{\circ} = 83.12$
(Fe) ₂ (P) ₁	$C_p = 71.555 + 0.02375T - 370000T^{-2}$
FeP [14]	$\Delta H_{298.15K}^{\circ} = -126100, S_{298.15K}^{\circ} = 47.77$
(Fe) ₁ (P) ₁	$C_p = 43.7878 + 0.01985T - 232000T^{-2}$
FeP ₂ [14]	$\Delta H_{298.15K}^{\circ} = -191100, S_{298.15K}^{\circ} = 104.77$
(Fe) ₁ (P) ₂	$C_p = 77.52563 + 0.009348T - 443846T^{-2} 1.1 \times 10^{-6}T^2$
Fe ₃ C [45]	$\Delta H_{298.15K}^{\circ} = 26944.46, S_{298.15K}^{\circ} = 51.05$
(Fe) ₃ (C) ₁	$C_p = 118.47637 + 0.0014T - 1181054T^{-2}$
	$\beta = 1.008, T_c = 485 \text{ K}, P = 0.28$

* optimized in the present study

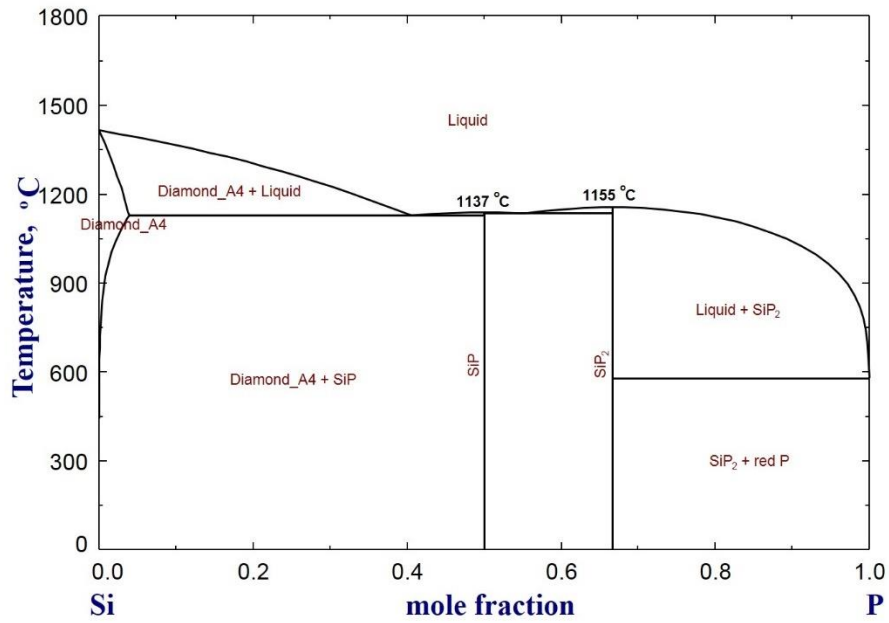
6.3.1 The Fe-Si-P System

6.3.1.1 Binary Systems (Fe-P, Si-P and Fe-Si Systems)

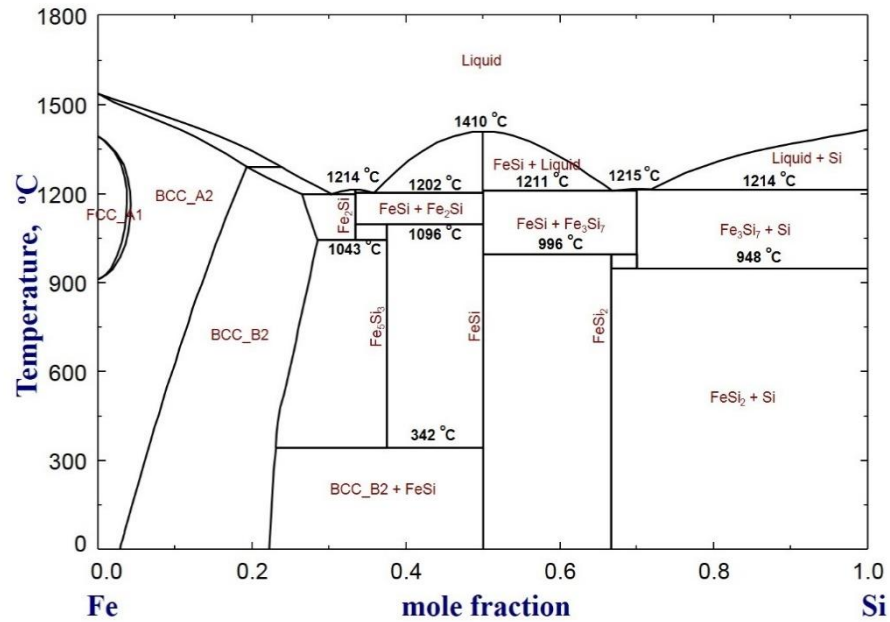
As the most fundamental P-containing system, the binary Fe-P system has been extensively optimized [9-14]. Discrepancies left in previous assessments based on substitutional model were discussed with comparison to experimental data in recent reassessment by present authors [14]. In developing the new Fe-P database, dephosphorization reactions at the metal/slag interface were taken into account to determine the thermodynamic properties of molten Fe-P alloys. The optimized phase diagram of the Fe-P system was plotted in **Fig. 6.1(a)**, based on the optimized parameters as summarized in **Table 6.3**.



(a)



(b)



(c)

Figure 6.1 Calculated phase diagrams of the (a) Fe-P, (b) Si-P, and (c) Fe-Si systems

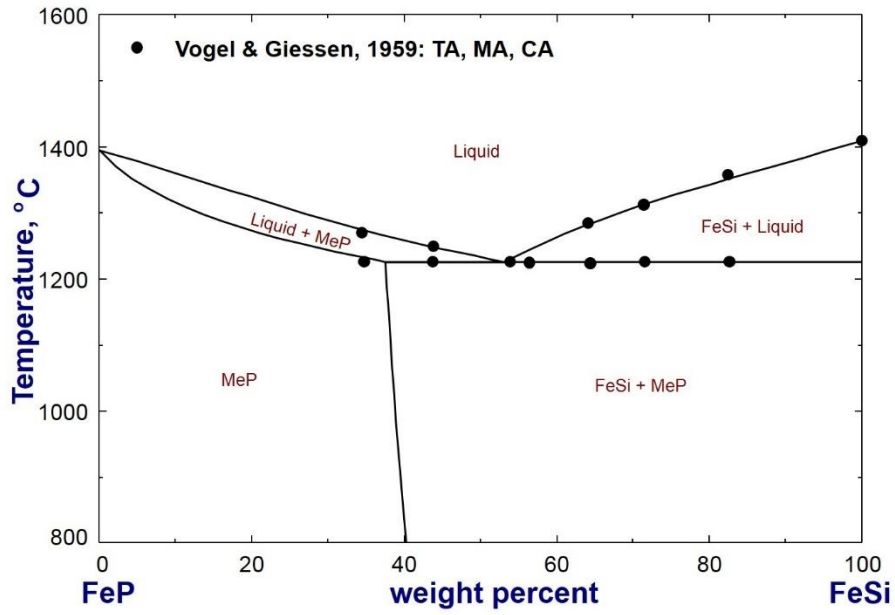
The Si-P system is crucial to silicon metallurgy industry. To describe the behavior of P in silicon accurately, Jung and Zhang [26] carried out systematic optimization of the Si-P system using the CALPHAD approach. The phase constitution of the Si-P system was built up by optimizing the molten Si-P alloys, diamond_A4 phase in the Si-rich region and stoichiometric SiP and SiP₂ compounds based on critical evaluation of available experimental data. Besides, dephosphorization reaction between metallurgical-grade molten Si and CaO-based slags was taken into account to validate the constructed Si-P thermodynamic database. The phase diagram of the Si-P system based on optimized model parameters in **Table 6.3** was plotted in **Fig. 6.1(b)**.

As mentioned above, Cui and Jung [24] recently optimized the Fe-Si system, in which the order/disorder transition in BCC solution was taken into account and the liquid solution were

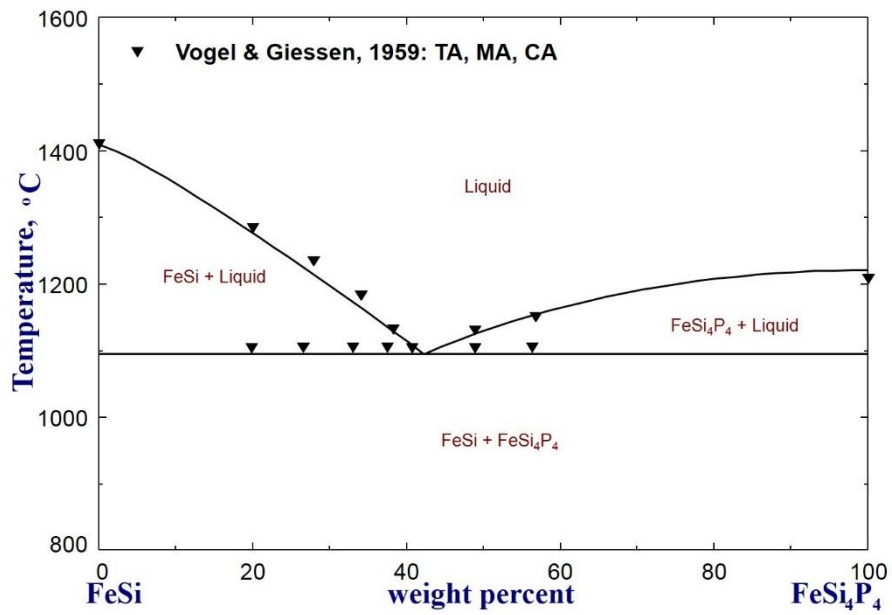
described using both Bragg-Williams Random Mixing model and Modified Quasichemical Model. For the compatibility in higher-order system, the parameter set based on MQM was adopted in the present modeling. **Fig. 6.1(c)** illustrates the calculated phase diagram of the Fe-Si system.

6.3.1.2 Ternary Fe-Si-P system

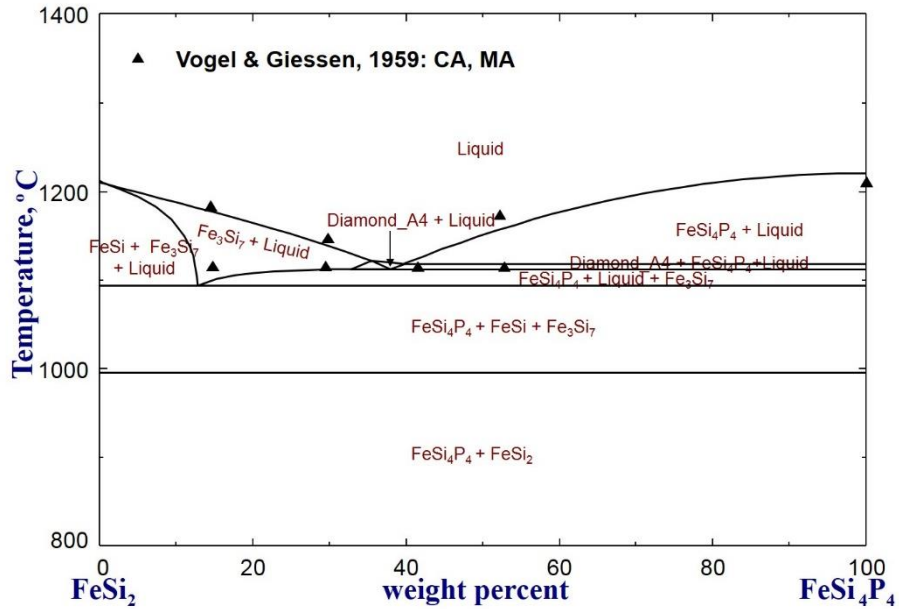
In the ternary Fe-Si-P system, Si was considered soluble in Fe_3P , Fe_2P and FeP to form Me_3P , Me_2P and MeP solid solutions to reproduce experimental data and give consistent description of the Fe-Si-P phase equilibria. However, no evidence shows P is soluble in the Fe_2Si , Fe_5Si_3 , FeSi , FeSi_2 , Fe_3Si_7 . Hence, the solubility of P was assumed to be 0 in these ferrosilicides. Besides, stoichiometric FeP_2 , SiP , SiP_2 and ternary compound FeSi_4P_4 are also stable in the ternary system. Vogel and Giessen [46] carried out a few sets of experiments on designated composition of Fe-Si-P alloys. The liquidus and solidus temperatures and microstructures of the target alloys were determined by means of thermal analysis and microscopic examination. Besides, the ternary stoichiometric compound, FeSi_4P_4 , was also confirmed with a maximum melting temperature of 1210 °C. The measured experimental data concerning pseudobinary $\text{FeSi} - \text{FeP}$, $\text{FeSi} - \text{FeSi}_4\text{P}_4$ and $\text{FeSi}_2 - \text{FeSi}_4\text{P}_4$ diagrams were compared with present calculations in **Fig. 6.2**. It is shown that the measured data were well reproduced in present modeling.



(a)



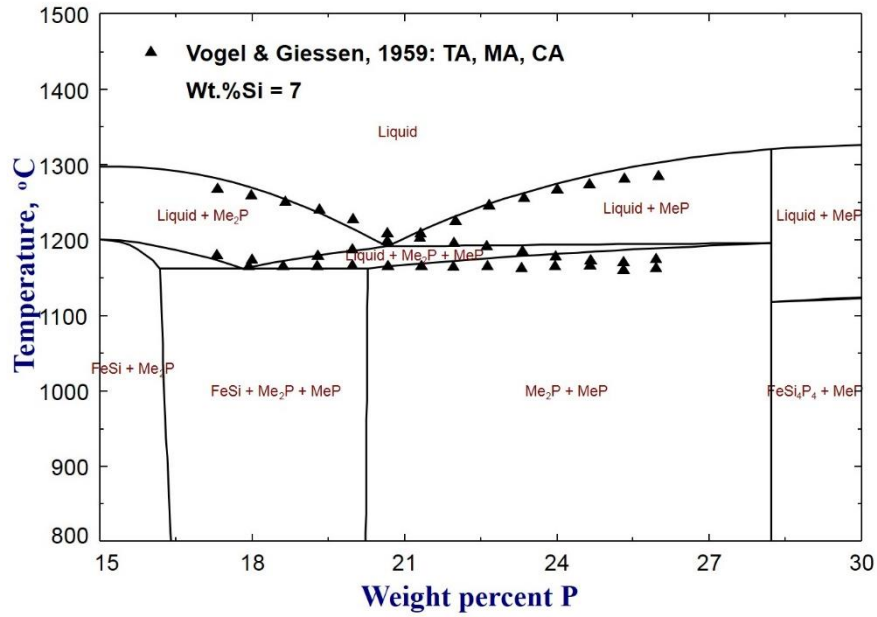
(b)



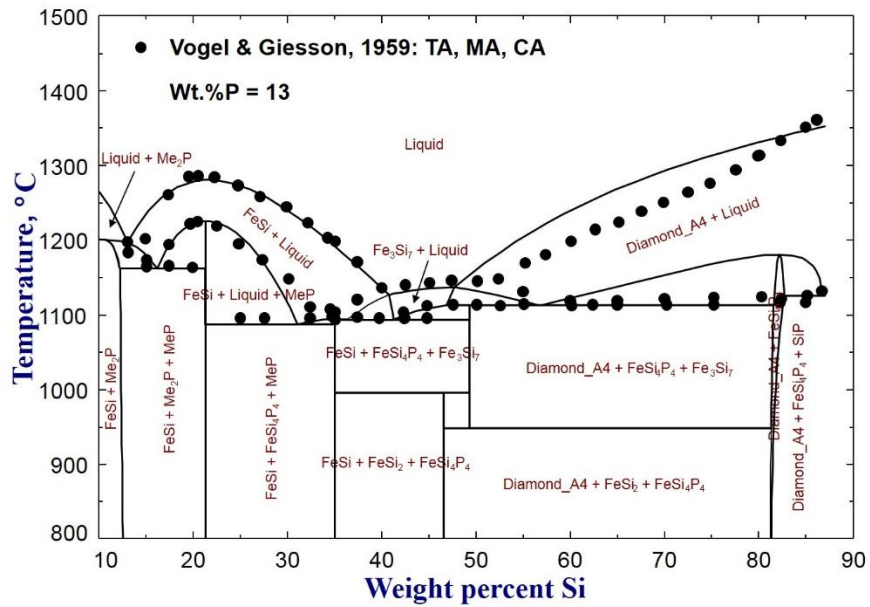
(c)

Figure 6.2 Pseudobinary (a) FeSi – FeP (b) FeSi – FeSi₄P₄ and (c) FeSi₂ – FeSi₄P₄ diagrams in the ternary Fe-Si-P system, compared to experimental data [46]

Fig. 6.3 shows calculated isopleths of the Fe-Si-P system at wt.%Si = 7 and wt.%P = 13 comparing with experimental data by Vogel and Giessen [46]. Both sets of data are explained in the present modeling, except those on the Si-rich corner at wt.%P = 13. The liquidus and solidus boundaries are positively deviated from the measurements, which can not be got rid off unless sacrificing the reproduction of all other experimental data.



(a)



(b)

Figure 6.3 Calculated isopleths of the Fe-Si-P system at (a) wt. %Si = 7 and (b) wt. %P = 13, compared to experimental data [46]

Kaneko et al. [47] measured the solubility of P in Fe-Si alloys containing up to 4 wt.% Si. Their experimental results were compared with present calculation in **Fig. 6.4**. As shown in the figure, fairly good agreement between the modeling and experiments was achieved. Besides, dissolution of P in BCC solution decreases from 2.28 wt.% to 1.28 wt.% with the increase of Si up to around 4 wt.%Si in the alloys.

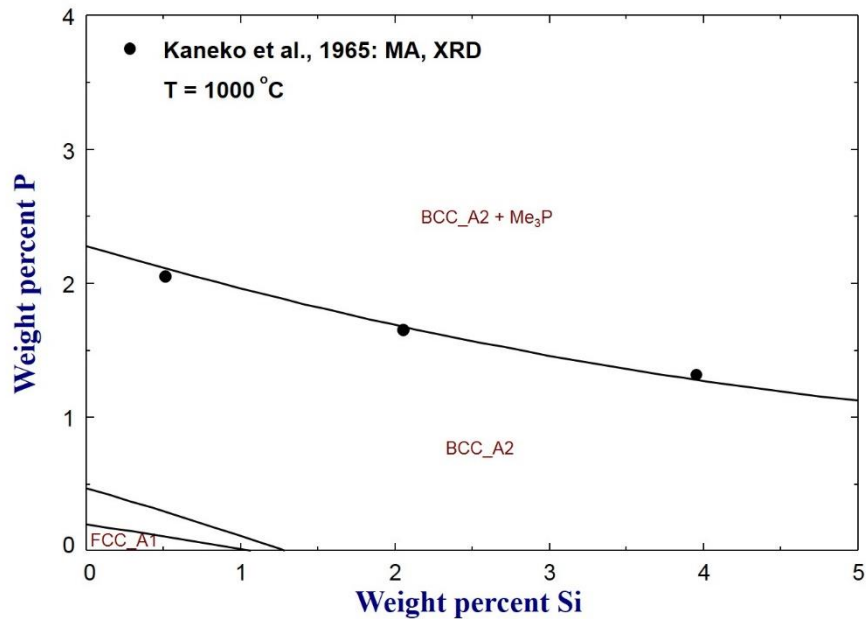


Figure 6.4 Calculated isothermal section of the Fe-Si-P system on the Fe-rich corner at 1000 °C, compared to experimental data [47]

The calculated liquidus surface projection of the Fe-Si-P system between 1000 °C and 1500 °C was compared with experimental data measured by Vogel and Giesson [46] in **Fig. 6.5**. In the figure, the liquidus isothermals between 1000 °C and 1500 °C were plotted in dash lines. All involved variant reactions of the Fe-Si-P system were summarized in **Table 6.5**. The calculated invariant temperatures are consistently in agreement with measured values while the calculated composition of some invariant points such as eutectic **E3**, **E5**, peritectic **U5** are slightly deviated from the

datapoints, and even the invariant reaction types are inconsistent between the calculation and experimental result, that is, eutectic reaction $L = \text{Diamond_A4} + \text{Fe}_3\text{Si}_7 + \text{FeSi}_4\text{P}_4$ in **E4'** was considered to be a mistake and corrected to peritectic reaction $L + \text{Diamond_A4} = \text{Fe}_3\text{Si}_7 + \text{FeSi}_4\text{P}_4$ labeled as **U4**.

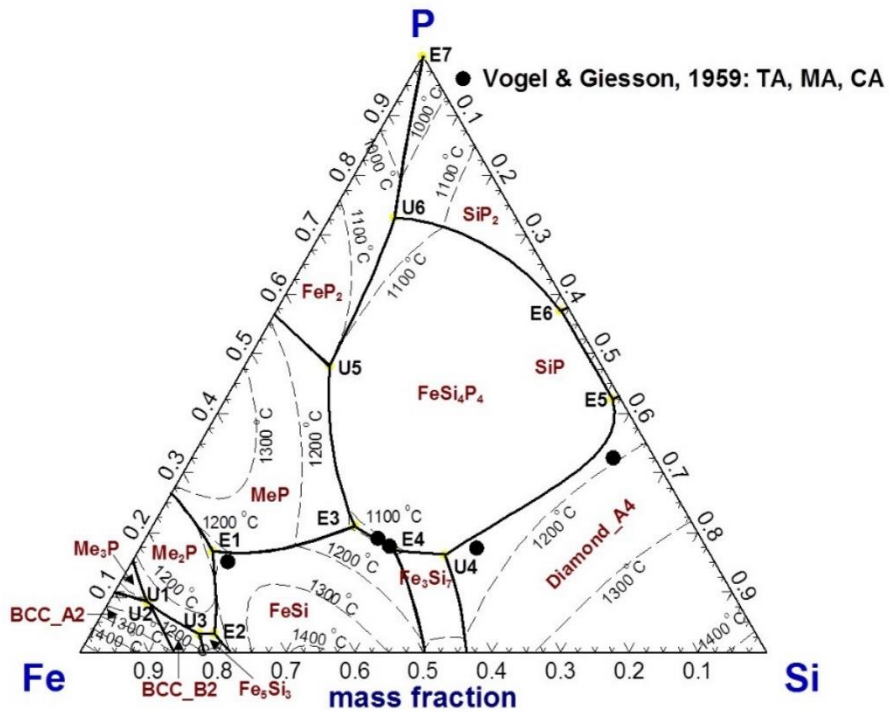


Figure 6.5 Calculated liquidus surface projection of the Fe-Si-P system between 1000 °C and 1500 °C, compared to experimental data [46]

Table 6.5 Invariant reactions of the Fe-Si-P system with experimental data [46]

Code	Invariant reactions	x_{Fe}	x_{Si}	x_{P}	$T, ^\circ\text{C}$
E1	$L = \text{MeP} + \text{Me}_2\text{P} + \text{FeSi}$	72.2	10.9	16.9	1163
		71.0	14.0	15.0	1166[46]
E2	$L = \text{Me}_2\text{P} + \text{Fe}_2\text{Si} + \text{Fe}_5\text{Si}_3$	79.0	18.0	3.0	1141
E3	$L = \text{FeSi} + \text{FeSi}_4\text{P}_4 + \text{MeP}$	49.4	29.5	21.1	1087
		47.1	34.0	18.9	1095 [46]
		45.7	37.3	17.0	1094
E4	$L = \text{FeSi} + \text{FeSi}_4\text{P}_4 + \text{Fe}_3\text{Si}_7$	46.0	36.4	17.6	1096 [46]
		1.1	56.4	42.5	1125
E5	$L = \text{SiP} + \text{FeSi}_4\text{P}_4 + \text{Diamond}_{\text{A4}}$	6.0	61.5	32.5	1116 [46]
E6	$L = \text{SiP} + \text{FeSi}_4\text{P}_4 + \text{SiP}_2$	1.4	41.3	57.3	1132
E7	$L = \text{Red}_{\text{P}} + \text{SiP}_2 + \text{FeP}_2$	0.075	0.035	99.89	580
U1	$L + \text{Me}_2\text{P} = \text{Me}_3\text{P} + \text{BCC}_{\text{A2}}$	86.1	5.4	8.5	1093
U2	$L + \text{BCC}_{\text{B2}} = \text{Me}_2\text{P} + \text{BCC}_{\text{A2}}$	85.9	5.8	8.3	1097
U3	$L + \text{BCC}_{\text{B2}} = \text{Me}_2\text{P} + \text{Fe}_5\text{Si}_3$	82.7	14.2	3.1	1164
U4	$L + \text{Diamond}_{\text{A4}} = \text{Fe}_3\text{Si}_7 + \text{FeSi}_4\text{P}_4$	38.7	45.0	16.3	1113
E4'	$L = \text{Diamond}_{\text{A4}} + \text{Fe}_3\text{Si}_7 + \text{FeSi}_4\text{P}_4$	33.5	49.2	17.3	1113 [46]
U5	$L + \text{MeP} = \text{FeP}_2 + \text{FeSi}_4\text{P}_4$	39.7	12.3	48.0	1099
U6	$L + \text{FeSi}_4\text{P}_4 = \text{SiP}_2 + \text{FeP}_2$	17.6	9.4	73.0	1027

The thermodynamic behavior of P in molten Fe with addition of Si was investigated experimentally by some researchers. Schenck et al. [48] obtained the activity coefficient of P

affected by Si by measuring vapor pressures of $P_2(g)$ above molten Fe-Si-P alloys at 1515 °C. Yamada and Kato [49,50] measured ions species of phosphorus in the gas phase measure the activity coefficient of P in the Fe-Si-P melts at 1600 °C. By using Knudsen effusion method (KEM), vapor pressures of different allotropic gaseous phosphorus (P_2 , P, P_4) can be measured individually. Ban-ya et al. [51] conducted transportation experiments to investigate effect of Si on the activity coefficient of P at 1400 °C. The experimental data were compared with present modeling results in **Fig. 6.6**. It is shown that inconsistency among the data becomes larger with increase of Si concentration. Compared to the other two sets of data, those obtained by Knudsen effusion method (KEM) are considered more reliable. According to present database, the interaction parameter ϵ_P^{Si} was determined as 11.02, which is very close to the 11.90 recommended by Yamada and Kato [49,50].

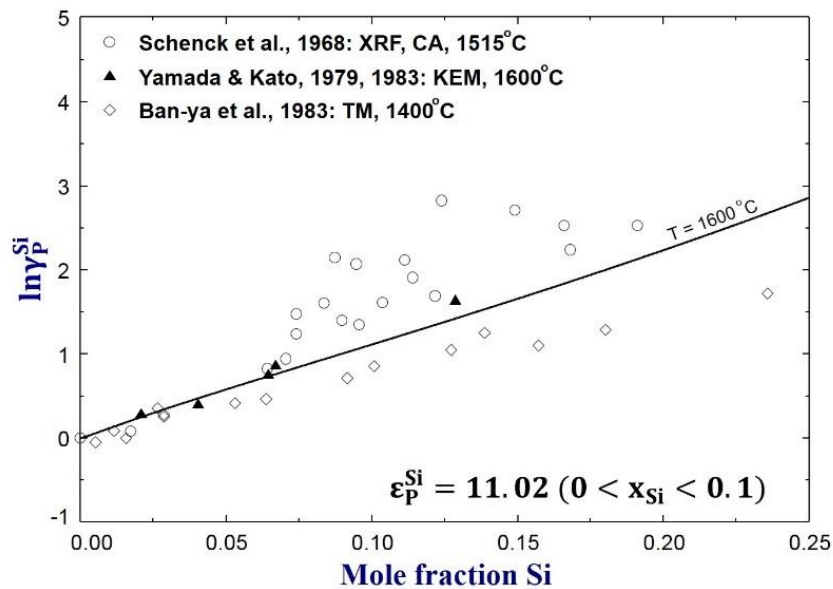


Figure 6.6 Effect of Si on the activity coefficient of P (γ_P^{Si}) in the liquid Fe-Si-P alloys from 1400 to 1600 °C, compared to experimental data [48-51]

Dissolution of phosphorus in molten Si-Fe alloys was investigated by Ueda et al. [52] at 1450 °C. The Si-Fe alloys containing a range of $0.08 < x_{Fe} < 0.63$ were equilibrated under a pressure of $P_{P_2(g)} = 0.184$ Pa. **Fig. 6.7** shows calculated solubility of $P_2(g)$ in Si-Fe alloys together with experimental data at 1450 °C. As shown in the figure, the solubility of P decreases slightly first and then increases sharply with increasing Fe content. The minimum solubility was reached at about 51 wt.%Fe. This is due to a maximized interaction between Fe and Si in the liquid solution.

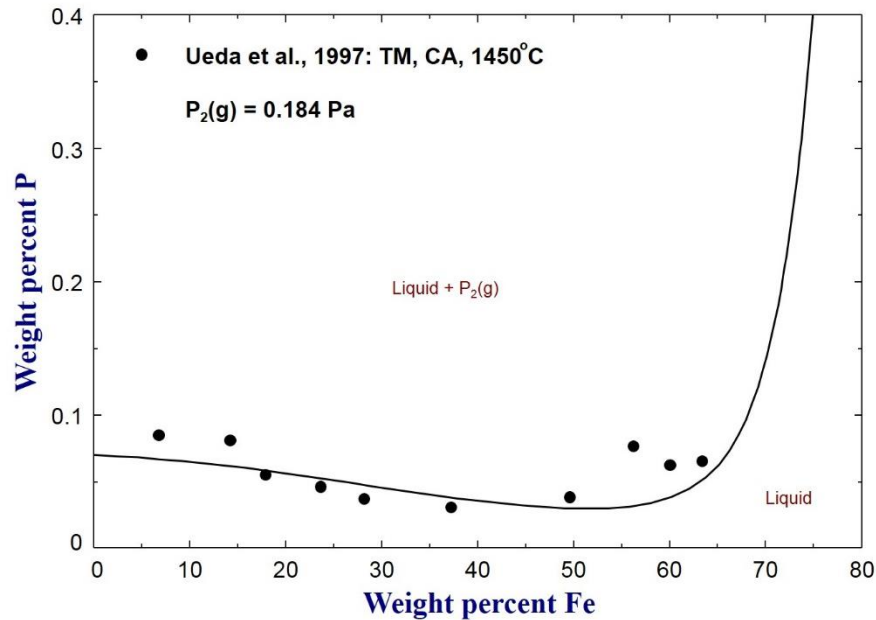


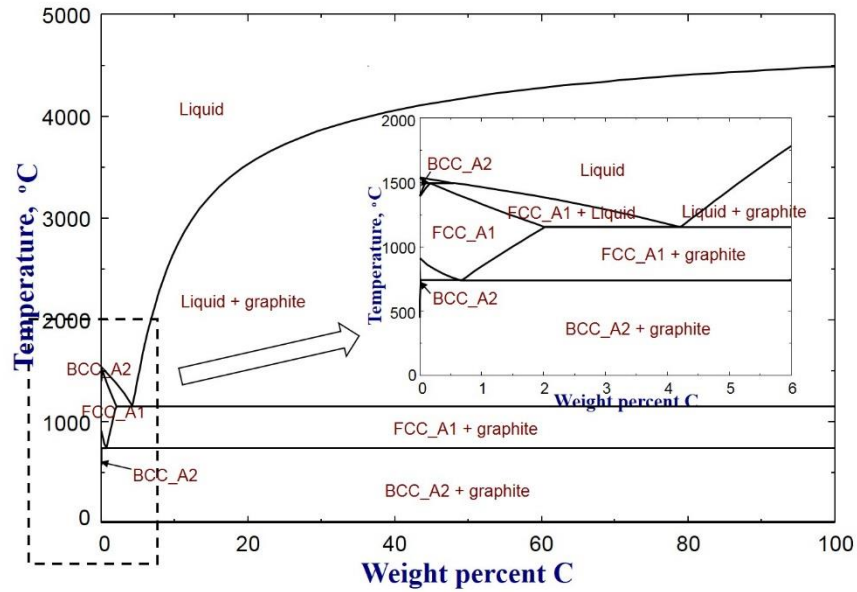
Figure 6.7 Calculated solubility of $P_2(g)$ in the Si-Fe melts at 1450 °C under the partial pressure of $P_{P_2(g)} = 0.184$ Pa, compared to experimental data [52]

6.3.2 The Fe-C-P System

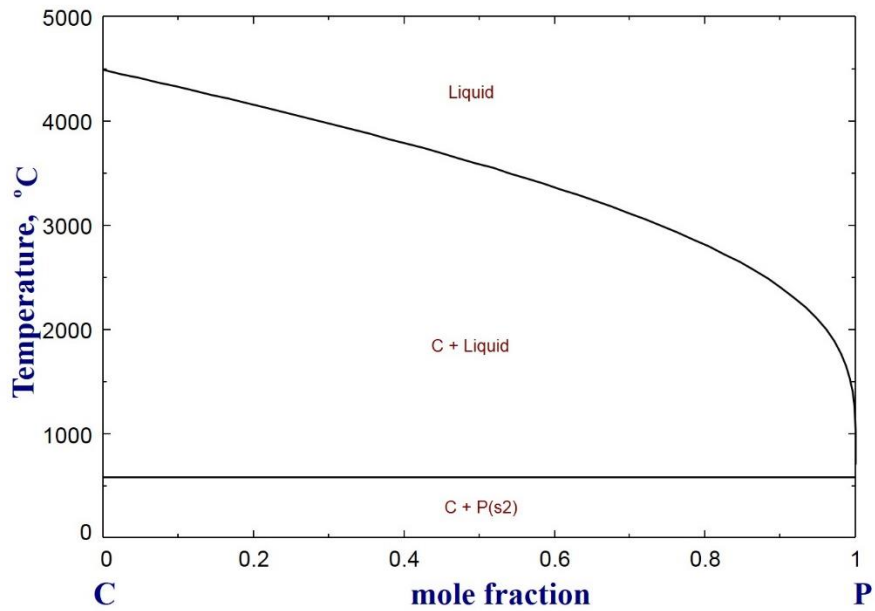
6.3.2.1 Binary Systems (Fe-C and C-P Systems)

As mentioned above, the Fe-C system optimized by Shubhank and Kang [32] adopted in the present study. The calculated Fe-C phase diagram is shown in **Fig. 6.8(a)** with enlarged Fe-rich side showing phase equilibria of liquid, BCC_A2 and FCC_A1. **Fig. 6.8(b)** shows phase diagram

of C-P system based on the present database. Solid P and C were assumed insoluble in each other and no intermediate compound was found stable in the C-P system. Liquid model parameter was avoided to reproduce experimental data in the ternary Fe-C-P system, which will be discussed later.



(a)

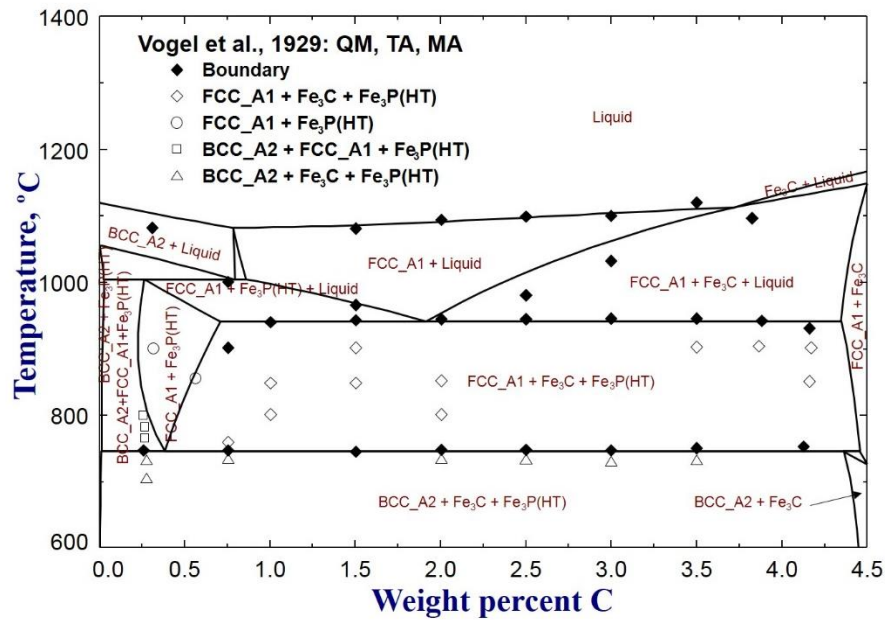


(b)

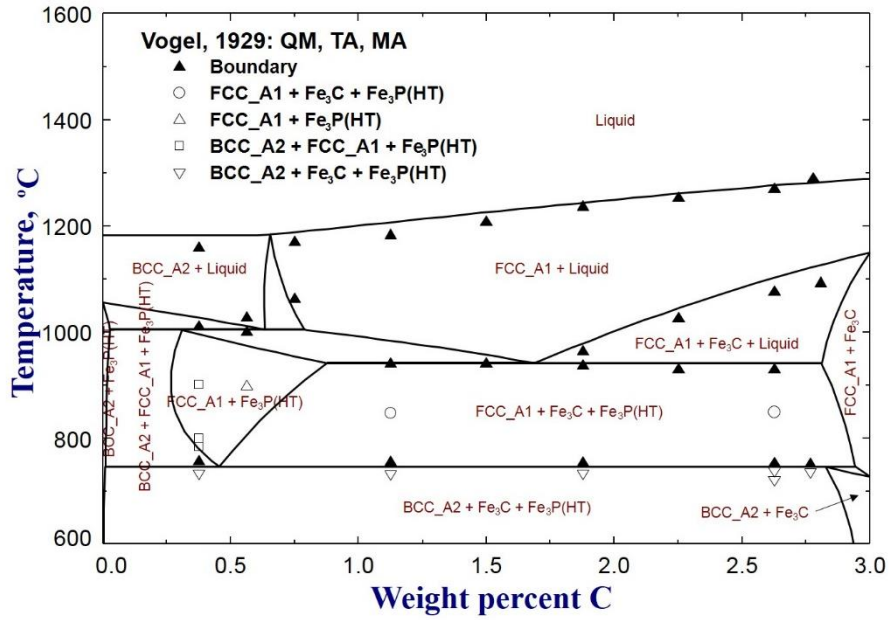
Figure 6.8 Calculated phase diagrams of the (a) Fe-C, and (b) C-P systems

6.3.2.2 Ternary Fe-C-P System

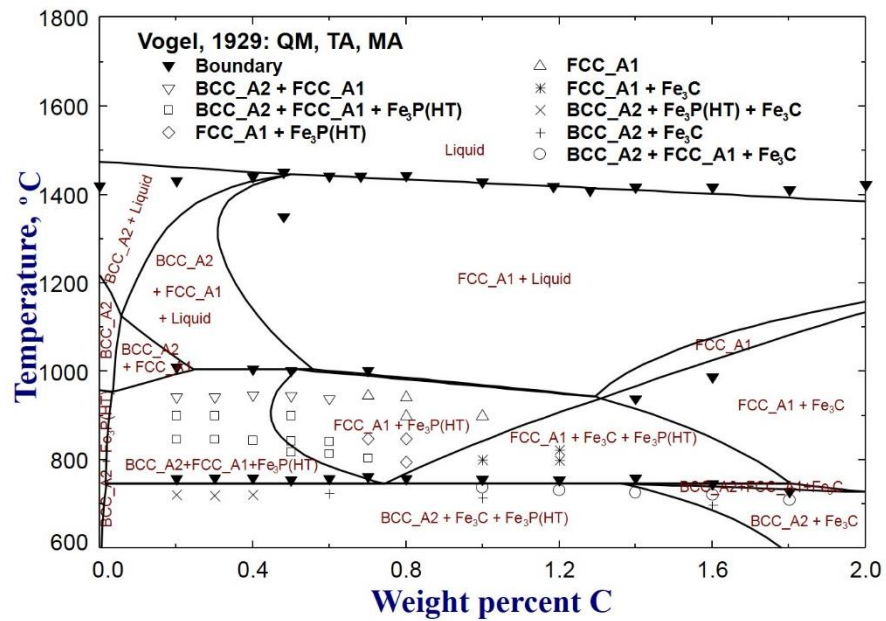
Vogel et al. [46] carried out series experiments on the Fe-rich region to investigate phase equilibria of the Fe-C-P system at various vertical sections: (1) $\text{Fe}_{91}\text{P}_9 - \text{Fe}_{95.5}\text{C}_{4.5}$, (2) $\text{Fe}_{92}\text{P}_8 - \text{Fe}_{97}\text{C}_3$, (3) $\text{Fe}_{98}\text{P}_2 - \text{Fe}_{98}\text{C}_2$, (4) $\text{Fe}_{98.4}\text{P}_{1.6} - \text{Fe}_{98.4}\text{C}_{1.6}$, (5) $\text{Fe} - \text{Fe}_{97}\text{P}_{1.5}\text{C}_{1.5}$. In the experiments, quenching method (QM), thermal analysis (TA) and metallographic analysis (MA) were employed to determine critical temperatures and crystal structures of target alloys. The experimental data were compared with present calculations in Fig. 6.9. It is shown that the calculations are in good agreement with experimental data.



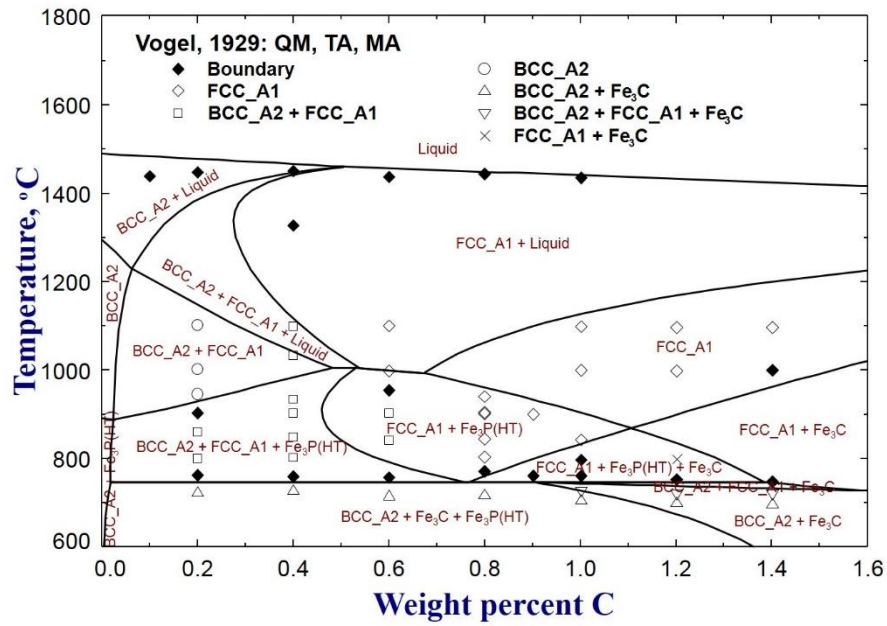
(a)



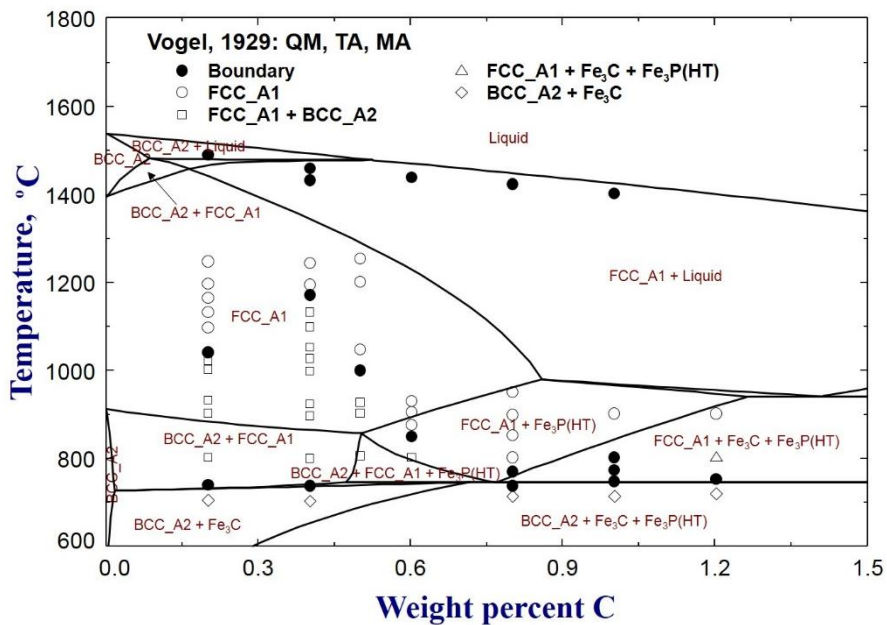
(b)



(c)



(d)



(e)

Figure 6.9 Calculated vertical phase diagrams of (a) $\text{Fe}_{91}\text{P}_9 - \text{Fe}_{95.5}\text{C}_{4.5}$, (b) $\text{Fe}_{92}\text{P}_8 - \text{Fe}_{97}\text{C}_3$, (c) $\text{Fe}_{98}\text{P}_2 - \text{Fe}_{98}\text{C}_2$, (d) $\text{Fe}_{98.4}\text{P}_{1.6} - \text{Fe}_{98.4}\text{C}_{1.6}$, and (e) $\text{Fe} - \text{Fe}_{97}\text{P}_{1.5}\text{C}_{1.5}$ in weight percent, compared to experimental data [53]

Fig. 6.10 illustrates calculated the metastable isopleth diagram of the Fe-C-P system at wt. %C = 2.4, compared to experimental results. Ohide and Ohira [54] studied the solidification process of the Fe-C-P alloys containing less than 8 wt.% P. The primary precipitation of austenite, secondary precipitation of cementite and solidus temperatures at fixed composition master alloys were determined by means of thermal analysis. Precipitated crystals were identified using metallographic analysis (MA). Fairly good agreement was achieved between experimental results and the present optimization.

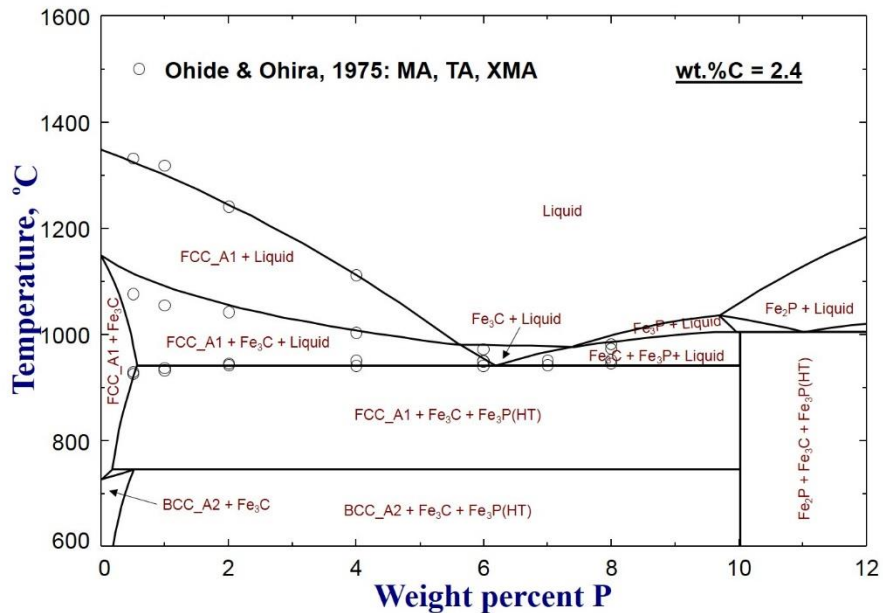


Figure 6.10 Variation of the temperature along with P content of the Fe-C-P system at wt. %C = 2.4, compared to experimental data [54]

Fig. 6.11 shows variation of the temperature with P content with along the metastable liquidus reaction Liquid = FCC_A1 + Fe₃C together with experimental data provided by Wust [55], Schichtki and Piwowarsky [56], Schumann et al. [57]. The liquidus and solidus temperatures up

to the eutectic point at around 7 wt.%P suggested by Schurmann et al. [57] were reasonably reproduced within experimental errors. In comparison, those liquidus data by Wust [55], Schichtki and Piwowarsky [56] are slightly lower than predicted values.

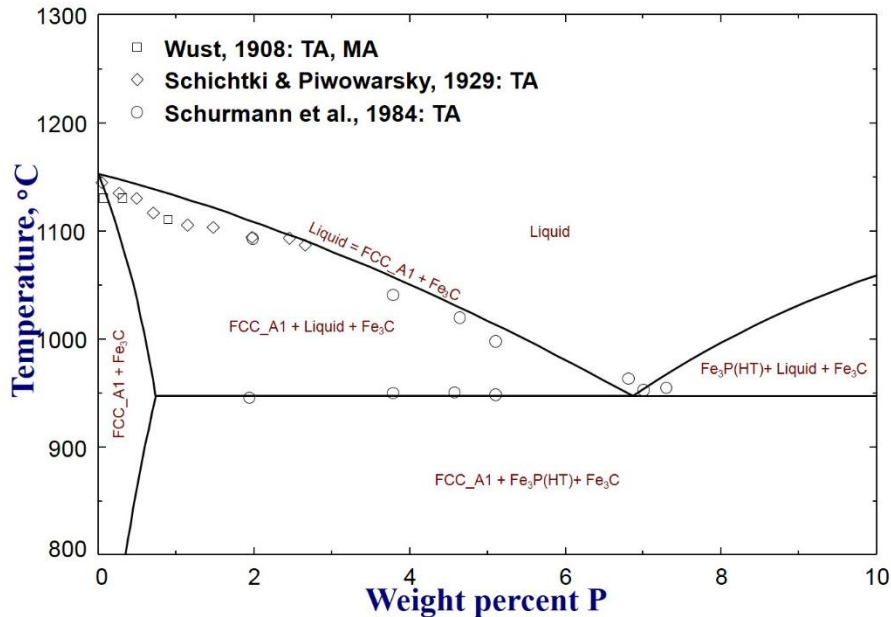
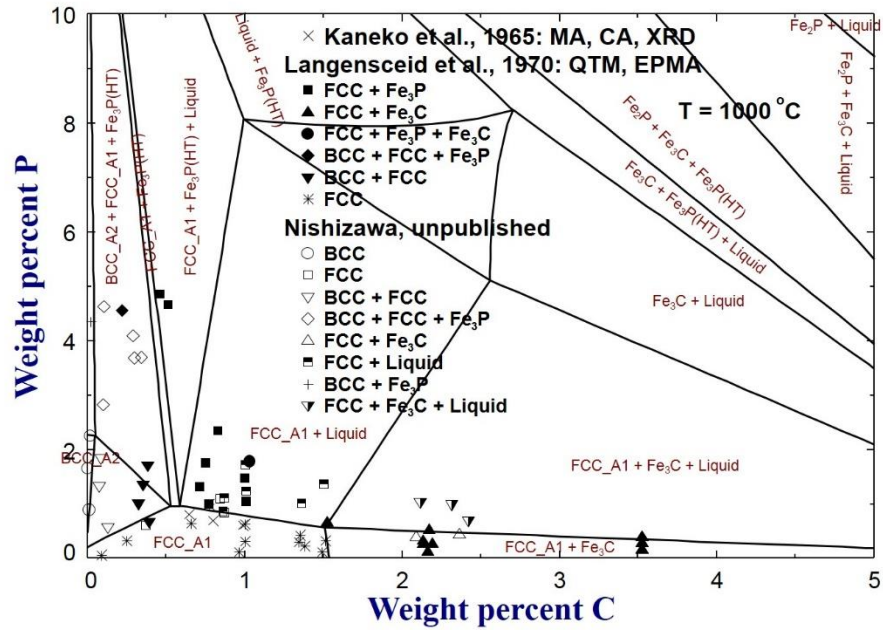
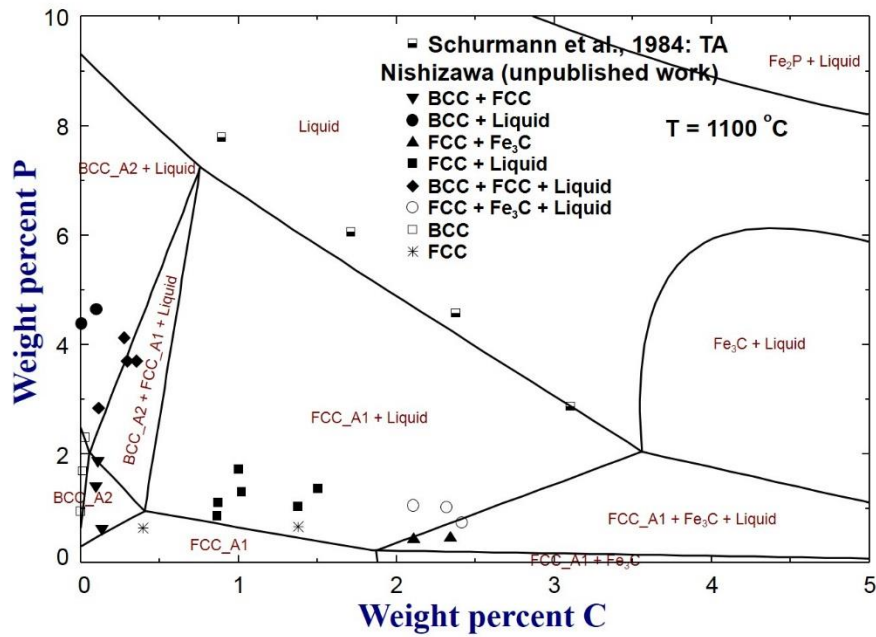


Figure 6.11 Variation of the temperature with P content along the metastable liquidus reaction
Liquid = FCC_A1 + Fe₃C, together with experimental data [55-57]

Various Fe-C-P alloys have been studied to investigate phase equilibria of ferrite, austenite, cementite and Fe phosphide on the Fe-rich corner. All available experimental data [47,57-60] ranging from 900 °C to 1100 °C were sorted by phases and compared with the calculations in **Fig. 6.12**. Compared to BCC_A2 phase, the solubility of C in FCC_A1 solid solution is much higher at all considered temperatures. More C and P dissolution result in precipitation of cementite and Fe₃P within the solution. As shown in the figures, the phase boundary on the Fe-rich side were basically reproduced, despite some scattering among the experimental data.



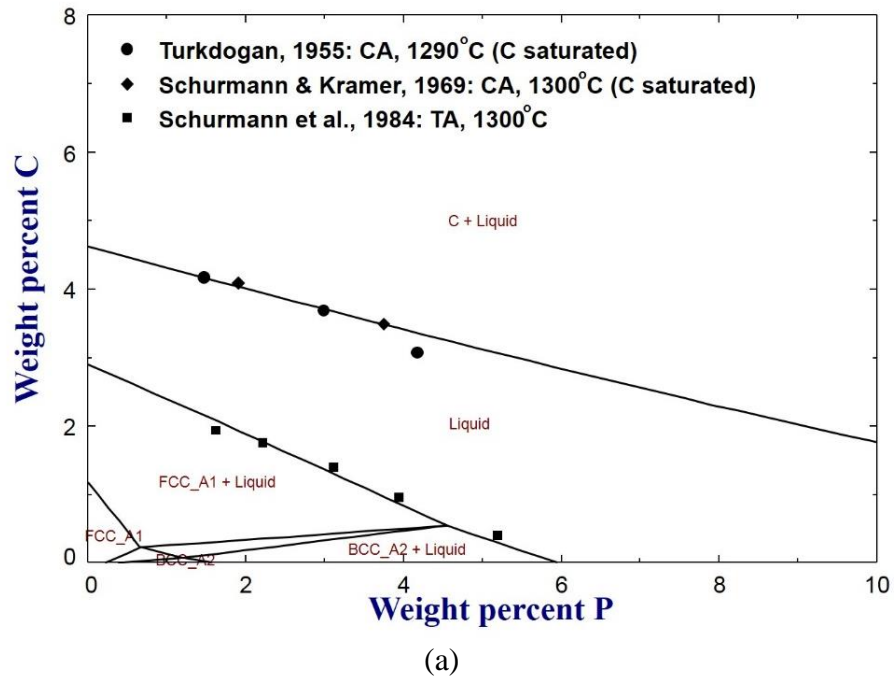
(c)

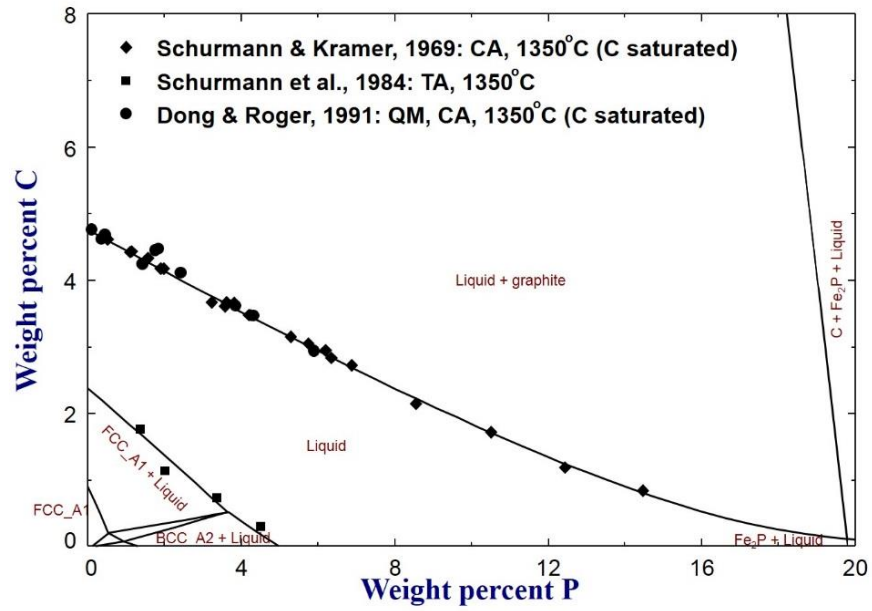


(d)

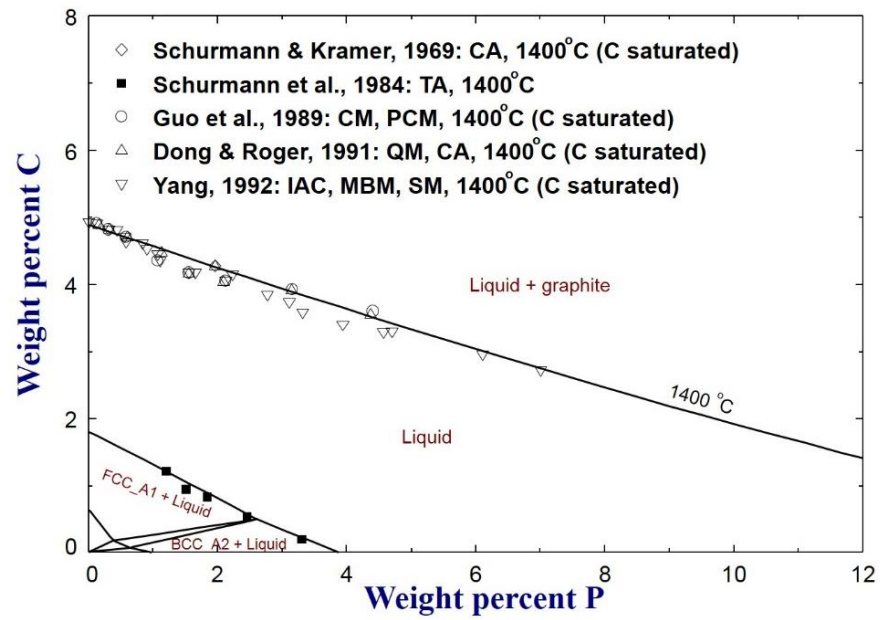
Figure 6.12 Calculated isothermal sections of the Fe-C-P system on the Fe-rich corner at (a) 900 °C, (b) 950 °C, (c) 1000 °C, and (d) 1100 °C, compared to experimental data [47,57-60]

The solubility of C in molten Fe with dissolution of P has been investigated by many researchers [57,61-68]. **Fig. 6.13** presents variation of saturated C concentration of the Fe-P melt with increasing P content from 1300 °C to 1600 °C. At all considered temperatures, the solubility of C decreases with the increase of P concentration. Besides, the available experimental data are basically consistent and well reproduced based on present Fe-C-P database.

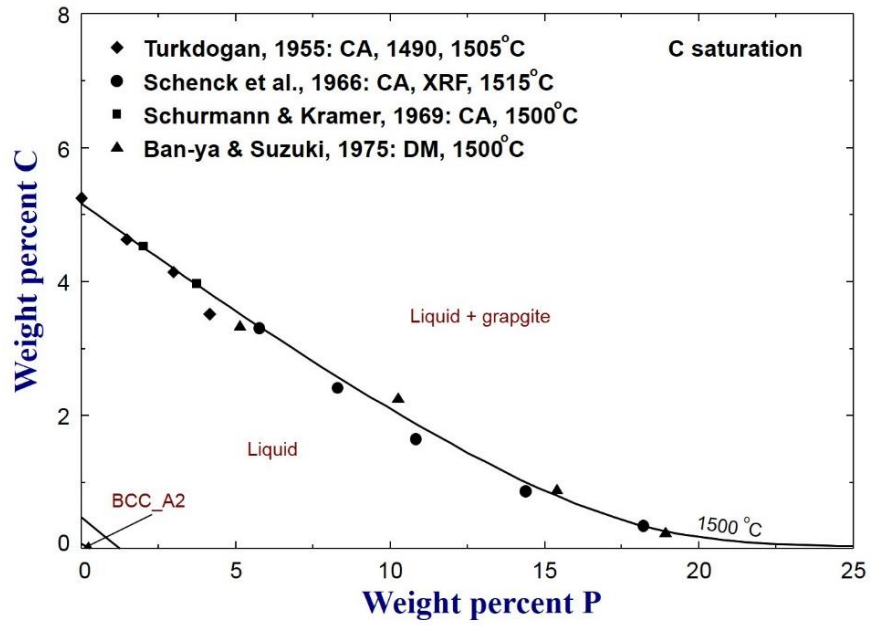




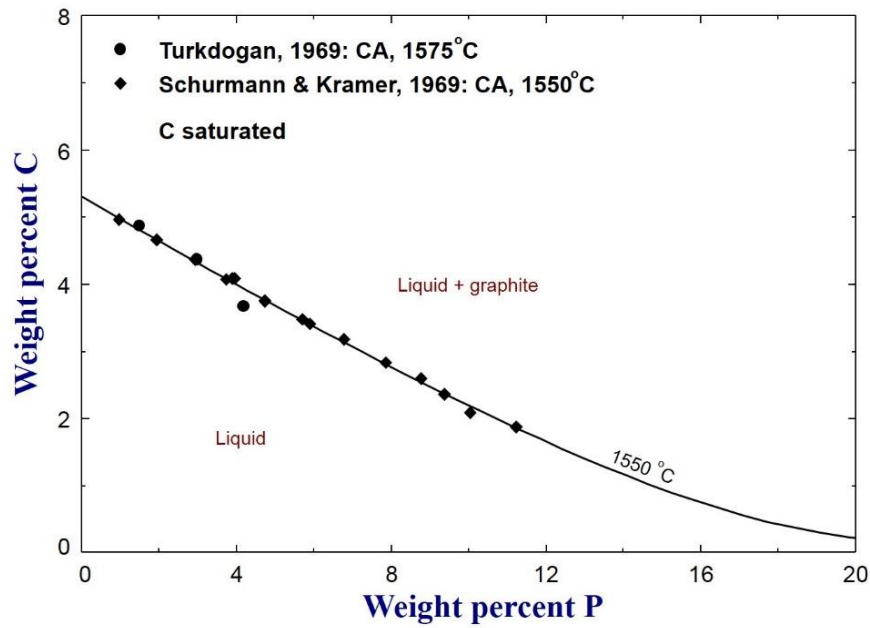
(b)



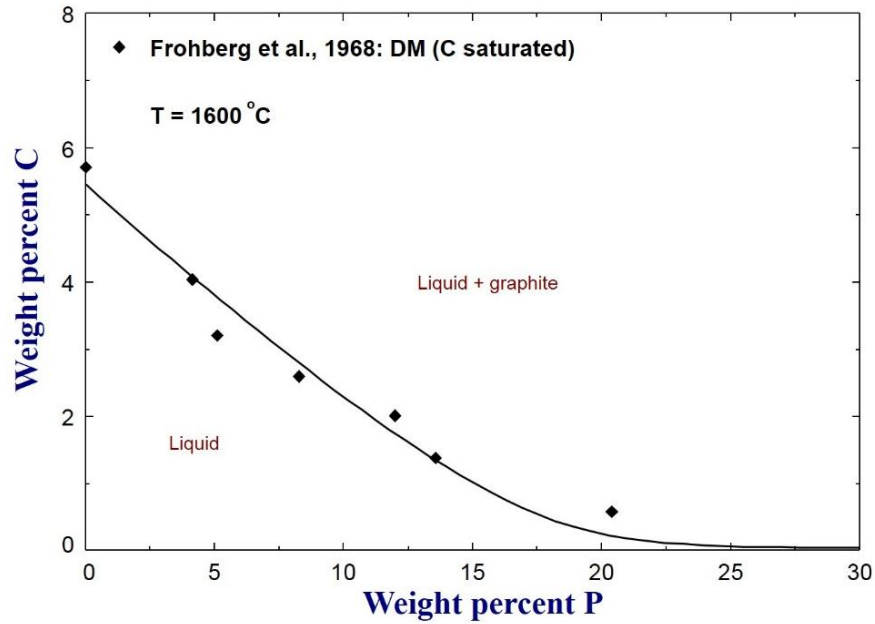
(c)



(d)



(e)



(f)

Figure 6.13 Calculated solubility of C in molten Fe with increasing P content between 1300 °C and 1600 °C, compared to experimental data [57,61-68]

The liquidus surface projection of the Fe-C-P system on the Fe-rich corner was plotted together with experimental results [55-57] in **Fig.6.14**. The isothermal lines from 1100 °C to 1500 °C were plotted in dashed lines and giving good reproduction on the experimental results by Schurmann et al. [57] using thermal analysis. Reasonable agreements were also achieved in various eutectic reactions of Liquid = Fe₃C + FCC_A1 and Liquid = BCC_A2 + FCC_A1, comparing to the data reported by Wust [55] and Schichtki and Plwowarsky [56]. Invariant reactions on the Fe-rich corner was summarized in **Table 6.6**.

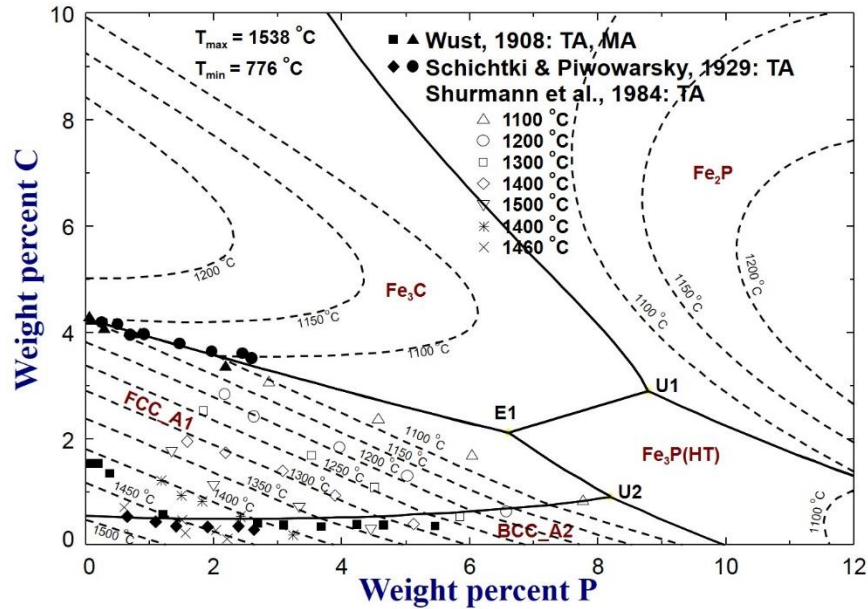


Figure 6.14 Calculated liquidus surface projection of the Fe-C-P system on the Fe-rich corner, compared to experimental data [55-57]

Table 6.6 Invariant reactions of the Fe-C-P system with experimental data [55-57]

Code	Invariant reactions	wt. %Fe	wt. %C	wt. %P	$T, ^\circ\text{C}$
U1	$L + \text{Fe}_2\text{P} = \text{Fe}_3\text{C} + \text{Fe}_3\text{P}(\text{HT})$	88.327	2.898	8.775	1005
U2	$L + \text{BCC_A2} = \text{FCC_A1} + \text{Fe}_3\text{P}(\text{HT})$	90.908	0.904	8.188	1004
E1	$L = \text{Fe}_3\text{P}(\text{HT}) + \text{Fe}_3\text{C} + \text{FCC_A1}$	91.293	2.107	6.600	941

6.4. Summary

The Fe-Si-P and Fe-C-P systems were thermodynamically optimized over the full composition range based on the critical evaluation of available experimental data. The liquid phases and solid solutions were described using the Modified Quasichemical Model (MQM) and Compound Energy Formalism (CEF), respectively. The Gibbs energy of the ternary compound FeSi_4P_4 was

optimized and the phase equilibria of the Fe-Si-P system in wide composition ranges were well reproduced. Thermodynamic properties of the liquid Fe-Si-P alloys in both Fe-rich and Si-rich side were optimized based on reported data. In the Fe-C-P system, all experimental data concentrated on the Fe-rich corner were used to optimize the liquidus, solidus BCC_A2 and FCC_A1 boundaries. Besides, the solubility of C in the Fe-P melts at various temperatures were excellently explained with very limited parameters. According to the present optimization, a consistent and accurate thermodynamic database of the Fe-Si-P and Fe-C-P system has been developed for describing the behavior of P in various conditions of Fe-Si and Fe-C alloys. The optimized database will be used as part of new FSstel database in FactSage software.

Acknowledgments

We gratefully acknowledge the Steelmaking Consortium Members, Hyundai Steel, Tata Steel Europe, Posco, Doosan Heavy Industry and Construction, SeAh Besteel, Nucor Steel, RioTinto, JFE Steel, Nippon Steel, RHI, Voestalpine, and Natural Science and Engineering Research Council of Canada for supporting the present project. This work was also supported by the National Research Foundation of Korea (NRF) grant funded by the Korean government (MSIT) (No. NRF-2020R1A5A6017701). We would also like to thank the McGill Engineering Doctorate Award (MEDA) program.

References

1. H. Okamoto, The Fe-P (Iron-Phosphorus) System, *Bull. Alloy Phase Diagram*, 1990, 11(4), p 404-412.

2. M. E. Schlesinger, The Thermodynamic Properties of Phosphorus and Solid Binary Phosphides, *Chem. Reviews*, 2002, 102(11), p 4267-4302.
3. R.W. Olesinski, N. Kanani, and G.J. Abbaschian, The Phosphorus-Silicon System, *Bull. Alloy Phase Diagram*, 1985, 6(2), p 130-133, 203-204.
4. T.G. Chart, Critical Assessment of the Thermodynamic Properties of the System Iron-Silicon, *High Temp. High Press.*, 1970, 4(2), p 461-470.
5. T.G. Chart, Critical Assessment of Thermodynamic Data for the Iron-Silicon System, *Natl. Phys. Lab. Div. Mater. Appl. Teddington, Uk.* 1982, 5, p 5-35.
6. H. Okamoto, The C-Fe (Carbon-Iron) System, *J. Phase Equilib.*, 1992, 53(5), p 543-565.
7. V. Raghavan, C-Fe-P (Carbon-Iron-Phosphorus), *J. Phase Equilib. Diffu.*, 2004, 25(6), p 541-542.
8. P. Perrot, Carbon-Iron-Phosphorus. In Iron Systems. Part 2, *Springer*, Berlin, Heidelberg, 2008, p 304-321.
9. P. Gustafson, Internal Report IM-2549, *Swedish Institute for Metals Research*, Stockholm, Sweden, 1990.
10. J. H. Shim, C. S. Oh, and D. N. Lee, Thermodynamic Properties and Calculation of Phase Diagram of the Fe-P System, *J. Korean. Inst. Met. Mater.*, 1996, 34(11), p 1385-1393.
11. H. Ohtani, N. Hanaya, M. Hasebe, S. I. Teraoka, and M. Abe, Thermodynamic Analysis of the Fe-Ti-P Ternary System by Incorporating First-principles Calculations into the CALPHAD Approach, *CALPHAD*, 2006, 30(2), p 147-158.
12. Z. M. Cao, K. P. Wang, Z. Y. Qiao, and G. W. Du, Thermodynamic Reoptimization of the Fe-P System, *Acta Phys. Chim. Sinica*, 2012, 28(1), p 37-43.

13. Z. M. Cao, W. Xie, K. P. Wang, C. J. Niu, G. W. Du, and Z. Y. Qiao, Thermodynamic Optimization of the Al-Fe-P Ternary System, *Acta Phys. Chim. Sinica*, 2013, 29(10), p 2148-2156.
14. Z. M. You and I. H. Jung, Critical Evaluation and Optimization of the Fe-P System, *Metall. Mater. Trans. B*, 2020. (published DOI: <https://doi.org/10.1007/s11663-020-01939-0>).
15. O. Kubaschewski, Iron-Binary Phase Diagrams, *Springer-Verlag*, Berlin, 1982. P 185.
16. E. Schürmann and U. Hensgen, Studies of the Melting Equilibria in the System Iron-Silicon, *Arch. Eisen.*, 1980, 51(1), p 1-4.
17. B.J. Lee, S.K. Lee, and D.N. Lee, Formulation of the A2/B2/D03 Atomic Ordering Energy and a Thermodynamic Analysis of the Iron-Silicon System, *CALPHAD*, 1987, 11(3), p 253-270.
18. J. Lacaze and B. Sundman, An Assessment of the Iron-Carbon-Silicon System, *Metall. Trans. A*, 1991, 22(10), p 2211-2223.
19. J. Miettinen, Reassessed Thermodynamic Solution Phase Data for Ternary Fe-Si-C System, *CALPHAD*, 1998, 22(2), p 231-256.
20. Y. F. Liang, S. L. Shang, J. Wang, Y. Wang, F. Ye, J. P. Lin, G. L. Chen, and Z. K. Liu, First-principles Calculations of Phonon and Thermodynamic Properties of Fe-Si Compounds, *Intermetallics*, 2011, 19, p 1374-1384.
21. K. Tang and M. Tangstad, A Thermodynamic Description of the Si-rich Si-Fe System, *Acta Metall. Sin. (English Letter)*, 2012, 25(4), p 249-255.
22. I. Ohnuma, S. Abe, S. Shimenouchi, T. Omori, R. Kainuma, and K. Ishida, Experimental and Thermodynamic Studies of the Fe-Si Binary System, *ISIJ Int.*, 2012, 52(4), p 540-548.

23. Y. Yuan, F. Pan, D. Li, and A. Watson, The Re-assessment of the Mg-Zn and Fe-Si Systems and Their Incorporation in Thermodynamic Descriptions of the Al-Mg-Zn and Fe-Si-Zn Systems, *CALPHAD*, 2014, 44, p 54-61.
24. S. L. Cui and I. H. Jung, Critical Reassessment of the Fe-Si System, *CALPHAD*, 2017, 56, p 108-125.
25. E.J. Øvrelid, K. Tang, T. Engh, and M. Tangstad, Crystal Growth of Silicon for Solar Cells. K. Nakajima and N. Usami, *Springer*, New York, 2009, p 1-255. (Chapter 13)
26. I. H. Jung and Y. M. Zhang, Thermodynamic Calculations for the Dephosphorization of Silicon Using Molten Slag, *TMS*, 2012, 64(8), p 973-981.
27. S. M. Liang and R. Schmid-Fetzer, Modeling of Thermodynamic Properties and Phase Equilibria of the Si-P System, *J. Phase Equilib. Diffu.*, 2014, 35(1), p 24-35.
28. W. Yan, Y. D. Yang, W. Q. Chen, M. Barati, and A. McLean, Thermodynamic Assessment of Si-P and Si-Fe-P Alloys for Solar Grade Silicon Refining via Vacuum Levitation, *Vacuum*, 2017, 135, p 101-108.
29. J. Miettinen and G. Vassilev-Urumov, Thermodynamic Description of Ternary Fe-X-P Systems. Part 8: Fe-Si-P, *J. Phase Equilib. Diffu.*, 2016, 37(5), p 540-547.
30. J. Chipman, Thermodynamics and Phase Diagram of the Fe-C System, *Metall. Trans.*, 1972, 3(1), p 55-64.
31. P. Gustafson, A Thermodynamic Evaluation of the Fe-C System, *Scand. J. Metall.*, 1985, 14(5), p 259-267.
32. K. Shubhank and Y. B. Kang, Critical Evaluation and Thermodynamic Optimization of Fe-Cu, Cu-C, Fe-C Binary Systems and Fe-Cu-C Ternary System, *CALPHAD*, 2014, 45, p 127-137.

33. R. Naraghi, M. Selleby, and J. Agren, Thermodynamics of Stable and Metastable Structures in Fe-C System, *CALPHAD*, 2014, 46, p 148-158.
34. J. H. Shim, C. S. Oh, and D. N. Lee, Thermodynamic Assessment of the Fe-C-P System, *Z. Metall.*, 2000, 91(2), p 114-120.
35. M. I. Gasik, O. I. Polyakov, A. Yu. Proidak, and M. M. Gasik, Thermodynamic Analysis of Phase Equilibriums of «Iron-Phosphorus-Carbon» System in Temperature-Concentration Range Corresponding to Composition Area of Industrial Ferrophosphorus, *Metall. I Gornorud. Promysh.*, 2008, (4), p 26-29.
36. D. Pelton, S. A. Degterov, G. Eriksson, C. Robelin, and Y. Dessureault, The Modified Quasichemical Model I-Binary Solutions, *Metall. Mater. Trans. B*, 2000, 31(4), p 651-659.
37. D. Pelton and P. Chartrand, The Modified Quasi-chemical Model: Part II. Multicomponent Solutions, *Metall. Mater. Trans. A*, 2001, 32(6), p 1355-1360.
38. M. Hillert, The Compound Energy Formalism, *J. Alloys Compounds*, 2001, 320(2), p 161-176.
39. W. Bale, P. Chartrand, S. A. Degterov, G. Eriksson, K. Hack, R. B. Mahfoud, and S. Petersen, FactSage Thermochemical Software and Databases, *CALPHAD*, 2002, 26(2), p 189-228.
40. T. Dinsdale, SGTE Data for Pure Elements, *CALPHAD*, 1991, 15(4), p 317-425.
41. P. Vončka Leitner, D. Sedmidubsky, and P. Svoboda, Application of Neumann-Kopp Rule for the Estimation of Heat Capacity of Mixed Oxides, *Thermoch. Acta*, 2010, 497(1-2), p 7-13.
42. G. Inden, Project Meeting CALPHAD V, Max-Planck-Inst, *Eisenforschung*, Dusseldorf, Germany, 1976, p 111.

43. M. Hillert and M. Jarl, A Model for Alloying in Ferromagnetic Metals, *CALPHAD*, 1978, 2(3), p 227-238.
44. W. Huang, An Assessment of the Fe-Mn System, *CALPHAD*, 1989, 13(3), p 243-252.
45. B. Hallstedt, D. Djurovic, J. Von Appen, R. Dronskowski, A. Dick, F. Kormann, T. Hickel, and J. Neugebauer, Thermodynamic Properties of Cementite (Fe_3C), *CALPHAD*, 2010, 34, p 129-133.
46. R. Vogel and B. Giessen, The System Iron-Phosphorus-Silicon, *Arch. Eisen.*, 1959, 10, p 619-626.
47. H. Kaneko, T. Nishizawa, K. Tamaki, and A. Tanifuji, Solubility of Phosphorus in α and γ -Iron, *Nippon Kinzoku Gakkai-Si*, 1965, 29, p 166-170.
48. H. Schenck, E. Steinmetz, and R. Gohlke, Controlling the Activity of Phosphorus in Molten Iron by Means of Carbon and Silicon, *Arch. Eisen.*, 1968, 2, p 109-111.
49. K. Yamada and E. Kato, Mass Spectrometric Determination of Activities of Phosphorus in Liquid Fe-P-Si, Al, Ti, V, Cr, Co, Ni, Nb, and Mo Alloys, *Tetsu-to-Hagané*, 1979, 65(2), p 273-280.
50. K. Yamada and E. Kato, Effect of Dilute Concentrations of Si, Al, Ti, V, Cr, Co, Ni, Nb and Mo on the Activity Coefficient of P in Liquid Iron, *Trans. Iron Steel Ins. Japan*, 1983, 23(1), p 51-55.
51. S. Ban-ya, N. Maruyama, and S. Fujino, The Effects of C, Si, Al, and B on the Activity of Phosphorus in Liquid Iron, *Tetsu-to-Hagané*, 1983, 69(8), p 921-928.
52. S. Ueda, K. Morita, and N. Sano, Thermodynamics of Phosphorus in Molten Si-Fe and Si-Mn Alloys, *Metall. Mater. Trans. B*, 1997, 28B(12), p 1151-1155.
53. R. Vogel, The System: Iron-Phosphorus-Carbon, *Arch. Eisen.*, 1929, 3(5), p. 369-381.

54. T. Ohide and G. Ohira, The Solidification Structures of Iron-Carbon-Phosphorus Ternary Alloys, *Brit. Foundryman*, 1975, 68(4), p 106-115.
55. F. Wust, Influence of Phosphorus on the System Iron-Carbon, *Metallurgie*, 1908, 5, p 73-87.
56. K. Schichtki and E. Piwowarsky, The Influence of the Alloying Elements Phosphorus, Silicon and Nickel on the Solubility of Carbon in Liquid Iron, *Arch. Eisen.*, 1929, 3, p 139-147.
57. E. Schurmann, U. Hensgen, and J. Von Schweinichen, Melt Equilibrium of the Ternary Systems Iron-Carbon-Silicon and Iron-Carbon-Phosphorus, *Giessereiforschung*, 1984, 36(4), p 121-129.
58. G. Langenscheid, H. A. Mathesius, and F. K. Naumann, Use of the Quantitative Microscope and the Electron-Beam Microprobe for Examining the Iron-Carbon-Phosphorus System at 900 to 1000 °C, *Arch. Eisen.*, 41, p 817-824.
59. H. P. Hofmann, K. Loehberg, and W. Reif, Solubility of Phosphorus in Iron and Iron-Carbon Alloys Below 1000 °C, *Arch. Eisen.*, 41(8), 1970, p 975-982.
60. T. Nishizawa, cited in 1990 Gustafson. (not published)
61. E. Turkdogan and L. E. Leake, Thermodynamics of Carbon Dissolved in Iron Alloys. I. Solubility of Carbon in Iron-Phosphorus, Iron-Silicon, and Iron-Manganese Melts, *J. Iron Steel Inst.*, 1955, 1, p 39-43.
62. E. Schurmann and D. Kramer, Influence of Temperature and Equivalent Effects of Alloying Elements on Carbon Solubility in Iron-rich Carbon-saturated Ternary and Multicomponent Melts, *Giessereiforschung*, 1969, 21(1), p 29-42.
63. Y. C. Dong and R. Selin, Activity of Components in Fe-C-S and Fe-C-P Ternary Melts, *J. Iron Steel Research*, 1991, 3(1), p 9-16.

64. S. X. Guo, Y. C. Dong, B. L. Zhu, and D. J. Li, Activity of P in the Ternary Fe-C(sat)-P Melt, *J. East China Insti. Metall.*, 1989, 9(2), p 22-27.
65. Y. D. Yang, Interaction Coefficients in Iron-Carbon-Phosphorus Ternary and Iron-Chromium-Carbon-Phosphorus Quaternary Solutions at 1400 °C, *Scand. J. Metall.*, 1992, 21, p 194-201.
66. H. Schenck, E. Steinmetz, and R. Gohlke, Chemical Activity of the Elements Phosphorus, Sulfur, Silicon, Copper, and Chromium in Molten Iron Solutions Saturated with Carbon, *Arch. Eisen.*, 1966, 37(12), p 919-924.
67. S. Ban-ya and M. Suzuki, Activity of Phosphorus in Liquid Fe-P and Fe-P-C Alloys, *Tetsu-to-Hagané*, 1975, 61(14), p 2933-2942.
68. M. G. Froberg, J. F. Elliott, and H. G. Hadrys, Thermodynamics of Complex Solutions Shown by the Example of Homogeneous Iron-Chromium-Phosphorus-Carbon Melts, *Arch. Eisen.*, 1968, 39(8), p 587-593.

Chapter 7: Comprehensive Scholarly Discussion

Phosphorous is a typical impurity element existing in high alloy steels. Despite a small quantity of P in steels, it is very important to understand the behavior of P because of its significant influence on steel qualities. Thermodynamic database based on the CALculation of PHase Diagrams (CALPHAD) method [1] is a powerful tool for process optimization and new materials design. The thermodynamic database of the high alloy Fe-Mn-Al-Si-C-P system was developed by means of thermodynamic optimization, aiming at obtaining one set of consistent Gibbs energies of all phases as functions of composition and temperature. In this study, all available phase equilibria and thermodynamic data including activity, entropy, enthalpy and Gibbs energy, etc were critically evaluated simultaneously. The discrepancies between available data were resolved in the critical evaluation process. In the P-containing systems, all experimental data are concentrated in the metal-rich regions while almost no data were reported on the P-rich side, because it's hard to obtain equilibrium data due to high vaporization pressure of P. Exceptionally, the thermodynamic property data for FeP_2 [2,3] and MnP_3 [4] were reported and considered in the present optimization. The consistency and accuracy of the optimization of low-order systems can be tested by the higher-order systems, because only one set of model parameters are used in the entire database.

In the present study, all thermodynamic calculations were performed in FactSage software [5], in which the well-established thermodynamic databases for the gases (FactPS) and oxides (FToxid) are available to assist the present modeling. The thermodynamic modeling also relies on the selection of the model. In this study, the Modified Quasichemical Model (MQM) [6,7] considering short-range ordering (SRO) and Compound Energy Formalism (CEF) [8] considering the crystal

structures were used to describe the liquid phase and solid solutions, respectively. For examples, the Fe-P system and Mn-P system exhibit very similar negative interactions and apparent short-range orderings happen in the composition of $n_i : n_P = 2:1$ ($i = \text{Fe, Mn}$) in both liquid solutions. In comparison, Al, Si and C have weaker interactions than Fe and Mn with P and a short-range ordering is probably happening at the composition of $n_j : n_P = 1:1$ ($j = \text{Al, Si, C}$) based on reported data. These short-range orderings were considered in the present modeling by using MQM. Besides, when extending from the binary systems to the ternary system, proper interpolation techniques [7] depending the nature of each binary system are available to predict the Gibbs energy of the ternary liquid. This gives more realistic description of the entropy of the liquid solution and increases the predictive ability of the database, compared to the conventional Bragg-Williams Random Mixing Model (BWRMM) with assumption of random mixing of entropy and an intrinsic Muggianu interpolation technique for all the systems. A good example for application of the interpolation technique is given by the Fe-Mn-P system, in which the binary Fe-Mn liquid solution is in almost ideal mixing while the Fe-P and Mn-P liquids exhibit very negative interactions, so the Toop-type interpolation technique (P as an asymmetric component) was introduced to the ternary Fe-Mn-P liquid solution. According to the present optimization, the behavior of the Fe-Mn-P system is excellently predicted without adding any ternary liquid parameters. In the Fe-Si-P, Fe-Al-P and Fe-C-P liquids, proper interpolation techniques depending on the nature of related binary systems were also introduced. It should be noted that thermodynamic properties of liquid P were optimized from very dilute region to the metallic side. The thermodynamic properties of P in very dilute region are of great importance to the P refining of metals.

Thermodynamic descriptions of the solid phases are associated with the liquid solution. The Gibbs energies of the solid phases and liquid solution, on one hand, have to satisfy their own thermodynamic properties, on the other hand, they have to compensate each other to reproduce the liquidus and solidus. Similar to the liquid solution, the Gibbs energies of solid phases in the higher-order systems are also affected by those in the lower-order system. For example, the Gibbs energy of BCC_A2 solid solution in the Fe-P system are adopted in all the (Fe-P)-containing ternary and multicomponent systems. The Gibbs energy of the ternary (Fe, Mn)₃P phase also relies on the Gibbs energies of Fe₃P and Mn₃P. That is, the optimization of binary systems plays a key role in the optimization of the multicomponent system. The lower-order systems were preliminarily optimized to test higher-order systems. Once the descriptions of higher-order systems cannot be satisfied with, then the lower-order systems have to be reoptimized until all the subsystems are consistently optimized. Because of the scale limitation of thesis, only the thermodynamic optimization results of binary Fe-P, Mn-P, Al-P, Si-P, C-P systems and ternary Fe-Mn-P, Fe-Al-P, Fe-Si-P, Fe-C-P systems are presented in current thesis. According to the present thermodynamic optimization, most of experimental data of these sub-systems were accurately reproduced.

The current database can be used not only for the phase diagram and thermodynamic property calculations at normal compositions and temperatures but also for the P refining in various dilute alloys within the Fe-Mn-Al-Si-C system. As shown in Chapter 3 and Appendix A, the present thermodynamic database can be applied for the dephosphorization calculations of steel and FeMn alloys with combination of existing database for gases (FactPS) and oxides (Oxides) in FactSage. The present calculations have been proved to be accurate, compared to available experimental data.

References

1. <http://www.calphad.com>.
2. G. Lewis and C. E. Myers, Vaporization Properties of Iron Phosphides, *J. Phys. Chem.*, 1963, 67(6), p 1289-1292.
3. W. Franke, K. Meisel, and R. Juza, The relationship of Phosphorus to Iron, *Z. Anorg. Chem.* 1934, 218(4), p 346-359.
4. W. Biltz, F. Wiechmann, and K. Meisel, The Systematic Study of Affinity. LXXVI. Tensiometric Analysis of the Higher Phosphides of Manganese, *Z. Anorg. Allgem. Chem.*, 1937, 234(2), p 117-129.
5. C. W. Bale, P. Chartrand, S. A. Degterov, G. Eriksson, K. Hack, R. B. Mahfoud, and S. Petersen, FactSage Thermochemical Software and Databases, *CALPHAD*, 2002, 26(2), p 189-228.
6. A. D. Pelton, S. A. Degterov, G. Eriksson, C. Robelin, and Y. Dessureault, The Modified Quasichemical Model I-Binary Solutions, *Metall. Mater. Trans. B*, 2000, 31(4), p 651-659.
7. A. D. Pelton and P. Chartrand, The Modified Quasi-chemical Model: Part II. Multicomponent Solutions, *Metall. Mater. Trans. A*, 2001, 32(6), p 1355-1360.
8. M. Hillert, The Compound Energy Formalism, *J. Alloys Compound*, 2001, 320(2), p 161-176.

Chapter 8: Summary and Suggestions for Future Work

8.1 Summary

The present research was conducted to develop a self-consistent thermodynamic database for the high alloy Fe-Mn-Al-Si-C-P steel system. For this objective, critical evaluation and thermodynamic optimization of all available literature data were performed to obtain one set of Gibbs energy functions for all phases within the systems. In the literature review, experimental data including the information of stable phases, crystal structures, thermodynamic properties, phase equilibria, etc. were collected. To resolve the discrepancies among all the collected data, a critical evaluation and preliminary assessment of the data was performed to check their consistency and reliability. Then thermodynamic modeling/optimization of the P-containing high alloy Fe-Mn-Al-Si-C-P system was performed from low-order systems to high-order systems to reproduce all reliable experimental data using the CALculation of PHase Diagrams (CALPHAD) [1] method.

In the present thermodynamic optimization, the liquid solutions were described using the Modified-Quasichemical Model (MQM) [2,3] considering the short-range ordering (SRO) of the liquid solutions. Using the MQM, the atom pair formation and introduction of coordination numbers provide greater flexibility in reproducing the SRO among liquid components and combining the binary parameters to the high-order solutions. Besides, geometric interpolation techniques [3] were used to predict the Gibbs energy of the ternary liquids based on optimized binary parameters. Determination of a proper interpolation technique depends on the nature of each binary liquid solution involved in the target ternary solution. A proper interpolation technique increases the predictive ability of the MQM model in higher-order liquid solutions. The solid

solutions were described using the Compound Energy Formalism (CEF) [4] with consideration of their crystallographic structures.

The Gibbs energies of pure elemental liquid and solid components were directly taken from the Scientific Group Thermodata Europe (SGTE) database [5]. The Gibbs energies for all related stoichiometric compounds were critically optimized based on available thermodynamic data including the heat capacities, enthalpies, entropies and other sources of Gibbs energy data. In the present study, thermodynamic properties of all intermediate phosphides and P in various liquid alloys, various types of phases diagrams of the Fe-Mn-Al-Si-C-P system were critically optimized to reproduce all the reliable experimental data. The thermodynamic database developed in the present study can also be used to predict unexplored phase diagrams and thermodynamic properties of other sub-systems of the Fe-Mn-Al-Si-C-P alloys at any compositions and temperatures. All the thermodynamic calculations were performed using the FactSage system [6] containing the Gibbs energy minimization routine.

The highlights of thermodynamic optimization in each chapter of current thesis are summarized as follows:

i. In Chapter 3, all available experimental data are critically evaluated for conducting thermodynamic optimization of the Fe-P system is using the CALculation of PHADiagram (CALPHAD) method. The Fe-P phase diagram, thermodynamic properties of P in liquid Fe and stability of each intermediate iron phosphides in the entire composition range have been critically optimized to resolve the discrepancies left in previous assessments. The behavior of P in both

liquid and solid Fe was accurately described in the present study. Besides, dephosphorization reactions of molten Fe-P alloys were calculated by combining the present database and the FToxid database in FactSage [6]. The distribution of P between liquid metal and slag at different temperatures were accurately calculated, compared to experimental data.

ii. In Chapter 4, thermodynamic modeling results of the Mn-P and Fe-Mn-P systems were presented. The Gibbs energies of binary stoichiometric manganese phosphides were determined by reproducing reliable experimental data. Besides, the ternary (Fe,Mn)₃P, (Fe,Mn)₂P, (Fe,Mn)P phosphides solutions were modeled as solid solutions with mutual dissolution of isomorphous Fe₃P and Mn₃P, Fe₂P and Mn₂P, FeP and MnP, respectively. The thermodynamic properties of the Fe-Mn-P liquid solution in both dilute region and high-P concentration region were accurately predicted without any additional parameters.

iii. In Chapter 5, the binary Al-P and ternary Fe-Al-P systems are thermodynamically optimized using the CALPHAD approach. The Al-P phase diagram data and thermodynamic properties of stoichiometric AlP compound were critically assessed for optimizing the binary Al-P and ternary Fe-Al-P systems. The discrepancies in the existing experimental diagrams of the Al-rich region of the Al-P system and various isopleths diagrams of Fe-Al-P system were resolved. More accurate and consistent descriptions on the Fe-Al-P system than previous assessments have been obtained in the present study.

iv. In Chapter 6, the Fe-Si-P and Fe-C-P systems are thermodynamically optimized by means of the CALPHAD approach. The ternary stoichiometric compound FeSi₄P₄ was considered as a stable

phase in the Fe-Si-P system for the first time. The phase diagrams of the pseudo-binary FeSi-FeP, FeSi-FeSi₄P₄, and FeSi₂-FeSi₄P₄ systems, isopleths at wt. %Si = 7 and wt. %P = 13 of the Fe-Si-P system, the solubility of P in BCC_A2 Fe-Si alloys, and thermodynamic properties of P in molten Fe-rich and Si-rich regions of Fe-Si alloys were all well reproduced. In the Fe-C-P system, various vertical diagrams of the Fe-rich region from low temperatures to high temperatures were critically evaluated and accurately optimized in the present study. At 1300 °C to 1600 °C, variations of the solubility of C in molten Fe with the P content were excellently reproduced in this modeling. In addition, the liquidus projection of the Fe-rich region of the Fe-C-P system was well predicted, compared to experimental data.

v. In Appendix A, the thermodynamic database for the Fe-Mn-Al-Si-C-P system was developed and applied to describe the behavior of P various high alloy system. Good predictions on the high-order systems given by the example of the Fe-Mn-C-P system, and the distribution of P between molten slag and high Mn hot metal, molten slag and high-C FeMn alloys are obtained, compared to available experimental data. Besides, by combination of the FToxid database and FactPS database with present new metallic thermodynamic database, the composition and quantity of the flux, temperature, initial Si content of the metal were optimized to enhance the dephosphorization of FeMn alloys.

8.2 Suggestions for Future Work

In the present study, all the sub-systems of the Fe-Mn-Al-Si-C-P system with experimental data available were optimized. Although the present thermodynamic optimization results are in good accordance with reliable experimental data, there are still some limitations needed to be addressed:

i. Basically, most experimental data of the P-containing systems are only concentrated in the region of $x_P < 0.5$ due to high vaporization pressure of P in the high-P region. Therefore, descriptions of the high-P region (liquidus, thermodynamic properties of high-P phosphides such as FeP₂, MnP₃, etc.) were determined using very limited literature information, or predicted from the phase equilibria and thermodynamic properties of the low P region where reliable experimental data are available. So, more data in the P-rich region are still very necessary. Besides, more advanced experimental techniques overcoming the difficulties of experiments for the P-rich region should be developed.

ii. In the Fe-Si-P system, experimental data on the liquidus, solidus and the solubility of P in Si-rich Fe-Si alloys are hardly reproduced simultaneously with reasonable model parameters. Further experimental studies on the Si-rich phase equilibria are necessary.

iii. The metallic Ni, Cr, Ti and Nb are very important alloying elements in steel. Therefore, it is very necessary to include these elements in the developed high alloy steel database in the future for more extensive applications.

iv. The impurities N, S and O are also very important elements in high alloy steels. They should be included together with P in the developed database for the steelmaking applications.

References

1. <http://www.calphad.com>.

2. D. Pelton, S. A. Degterov, G. Eriksson, C. Robelin, and Y. Dessureault, The Modified Quasichemical Model I-Binary Solutions, *Metall. Mater. Trans. B*, 2000, 31(4), p 651-659.
3. D. Pelton and P. Chartrand, The Modified Quasi-chemical Model: Part II. Multicomponent Solutions, *Metall. Mater. Trans. A*, 2001, 32(6), p 1355-1360.
4. M. Hillert, The Compound Energy Formalism, *J. Alloys Compound*, 2001, 320(2), p 161-176.
5. T. Dinsdale, SGTE Data for Pure Elements, *CALPHAD*, 1991, 15(4), p 317-425.
6. W. Bale, P. Chartrand, S. A. Degterov, G. Eriksson, K. Hack, R. B. Mahfoud, and S. Petersen, FactSage Thermochemical Software and Databases, *CALPHAD*, 2002, 26(2), p 189-228.

Chapter 9: Contribution to Original Knowledge

The present work is a comprehensive attempt to develop a thermodynamic database of the high alloy Fe-Mn-Al-Si-C-P steel system. Critical evaluation and assessments of all available literature data were performed for the thermodynamic optimization using the CALculation of PHADiagram (CALPHAD) approach. The main original contributions to knowledge from this work are listed as follows:

i. Thermodynamic modeling of liquid solutions of the Fe-P, Mn-P, Al-P, Si-P and C-P systems was performed for the first time using the Modified Quasichemical Model (MQM), considering the short-range ordering of the liquid solutions.

ii. In the Fe-P system, phase equilibria of BCC_A2 phase at both low and high temperatures were accurately described for the first time. Besides, various sources of experimental data (Heniran standard state, Raoultian standard state, 1 wt.% standard state, partial pressure of gaseous $P/P_2/P_4$, etc.) for the activity of P in molten Fe at different temperatures were critically assessed together to describe the thermodynamic properties the Fe-P liquid solution. For the first time, the Fe-P database can be used to not only calculate conventional phase diagrams and thermodynamic properties at normal composition range, but also calculate the thermodynamic behavior of P in very dilute region, which has very important applications for the steelmaking process.

iii. The Fe-Mn-P, Fe-Al-P, Fe-Si-P and Fe-C-P systems were thermodynamically optimized over the entire composition range using the MQM for the first time. Proper geometric interpolation

techniques were used to predict the Gibbs energies of the ternary liquids for the first time, which increased the predictive ability and reduced the number of model parameters added to the database.

iv. In the Fe-Mn-P system, the activities of Fe, Mn and P were accurately predicted in the entire composition of liquid solutions at various temperatures without any additional parameters, which proves high reliability of present database. The present database can be used to do dephosphorization calculations of high Mn steels and Mn alloys.

v. The Al-P system was accurately optimized by reproducing thermodynamic properties of stoichiometric AlP compound, the liquidus of the Al-rich region and the melting point of AlP were simultaneously for the first time. Besides, the ternary stoichiometric compound FeSi_4P_4 was considered in the present optimization for the first time.

vi. The present thermodynamic database can be utilized to predict unexplored phase diagrams and thermodynamic properties of the Fe-Mn-Al-Si-C-P system at any temperatures and compositions. This database can be also used to do dephosphorization calculations of any system within Fe-Mn-Al-Si-C.

Appendix A: Application of the Present Thermodynamic Database to the Dephosphorization of Ferromanganese (FeMn) Alloys

Zhimin You¹, In-Ho Jung²

1. Department of Mining and Materials Engineering, McGill University, 3610 University Street, Montreal, QC, H3A 0C5, Canada

2. Department of Materials Science and Engineering, and Research Institute of Advanced Materials (RIAM), Seoul National University, 1 Gwanak-ro, Gwanak-gu, Seoul, 08826, South Korea

(to be submitted October 2020)

Abstract

In the production of FeMn alloys, the impurity such as P originated from the raw materials and processing route needs to be tightly controlled. The BaO-based fluxes are considered more effective than CaO-based fluxes and reducing dephosphorization agents in the P removal of FeMn alloys. In the present study, the thermodynamic database for the Fe-Mn-Si-Al-C-P system was developed using the CALculation of PHADiagram (CALPHAD) method, and it has been applied to determine the optimal conditions (flux composition, flux quantity, temperature, initial Si content) for the P refining using the BaO-MnO-BaF₂ flux. All the thermodynamic calculations were performed using the FactSage software with presently developed database and existing thermodynamic databases for oxides and gases.

Key words: FeMn alloys, Dephosphorization, CALPHAD, BaO-MnO-BaF₂ flux, Thermodynamic Database

A. 1 Introduction

Ferromanganese (FeMn), as one of the typical bulk ferroalloys, is widely applied in the steelmaking process, because of its roles as the deoxidizer and sulphide former (30%), and alloying agent (70%) of the steels [1]. Manganese (Mn), as the dominant component of FeMn alloys, contributes to enhancing the steel mechanical properties such as hardenability, tensile strength, toughness, etc. [2]. In particular, the demand for high quality FeMn alloys is increasing with the production of high Mn steels such as Twin Induced Plasticity (TWIP) and Transformation Induced Plasticity (TRIP) steels.

FeMn alloys are usually produced by reduction of Mn ores either in Blast Furnace (BF) or Submerged Arc Furnace (SAF) at the temperature above 1200 °C. Mn ores mainly exist in the form of the oxide mixture (MnO_2 , Mn_2O_3 , Mn_3O_4 , MnO , Fe_2O_3 , Fe_3O_4 , etc.) [3]. Reduction of Mn oxides into metallic Mn is done by either carbothermic or silicothermic reduction process. That's why C and Si always present with Mn and Fe in the FeMn alloys. According to the C content, FeMn alloys are classified into three grades: standard high-C FeMn (74-82 wt.%Mn and 6.0-7.5 wt.%C), medium-C FeMn (80-85 wt.%Mn and 1.0-1.5 wt.%C), and low-C FeMn (80-90 wt.%Mn and 0.1-0.75 wt.%C) [1,4]. High-C FeMn alloys are produced by carbothermic reduction either in BF process or SAF process. Medium-C FeMn alloys are produced by partial oxidation of high-C FeMn alloys or silicothermic reduction of Mn ores using SAF process. In comparison, low-C FeMn alloys can only be produced by silicothermic reduction process in SAF. Since the mid-20th century, BF process has been gradually replaced by SAF process for the FeMn alloys production [5] because of demands for higher-grade FeMn alloys, less reductant (coke) consumption and longer refractory life of SAF. However, certain volume of FeMn alloys are now still produced with

BF process because low grade Mn ores (as low as 28 wt.%Mn) can be processible in BF process with high consumption of C [6]. In the production of FeMn alloys, however, it is hard to avoid the impurities like P originated from the raw materials and processing route. The content of P in FeMn alloys can be 0.4 to 0.6 in weight percent, so P can be directly transferred to the steels through the alloying process. Though the P is in a small quantity in steels compared to other metallic components, the presence of P in steels can cause serious quality defects like weld brittleness and inner cracks. It is thus very necessary to tightly control the P in molten FeMn alloys.

To understand the behavior of P in FeMn alloys, it is of great importance to know the thermodynamic properties of P in the FeMn alloys. In the present study, the thermodynamic database of the Fe-Mn-Al-Si-C-P system was constructed using the CALculation of PHADiagram (CALPHAD) method. In particular, the liquid solutions and solid solutions were described using the Modified Quasichemical Model (MQM) [7,8] considering the short-range ordering and Compound Energy Formalism (CEF) [9] considering their crystallographic structures. All available phase diagram data and thermodynamic property data of the sub-systems of the Fe-Mn-Al-Si-C-P system were critically evaluated for optimizing the consistent Gibbs energy functions of all the phases in the corresponding systems. The developed thermodynamic database in this study was combined with FToxid database for oxides and FactPS database for gas to calculate complex dephosphorization reactions among the metal, slag and gas phases [10]. According to the present calculations, the optimal flux compositions and conditions was determined to improve the dephosphorization efficiency of high-C FeMn alloys. All the thermodynamic calculations were performed using the FactSage software [11].

A. 2 Thermodynamic Models

A. 2. 1 Pure Elements and Stoichiometric Compounds

In the sub-systems of the Fe-Mn-Al-Si-C-P system, the Gibbs energies of all the pure elemental substances were taken from the Scientific Group Thermodata Europe (SGTE) database compiled by Dinsdale [12], while the Gibbs energies of involved stoichiometric compounds were determined based on the available thermodynamic data including the heat capacity, standard enthalpy of formation and standard entropy at 298.15 K, as shown below:

$$G_T^\circ = \left(\Delta H_{298.15K}^\circ + \int_{298.15K}^T C_P dT \right) - T \left(S_{298.15K}^\circ + \int_{298.15K}^T \frac{C_P}{T} dT \right) \quad (\text{A.1})$$

where G_T° is the Gibbs energy at temperature T , $\Delta H_{298.15K}^\circ$ and $S_{298.15K}^\circ$ are the standard enthalpy of formation and standard entropy at 298.15 K, and C_P is the heat capacity. The heat capacity of each stoichiometric compound was expressed as a function of temperature by fitting experimental C_P data. In the case of compounds without available experimental C_P data, their C_P were assessed using the Neumann-Kopp (NK) rule [13] or the C_P functions of neighboring compounds.

When a pure element or stoichiometric compound exhibits either antiferromagnetic or ferromagnetic transition, then an additional magnetic contribution term G^{mg} will be also taken into account in the determination of its Gibbs energy using the empirical expression proposed by Inden [14] and modified by Hillert and Jarl [15].

$$G^{\text{mg}} = RT \ln(\beta + 1) g(\tau) \quad (\text{A.2})$$

Here τ is calculated by T/T^* and T^* is the critical temperature of magnetic transition associated with Neel temperature T_N for antiferromagnetic materials and Curie temperature T_C for

ferromagnetic materials. β is the average magnetic moment per mole of atoms expressed in Bohr magnetons. $g(\tau)$ is a polynomial function derived by Hillert and Jarl [15].

A. 2. 2 Solid Solutions

In the present study, the Gibbs energies of the solid solutions were described using the Compound Energy Formalism (CEF) [9] with consideration of their crystallographic structures. For all the sub-systems of the Fe-Mn-Al-Si-C-P system, there exists many different solid solutions including the disordered FCC_A1, BCC_A2, HCP_A3, CBCC_A12, CUB_A13, Diamond_A4, Me_nP ($n = 3, 2, 1$), Cementite, etc. and the ordered BCC_B2, L12 phases. The calculation of the Gibbs energy of a solid solution depends on its sublattice model. For example, the Gibbs energy of a solid solution with a two-sublattice $(A, B)_p(C, D)_q$ is calculated using the following equation:

$$\begin{aligned} G_S^{sol.} = & y_A y_C G_{A:C} + y_A y_D G_{A:D} + y_B y_C G_{B:C} + y_B y_D G_{B:D} \\ & + pRT (y_A \ln y_A + y_B \ln y_B) + qRT (y_C \ln y_C + y_D \ln y_D) \\ & + \sum_{i=0,1,2,\dots} \left(\sum_{m=C,D} y_A y_B y_m^i L_{A,B;m} + \sum_{n=A,B} y_n y_C y_D^i L_{n:C,D} \right) + \sum_{i=0,1,2,\dots} y_A y_B y_C y_D^i L_{A,B:C,D} + G^{mg} \end{aligned} \quad (A.3)$$

where y_A , y_B and y_C , y_D are the site fractions of component A, B in the first sublattice ($y_A + y_B = 1$) and components C, D in the second sublattice ($y_C + y_D = 1$), respectively. $G_{A:C}$, $G_{A:D}$, $G_{B:C}$, $G_{B:D}$ are Gibbs energies of the end-members $A_p C_q$, $A_p D_q$, $B_p C_q$, $B_p D_q$, respectively. ${}^i L_{A,B;m}$ and ${}^i L_{n:C,D}$ are interaction parameters between A and B of the first sublattice and between C and D of the second sublattice. ${}^i L_{A,B:C,D}$ is the reciprocal interaction parameter with the first sublattice occupied by components A, B and the second sublattice occupied by components C, D. G^{mg} is the magnetic Gibbs energy contribution. For other solid solutions with different sublattices, the Gibbs

energies can be calculated using the analogous approach depending on their crystallographic sublattice arrangements.

A. 2. 3 Liquid Solution

The Modified Quasichemical Model (MQM) [7,8] considering the short-range ordering (SRO) of the nearest-neighbor atoms was used to describe the liquid solutions because it gives a more realistic description of the entropy of the liquid solution, compared to the conventional Bragg-Williams Random Mixing Model (BWRMM). In the binary A-B liquid solution, for example, the atom pair exchanging reaction was considered and expressed as follows:



where (i-j) represents the nearest-neighbor pair between components i and j , and Δg_{AB} is the Gibbs energy change of forming 2 moles (A-B) pairs. The Gibbs energy of the liquid solution is calculated using the following equation:

$$G_L^{sol.} = (n_A G_A^o + n_B G_B^o) - T \Delta S^{conf.} + n_{AB} (\Delta g_{AB} / 2) \quad (\text{A.5})$$

where n_A and n_B are the numbers of moles of A atoms and B atoms. G_A^o and G_B^o are the molar Gibbs energies of pure A and B components. $\Delta S_{AB}^{conf.}$ is the configurational entropy of mixing given by random distribution of the (A-A), (B-B) and (A-B) pairs, which describes the SRO of the liquid solution. Δg_{AB} is the model parameter for reproducing the Gibbs energy of the binary A-B solution and can be expanded as a polynomial in terms of the atomic pair fractions X_{AA} and X_{BB} as follows:

$$\Delta g_{AB} = \Delta g_{AB}^o + \sum_{i \geq 1} \Delta g_{AB}^{i0} X_{AA}^i + \sum_{j \geq 1} \Delta g_{AB}^{0j} X_{BB}^j \quad (\text{A.6})$$

here, Δg_{AB}^o , g_{AB}^{i0} and g_{AB}^{0j} are the adjustable model parameters that can be functions of the temperature. In the MQM, the coordination number of each component was considered and

allowed to vary with composition to reproduce the SRO of the solution. When extending from the binary systems to the ternary system, proper geometric interpolation techniques are available to predict the Gibbs energy of the ternary liquid solution. Determination of the interpolation technique depends on the nature of involved binary systems. If necessary, ternary correction terms can be further introduced to give a more precise description of the ternary system.

A.3 Prediction of Present Database

In the present study, new metallic database for the Fe-Mn-Al-Si-C-P system was developed to describe the thermodynamic behavior of impurity P in various Fe-Mn-Al-Si-C alloys. In the development of this new database, the Gibbs energies of all the phases were determined by reproducing all the available reliable experimental data. The low-order subsystems were first optimized to obtain the model parameters and then extended to high-order subsystems. Since only binary and ternary parameters are added in the database, so thermodynamic description of multi-component systems completely relies on the accuracy of these low-order parameters. In the present study, the thermodynamic descriptions are kept consistent throughout all the subsystems. **Fig. A.1** presents the solubility of C at different P contents of the liquid Fe-Mn-C-P solution at 1400 °C, compared to experimental data [16,17]. It shows that the predicted solubility of C in both high-Mn hot metal (**Fig. A.1(a)**) and FeMn alloys (**Fig. A.1(b)**) from the present database are in excellent agreement with available experimental data.

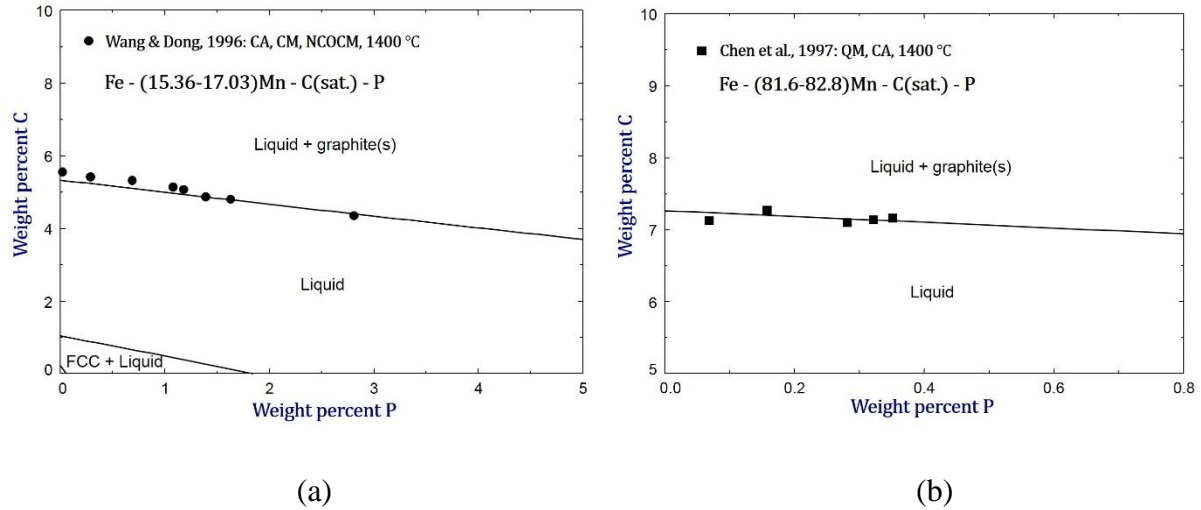
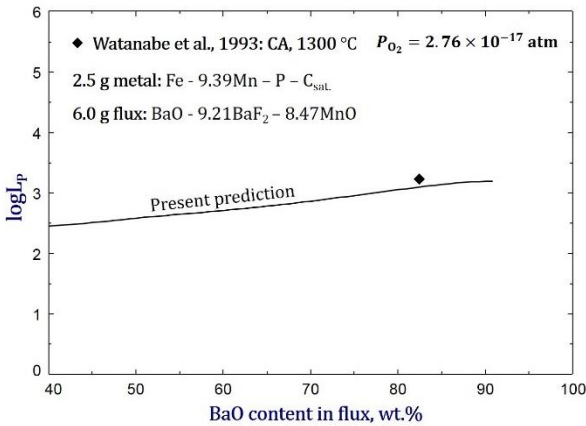
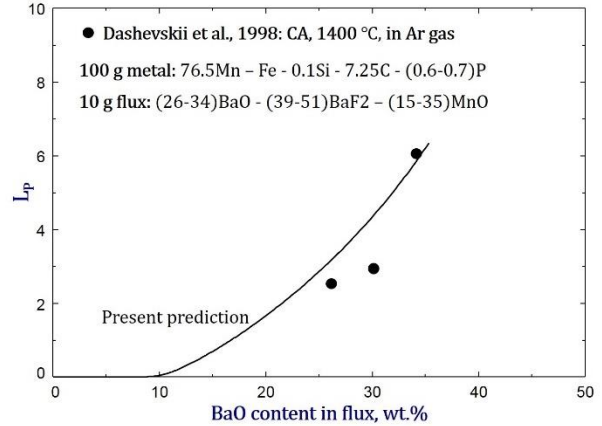


Figure A.1 Solubility of C affected by the P content in the (a) high Mn hot metal and (b) FeMn alloys of the Fe-Mn-C-P system at 1400 °C, compared to experimental data [16,17]

The accuracy of description of the thermodynamic behavior of P among the metal, oxides and gas phase were tested against the available experimental data, with the combination of the well-constructed FTOxid database for oxides and FactPS database for gases. For example, it can be seen from **Fig. A.2** that the predicted partition coefficient of P between molten slag and hot metal, (**Fig. A.2(a)**) molten slag and high-C FeMn alloys (**Fig. A.2(b)**) from the present database and previously developed FTOxid and FactPS database in FactSage are in excellent agreement with available experimental data [18,19]. Therefore, it is believed that the thermodynamic database developed in this work is reliable for the dephosphorization calculations of the FeMn alloys in a wide composition range.



(a)



(b)

Figure A.2 Predicted P partition coefficient between molten slag and (a) high Mn hot metal and (b) high-C FeMn alloys based on present database, compared to experimental data [18,19]

A.4 Phosphorous Refining of Ferromanganese Alloys

A.4.1 Dephosphorization Approaches

In the production of FeMn alloys, it is hard to remove the P from molten alloys because of high affinity of Mn to P. Therefore, appropriate approaches for tightly control P in molten FeMn alloys are of great importance. Among various approaches for the dephosphorization, the physical beneficiation technique is not suitable for the removal of P since the vapor pressure of Mn is even higher than that of P at the smelting temperatures of FeMn alloys. Till now, the P of FeMn alloys is mainly removed through two approaches: (i) adding basic fluxes under reducing conditions, and (ii) adding basic fluxes under oxidizing conditions.

For the dephosphorization under reducing conditions, CaC_2 - CaF_2 , CaSi - CaF_2 and Ca - CaF_2 are commonly used as the fluxes to treat molten alloys. Zhu et al. [20], Harashima et al. [21], Wang and Shao [22], and Karbowniczek et al. [23] studied the dephosphorization of FeMn alloys using

the CaSi/CaC₂-CaF₂ fluxes under reducing conditions. In their experiments, the P removal efficiencies were relatively high, but it is only applicable for FeMn alloys containing low C content because the combination of Ca and P is restricted with high C in the molten alloys. In addition, Ca₃P₂ as the dephosphorization product under reducing conditions is likely to form toxic phosphine (PH₃) once in contact with the moisture [24]. And also, it is hard to maintain a very low oxygen potential during the production. Concerning these limitations, dephosphorization under reducing conditions has not been widely accepted by the steelmakers.

For the dephosphorization under oxidizing conditions, in comparison, the alkali oxide, CaO- and BaO-based fluxes are usually added to the melts for forming the slag with proper chemistry. The P refining of FeMn alloys is mainly conducted using basic fluxes under oxidizing conditions. Li₂CO₃, K₂CO₃-KF, Na₂CO₃-KF and Na₂CO₃-NaF are common alkali oxide-based fluxes used to remove the P. Wang and Shao [22] investigated the dephosphorization behavior of pig iron and FeMn alloys using the Na₂CO₃ flux. It was found that Na₂CO₃ behaved a good performance on the dephosphorization of pig iron but a much poorer efficiency on that of FeMn alloys. In their experiments, the dephosphorization rate of alloys containing 10 wt.%Mn dropped to 20% after 10 mins treatment. Fujita et al. [25] observed that the P was hardly removed from high Mn ferroalloys using either Li₂CO₃ flux or Na₂CO₃-NaF flux. As is well known, CaO-based fluxes are widely applied to the steelmaking process and show very good performance on the P removal. Some researchers [18,25-27] studied the P refining of FeMn alloys using CaO-based fluxes, which unfortunately turned out be inefficient to remove P from the metal. Though CaO exhibits high basicity and can react with P to produce calcium phosphates under oxidizing conditions, the presence of high Mn causes the decrease of the P activity because of very negative interaction

between Mn and P. To improve the dephosphorization efficiency, many efforts were donated to develop new flux systems that are more effective than CaO-based fluxes. According to many attempts, BaO-based fluxes are probably the alternative agents because BaO is more basic than CaO. In previous experiments, various BaO-based fluxes including BaCO₃ [18,25,28,29], BaCO₃-BaF₂ [30], BaO-BaCl₂-MnO₂ [31], BaO-BaF₂-MnO [18,19,30,32-34], BaCO₃-BaCl₂-MnO₂ [26], BaCO₃-BaF₂-MnO₂ [35], BaCO₃-BaF₂-MnO₂-Fe₂O₃ [36], BaCO₃-MnO₂-Fe₂O₃ [27], BaO-BaF₂-MnO₂-Fe₂O₃ [37] were selected as the dephosphorization agents for high-Mn steels and FeMn alloys in a wide composition range. It was consistently recognized that BaO-based fluxes exhibit a much higher dephosphorization efficiency than CaO-based fluxes [19,25,27-29]. Besides, Fujita et al. [25] also found that dephosphorization reaction of high-Mn (wt.%Mn = 5 - 60) and high-C (wt.%C = 3.0 - 6.7) pig irons using the BaCO₃ flux proceeded faster than that using CaCO₃-based, Na₂CO₃-based and Li₂CO₃-based fluxes. On the other hand, Guo and Dong [37] investigated the equilibrium distribution of P between high-C FeMn alloys and various BaO-halide slags at 1400 °C. They found that the phosphate capacity of the slag differed with the type of halide in the order BaF₂ > BaCl₂ > CaF₂ > CaCl₂, which is consistent with the results obtained by Chaudhary et al. [30]. However, the loss of Mn was relatively high in the experiments of Chaudhary et al. [30], because the generated CO₂ from the decomposition of BaCO₃ created high oxygen potential, which caused oxidation of Mn and the Mn oxide would transferred from the metal to the top slag. This problem also existed in other experiments using BaCO₃-based fluxes [25,26,36,38], unless other sources of Mn like MnO₂ were added to compensate the Mn loss [27,35,36]. Ahundov et al. [32] conducted equilibrium experiments between the molten BaO-BaF₂-MnO and C-saturated hot metal containing Mn up to 21 wt.% at 1200 °C to 1300 °C under the CO atmosphere. From the experiments, a partition ratio of 50 for P between Fe-8wt.%Mn-C(sat.) and BaO-BaF₂-MnO flux

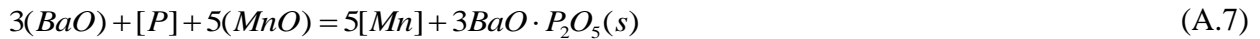
was obtained at 1200 °C. Watanabe et al. [19] obtained a partition ratio of P as high as 1730 between the BaO-8.47wt.%MnO-9.21wt.%BaF₂ flux and the Fe-9.39wt.%Mn-C(sat.) alloys at 1300 °C, which can be reproduced based on the present database, as shown in **Fig. A.2(a)**. According to the experimental studies [24,18,30,33,34], the BaO-BaF₂-MnO fluxes exhibited very good performances in the P refining of various composition ranges of FeMn alloys with very limited Mn loss. In the dephosphorization of FeMn alloys under oxidizing conditions, it has been commonly recognized that the dephosphorization can be promoted with: (i) high basicity, (2) relatively low temperatures, (3) relatively high oxygen potential, (4) fluxes with proper chemistry and (5) appropriate flux quantity, etc.

Overall, the physical beneficiation technique is not suitable for removing the P from FeMn alloys. Despite high dephosphorization rate using the fluxes such as CaC₂-CaF₂, CaSi-CaF₂ and Ca-Si-CaF₂, etc. under reducing conditions, it is not suitable for the industrial application due to environmental concerns, harsh oxygen potential and strict limitation of C content in the alloys. Under oxidizing conditions, CaO-based and alkali oxide-based fluxes are not acceptable because of low dephosphorization efficiency in refining the FeMn alloys containing high Mn. In comparison, BaO-based fluxes with higher basicity than CaO-based fluxes show much better performance in the dephosphorization of both hot metal and Mn alloys in a wide composition range. However, dephosphorization with BaCO₃-based fluxes can result in a high loss of Mn without additional source of Mn. Adding MnO to BaO-based fluxes can develop oxidizing conditions and avoid high loss of Mn simultaneously. As a consequence of high-melting temperature of the BaO-MnO system, BaF₂, as the most effective fluxing agent among various halides, can increase the activity coefficient of MnO and facilitates the melting of BaO-MnO fluxes

at moderate temperatures, which provides beneficial conditions for accelerating the metal/slag reactions and cutting down the Mn loss. Therefore, the BaO-MnO-BaF₂ fluxes are considered promising in the P refining of FeMn alloys.

A.4.2 Determination of the Flux Composition

As discussed above, the BaO-MnO-BaF₂ flux is very promising in the P refining of high Mn alloys. The dephosphorization reaction occurred at the interface between the BaO-MnO-BaF₂ flux and FeMn alloys is described as follows:



As can be seen in the reaction, MnO acts as the source of oxygen for oxidizing soluble P into P₂O₅ while BaO provides high basic conditions that promotes the occurrence of dephosphorization reactions by reducing the activity of P₂O₅ in the slag. However, combination of BaO with MnO is not enough for removing the P from the Mn alloys due to high melting point of MnO (1785 °C). Hence, BaF₂ is usually added to the BaO-MnO flux to facilitate the melting of flux and improve the fluidity of the slag. Besides, it also was reported that addition of BaF₂ reduce the activity coefficient of MnO and the loss of Mn [19,39]. Whereas dephosphorization of FeMn alloys is a process encompassing very complex reactions. To enhance the dephosphorization efficiency, it is necessary to optimize the parameters including the composition of flux and metal, quantity of flux, temperature, oxygen potential etc.

Table A.1 Chemical composition (wt.%) of starting high-C FeMn alloy (100 grams)

Components	Mn	Fe	Si	P	C
Composition	76	16.2	0.3	0.5	7.0

In the present study, the dephosphorization reactions between high-C FeMn alloys and molten slag was modelled based on the present new thermodynamic database and previously well-optimized FToxid database and FactPS database in FactSage 7.3. In the previous laboratory studies [18,19,24,33,34], the quantity of flux varied a lot among different experiments, but usually the amount of 10 to 20wt.% of the charged metal were added for the P refining treatment. In this modeling, 15 grams flux (15 wt.%) was set to treat 100 grams high-C FeMn alloy. The chemical composition of the typical high-C FeMn alloy is given in **Table A.1**. As a result of high melting point of MnO, the initial amount of MnO in the flux was set as 10, 15, 20 and 25 wt.% of the flux amount. Under fixed amount of MnO, the amount of BaO and BaF₂ changes with each other. Besides, let's assume dephosphorization reactions occurs at 1300 °C. Variations of the P content in the metal with the BaO content of the flux are plotted in **Fig. A.3**. As can be seen, the P is hardly removed with 10 wt.%MnO in the flux. This is probably due the existence of Si in the FeMn alloy, which will be discussed later. With 15, 20 and 25 wt.%MnO in the flux, the P content starts to decrease when the BaO content is more than 20.5 wt.%, and then it decreases to minimum values with the increase of the BaO in the flux. Obviously, the smaller minimum P content can be obtained by higher MnO content in the flux. From the figure, it can be seen the P content can be reduced from 0.50 to 0.377, 0.252 and 0.132 wt.% with 15, 20, and 25 wt.%MnO in the flux, respectively. To obtain these minimum P contents, 31, 37.33, 44 wt.%BaO need to be added in the flux respectively.

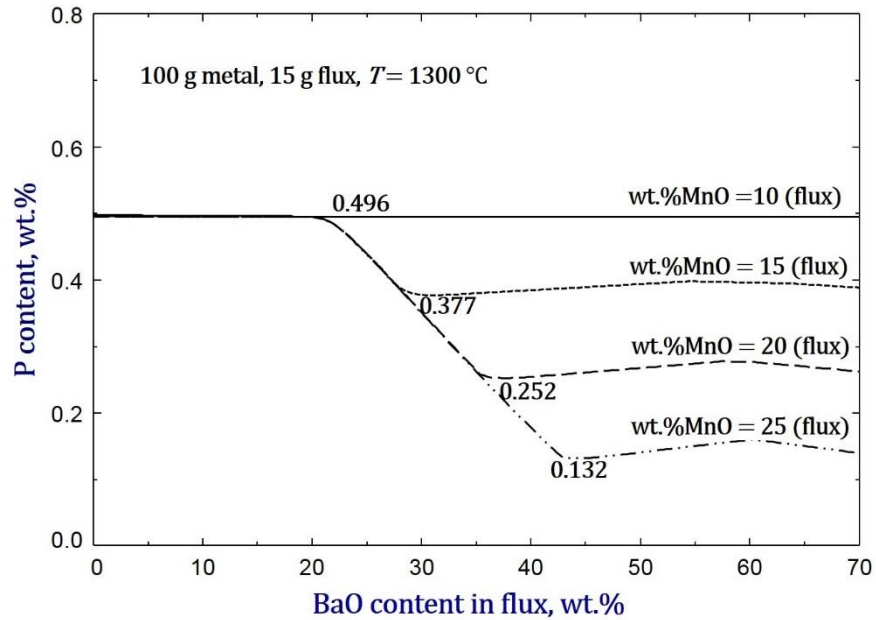


Figure A.3 Variation of the P content in metal (100 g) with the contents of BaO and MnO in the flux (15 g) at 1300 °C

Fig. A.4 shows variations of the quantity of all stable phases with the BaO content in the flux at 1300 °C when the MnO content is set as 10, 15, 20 and 25 wt.% of the flux. As shown in **Fig. A.3** and **Fig. A.4**, All minimum P contents can be achieved with no formation of solid phases, except that when 25 wt.%MnO is added to the flux, solid bC_2S (mainly Ba_2SiO_4) is precipitated within the molten slag, which greatly deteriorates the fluidity of the slag and slows down the metal/slag reactions. Therefore, 25 wt.%MnO in the flux is not acceptable though a lowest P content is calculated, as indicated in **Fig. A.4**, because in is hard to reach the complete equilibrium condition in the real case of solid phases precipitating within the molten slag.

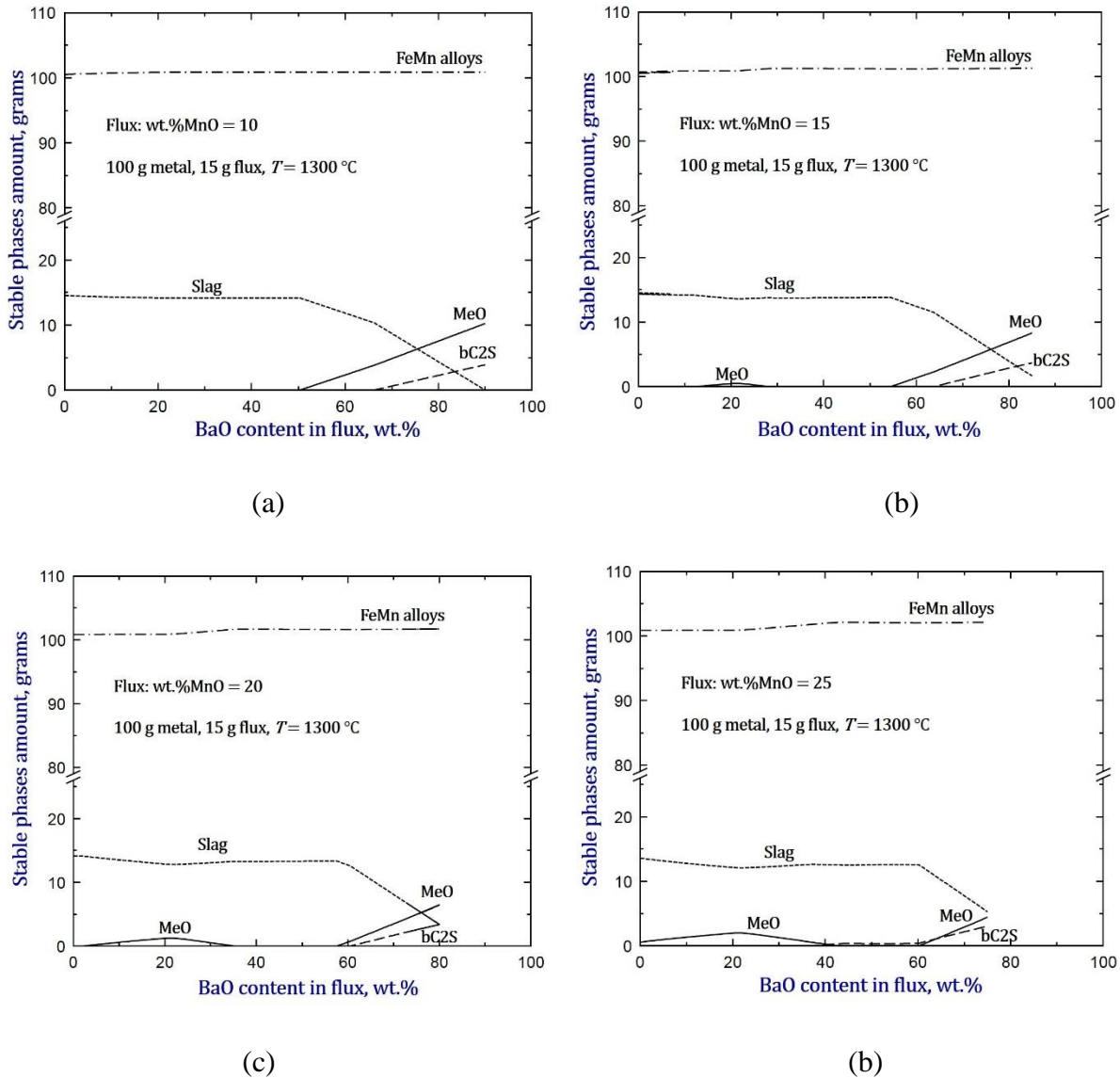


Figure A.4 Variations of the amounts of all stable phases with the BaO content at 1300 °C when (a) wt.%MnO = 10, (b) wt.%MnO = 15, (c) wt.%MnO = 20, and (d) wt.%MnO = 25 of the flux

To maximize the dephosphorization efficiency, the optimal configuration of the flux needs to be determined. According to the above calculations, the optimal MnO content of the flux is between 20 wt.% and 25 wt.%. By using the same approach, an amount of 22.67 wt.%MnO of the flux is calculated, which is the critical flux amount for current conditions to obtain the best

dephosphorization efficiency at 1300 °C. Under the same conditions, the calculated P content and the quantity of all stable phases at different BaO contents are plotted in **Fig. A.5**. It shows a minimum P content of 0.187 wt.% (dephosphorization rate: 62.6%) can be obtained without solid phase formation in the molten slag when 15 grams flux in the composition of 41wt.%BaO - 22.67wt.%MnO - 36.33wt.%BaF₂ is used for the dephosphorization, as listed in **Table A.2**.

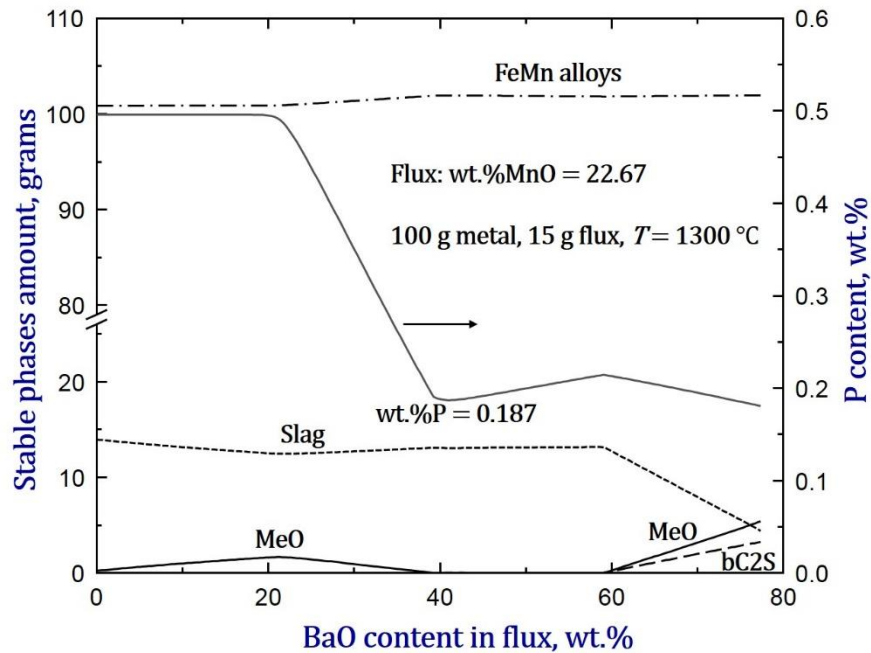


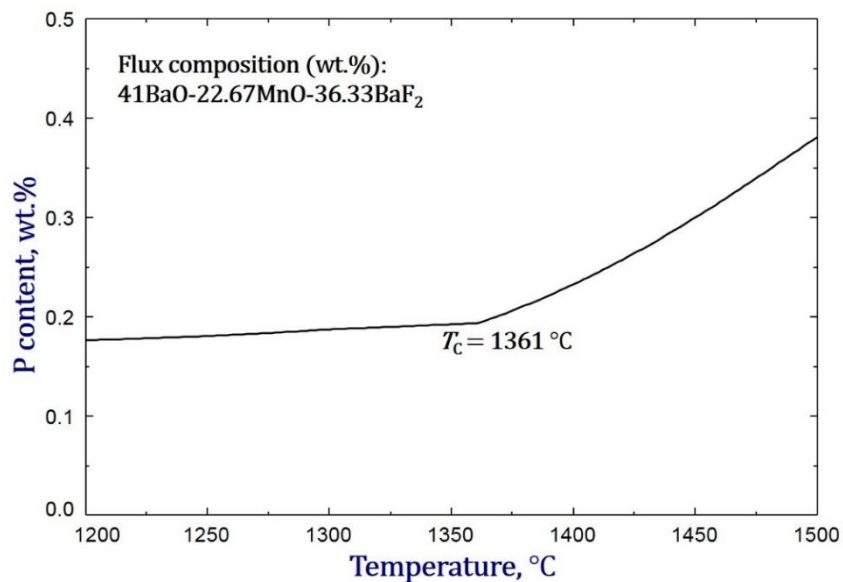
Figure A.5 Variations of the amount of all stable phases and the dissolved [P] content of FeMn alloys with the BaO content at 1300 °C when $m(\text{MnO}) = 22.67$ wt.% of the flux

Table A.2 Optimal composition (wt.%) of the BaO-MnO-BaF₂ flux

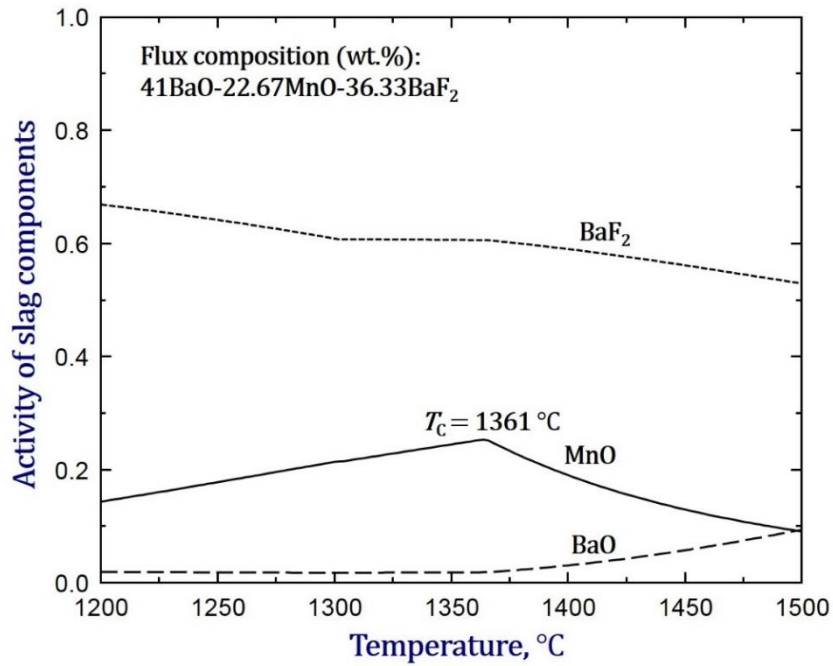
Components	BaO	MnO	BaF ₂
Composition	41.0	22.67	36.33

A.4.3 Effect of Temperature on Dephosphorization

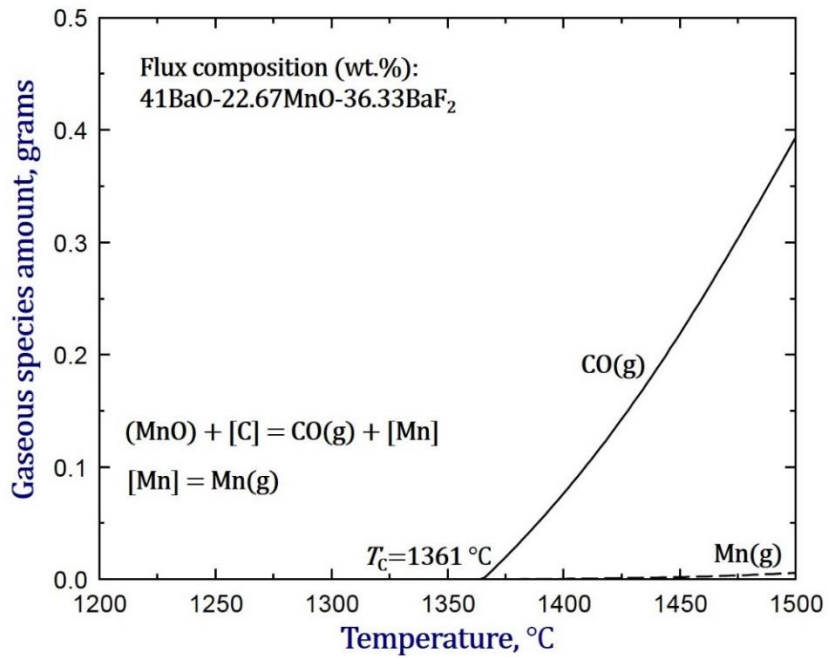
It is well known that relatively low temperatures can improve the dephosphorization rate of steels, because dephosphorization reaction is exothermal. According to the determined optimal composition of the flux (41wt.%BaO - 22.67wt.%MnO - 36.33wt.%BaF₂), the effect of temperature on the dephosphorization of high-C FeMn alloys is investigated. **Fig A.6** presents variations of P in the alloys, activities of slag components, CO(g) and Mn(g) vapor with the temperature. As shown in **Fig. A.6(a)**, the P content of the alloys after dephosphorization increases slightly with the temperature until 1361 °C, then it increases more significantly at $T > 1361$ °C, because the activity of MnO in slag starts to decrease sharply with increasing temperature above 1361 °C, as shown in **Fig. A.6(b)**. Though the activity of molten BaO in the slag keeps increasing, the sharp drop of MnO activity outweighs the slight increase of the activity of BaO. This is probably caused by the sudden formation of CO(g) gas, as can be seen in **Fig. A. 6(c)**. At 1361 °C, the P content is removed from 0.50 wt.% to 0.194 wt.% by adding 15 grams of the optimal flux to 100 grams high-C FeMn alloys.



(a)



(b)



(c)

Figure A.6 Effect of the temperature on the (a) dephosphorization efficiency, (b) activity of each slag component, and (c) formation of gas species

A.4.4 Effect of Flux Quantity on Dephosphorization

Dephosphorization rate, on one hand, can be restricted by increasing the temperature. On the other hand, dephosphorization reaction proceeds faster at higher temperatures. However, the Mn loss also increases with the increase of temperature. As discussed above, the final P content increases slightly from 0.187 wt.% to 0.197 when the temperature increases from 1300 °C to 1361 °C. **Fig. A.7** shows the composition of each metallic component using the optimal flux at 1361 °C. It is shown the P content does not change until more than 7.5 grams flux is added, then it continuously decreases to 0.098 wt.% (dephosphorization rate: 80.4%) when 18 wt.% flux of charged alloys is added. That is, the dephosphorization rate can be increased from 62.6% to 80.4% by adding 3 wt.% more flux (41wt.%BaO - 22.67wt.%MnO - 36.33wt.%BaF₂) at 1361 °C.

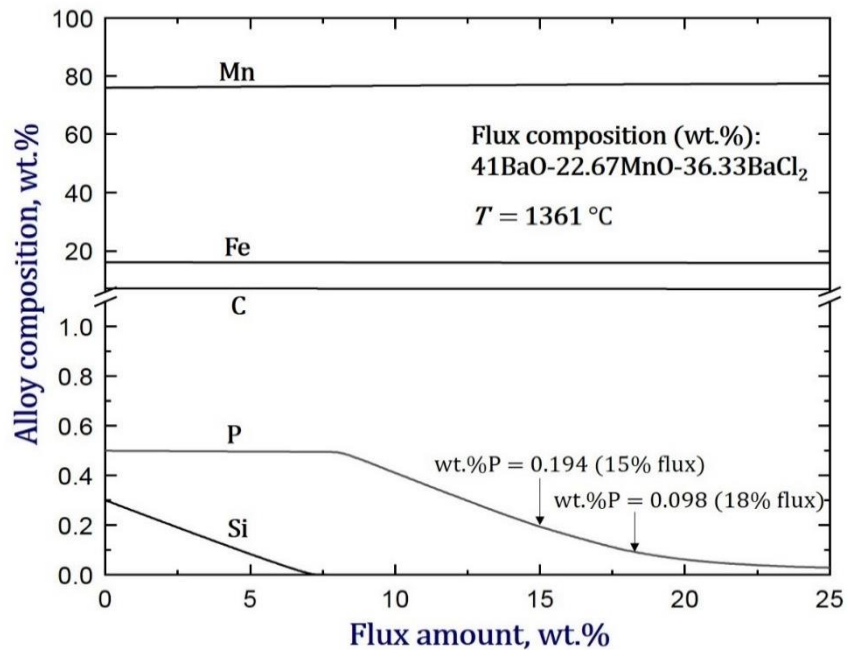
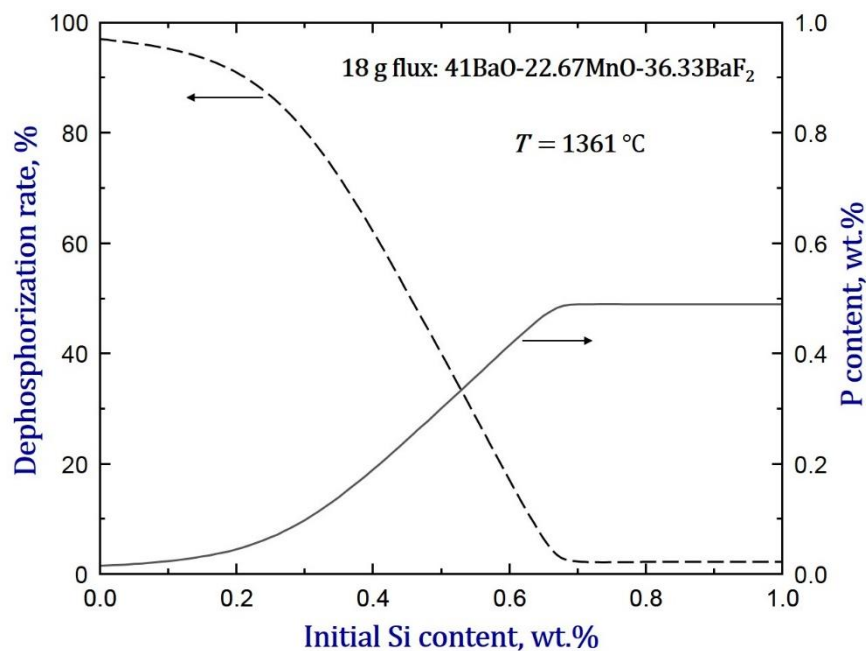


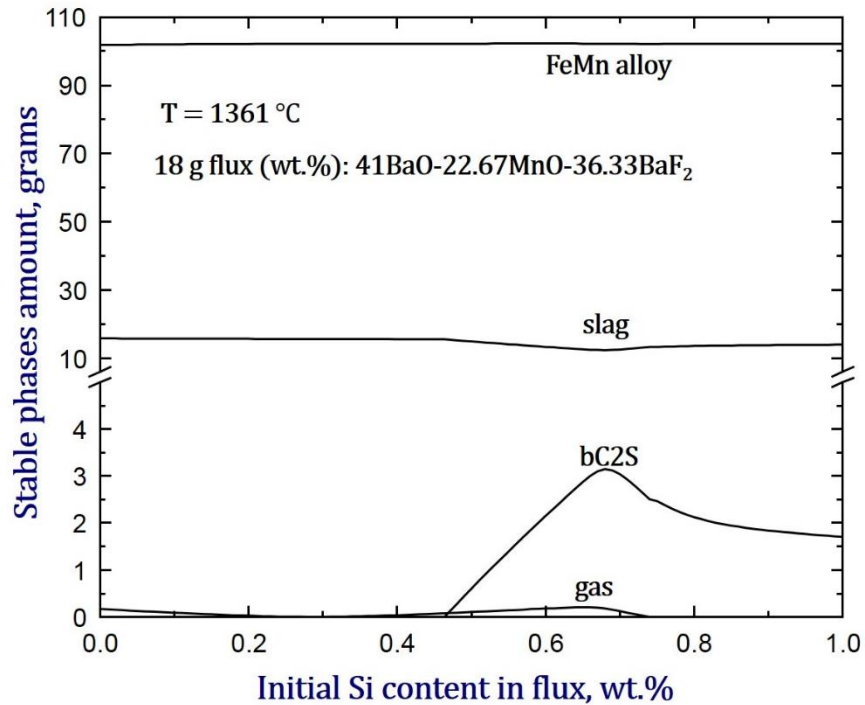
Figure A.7 Variation of each alloy component with the added amount of flux in the composition of 41wt.%BaO-22.67wt.%MnO-36.33wt.%BaCl₂ at 1361 °C

A.4.5 Effect of Initial Si Content on Dephosphorization

It is interesting to see from **Fig. A.7** the P content doesn't change but Si content decreases quickly with increasing flux amount. When almost all the Si is removed, the P content starts to decrease with more than 7.5 wt.% of flux. To investigate the effect of Si on the dephosphorization of FeMn alloys, the final P content and dephosphorization rate at 1361 °C with initial Si ranging from 0 to 1 wt.% are calculated in **Fig. A.8(a)**. Obviously, the final P content increases significantly with the increase of initial Si content in the metal. When Si content is above 0.7 wt.%, dephosphorization reaction almost doesn't happen, because oxidation of dissolved Si consumed the MnO to produce SiO₂ and further react with BaO to precipitate solid Ba₂SiO₄ phase, as indicated in **Fig.A.8(b)**. It is thus necessary to tight control the initial Si content for having high dephosphorization efficiency. As shown in **Fig. A.8(a)**, for example, the initial Si content should be no more than 0.36 wt.% for removing no less than 70% P from the alloys.



(a)



(b)

Figure A.8 Effect of the initial Si content of the flux on (a) dephosphorization efficiency and (b) formation of stable phases

Overall, BaO-based fluxes are more effective in the dephosphorization of various composition of FeMn alloys, compared to CaO-based fluxes and reducing dephosphorization fluxes. The BaO-MnO-BaF₂ flux is very promising because of high dephosphorization efficiency, low Mn loss and friendly environmental concern. The thermodynamic database for high alloy steel developed in the present study can be applied to optimize the chemistry and quantity of the flux and other conditions, with combination of the FToxid database and FactPS database. The flux in the amount of 15 to 18 wt.% charged metal and in the composition of 41wt.%BaO - 22.67wt.%MnO - 36.33wt.%BaF₂ is determined as the optimal flux for the dephosphorization treatment of high-C FeMn alloys at 1300 to 1361 °C.

Summary

In the present study, a thermodynamic database for the Fe-Mn-Al-Si-C-P system was constructed using the Modified Quasichemical Model and Compound Energy Formalism. The present database has been confirmed to be accurate in calculating the dephosphorization of both hot metal and FeMn alloys in a wide composition range. Effects of the composition of flux and alloys (initial Si content), quantity of flux, temperature, initial Si content etc. on the dephosphorization reactions are investigated. According to the present calculations, the flux in the quantity of 15 to 18 wt.% flux in the composition of 41wt.%BaO-22.67wt.%MnO-36.33wt.%BaF₂ is determined as the optimal flux for dephosphorization of high-C FeMn alloys at 1300 to 1361 °C. All the thermodynamic calculations were performed using the FactSage software with presently developed database and existing thermodynamic databases for oxides and gases.

Acknowledgements

We gratefully acknowledge the Steelmaking Consortium Members, Hyundai Steel, Tata Steel Europe, Posco, Doosan Heavy Industry and Construction, SeAh Besteel, Nucor Steel, RioTinto, JFE Steel, Nippon Steel, RHI, Voestalpine, and Natural Science and Engineering Research Council of Canada for supporting the present project. This work was also supported by the National Research Foundation of Korea (NRF) grant funded by the Korean government (MSIT) (No. NRF-2020R1A5A6017701). We would also like to thank the McGill Engineering Doctorate Award (MEDA) program.

References

1. J. Safarian and L. Kolbeinsen, Purity Requirements for Mn-alloys for Producing High Manganese Trip and Twip Steels, Infacon XIII, *Thirteenth International Ferroalloys Congress*, Almaty, Kazakhstan, 9-12 June 2013, p 175-184.
2. SATYENDRA. Ispatguru System of Referencing, 2014, <http://ispatguru.com/manganese-in-steels/>.
3. I. S. Cardakli, Production of High Carbon Ferromanganese from a Manganese Ore Located in Erzincan, *Maters Dissertation*, Middle East Technical University, 2010.
4. American Society for Testing Materials (ASTM): Annual book of ASTM standards, *Ferrous Castings Ferroalloys*, 1993, 01-02, p 59-61.
5. <https://en.wikipedia.org/wiki/Ferromanganese>.
6. E. Jipnang, P. Monheim, and H. Oterdoom, Process Optimisation Model for FeMn and SiMn Production. *The Thirteenth International Ferroalloys Congress, Efficient Technologies in Ferroalloy Industry*, Almaty, Kazakhstan. 9-12 June 2013, p 811-820.
7. D. Pelton, S. A. Degterov, G. Eriksson, C. Robelin, and Y. Dessureault, The Modified Quasichemical Model I-Binary Solutions, *Metall. Mater. Trans. B*, 2000, 31(4), p 651-659.
8. D. Pelton and P. Chartrand, The Modified Quasi-chemical Model: Part II. Multicomponent Solutions, *Metall. Mater. Trans. A*, 2001, 32(6), p 1355-1360.
9. M. Hillert, The Compound Energy Formalism, *J. Alloys Compound*, 2001, 320(2), p 161-176.
10. C. W. Bale, E. Bélisle, P. Chartrand, S. A. Decterov, G. Eriksson, K. Hack, I. H. Jung, Y. B. Kang, J. Melancon, A. D. Pelton, C. Robelin, and S. Petersen, FactSage Thermochemical Software and Databases-recent Developments, *CALPHAD*, 2009, 33(2), p 295-311.

11. C. W. Bale, P. Chartrand, S. A. Degterov, G. Eriksson, K. Hack, R. B. Mahfoud, and S. Petersen, FactSage Thermochemical Software and Databases, *CALPHAD*, 2002, 26(2), p 189-228.
12. A. Dinsdale, SGTE Data for Pure Elements, *CALPHAD*, 1991, 15(4), p 317-425.
13. J. Leitner, P. Vončka, D. Sedmidubsky, and P. Svoboda, Application of Neumann-Kopp Rule for the Estimation of Heat Capacity of Mixed Oxides, *Thermoch. Acta*, 2010, 497(1-2), p 7-13.
14. G. Inden, Project Meeting CALPHAD V, Max-Planck-Inst, *Eisenforschung*, Dusseldorf, Germany, 1976, p 111.
15. M. Hillert and M. Jarl, A Model for Alloying in Ferromagnetic Metals, *CALPHAD*, 1978, 2(3), p 227-238.
16. S. Wang and Y. Dong, Thermodynamic Properties of Phosphorus and Manganese in Ferromanganese Melts, *J. Iron and Steel Research*, 1996, 8(2), p 1-5.
17. Er. Chen, Y. Dong, and S. Guo, Thermodynamics of Mn-based Mn-Fe-P-C Systems, *J. East China Uni. Metall.*, 1997, 14(3), p 196-202.
18. V.Ya. Dashevskii, V.I.Kashin, N.P.Lyakishev, B.F.Velichko and A.V.Koval, Dephosphorization of Manganese Ferroalloys with CaO & MnO Based Slag-Forming Mixtures, *The Proceedings of INFACON 8: BaO-Based Fluxes Has Better Performance on De-P, Compared to CaO-Based Fluxes*, *The Chinese Society for Metals*, Beijing, China, June 7-10, 1998.
19. Y. Watanabe, K. Kitamura, I. P. Rachev, F. Tsukihashi, and N. Sano, Thermodynamics of Phosphorus and Sulfur in the BaO-MnO Flux System between 1573 and 1673 K, *Metall. Trans. B*, 1993, 24(2), p 339-347.

20. B. Zhu, M. Deng, Y. He, and D. Li, A Study on Reducing Dephosphorization of Fe-Mn alloys, *HuaDong, J. East China Inst. Metall.*, 1991, 8(1), p 1-7.
21. K. Harashima, Y. Fukuda, H. Kajioka, and Y. Nakamura, Dephosphorization and Desulfurization of High Chromium Steel and High Manganese Steel with CaC_2 - CaF_2 Flux and Decomposition of CaC_2 , *Tetsu-to-Hagane*, 1986, 72(11), p 1685-1692.
22. D. Wang and X. Shao, Experimental Study on Dephosphorization of Ferro-Manganese, *Iron and Steel*, 1983, 18(4), p 14-21.
23. M. Karbowniczek, A. Michaliszyn, Z. Wcisto, and W. Slezak, Dephosphorization of Ferromanganese, *Acta Metall. Slovaca Conf.*, 2014, 4, p 138-144.
24. P. N. Chaudhary, R. K. Minj, and R. P. Goel, Development of a Process for Dephosphorisation of High Carbon Ferromanganese, *INFACON XI*, New Delhi, India, February 18-21, 2007, p 288-296.
25. M. Fujita, H. Katayama, A. Yamamoto, and M. Matsuo, Dephosphorization of Fe-Mn-C Alloy with BaCO_3 , *Tetsu-to-Hagané*, 1988, 74(5), p 816-822.
26. B. Zhu, M. Deng, Y. Dong, and D. Li, Thermodynamic Analysis on Oxidizing Dephosphorization, *J. East China Inst.*, 1993, 10(12), p 13-18.
27. S. Wang, Y. Dong, and D. Li, Study on the Desiliconization and the Dephosphorization of Fe-Mn Alloys, *J. East China Inst. Metall.*, 1994, 11(3), p 8-13.
28. Z. T. Ma, R. Ni, C. Zheng, and J. Wang, Dephosphorization of Mn-based Alloys, *Steel Research*, 1992, 63(3) p 112-119.
29. S. Wang and Y. Dong, The Study of Dephosphorization of Ferro-Manganese Alloy with Barium Carbonate Flux, *Ferro-Alloys*, 2000, (5), p 4-7.

30. P. N. Chaudhary, R. P. Goel, and G. G. Roy, Dephosphorization of High Carbon Ferromanganese Using BaCO₃ based Fluxes, *Ironmaking and Steelmaking*, 2001, 28(5), p 396-403.
31. T. Matsuo and K. Maya, *Current Adv. Mater. Process*, 1990, 3, p 119.
32. N. Ahundov, F. Ogly, F. Tsukihashi, and N. Sano, Equilibrium Partitions of Manganese and Phosphorus between BaO-BaF₂ Melts and Carbon Saturated Fe-Mn Melts, *ISIJ International*, 1991, 31(7), p 685-688.
33. X. Liu, O. Wijk, R. Selin, and J. O. Edström, Phosphorus Equilibrium between BaO-BaF₂-MnO Fluxes and Ferro-Manganese Melts, *Steel Research*, 1995, 66(3), p 96-102.
34. P. N. Chaudhary, R. K. Minj, R. Krishna, and R. P. Goel, Selective Removal of Phosphorus from High Carbon Ferromanganese-An Improved Process, *Metals Materials and Processes*, 2004, 16(2-3), p 217-226.
35. B. Wu, Y. Dong, S. Wang, E. Chen, Y. Zhou, and H Wang, Experimental Study on Dephosphorization of Ferromanganese Melt by BaCO₃-based Flux, *Steelmaking*, 2002, 18(3), p 44-48.
36. H. Wang, S. Wang, Y. Zhou, B. Wu, and Y. Dong, Study on Component Change for Oxidation Dephosphorization of Mn-Fe Alloy under Vacuum Condition, *Ferro-Alloys*, 2004, 175(2), p 24-27.
37. S. Guo and Y. Dong, Experimental Study on Dephosphorization of Ferromanganese Alloys by BaO-Halide Fluxes, *Iron and Steel*, 1998, 33(1), p 26-29.
38. Y. E. Lee, Proceedings of Sixth Iron and Steel Congress, Nagoya, *ISIJ*, 1990.
39. S. C. Shim, F. Tsukihashi, and N. Sano, Thermodynamic Properties of the BaO-MnO Flux System, *Metall. Trans. B*, 1993, 24(2), p 333-337.